

THE MOLECULAR INTERSTELLAR MEDIUM FROM $z=0-6$

by

Desika Narayanan

A Dissertation Submitted to the Faculty of the
DEPARTMENT OF ASTRONOMY
In Partial Fulfillment of the Requirements
For the Degree of
DOCTOR OF PHILOSOPHY
In the Graduate College
THE UNIVERSITY OF ARIZONA

2007

THE UNIVERSITY OF ARIZONA
GRADUATE COLLEGE

As members of the Dissertation Committee, we certify that we have read the dissertation prepared by Desika Narayanan entitled "The Molecular Interstellar Medium from $z=0-6$ " and recommend that it be accepted as fulfilling the dissertation requirement for the Degree of Doctor of Philosophy.

Christopher K. Walker

Date: 2 November 2007

Romeel Davé

Date: 2 November 2007

Arjun Dey

Date: 2 November 2007

Xiaohui Fan

Date: 2 November 2007

Final approval and acceptance of this dissertation is contingent upon the candidate's submission of the final copies of the dissertation to the Graduate College.

I hereby certify that I have read this dissertation prepared under my direction and recommend that it be accepted as fulfilling the dissertation requirement.

Dissertation Director: Christopher K. Walker

Date: 2 November 2007

STATEMENT BY AUTHOR

This dissertation has been submitted in partial fulfillment of requirements for an advanced degree at The University of Arizona and is deposited in the University Library to be made available to borrowers under rules of the Library.

Brief quotations from this dissertation are allowable without special permission, provided that accurate acknowledgment of source is made. Requests for permission for extended quotation from or reproduction of this manuscript in whole or in part may be granted by the head of the major department or the Dean of the Graduate College when in his or her judgment the proposed use of the material is in the interests of scholarship. In all other instances, however, permission must be obtained from the author.

SIGNED: Desika Narayanan

ACKNOWLEDGMENTS

There's a ton of people to thank, and only a limited amount of cache in my brain, so its pretty likely that I'll forget a large number of people who *ought* to be thanked. But, in reality, who's ever gonna look at this page? My parents maybe? My grandparents? My advisor? Some poor graduate student years from now who thinks they'd like to do radiative transfer simulations in galaxies and looks to my thesis for advice. I remember haunting the LPL library so many years ago searching for Phil Maloney's thesis who did some of the first simulations of molecular line emission in galaxy models. So maybe there's some grad student in the year 2020 or something who'll be looking for a thesis idea, and for some odd reason thinks it worthwhile to read my thesis. Man, a grad student in 2020 would have been born the year I graduated high school. I guess that makes me pretty old. In any case, if you're reading this, it might be easier to just Google my name (will Google be around in 2020?) and email me asking for advice.

That said, you're here, my thesis is due tomorrow, and the 'acknow.tex' file is currently only acknowledging Ben Oppenheimer's mom for services rendered. And this probably has to be fixed. So...here come some acknowledgements. Sorry if I forgot you. Also, sorry if for some reason you don't agree with the ordering of names. I don't really know how to order them, so just figured I'd put my advisor first, parents last, and everyone else in between. I thought about writing a random number generator to place the names, but that's way too much work for a thesis due tomorrow. Hopefully I don't forget anyone...this is mostly gonna go as a stream of consciousness thing.

So right, first and foremost the hugest thanks go to my advisor, Chris Walker. Chris was/is the ideal advisor. Its sort of like I was a car with a broken steering wheel, and he'd let me drive in a sort of random path, but gently nudge me in the right direction from time to time to make sure I was heading toward a goal. By allowing me the freedom to explore scientfic ideas by myself, make mistakes, but make sure I always could see the forest for the trees, Chris allowed me the most enriching graduate education I could imagine. Chris also showed an unbelievable enthusiasm for science which was infectious. When I came to him telling him I wanted to work on projects that were only tangentially related to proto-stars, he embraced the opportunity for us to learn about the field together. Turns out alot of the observed effects in galaxy mergers is pretty similar to what you see in protostars. But more than any of this stuff, Chris offered encouragement during times of academic molasses. One example that comes to mind was the summer of 2004, my first summer here at Steward. I spent the entire summer literally looking for a single bug in my radiative transfer code that was causing a photon 'leak'. My photons were escaping and I couldn't figure out where they were going. Chris sat there patientially as days of my bringing random plots in turned into weeks, and offered interpretation of the plots helping me hunt down

where the bug would be. All the time making sure I could see the forest for the trees, of course. So yeah, if you're a young grad student and at Steward, and looking for a good project, go talk to Chris.

Secondly, Romeel Davé provided great advice and help throughout the grad school process, especially when I started on the bulk of my thesis on galaxy mergers. Romeel was really good at helping me focus projects on interesting topics, especially when the field was somewhat hot (like the $z \sim 6$ chapter, for example). Conversations over coffee or group meetings at Local Dough helped progress works in a really fun way.

Most of the projects in this thesis couldn't have been done without the extensive collaborative help of T.J. Cox. T.J. was/is the ideal collaborator. From extremely prompt replies to emails and requests for models to providing a discerning and skeptical view of any results, all of the works greatly benefited from T.J.'s contributions. A typical email from T.J. might start off with 'I just attended this conference and think that we could make a huge impact on this field, that field, and this group of papers if we just did this...'. And of course fun projects always came out of these types of conversations.

A huge thanks to Lars Hernquist who found the prospect of combining their hydrodynamic models with our radiative transfer codes exciting enough to take a chance on the collaboration. A collaboration which I've learned an extraordinary amount from, had a ton of fun working in, and benefited greatly from (by way of a thesis!).

Thanks additionally go to other members the galaxy-merger collaboration, Phil Hopkins, Brant Robertson, Tiziana Di Matteo, Sukanya Chakrabarti, Yuexing Li, and Volker Springel.

Many on the radio side here at Steward also spent countless hours with me explaining the ins and outs of molecular astrophysics. Craig Kulesa, especially, managed somehow to be unfathomably patient with me when I'd bring horrifically simple questions to him about radiative transfer, chemical reaction networks, or plain old coding.

More thanks along the lines of the radio group go to Chris Groppi, Abby Hadden, Chris Martin, John Bieging, Alan Boss, and my favorite telescope operators of all time, Bob Stupak (from the late night halls of CfA!), Bob Moulton, and Patrick who I've spent many many many late nights with at the SMT and on the computer observing remotely via IM. Tom Folkers and Bill Peters helped me out in times of dire technical need on the mountain. Thanks also to Cathi Duncan who squeezed out all the extra SMT time necessary for the observing paper in this thesis. Cathi kindly put up with my begging and pleading for more SMT time as we got snowed out continually for months on Mt. Graham. The expertise of all these people keep the Arizona Radio Observatory going, and the SMT alive. The SMT is a world class telescope, and the operators and downtown crew are the reason behind it.

While I'm still thanking astronomers, huge thanks go to my undergraduate advisor, Fred Hamann. I started working with Fred the first week of my sophomore year in college. I heard third hand a quote from him which completely describes him as an advisor. Someone asked 'I heard you're overseeing Desika on this project...' and his response was 'We're working *together* on this project.' Fred carefully walked the line of holding my hand while allowing me to do what I thought was best at times that was necessary to encourage the astronomy-challenged undergrad that I was. Undergraduate advisement like that was crucial to feeling the ability to think independently in grad school.

Many thanks go to the varied observers in the molecular line community who had great conversations with me, whether or not they believed my models. In no order, Linda Tacconi, Daisuke Iono, Thomas Greve, Padelis Papadopolous, Min Yun, Fabian Walter, Reinhard Genzel, Nicolas Bouche, Nick Scoville, Dominik Riechers, Chris Carilli, Xiaohui Fan. Probably many others.

Kristian Finlator provided perhaps more calming advice than he probably realizes during the breaks where we'd find each other randomly in the interaction area and chat about general coding or research frustrations or breakthroughs. We studied together for the written prelims, and interestingly he was the first person to see me pass both my oral prelim and oral thesis defense.

Big thanks to my prelim and thesis committee members, Chris Walker, Romeel Dave, Arjun Dey, Xiaohui Fan, Casey Papovich and George Rieke for providing great comments on my thesis, and of course for passing me during these exams!

And finally, probably I ought to thank all those teachers from K-12 who made a huge impact on my life. At least the ones I can remember (which I guess means they were the good ones?). Either way, good teachers are worth a hundred times their weight in gold, so vote to increase their salaries.

Mrs Hogan, Mrs Harmon, Mrs Roberts, Mrs Reneke, Mrs Brantley, Mrs Heggestad, Mrs Perry and Mrs Forbes dealt with me as an elementary schooler while I consistently got 'talks too much in class' on my report card. Mr Kurts, Mrs Mulhearn, Mr Fuller, Mr Prescott and Mr Wilson dealt with me through the years where I learned how much fun it was to be a pain in the ass. And in high school, Mr Johnson, Mrs Herschleb, Mr Howland, Mrs Barnett, Ms Row, Mr Wyness, Ms Christensen, Mr Pierce, Mrs Standiford, Mr Avendano, Mrs Haedo, Dr Moulton, Mr Blaskowski, Mr Jones, Mrs Birdsey, Mr Racciopi, Mrs Moretta, Mr Huckabee and probably others whose names I can't remember were phenomenal teachers.

In college I had a number of fantastic professors. In Astronomy, Elizabeth Lada, Richard Elston, John Oliver and Fred Hamann. In physics, Steve Detweiler, Khandker Muttalib, Fred Sharifi, Selman Herschfield, David Rietze, Alan Dorsey, Kevin Ingersent.

And now to the personal people - the people who made my day to day life what it was. Because, in the end, it's just astronomy, and it's the people that're willing to go to No Anchovies with you at a moment's notice that make life what

it is. Note alot of these people I also worked with, though will remember them more for their role in my non-astronomy life.

The Steward Mug Club were with me through the thick and thin of grad school. From those hot summer nights sitting on the Gentle Ben's balcony with Brandon and Annie (Kelly) to lazy dinners at Aleks (Diamond-Stanic) and Maggie's house to hikes, working out and hearing Dorf stories from Jon 'Action-Jackson' Trump, you couldn't have asked for a better crew of people to enjoy Tucson with.

Shane Bussmann and his dry sense of humour and Tiffany Bartz and her snow-spraying hijinx were phenomenal people that I got to not only collaborate with academically, but enjoy a BBQ or two with as well.

A number of people were just flat out amazing to hang out with. (Andy) Skemer and (Brandon) Swift, the Stephs (Steph Cortes, Steph Juneau, and Stefan Herbert-Fort), Kevin 'I can grow a mustache in a day' Flaherty, Jared Gabor, Amy Stutz, Iva Momcheva make up potentially the smartest dot funnest group of people I've known. From halloween parties to the All souls parade to gladiator fighting over the pool to brewing to man-dates to camping to climbing to enjoying hour and a half lunches gabbing, gossiping, and making fun of undergrads walking by in their ridiculous clothing.

Lots of bno's at Plush (big nights out) were had and to be remembered with postdocs while here in Tucson, Dave Sand, Rory Barnes, Yancy Shirley, Mike Cushing, Alison Coil rounding out some of the postdoc people.

Also lots of non astronomers made life outside the halls of Steward fun and exciting. Luke Griffin, Poorvee Vyas, Marie Kessler, Jordy VandeBunte, Ashwin Bijanki, Kit Bartels, Ingrid Daubar Spitale, Sara Gamble, Krista Nunn, as some of the non-astronomers. Other superfun non-astronmers who made my life a little more sane - the cast and crew of New Kevin Improv Comedy for the Masses, The Great Poet L.S. Griffin (double shout out!), Joe Marotta, Boris Glebov, Shuan Clayton, Timmy Budinger, Al Weber, Fernee Fama, Arnie Niekamp, and who knows...maybe more.

Big ups to Ben Oppenheimer and Casey Meakin both for playing the arrogant theorist with me, as well as the late nights at Cigar and Bloody Mary Night, the dancing at IBTs, the scamming on people at Ches, and the hijinx, pranks and railing on Ben's mom that I'll remember forever.

And to the family. My grandparents throughout my life have provided me with nothing but the best wishes and encouragement for academic progress. They were the kind of grandparents who fattened me up when I was a kid, bought me all the books I could get my hands through, played cards with me as a kid, and made their first trip to the US in so many years just to see my high school graduation.

My brother. If for nothing else, for keeping me sane by keeping me on my toes with good fart jokes. But also for growing into a person who knew how to time

a visit to Tucson when I'd need it the most, and someone I could hang out with on a long car ride without having to say a word to, and have the greatest time all day long.

And finally, my parents. As alluded to in the dedication, they taught me that its okay to like doing what you're doing, and to wake up excited to go to school or work is an amazing thing. Its impossible to recount all the small things they did while growing up to encourage me at school. So many things stick out that are totally exemplary of the support they showed throughout. Like when I'd have to wake up at 4 or 5 something to catch the bus, a few days a week my mom would get up with me and cook me eggs and potato bread, my favorite breakfast, and sit with me so I wouldn't have to eat alone while it was still dark out. Or when I couldn't figure out what an eigenvector was in my math methods class in college and my dad would read over my notes and reexplain it all to me while I was making moron mistakes about simple oscillators or something. Or when my mom would try to lighten the mood on the phone in the stressfull weeks before the written prelim in grad school by telling me a different story about something stupid I did as a kid on the phone every day. Through being there for me when times in grad school sucked to putting up with the arrogance I loved to show when things were going well, they provided the perfect amount of encouragement and backing throughout my education.

DEDICATION

For my parents, who taught me that going to school doesn't have to suck. And to Butthead Junior...for you know...being a Butthead.

TABLE OF CONTENTS

LIST OF FIGURES	13
LIST OF TABLES	16
ABSTRACT	17
CHAPTER 1 INTRODUCTION	18
CHAPTER 2 3-DIMENSIONAL NON-LOCAL THERMODYNAMIC EQUILIBRIUM	
RADIATIVE TRANSFER ON GALAXY-WIDE SCALES	26
2.1 Chapter Preface	26
2.2 Chapter Introduction	27
2.3 Radiative Transfer Methodology	27
CHAPTER 3 MOLECULAR LINE EMISSION FROM GRAVITATIONALLY UN-	
STABLE PROTOPLANETARY DISKS	37
3.1 Chapter Abstract	37
3.2 Chapter Introduction	38
3.3 Numerical Methods	41
3.3.1 Hydrodynamics	41
3.3.2 Radiative Transfer	43
3.3.3 The Model and Parameters	46
3.3.4 Chemistry of HCO^+	47
3.4 Images	48
3.4.1 Molecular Transition	48
3.4.2 Inclination	53
3.4.3 Abundances	56
3.5 Line Profiles	56
3.5.1 Non-LTE Effects: Radiative Pumping in the Vicinity of	
Dense Gas Clumps	56
3.5.2 Effects of Abundance and Resolution	59
3.6 Spectral Maps	63
3.7 Chapter Conclusions	63
CHAPTER 4 THE ROLE OF GALACTIC WINDS ON MOLECULAR GAS EMIS-	
SION FROM GALAXY MERGERS	65
4.1 Chapter Abstract	65
4.2 Chapter Introduction	66
4.3 Numerical Methods	70
4.3.1 Hydrodynamics	70
4.3.2 Overview of A Major Merger	73

4.3.3	General Wind Properties in the Simulations	76
4.4	Isolated Disk Galaxy	79
4.5	CO Morphology in Mergers with Winds	84
4.5.1	General Properties of CO Morphology	84
4.5.2	Molecular Outflows	87
4.5.3	CO Half-Light Radius	101
4.6	Signatures of Winds in CO Line Profiles	103
4.6.1	Overview	103
4.6.2	The Driving Force Behind High Velocity Peaks in CO Emission Profiles	107
4.6.3	Distinguishing Characteristics	110
4.7	Discussion	115
4.8	Chapter Conclusions and Summary	119
CHAPTER 5 THE NATURE OF CO EMISSION FROM $z \sim 6$ QUASARS		122
5.1	Chapter Preface	122
5.2	Chapter Abstract	122
5.3	Chapter Introduction	124
5.4	Numerical Methods	127
5.4.1	Cosmological Simulations	128
5.4.2	Galaxy Merger Simulations	130
5.4.3	Evolution of Model Quasars	132
5.5	Excitation and Luminosity of CO	133
5.6	Molecular Gas Morphology	137
5.7	CO Emission Lines	142
5.7.1	General Nature of Modeled Line Profiles	142
5.7.2	Effect of Merger Remnant Structure and Disk Formation on Line Widths	149
5.7.3	CO Line Width-Quasar Luminosity Relation: Potential Selection Effects	153
5.7.4	Interpretation of $z \sim 6$ Quasar Observations	158
5.8	Spheroid, Black Hole, and Dynamical Mass	160
5.9	Comparisons to Other High Redshift Populations	164
5.9.1	Quasars	164
5.9.2	Submillimeter Galaxies	168
5.10	Chapter Summary and Conclusions	171
CHAPTER 6 WARM-DENSE MOLECULAR GAS IN THE ISM OF GALAXIES .		175
6.1	Chapter Abstract	175
6.2	Chapter Introduction	176
6.3	Selection and Observations	179
6.4	CO (J=3-2)/(J=1-0) Line Ratio	181

6.5	Line Profiles	182
6.6	Source of IR Luminosity	187
6.6.1	L_{IR} versus $L_{\text{CO } J=3-2}$	187
6.6.2	L_{IR} versus Mass of Star-Forming Molecular Gas	191
6.7	Chapter Summary	192
CHAPTER 7 MOLECULAR STAR FORMATION RATE LAW INDICATORS IN GALAX-		
	IES	200
7.1	Chapter Abstract	200
7.2	Chapter Introduction	201
7.3	Numerical Methods	205
7.3.1	Hydrodynamics	205
7.3.2	Non-LTE Radiative Transfer	208
7.4	Origin of Observed SFR-CO and SFR-HCN Slopes	212
7.4.1	General Argument	212
7.4.2	Quantitative Reasoning	215
7.4.3	Implications of Results	226
7.5	Testable Predictions	229
7.6	Comparison with Observations	232
7.7	Relationship to Other Models and Interpretations	235
7.8	Conclusions and Summary	238
CHAPTER 8 CONCLUDING REMARKS AND WAYS FORWARD		241
REFERENCES		246

LIST OF FIGURES

2.1	Sample H_2 column density distribution for subgrid modeling of GMCs	32
2.2	Performance of <i>Turtlebeach</i> from radiative transfer test problems . .	36
3.1	Equatorial density contours for protoplanetary disk	41
3.2	Effect of transition choice on model HCO^+ image of proto-GGP region	42
3.3	Effect of angular resolution on model HCO^+ image of proto-GGP region	49
3.4	Effect of inclination on model HCO^+ image of proto-GGP region .	50
3.5	Effect of abundances on model HCO^+ image of proto-GGP region .	51
3.6	HCO^+ J=7-6 line profiles through proto-GGP	53
3.7	HCO^+ J=7-6 line profiles through secondary dense clump	54
3.8	HCO^+ J=7-6 line profiles at 0.5 depletion for various telescopes . .	55
3.9	HCO^+ J=7-6 line profiles at 0.1 depletion for various telescopes . .	57
3.10	HCO^+ J=7-6 line profiles at 0.01 depletion for various telescopes . .	59
3.11	Spectral map at 0.5 depletion	61
3.12	Spectral map at 0.1 depletion	62
4.1	SFR, BHAR and L_{bol} for model BH	74
4.2	Feedback energy rates (instantaneous and integrated) for merger model BH	77
4.3	Column density for fiducial disk galaxy to exhibit our methods . .	80
4.4	Simulated CO (J=1-0) through (9-8) emission for fiducial disk galaxy	81
4.5	Model CO SED for fiducial disk galaxy	82
4.6	Model CO (J=1-0) emission contours from merger sbBH	85
4.7	Model CO (J=1-0) emission contours of outflow entrained in black hole-feedback driven winds in merger model BH	90
4.8	Excitation properties of black hole-feedback driven outflow in merger model BH	91
4.9	CO (J=1-0) emission contours of outflow strength as a function of merger wind model	92
4.10	Mass of imageable outflows as a function of merger evolution . . .	95
4.11	Model CO (J=1-0) emission contours from black hole feedback-driven outflow in coplanar merger model	97
4.12	Mass of imageable outflows as a function of merger evolution for models BH and co-BH	98
4.13	CO halfflight radius as a function of time for model with and without AGN feedback-driven winds	99

4.14	Average half-light radius as a function of CO transition for various wind models in mergers	100
4.15	CO (J=1-0) line profiles as a function of CO morphology in model BH	104
4.16	Goodness of fit for a single Gaussian fit to spectra from model BH as a function of time	105
4.17	Physical origin of high velocity peaks as a function of BHAR, SFR and L_{bol} in merger model BH	112
4.18	Physical origin of high velocity peaks as a function of SFR and L_{bol} in merger model no-winds	113
4.19	Number of high velocity peaks as a function of limiting velocity for three different wind models in mergers	114
5.1	Peak of CO SED as a function of $z \sim 6$ quasar host galaxy buildup and evolution	134
5.2	CO SED at three points during peak of $z \sim 6$ quasar activity	135
5.3	Velocity-integrated CO intensity (multi-transition), SFR, and L_{bol} as a function of redshift for $z \sim 6$ quasar	138
5.4	Evolution of CO (J=1-0) emission contours from $z \sim 6$ quasar host galaxy	139
5.5	CO (J=3-2) emission from quasar host galaxy at peak of quasar phase across 9 sightlines	143
5.6	Excitation dependent CO morphologies in $z \sim 6$ quasar host galaxy	144
5.7	Model CO (J=6-5) from three $z \sim 6$ quasar host galaxies	145
5.8	Velocity dispersion in CO (J=6-5) emission lines for three $z \sim 6$ quasar host galaxies as a function of redshift	147
5.9	Histogram of sightline-dependent line widths as a function of $z \sim 6$ quasar halo mass	148
5.10	CO (J=1-0) morphology and emission lines from coplanar binary $z \sim 6$ merger	151
5.11	Fraction of rotationally supported gas as a function of redshift for $z \sim 6$ quasar host galaxies	154
5.12	CO (J=6-5) emission line width versus B -band luminosity in $z \sim 6$ quasar host galaxy	156
5.13	Percent of sightlines with line widths compatible with observations in most massive $z \sim 6$ quasar host galaxy	157
5.14	Model dynamical masses derived for most massive $z \sim 6$ quasar host galaxy	165
6.1	DSS and 2MASS images and CO (J=3-2) spectra of sources	195
6.2	DSS and 2MASS images and CO (J=3-2) spectra of sources	196
6.3	DSS and 2MASS images and CO (J=3-2) spectra of sources	197

6.4	DSS and 2MASS images and CO (J=3-2) spectra of sources	198
6.5	Observed L_{IR} versus CO (J=3-2) luminosity for galaxies	199
7.1	Model SFR-CO and SFR-HCN relations	211
7.2	Molecular line luminosity versus sightline-averaged mean density for CO and HCN	216
7.3	Distribution of mean cloud densities in fiducial disk galaxy	217
7.4	CO and HCN luminosity versus mean cell density on cell by cell basis for fiducial disk galaxy	218
7.5	Normalized level populations for three cells in fiducial disk galaxy	220
7.6	Light to density ratio along nuclear LOS in fiducial disk galaxy . .	224
7.7	Fractional photon creation for subthermally excited gas in merger simulation	228
7.8	Predicted indices between SFR-CO and SFR-HCN relations in galax- ies	230
8.1	$N_{\text{H}_2}/I_{\text{CO}}$ distribution for fiducial disk galaxy	245

LIST OF TABLES

4.1	Progenitor Galaxies and Wind Models	75
5.1	$z \sim 6$ Quasar Models	130
6.1	Observation Information	193
6.2	Physical Properties of Observed Galaxies	194

ABSTRACT

I investigate the emission properties of the molecular interstellar medium in protoplanetary disks and galaxy mergers, though focus largely on the latter topic. I utilize both numerical models as well as observations to relate the emission characteristics to physical models for the formation and evolution of gas giant planets and galaxies. The main results of this thesis follow. (1) Gas giant protoplanets may be detectable via self-absorption signatures in molecular emission lines with sufficiently high critical density. Given the spatial resolution of e.g. ALMA, gas giant planets in formation may be directly imageable. (2) Starburst and AGN feedback-driven winds in galaxies can leave imprints on the molecular line emission properties via morphological outflows and high velocity peaks in the emission line spectra. Methods for distinguishing between high velocity peaks driven by dynamics versus those driven by winds are discussed. (3) CO line widths on average trace the virial velocity of $z \sim 6$ quasar host halos. Thus, if the earliest quasars formed in $\sim 10^{13} M_{\odot}$ halos, they are predicted to have broad molecular line widths. Selection effects may exist which tend quasars selected for optical luminosity toward molecular line widths narrower than the sightline-dependent mean. (4) Using the SMT, I observe a roughly linear relation between infrared luminosity and CO (J=3-2) luminosity in local galaxies confirming the results of recently observed L_{IR} -HCN (J=1-0) relations. Subsequent modeling shows that observed SFR-molecular line luminosity relations owe to the average fraction of subthermally excited gas in galaxies, and are simply reflective of the assumed Schmidt law governing the SFR.

CHAPTER 1

INTRODUCTION

*People are always inventing some random reason or another to say why physics doesn't work.*¹

-Volker Springel

The formation and evolution of many astrophysical objects is driven by a competition between gravitational forces (and cooling) and energy injected into the system (often referred to as 'negative feedback' though in this work I will simply refer to it as 'feedback'). Examples of this grossly generalized scenario can be seen on a large dynamic range of size scales. At the lowest end both high mass star formation, in which the self-gravity of the collapsing protostar has to combat its own radiation pressure (e.g Krumholz, McKee & Klein 2005), and gas giant planet formation (in which the planet has to form on timescales less than that of photoevaporation by the parent protostar; e.g., Boss 2001, 2004) follow this cartoon picture for formation and evolution.

At larger scales (which we will primarily concentrate on for this thesis, save for Chapter 3 where we take the scenic route and foray into gas giant planet formation) the formation and evolution of galaxies can be seen to be constrained by similar physical processes. For example, the rate at which stars can form in the nuclear regions of galaxies is often in competition with feedback energy from the starburst itself (e.g., Mihos & Hernquist, 1996) as well as accreting supermassive

¹Throughout this thesis, you, the lucky reader, will find a collection of my favorite quotes I've heard throughout grad school in conversations with various people. They're sometimes pertinent, always said in jest, and hopefully at the very least a mild mental respite from the ~200 pages of science that this thesis constitutes.

black holes (e.g., Croton et al. 2006; Springel, Di Matteo & Hernquist 2005b). In fact, a feedback-driven scenario for galaxy evolution through the cosmos offers the tantalizing prospect of unifying a wide variety of observed galaxy populations and phenomena. Indeed energy released by starburst events and accreting black holes may provide a physical motivation for a wide range of seemingly disparate observed properties of galaxy populations from the first galaxies until the present day. The origin of some extremely luminous sources such as (ultra)luminous infrared galaxies have been ascribed to an interplay between stellar and black hole feedback (e.g., Sanders et al., 1988; Sanders and Mirabel, 1996). Moreover, feedback associated with starbursts and active galactic nuclei (AGN) have been invoked by numerous authors to help explain the buildup and maintenance of the red sequence (e.g., Croton et al., 2006; Springel, Di Matteo & Hernquist, 2005b), the formation of quasars from $z=0-6$ (e.g., Fabian 1999; Hopkins et al. 2005a; Silk & Rees 1998), observed superwinds in galaxies (e.g., Heckman et al. 2000; Martin 2005; Tremonti, Moustakas & Diamond-Stanic 2007), the relationship between bulge mass and black hole mass in galaxies (Magorrian et al. 1998), observed infrared colors of galaxies (e.g., Farrah et al. 2003; Sanders, Scoville & Soifer 1991), the mass-metallicity relationship in galaxies (Finlator & Davé 2007; Tremonti et al 2004), as well as a host of theoretical and observed properties of galaxies both at low and high redshift.

Central to a feedback-driven evolutionary scenario for galaxies is the role of the molecular (H_2) star-forming interstellar medium (ISM). Not only does the molecular ISM serve as the nascent birthplace for the observed stars in galaxies, it can feed accreting supermassive black holes in the central kiloparsec (e.g., Bryant & Scoville, 1999). In this sense, molecular gas in galaxies serves as the fuel for the two main sources of feedback postulated to play a major role in galactic

evolution.

Owing to the high temperatures needed to excite the first quadrupole transition of molecular hydrogen, the molecular interstellar medium is most easily traced via ground-vibrational state rotational transitions in tracer molecules such as CO, HCN and HCO^+ . These transitions reside, by and large, in the millimeter and sub-millimeter wavelength regime of the electromagnetic spectrum. Because of the challenges inherent in millimeter and submillimeter-wave detector technology, large datasets of molecular line emission from extragalactic sources have only become available over the last decade and a half, and most of these lie within ~ 100 Mpc. That said, despite the relatively short history of extragalactic molecular astrophysics, rich data sets exist which have provided a variety of observational clues as to the physical properties of the star forming (and black hole fueling) gas in various types of galaxies. In the 1980s and early 1990s, a number of pioneering observational surveys with the former NRAO 12m mm-wave telescope quantified the molecular gas content in nearby galaxies via detections of the ^{12}CO ($J=1-0$) rotational transition (see e.g., Sanders, Scoville & Soifer, 1991, Sanders & Mirabel, 1996, and references therein). These studies gave the first direct measurements of the total amount of molecular gas available to form stars, and the relationship of this quantity to other observable and inferred properties (e.g., star formation rate [SFR], optical morphology, dust mass). For example, observations by Tacconi et al. (1999) demonstrated the presence of copious amounts of molecular gas in ongoing merger NGC 6240 which is known to have accreting central black holes (Komossa et al. 2003), suggesting that star formation and central black hole growth in this source were ongoing co-evally.

The 1990s hosted two major technological developments which afforded a number of major discoveries regarding the molecular ISM in galaxies. First,

millimeter-wave interferometry allowed for higher spatial resolution studies of the same systems which, until then, only had globally averaged measurements made. Observations of this nature demonstrated the nature of the distribution of the molecular gas in galaxies (and, as before, their relation of this quantity to other physical properties; Bryant & Scoville, 1999), as well as the first direct quantification of the elusive CO-H₂ conversion factor (χ_{CO}) in starburst galaxies and galaxy mergers (Downes & Solomon, 1998). Second, as sensitive submillimeter-wave detectors and dishes became more prevalent (such as the Heinrich Hertz Submillimeter Telescope, the Caltech Submillimeter Telescope and the James Clerk Maxwell Telescope), studies pushing into higher-lying transitions of CO (as well as a host of other molecules) quantified the excitation conditions of the molecular gas, and related these observations to our knowledge of star formation processes in Galactic giant molecular clouds (GMCs; e.g., Rigopoulou et al., 1996; Yao et al., 2003).

Observations of molecular gas in the Universe have extended through the last decade to higher redshifts (e.g., $z \lesssim 6$; see Solomon & Vanden Bout, 2005 and references therein). Determinations of molecular gas content (e.g., Walter et al. 2003), excitation conditions (e.g., Weiß et al. 2007) and dynamical masses of host galaxies (e.g., Greve et al. 2005; Walter et al. 2004) have provided detailed information regarding the formation of early Universe galaxies and the potential interplay between star formation and black hole growth so crucially essential to many models of galaxy formation and evolution (e.g., Springel, Di Matteo & Hernquist, 2005a).

While rich datasets regarding the physical nature of the star-forming molecular gas in both the local Universe through higher redshifts continue to pour in, owing to the high computational power necessary to resolve the appropriate physics, the development of concomitant interpretative theoretical models have

been relatively lagging. Hydrodynamic models of galaxy evolution (e.g., Mihos & Hernquist 1996; Springel et al. 2005) have made great headway in formulating theoretical models for galaxy evolution in a merger-driven scenario. However, a direct application of these simulations to wavelength-specific observations is a nontrivial endeavour. In order to couple hydrodynamic models to physical observables, three dimensional radiative transfer is necessary. In the case of line transfer through the molecular ISM, these calculations must consider excitation and deexcitation processes from both collisions and radiation, as well as velocity fields across three dimensions which can be computationally taxing.

However, despite the technical challenges, radiative transfer and hydrodynamic simulations for the extragalactic molecular Universe holds great potential. To zeroth order, a great deal can be learned by a suite of models which can simply *reproduce* the observed properties of molecular gas emission in galaxies - models which can understand even the most seemingly simple and well understood of observed properties of galaxies can often provide a rather interesting physical interpretation. As an example, high resolution observations by Bryant & Scoville (1999) measured the effective radius of CO emission in advanced galaxy mergers. Subsequent calculations by Narayanan et al. (2007b) showed that winds associated with star formation and/or black hole growth in these systems were necessary to dispel the diffuse gas and reproduce these observed results. Moreover, only when simulations can faithfully reproduce existing observations can they be trusted for their predictive power.

Second, numerical simulations which are able to relate physical models to observable properties of galaxies have the potential to offer interpretation for existing observed relations which have debated physical origins. As an example, the largest ever compiled dataset of HCN ($J=1-0$) emission from local galaxies sug-

gested that stars may form at a rate linearly proportional to the amount of dense ($n \gtrsim 10^5 \text{ cm}^{-3}$) molecular gas in galaxies (Gao & Solomon, 2004a,b). Conflicting interpretations have suggested that the origin of these relations may be due to chemistry-driven effects (e.g., Lintott & Viti, 2006), properties of self-similar scalings in GMCs (Wu et al., 2005), and free-fall time arguments (e.g., Krumholz & Thompson, 2007). In this sense, interpretive theoretical models of molecular emission on galaxy-wide scales would be helpful in disentangling the physical mechanism (or combination of) driving the observed relations.

Finally, simulations of these sorts have a great deal to offer regarding their predictive power for this field. For example, while observations have pushed the limits of detector technology in probing the state of molecular gas in galaxies all the way to redshift ~ 6 , (as of the time of the writing of this thesis) the number of such detected galaxies remains comfortably under 50 (Solomon & Vanden Bout, 2005). Interpretation of emission from non-uniform molecular transitions from a smattering of galaxies over a large range of redshifts which are likely very different beasts from local sources remains impossibly difficult. In this regime, theoretical models perhaps show their most potential for large contributions to the field. Moreover, inherent in predictive capabilities of models is the underlying prospect of outlining observable tests that have model-distinguishing power.

It is in this manner that this thesis attempts to provide a contribution to existing research efforts in astronomy and astrophysics. In this work, I build on the body of observational and theoretical literature in an attempt to provide observational data, interpretive simulations, and model-distinguishing predictions concerning molecular gas emission in galaxies from $z=0-6$. I present molecular line observations of local starburst galaxies, as well as the first self-consistent radiative transfer calculations in three dimensions relating observable properties of

the molecular interstellar medium in galaxies to physical models of galaxy formation and evolution. The presented results are somewhat circular in that the theoretical tools developed are used (in part) to present interpretation for the observations taken for this thesis.

This thesis is organized as follows. I begin in Chapter 2 by detailing the numerical methodology used in our radiative transfer simulations. I show a direct example of the power of coupling of our radiative transfer simulations with hydrodynamic modeling in Chapter 3 where I apply these techniques to high resolution models of gas giant planet formation. I then begin our adventure into extragalactic regimes by first tackling problems related to local galaxy mergers in Chapter 4. I make predictions as to the effects of starburst and AGN feedback-driven winds on molecular gas emission in galaxy mergers, and in some sense, set the zero point for the extragalactic capabilities of our simulations. This is important as I take a much bigger plunge with our theoretical methods in Chapter 5 into a rather unconstrained arena where I explore the nature of CO emission in the very first quasars, having formed less than a billion years after the Big Bang. Then, just when it would appear as though a theme of expanding farther from the solar circle with our theoretical methodology was in place, I bring you, the intrepid reader, on a hairpin turn back to CO observations of the local Universe in Chapter 6. This is important especially coupled with the following chapter (Chapter 7) as the combination of the two provide a direct example of observations with complicated interpretations, and simulations which attempt to bring some physical motivation behind the observed relations. The central theme behind these latter two chapters is understanding the relationship between molecular gas emission in galaxies and Kennicutt-Schmidt relations which are thought to perhaps govern the rate at which stars form. Additionally (and I hope interest-

ingly), the physics driving the observable effects of molecular star formation rate indicators is similar to those seen in gas giant protoplanets in the vicinity of hot protostars. In this sense, Chapter 7, the final chapter, aims to tie together many of the observational and theoretical topics presented in this thesis. Because I take great pains to provide detailed summaries in the individual chapters, I refrain from summarizing in the concluding chapter, Chapter 8, but rather wax on potential directions for models such as those presented in this work in this section, and provide outlook for the major solvable problems in theoretical molecular astrophysics in the coming decade.

CHAPTER 2

3-DIMENSIONAL NON-LOCAL THERMODYNAMIC EQUILIBRIUM RADIATIVE TRANSFER ON GALAXY-WIDE SCALES

Being a theorist is easy - first you write your code in 1 dimension, expand it to two and three dimensions, parallelize it, run it, and then you're done and you graduate!

- Casey Meakin

2.1 Chapter Preface

Understanding the simulated molecular line emission characteristics from astrophysical sources requires non-local thermodynamic equilibrium (LTE) radiative transfer. In this section, we describe the methodology employed throughout this thesis (save for Chapter 6 in which we employ a one-dimensional analog to the following algorithm).

The following algorithms have been incorporated into the code *Turtlebeach*¹ which has primarily been applied to extragalactic scenarios. Because the spatial resolution characteristic of simulations on galaxy-wide scales typically is not sufficient to resolve the dynamic range in densities seen in GMCs, we describe a subgrid formalism for simulating the effects of a mass spectrum of GMCs. The inclusion of GMCs in a subgrid manner is of course not necessary for Chapter 3, where we describe simulations on AU scales of circumstellar regions, and we therefore describe the algorithm an additional time in that chapter as written without the subgrid methodology.

¹*Turtlebeach* = The Ultimate Radiative Transfer Lambda iteration Bernes Algorithm Code Hoohah!

2.2 Chapter Introduction

Simulating molecular line emission on galaxy-wide scales has a relatively short history owing to the computational costs associated with the hydrodynamics and radiative transfer. Early works by Silk & Spaans (1997) and Combes, Maoli & Omont (1999) focused on simulating molecular emission from high- z objects, using idealized galaxy systems. Wada & Tomisaka (2005) pioneered incorporating three-dimensional non local thermodynamic equilibrium (non-LTE) radiative transfer calculations into hydrodynamic simulations of AGN, focusing specifically on predicted emission from the circumnuclear molecular torus. More recent works have folded non-LTE radiative transfer codes into self-consistent hydrodynamic simulations of galaxy mergers. These works have been performed in mergers scaled for low redshift (Narayanan et al. 2006a), as well as those appropriate for higher- z systems (Greve & Sommer-Larsen, 2006; Narayanan et al. 2007a).

2.3 Radiative Transfer Methodology

Submillimeter and millimeter wave radiation from molecules is dependent on the distribution of level populations which depend both on collisions with other molecules and atoms, as well as the incident radiation field. The excitation of molecular gas is highly sensitive to both variations in the temperature and density distribution, as well as the incident radiation field. There are usually large differences in the collisional densities necessary to excite different energy levels. For example, in the case of CO, the critical density to collisionally populate the $J=1$ state is $n_{\text{crit}} \sim 10^2\text{-}10^3 \text{ cm}^{-3}$ while the $J=3$ state typically requires $n_{\text{crit}} \sim 10^4 \text{ cm}^{-3}$. The latter density is characteristic of dense cores in GMCs, whereas the former is typical of more diffuse GMC atmospheres.

The non-LTE radiative transfer calculations for the galaxy-scale simulations were implemented during post-processing of the hydrodynamic simulations. The simulation outputs were typically smoothed to a resolution of $\sim 80\text{-}250$ pc in order to defray computational costs associated with the radiative transfer simulations. In order to model the strongly density-dependent excitation rates in our simulations, we have expanded the Bernes (1979) non-LTE Monte Carlo radiative transfer algorithm to include a mass spectrum of GMCs in a subgrid manner. Our methodology follows.

The molecular gas fraction in galaxies is determined by the metallicity, dust content, interstellar radiation field, density and temperature (Hollenbach, Werner & Salpeter 1971; Pelupessy, Papadopoulos & van der Werf 2006). However, owing to limited spatial resolution, this calculation cannot be done explicitly as the location of individual stars and clouds are not known. We therefore assume that half of the cold neutral gas mass in each grid cell (typically of order $\sim 150\text{-}250$ pc on a side) is in atomic form and half in molecular, as motivated by local volume surveys of star forming galaxies (e.g., Keres, Yun & Young 2003).

In our formulation, the cold molecular gas is assumed to be bound in a mass spectrum of GMCs in each grid cell

$$\frac{dN}{dM} \propto M^{-\beta} \quad (2.1)$$

where we take $\beta=1.8$ (Blitz et al. 2006). The GMCs are modeled as singular isothermal spheres (SISs) where the density (n) is given by:

$$n = n_0 \left[\frac{r_0}{r} \right]^\alpha \quad (2.2)$$

The radius of the cloud is determined by the Galactic GMC mass-radius relation (Rosolowsky, 2005, 2007; Solomon et al. 1987), resulting in a global density distri-

bution for all m clouds in a grid cell of

$$n = \frac{1}{r^\alpha} \left[\sum_m r_{0,m}^\alpha n_{0,m} \right] \quad (2.3)$$

We utilize a cloud power-law index of $\alpha=2$ (Walker, Adams & Lada 1990). Observational evidence suggests that a range of power law indices in GMCs from $\alpha=1-2$ may be appropriate (Andre, Ward-Thompson & Motte 1996; Fuller & Myers 1992; Ward-Thompson et al. 1994), although our results are not very sensitive to the choice of power law index within this range.

Formally, we build an emergent spectrum by integrating the equation of radiative transfer along the line of sight:

$$I_\nu = \sum_{z_0}^z S_\nu(z) \left[1 - e^{-\tau_\nu(z)} \right] e^{-\tau_\nu(\text{tot})} \quad (2.4)$$

where I_ν is the frequency dependent intensity, S_ν is the source function, τ is the optical depth, and z is the position along the line of sight.

If the level populations are in LTE, then the source function, S_ν , can be simply replaced by the Planck function. However, when considering the propagation of lines through a medium with insufficient density for collisions to thermalize the level populations (e.g., $n \ll n_{\text{crit}}$), the effects of radiative excitation and de-excitation must be considered. In this case, the source functions must be calculated explicitly.

The source function from each cloud, m , for a given transition from upper level to lower level $u \rightarrow l$ is given by

$$S_{\nu,m} = \frac{n_{u,m} A_{ul}}{(n_{l,m} B_{lu} - n_{u,m} B_{ul})} \quad (2.5)$$

where the level populations are assumed to be in statistical equilibrium, and determined through the rate equations:

$$n_{l,m} \left[\sum_{k < l} A_{lk} + \sum_{k \neq l} (B_{lk} J_\nu + C_{lk}) \right] =$$

$$\sum_{k>l} n_{k,m} A_{kl} + \sum_{k \neq l} n_{k,m} (B_{kl} J_\nu + C_{kl}). \quad (2.6)$$

A , B_{kl} and B_{lk} are the Einstein rates for spontaneous emission, stimulated emission, and absorption, respectively, C are the collisional rate coefficients, the indices l and k represent different energy levels, and J_ν is the mean intensity through a given grid cell:

$$J_\nu = \frac{1}{4\pi} \int I_\nu d\Omega \quad (2.7)$$

As is evident by the previous four equations, the problem is circular: the observed intensity depends on the source function which is determined by the level populations. When in a non-LTE regime ($n \ll n_{\text{crit}}$), collisions alone do not determine the level populations, but rather the mean intensity field (e.g., radiation from gas in other grid cells) plays a role as well. The solution is achieved by means of iteration.

The initial level populations in a grid cell are estimated based on the global density and temperature distribution for all clouds in a grid cell (Equation 2.3). We emit model photons which represent many real photons from the mass spectrum of GMCs in each grid cell. The model photons are given a weight W proportional to the total number of molecules in the upper state of a given transition in a cell, and the Einstein A rate coefficient for the transition. The photons are emitted isotropically in 3 dimensions and have line frequency randomly drawn from the line profile function:

$$\phi(\nu) = \frac{1}{\sigma\sqrt{\pi}} \exp \left\{ - \left(\nu - \nu_0 - \mathbf{v} \cdot \hat{\mathbf{n}} \frac{\nu_{ul}}{c} \right)^2 / \sigma^2 \right\} \quad (2.8)$$

where \mathbf{v} represents the velocity vector, and the effects of the local kinetic temperature and microturbulent velocity field are accounted for via

$$\sigma = \frac{\nu_0}{c} \left[\frac{2kT}{m} + V_{\text{turb}} \right]^{\frac{1}{2}} \quad (2.9)$$

The photon then takes a step over distance s through the next grid cell. After taking a step, the weight is attenuated by a factor $e^{-\tau}$ where the opacities are given by

$$\alpha_\nu(\text{dust}) = \kappa_\nu \rho_{\text{dust}} \quad (2.10)$$

$$\alpha_\nu^{ul}(\text{gas}) = \frac{h\nu_{ul}}{4\pi} \phi(\nu) (n_l B_{lu} - n_u B_{ul}) \quad (2.11)$$

and

$$\tau_{\nu,m} = (\alpha_{\nu,m}(\text{dust}) + \alpha_{\nu,m}(\text{gas})) \times s \quad (2.12)$$

The column seen by a photon in a grid cell is calculated via a Monte Carlo approach. Specifically, we calculate the distribution of potential column densities a photon could see through a given grid cell by simulating a sample of the subgrid cells individually on higher resolution grids. In these higher resolution grids, we place GMCs at random locations with masses drawn from the power-law mass spectrum, and radii given by the Galactic mass-radius relation. We do this numerous times until the distribution of potential columns through the cell converges. The distribution of columns is found to scale in a self-similar manner with grid cell (molecular) mass. We then explicitly draw from this distribution to determine the column seen by a model photon as it enters a given grid cell. To illustrate this, we plot an example of the distribution of column densities in Figure 2.1. The photon continues to propagate through grid cells in this manner until the weight is negligible, or the photon has left the grid.

Once a sufficiently large number of model photons have been emitted to simulate the mean radiation field, J_ν , the level populations can be updated via the rate equations. In the rate equations (also commonly called the equations of statistical equilibrium), the terms involving the mean intensity represent the radiatively induced excitations (absorption) and stimulated emission in a given cell of clouds

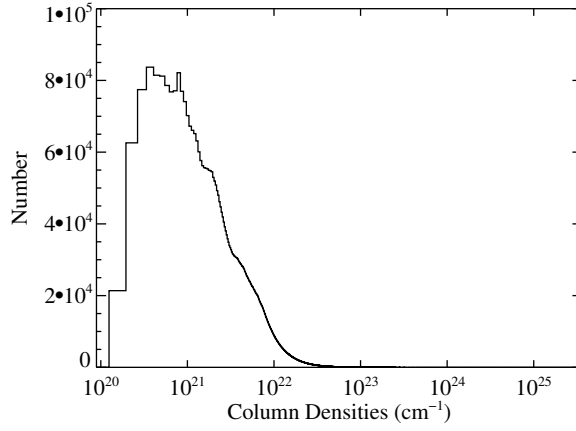


Figure 2.1 Representative distribution of column densities for a grid cell of mass $\sim 3 \times 10^6 M_{\odot}$. Distribution of columns is derived by randomly placing clouds drawn from a mass spectrum until the distribution converges. Photons entering a grid cell see a column randomly drawn from a distribution such as this in order to simulate the actual column seen by a photon in a statistical manner.

m' . We may rewrite these equations by defining the number of excitations of a molecule in lower state l by

$$S_{lu,m'} = \frac{h\nu_{ul}}{4\pi} \phi(\nu) B_{lu} \frac{sW_0}{V_{m'}\tau} (1 - e^{-\tau(\text{tot})}) \quad (2.13)$$

where V is the volume of the cell and W_0 is the original weight of the photon.

Following Bernes (1979), we then rewrite the equations of statistical equilibrium as

$$\begin{aligned} n_l \left[\sum_{k<l} A_{lk} + \sum_{k \neq l} (S_{lk,m'} + C_{lk}) \right] = \\ \sum_{k>l} n_k A_{kl} + \sum_{k \neq l} n_k \left[\frac{g_l}{g_k} S_{lk,m'} + C_{kl} \right] \end{aligned} \quad (2.14)$$

where g are the statistical weights of the level.

After a single generation of photons has been emitted, the $S_{lu,m'}$ is calculated for each grid cell, m' . We can then use the analog of the previous equation to calculate the updated level populations for the N individual radial cells that make up the subgrid spectrum of GMCs. The relative contribution of each of the N cells to the total number of excitations ($S_{lu,m'}$) in a given grid cell is determined via the column across that region.

New level populations are calculated for each of the N cells in the spectrum of GMCs via matrix inversion and then summed to give the total populations for their parent grid cell. New weights W are given to a new generation of emergent photons, and the process is iterated upon until the level populations across the grid are converged. For most galaxy simulations, typically 12×10^6 model photons were emitted per iteration and the boundary conditions for the radiative transfer included the 2.73K microwave background.

This method has the distinct advantages of being able to simulate the effects of dense cores as well as diffuse atmospheres of clouds. Because we divide the

GMCs into a series of sub-grid cells, we are not constrained to using a single density in our rate equations, and thus the collisional excitation characteristic of dense cores can be well-represented while the influence of radiation on more diffuse regions can likewise be accounted for. Moreover, we are able to include these features in our calculations without expanding the grid to computationally prohibitive sizes.

Our subgrid formulation is dependent on a series of assumptions as well. First, owing to limited spatial resolution, we are forced to assume a constant H_2 gas fraction constrained by observational surveys. This molecular gas in a given grid cell is assumed to be bound in GMCs. The GMCs are realized as SISs in our model whereas clouds are understood observationally to be fractal in nature (e.g., Elmegreen & Falgarone 1996). The clouds within each grid cell are all at the same temperature, and individually isothermal (though temperatures are allowed to vary from grid cell to grid cell, and thus temperature gradients exist across the galaxy). Additionally, we are not able, through these methods, to capture how clouds within a grid cell affect each other.

The temperatures in the cold phase of the ISM in the hydrodynamic models are fixed at 1000K (Springel & Hernquist 2003). This choice is arbitrary and has no effect on the hydrodynamic simulations. Typically, temperatures in molecular clouds range from 10-100K; temperatures of 1000K would systematically put too much weight on the collisional coefficients in the rate equations, resulting in overly excited level populations. We refine the temperatures in our radiative transfer models by assuming the gas and dust in a given cell are in thermal equilibrium, and that the heating sources are dominated by O and B stars. The gas cools via metal line cooling which is calculated using a mean escape probability radiative transfer code (Kulesa 2002; Kulesa et al. 2005). Using these methods,

we find typical isothermal cloud temperatures ranging from 10K-120K (nominally 10-30 K for simulations scaled for the local Universe, though temperatures can approach ~ 120 K for the $z \sim 6$ models).

The level population calculations are sensitively dependent on the accuracy of the rate coefficients. We have obtained our coefficients from the *Leiden Atomic and Molecular Database* (Schoier et al. 2005). In order to independently test our radiative transfer codes, we have run the test problem of an inside-out collapsing sphere published by van Zadelhoff et al. (2002). We present the results of this test in Figure 2.2, and direct the reader to van Zadelhoff et al. (2002) for details on the test problem and solutions.

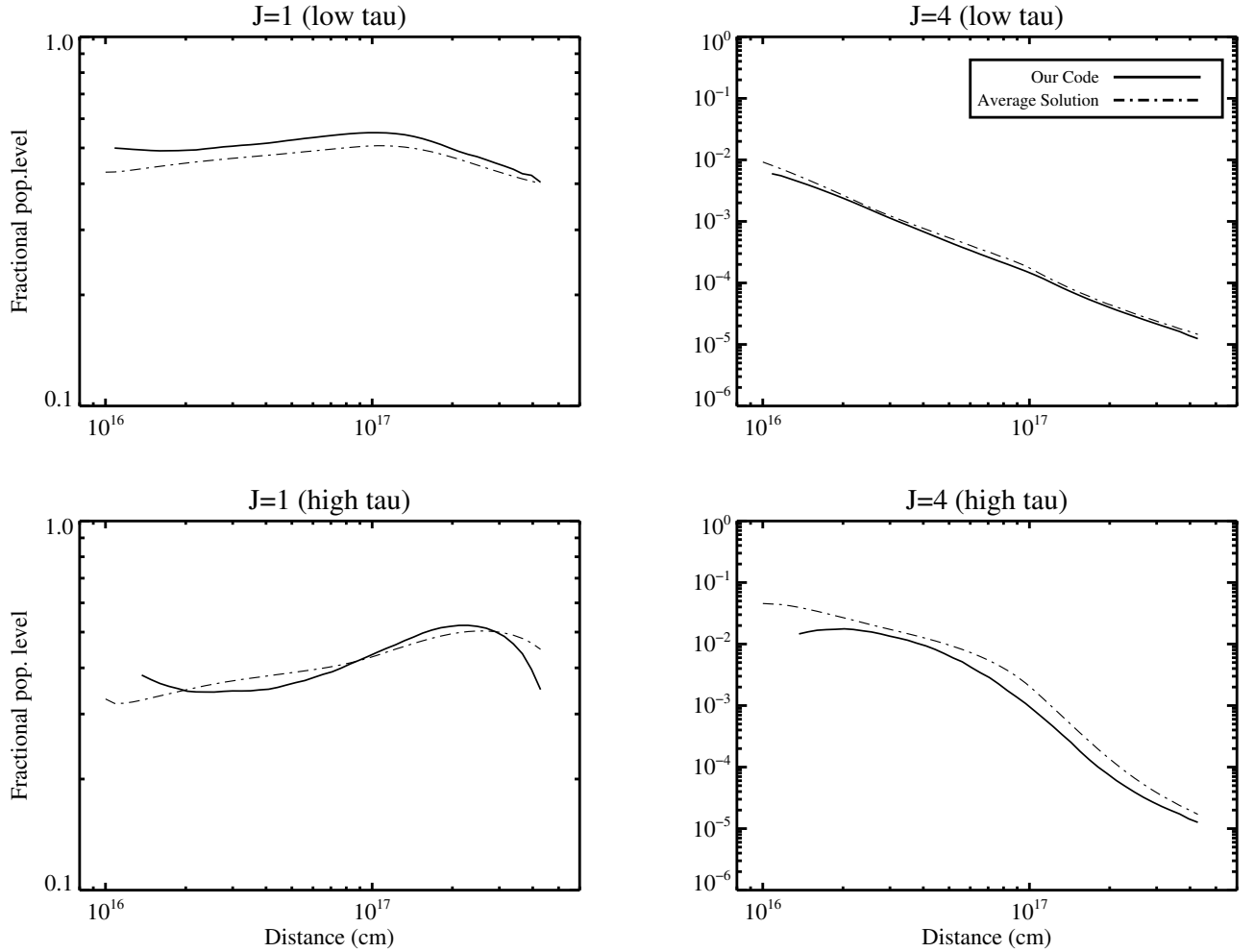


Figure 2.2 Solutions of our radiative transfer codes to test problems “2a” and “2b” of van Zadelhoff et al. (2002). The ordinate is fractional populations of the J=1 and J=4 levels of HCO⁺ and the abscissa is radial distance out from center of a 1-dimensional inside-out collapsing cloud. The solid line is our solution, and the dash-dot line is the average solution to the problem taken from seven other researcher’s codes.

CHAPTER 3

MOLECULAR LINE EMISSION FROM GRAVITATIONALLY UNSTABLE
PROTOPLANETARY DISKS

You seem to get a kick out of making these computer movie things. Maybe you should do some sort of computer programming.

-Tony Stark

3.1 Chapter Abstract

In the era of high resolution submillimeter interferometers, it will soon be possible to observe the neutral circumstellar medium directly involved in gas giant planet (GGP) formation at physical scales previously unattainable. In order to explore possible signatures of gas giant planet formation via disk instabilities, we have combined a 3D, non-local thermodynamic equilibrium (LTE) radiative transfer code with a 3D, finite differences hydrodynamical code to model molecular emission lines from the vicinity of a $1.4 M_J$ self-gravitating proto-GGP. Here, we explore the properties of rotational transitions of the commonly observed dense gas tracer, HCO^+ . Our main results follow. 1. Very high lying HCO^+ transitions (e.g., $\text{HCO}^+ J=7-6$) can trace dense planet forming clumps around circumstellar disks. Depending on the molecular abundance, the proto-GGP may be directly imageable by the Atacama Large Millimeter Array (ALMA). 2. HCO^+ emission lines are heavily self-absorbed through the proto-GGP's dense molecular core. This signature is nearly ubiquitous, and only weakly dependent on assumed HCO^+ abundances. The self-absorption features are most pronounced at higher angular resolutions. Dense clumps that are not self-gravitating only show minor self-absorption features. 3. Line temperatures are highest through

the proto-GGP at all assumed abundances and inclination angles. Conversely, due to self-absorption in the line, the velocity-integrated intensity may not be.

3.2 Chapter Introduction

Since the discovery of 51 Pegasus, there have been numerous detections of Jupiter-sized extrasolar planets through radial velocity experiments, transiting of parent stars and direct imaging (for recent reviews, see Udry, Fischer & Queloz, 2006, Charbonneau et al. 2006 and Beuzit et al. 2006).

Concomitant to the problem of characterizing the nature of these gas giant planets (GGPs) is developing the theoretical constructs which describe the nature of GGP formation. Two major theories have been developed concerning the physics of GGP formation. Core accretion begins with the formation of planetesimals through the collisional coagulation and sticking of progressively larger solid bodies in the circumstellar environment. Once \sim kilometer sized planetesimals are formed, runaway accretion to Mars-sized bodies can occur. When the planetary embryos reach a mass of ten Earth masses or so, disk gas is accreted dynamically, resulting in GGP formation. Core accretion is the generally favored mechanism for forming Jupiter and Saturn (Pollack et al. 1996; Goldreich, Lithwick, & Sari 2004a). The core accretion model has been challenged in explaining how a solid core can form on timescales less than the disk dissipation times of $\sim 10^6$ - 10^7 yr (Pollack et al. 1996; Ikoma, Nakazawa, & Emori, 2000). However it should be noted that recent models by Rafikov (2003) and Goldreich, Lithwick & Sari (2004b) have suggested a core accretion mechanism that is not incompatible with the short-lived disk lifetimes. Additional problems of the core-accretion model include resolving theoretical GGP core masses with those of Jupiter and Saturn (Mejia 2004; Saumon & Guillot 2004).

As an alternative to core-accretion, the disk instability mechanism has been investigated in many models by Boss (2001, 2004), Mejia (2004), and Mayor et al. (2005). In this theory, marginally unstable gaseous disks contract gravitationally to form GGPs. Models of gravitationally unstable disks suggest planets can form on rapid ($\sim 10^3$ yr) time scales (Boss 1997, 1998), but require disks to cool efficiently in order for gravitationally bound clumps to form. Boss (2004) has shown that convective cooling through protoplanetary disks can be quite efficient. Hybrid mechanisms for GGP formation have been suggested as well (Currie, 2005).

It is clear that both leading theories in the formation of GGPs have their shared successes and challenges in current models. Observations of protoplanetary disks will be key in constraining the two models. Because the gravitational instability method involves the accumulation of large clumps of cool gas from the circumstellar disk, molecular line observations may be helpful in revealing the nature of GGP formation. Indeed, in the era of high-resolution millimeter and submillimeter wave interferometers, clumps of cool and dense gas may indeed be directly imageable in nearby circumstellar disks.

Rotational transitions ($J+1 \rightarrow J$) in interstellar molecules have long been used to better understand the nature of cold gas in star-forming environments (for a recent review, see Evans 1999). Serving as a proxy for the observationally elusive molecular hydrogen (H_2), excitation analysis of lines from molecules such as CO, CS, HCO^+ , HCN and others can provide diagnostics for the physical conditions in the cold molecular gas.

Through the use of submillimeter and millimeter wave interferometers, direct imaging of cold circumstellar disks have recently been made possible (e.g., Patel et al. 2005, Qi et al. 2004). Submillimeter molecular line emission has been used to estimate molecular depletion factors (e.g., Andrews & Williams 2005; van

Zadelhoff et al. 2001), as well as provide information concerning kinematics in the circumstellar environment (e.g., Qi et al. 2003). It is additionally possible to constrain disk molecular gas masses through such observations (e.g., Hogerheijde et al. 2002). Recent CO (J=6-5) observations of TW Hya by Qi et al. (2006) has shown that molecular excitation can be quite high due to the dense gas present in protoplanetary disks.

In addition to observational data sets of molecular line emission from protoplanetary disks, radiative transfer modeling of the emission patterns can provide powerful constraints as to the physical conditions in the molecular gas. As an example, Qi et al. in the aforementioned study of TW Hya used a 2D non-LTE Monte Carlo model to derive vertical temperature distributions in the disk. Similar studies have been performed to calculate temperature and/or density distributions by Kessler (2004), and Semenov et al. (2005), among many others.

In order to fully utilize the new generation of interferometers to probe planet formation, submillimeter and millimeter wave emission modeling of GGP forming disks is needed. Progressive works by Wolf & D'Angelo (2005), Moro-Martin, Wolf & Malhotra (2005), and Varniere et al. (2006) have studied the effects of protoplanets in disks on infrared SEDs through the use of radiative transfer modeling. A necessary complementary dataset to these works is models of molecular line emission from planet forming circumstellar disks.

In this study, we take the first step in this direction by applying a newly developed 3D non-LTE radiative transfer code to a model of a gravitationally unstable protoplanetary disk (Boss, 2001). We will discuss the emission patterns by way of contour maps and emission line profiles. This chapter is organized as follows: in § 3.3, we discuss the numerical methods involved concerning hydrodynamics, radiative transfer, and chemistry; in § 3.4 we present synthetic images of HCO^+

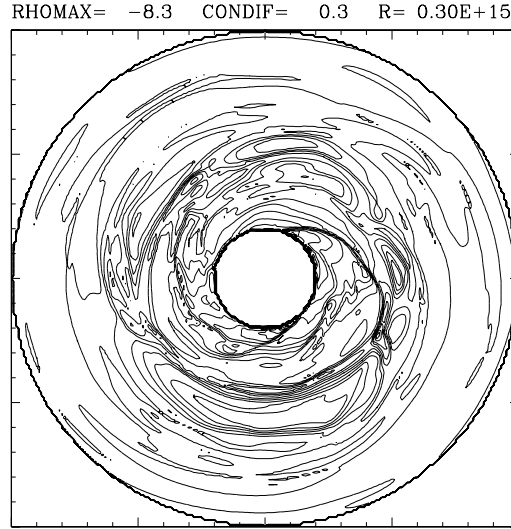


Figure 3.1 Equatorial density contours for hydrodynamic snapshot. Contours denote changes by a factor of 2 in density, with $\rho_{\max}=5.0\times 10^{-9}\text{gm cm}^{-3}$. The maximum density clump is located at ~ 4 o'clock in this image. For radial temperature and density profiles through the proto-GGP, please see Boss (2001).

emission in the disk; in § 3.5 we discuss emission line profiles; in § 3.6 we briefly discuss spectral maps and in § 3.7 we summarize.

3.3 Numerical Methods

3.3.1 Hydrodynamics

We have run three dimensional hydrodynamic models using a finite-differences code to model the gravitationally unstable protoplanetary disk as fully described in Boss (2001). The code has been shown to be accurate to second order in space and time (Boss & Myhill 1992). The spherical grid is uniformly spaced in the radial direction between 4 and 20 AU. The azimuthal grid is uniform, and the polar grid spaced such that the resolution grows toward the midplane (with a maxi-

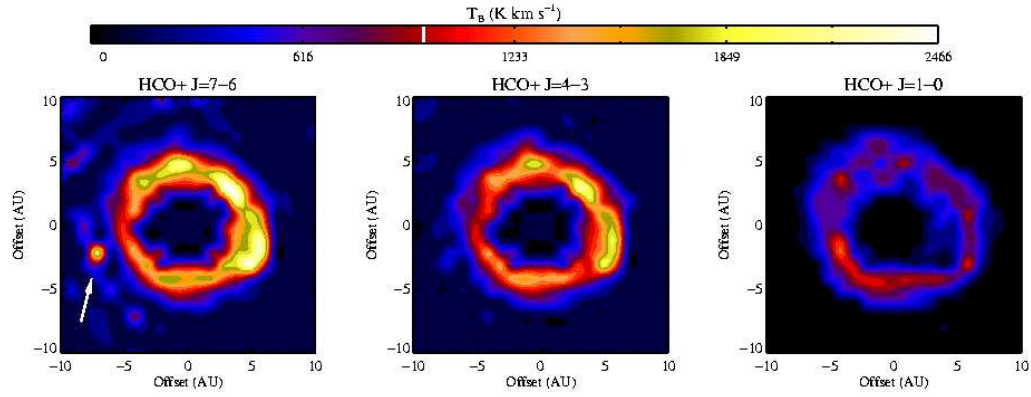


Figure 3.2 The effect of transition choice on the image: HCO⁺ transitions J=7-6, 4-3, 1-0. The proto-GGP is evident only in the highest HCO⁺ transitions due to the high critical density needed to image the dense object. The synthesized images are the mirror image of the density contours in Figure 3.1, and thus the proto-GGP is at ~ 8 o'clock in the left most panel. The intensity is in units of K-km s⁻¹ and is on a fixed scale for the entire figure.

imum resolution of $\Delta\theta=0.3^\circ$). The model includes a central protostar of $1 M_\odot$ and a disk of $0.091 M_\odot$. The protostar wobbles in response to the evolving disk, such that the center of mass of the system is preserved. The initial disk surface density is assumed to vary with radius as $\sigma \propto r^{-1/2}$ to $\sigma \propto r^{-1}$ through the inner disk, and $\sigma \propto r^{-3/2}$ in the outer disk. The initial density distribution is seeded with perturbations of the form $\cos(m\phi)$ where $m=1,2,3,4$ with an amplitude of 0.01. Random noise is included at a lower amplitude.

3.3.2 Radiative Transfer

Here, we revisit the algorithm used for the radiative transfer simulations. While they are similar to the methods discussed in Chapter 2, in this section we bypass the subgrid modeling as the spatial resolution in the hydrodynamic simulations was sufficient. This section is moderately redundant with Chapter 2, and may thus be skipped without loss of continuity if desired.

We build the emergent spectrum by integrating the equation of radiative transfer over numerous lines of sight through the hydrodynamic snapshot (e.g., Walker, Narayanan & Boss 1994). The solution to the equation of radiative transfer has the numerical form

$$I_\nu = \sum_{z_0}^z S_\nu(z) \left[1 - e^{-\tau_\nu(z)} \right] e^{-\tau_\nu(\text{tot})} \quad (3.1)$$

where S_ν is the source function, and τ is the optical depth. If local thermodynamic equilibrium (LTE) conditions hold, then the source function can be replaced by the Planck function. LTE is a fair approximation when the density is much greater than the critical density and collisions thermalize the gas, e.g.,

$$n \gg \frac{A_{ul}}{\sum C_{ul}} \quad (3.2)$$

where A is the Einstein rate coefficient for spontaneous emission, C are the collisional rate coefficients, and u,l correspond to the upper and lower states of a

given transition. However, when considering either low density environments, or molecular species with high dipole moments (and thus high Einstein A coefficients), the approximation of LTE may no longer hold. In these situations, the source function must be calculated explicitly.

In order to find the source function, an iterative procedure can be employed. We have developed a three-dimensional non-LTE radiative transfer code based on the Monte Carlo method. The first work to detail a Monte Carlo algorithm for non-LTE line transfer was by Bernes (1979). Future workers improved the algorithms and expanded to two and three dimensions (Choi et al. 1995; Juvela et al. 1997; Park & Hong 1998; Hogerheijde & van der Tak 2000; Schoier 2000). Monte Carlo techniques in radiative transfer are powerful in that they offer a large amount of flexibility for different geometries and are easily parallelized. Due to the statistical nature of Monte Carlo, the solutions include shot noise, and can be slow to converge in cases of high ($\tau \gtrsim 100$) optical depths.

The non-LTE radiative transfer code we have developed operates on the following principles, adapted from Bernes (1979): the goal is to solve for the steady state distribution of energy states among the molecules. Once these level populations are known, the source function for a given transition can be calculated by:

$$S_\nu = \frac{n_u A_{ul}}{(n_l B_{lu} - n_u B_{ul})} \quad (3.3)$$

where B are the Einstein rate coefficients for absorption and stimulated emission. However, the problem is circular: the level populations in any grid cell depend on the mean intensity field through that point.

$$J_\nu = \frac{1}{4\pi} \int I_\nu d\Omega \quad (3.4)$$

The intensity field depends on the emission from other cells which in turn is given by their source functions. Hence, it is necessary to guess the level populations,

solve for the mean intensity field, calculate updated level populations and iterate until the level populations have converged.

The radiation field is modeled by photon ‘packets’ that represent many real photons. The number of photons each model packet represents is proportional to the Einstein- A for the transition and the number of molecules or atoms in the upper state of the transition in the emitting grid cell. The photons are isotropically emitted in a spontaneous manner with a line frequency drawn from the line profile function:

$$\phi(\nu) = \frac{1}{\sigma\sqrt{\pi}} \exp \left\{ - \left(\nu - \nu_0 - \mathbf{v} \cdot \hat{\mathbf{n}} \frac{\nu_{ul}}{c} \right)^2 / \sigma^2 \right\} \quad (3.5)$$

where ν is the frequency of the emitted photon, ν_0 is the rest frequency of the transition, \mathbf{v} is the velocity of the emitting clump of gas, and σ is the standard deviation of the profile function. The standard deviation is the Doppler width determined by the local kinetic temperature and microturbulent velocity:

$$\sigma = \frac{\nu_0}{c} \left[\frac{2kT}{m} + V_{\text{turb}}^2 \right]^{\frac{1}{2}} \quad (3.6)$$

We assume a constant microturbulent velocity of 0.2 km s^{-1} . The photon then takes a step of a given distance s , passing through gas with opacity:

$$\alpha_\nu(\text{dust}) = \kappa_\nu \rho_{\text{dust}} \quad (3.7)$$

$$\alpha_\nu^{ul}(\text{gas}) = \frac{h\nu_{ul}}{4\pi} \phi(\nu) (n_l B_{lu} - n_u B_{ul}) \quad (3.8)$$

After passing through this grid cell, the number of real photons the model photon packet represents is diminished by a factor $e^{-\tau}$ due to absorptions. The model photon continues to take steps in the same direction until it either leaves the grid or the number of photons it represents has become negligible. When all of the photons have been emitted, the mean intensity is known through each grid point.

The updated level populations are then calculated with the equations of statistical equilibrium

$$n_l \left[\sum_{k < l} A_{lk} + \sum_{k \neq l} (B_{lk} J_\nu + C_{lk}) \right] = \sum_{k > l} n_k A_{kl} + \sum_{k \neq l} n_k (B_{kl} J_\nu + C_{kl})$$

which are solved through standard matrix inversion methods. With the new level populations in hand, the process can be repeated with a new calculated radiation field. These radiative transfer calculations are then iterated over until the level populations are found to converge. Convergence in non-LTE radiative transfer simulations depends both on the number of model photons realized in the iteration, as well as the optical depth.

3.3.3 The Model and Parameters

We have run our non-LTE radiative transfer code for HCO^+ rotational transitions through model HR of Boss (2001). In this model, a 1.4 Jupiter-mass dense clump of gas is formed through gravitational instabilities in the circumstellar disk. The maximum density through the proto-GGP is $5.0 \times 10^{-9} \text{ g cm}^{-3}$, and it orbits at a semimajor axis of ~ 10 AU. The temperature through the proto-GGP ranges from ~ 100 -150 K.

For the radiative transfer calculations, we considered HCO^+ molecular line emission, as well as thermal continuum emission with opacities given by Boss & Yorke (1990). The radiative transfer calculations were run on one snapshot of the hydrodynamic model for which we show the midplane density contours in Figure 3.1. The boundary conditions for the non-LTE transfer included photons from the 2.73 K cosmic microwave background. However, when convolving our resultant images to beams larger than the grid, we assumed no contribution from the CMB outside of the grid. Our grid for the calculations was spherical in nature

with $(N_r, N_\phi, N_\theta) = (100, 512, 43)$. We emitted roughly 3.11×10^8 photons per iteration. The calculations typically took 2 weeks on 14, 2GHz, AMD-64 processors.

3.3.4 Chemistry of HCO^+

Abundances in protoplanetary disks can be wildly variable due to the wide range of temperatures and densities involved, in addition to variable X-ray and UV fluxes. Our purpose is to investigate gross emission features from dense gas clumps in circumstellar disks and a full model of the complex chemical reaction networks in disk environments (e.g., Aikawa & Herbst 1999; Semenov, Wiebe, & Henning 2004) is beyond the scope of this paper. We approximate the impact of disk chemistry by running models at different HCO^+ abundances and analyzing their imprint on emission features. We note that regardless of the depletion model, abundances remain constant throughout the disk.

There are commonly two methods of introducing chemical depletion in disks: a uniform depletion (with respect to H_2) factor across the entire disk, and a jump depletion where grain depletion only comes into play below a certain temperature threshold. The formation of HCO^+ depends directly on the abundance of CO, and thus the HCO^+ abundance is assumed to follow the CO characteristic depletion. CO freeze-out typically occurs at $T \leq 22\text{K}$, thus implying a necessary HCO^+ depletion at low temperatures. However, the abundance of HCO^+ can be altered from typical interstellar values for a variety of other factors: photodissociation can occur in the hot inner regions of the disk due to the enhanced UV flux of a young star, or through interstellar cosmic rays. We therefore utilize a uniform depletion from standard ISM abundances taken from Lee, Bettens & Herbst, (1996). This assumption may limit the predicted detectability of massive gas clumps in a circumstellar disk. In a study of the fractional ionization in disks, Semenov et al. (2004) find the dominant ion in the intermediate layer and mid-

plane to be HCO^+ at the radii where the densest gas clumps in our models form (10 AU), whereas the fractional HCO^+ drops in the surface layers. By uniformly depleting the HCO^+ abundance, we may be decreasing emergent flux.

van Zadelhoff et al. (2001) estimate depletions ranging from 0.1-0.001 from standard ISM abundances for disks TW Hya and LkCa 15. Dutrey et al. (1997) find an average HCO^+ abundance of $7.4 \times 10^{-10} / \text{H}_2$, corresponding to a depletion of ~ 0.15 . We have run three models corresponding to depletion factors of 0.5, 0.1 and 0.01. While simple depletion models are likely not valid for the extremely dense cores of proto-GGPs, as we discuss in § 3.5.1, the specifics of the chemistry in the densest regions of the disk may not contribute significantly to the emergent HCO^+ flux.

3.4 Images

High angular resolution interferometers such as ALMA will be able to achieve unprecedented imaging capabilities of Galactic circumstellar disks. Utilizing our radiative transfer codes, we have created synthetic intensity contour maps of the HCO^+ emission from the gravitationally unstable protoplanetary disk in our models, and present them in this section. The parameter space we explore includes rotational transition, inclination angle, and abundance.

3.4.1 Molecular Transition

In Figure 3.2 we show model contours of spectral line intensity of the protoplanetary disk as viewed through the HCO^+ J=1-0, 4-3 and 7-6 transitions at 1/2 ISM abundance. The disk is face on ($i=90^\circ$) in each image.

The GGP in our simulation achieves a maximum density of $n=3.0 \times 10^{15} \text{ cm}^{-3}$. At these high densities, and warm temperatures ($\sim 100 \text{ K}$), collisions will ensure that most of the HCO^+ molecules are excited well above the ground state. Indeed,

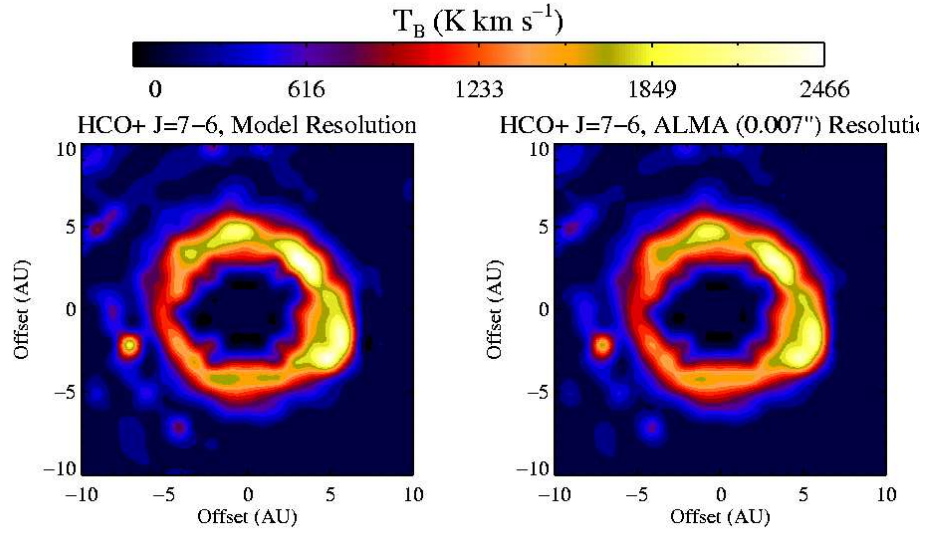


Figure 3.3 The effect of angular resolution on the image: HCO⁺ transitions J=7-6. The left column is at model resolution. The right column is a simulated ALMA image at 0.007'' (the most extended baseline of ALMA, Bastian 2002) for a source distance of 140 pc. The synthesized images are the mirror image of the density contours in Figure 3.1, and thus the proto-GGP is at ~8 o'clock in each panel. No noise has been added to this figure (or future figures in this chapter). The intensity is in units of K-km s⁻¹ and is on a fixed scale for the entire figure.

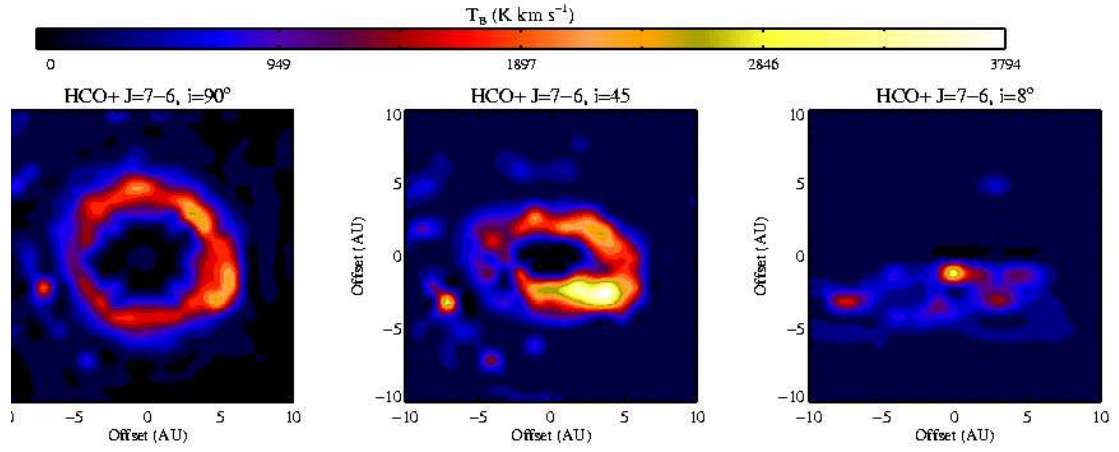


Figure 3.4 The effect of inclination on the image: HCO^+ transition $J=7-6$. The inclinations are 90° (face on), 45° and 8° . 8° is roughly the minimum inclination angle at which the proto-GGP did not get lost in the emission of the disk. The synthesized images are the mirror image of the density contours in Figure 3.1, and thus the proto-GGP is at ~ 8 o'clock in each panel.

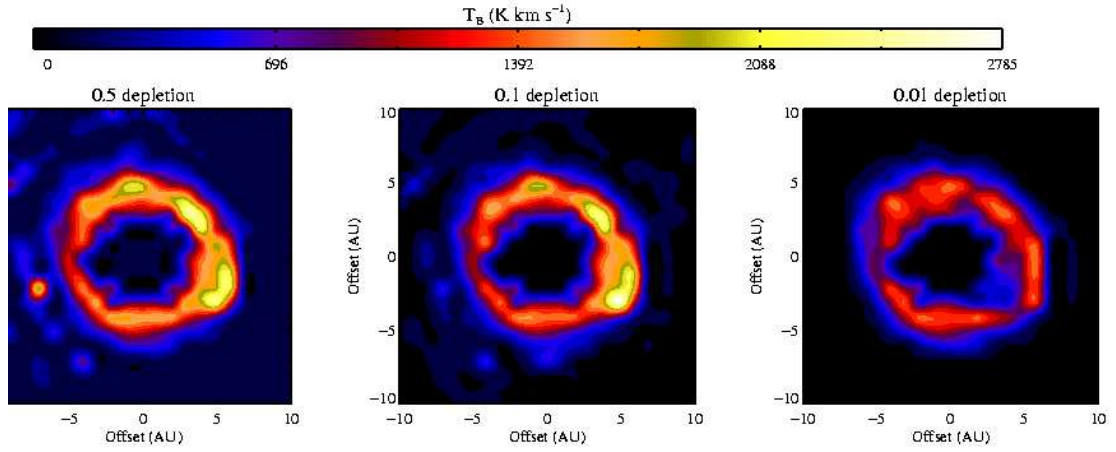


Figure 3.5 The effect of HCO^+ abundance on the image. Abundances (from left) are $1 \times 10^{-9}/\text{H}_2$, $5 \times 10^{-10}/\text{H}_2$, $5 \times 10^{-11}/\text{H}_2$. The proto-GGP is only visible in the image at the highest HCO^+ abundance. The synthesized images are the mirror image of the density contours in Figure 3.1, and thus the proto-GGP is at ~ 8 o'clock in the leftmost panel.

as our simulations show, the GGP is only fully visible at the highest HCO^+ transitions. While lower transitions in HCO^+ may be able to detect dense clumps in the circumstellar disk, the densest clumps that may be self-gravitating can be identified using high-density tracers. For the HCO^+ J=7-6 transition ($n_{\text{crit}} \sim 10^7 \text{ cm}^{-3}$), the proto-GGP emits quite prodigiously while the clumps in the remaining parts of the disk begin to fade. The high J levels of dense gas tracers serve as an efficient method of filtering out low density gas that may not be directly associated with the protoplanet. We have not explored any transitions beyond HCO^+ J=7-6. It may be, however, that the proto-GGP is even more distinct at higher (THz) HCO^+ transitions. For the transitions we have modeled, the densest clumps in the circumstellar disk are most visible in HCO^+ J=7-6. We will therefore explore the effects of inclination and abundance primarily in this transition.

With its most extended baseline, ALMA will be able to achieve a spatial resolution of $0.007''$ at HCO^+ (J=7-6, $\nu_0=624 \text{ GHz}$) (Bastian 2002). At the distance of Taurus Molecular Cloud, $\sim 140 \text{ pc}$, this angular resolution (1 AU) is quite comparable to our model resolution of $\sim 0.5 \text{ AU}$. In Figure 3.3, we have simulated an observation of our circumstellar disk by setting it at a distance of 140 pc and convolving it with the $0.007''$ ALMA beam. We assume no lost flux and a circular Gaussian beam. The proto-GGP and other dense clumps are quite visible. As an example, in one hour of integration, the 64-element ALMA array should be able to image the dense protoplanet in Figure 3.3 with a signal to noise ratio of $\sim 3-4$. Additionally, as we will show in § 3.5, signatures of dense clumps may be evident even in single-dish sub-mm telescopes through signatures in the emission line profile.

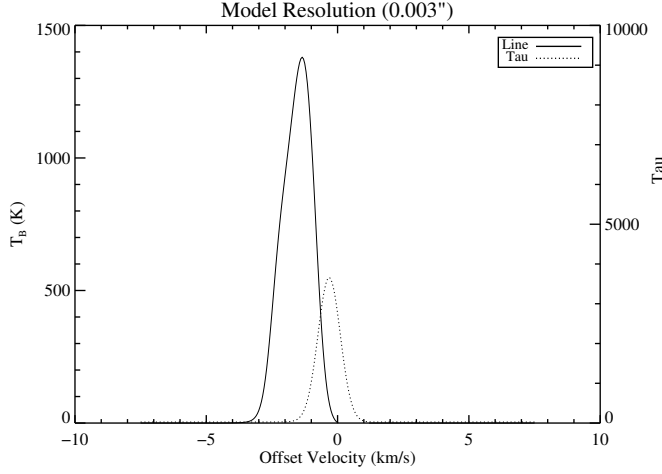


Figure 3.6 HCO^+ J=7-6 spectral line profile at model resolution through the proto-GGP with optical depth overplotted. The central density is $\sim 10^{15} \text{cm}^{-3}$, and the line is completely self-absorbed at line center. The emission is primarily due to radiatively pumped gas in the outer layer of the proto-GGP.

3.4.2 Inclination

As we will discuss in § 3.5.1, the emission from the proto-GGP is largely from the outer layers. Consequently, the inclination angle of the disk does not affect the results significantly. As seen in Figure 3.4, even at nearly edge-on inclinations, the proto-GGP is still visible at HCO^+ J=7-6. However, due to increasing column through the disk in low-inclination scenarios, other dense clumps in the disk begin to emit at similar intensities as the proto-GGP, thus confusing observations. Because of this effect, we have found that the minimum angle in our models that the proto-GGP is visible is $i \sim 8^\circ$. Inclination effects can quickly wash out signatures of the proto-GGP in the spectral line profile (see §3.5).

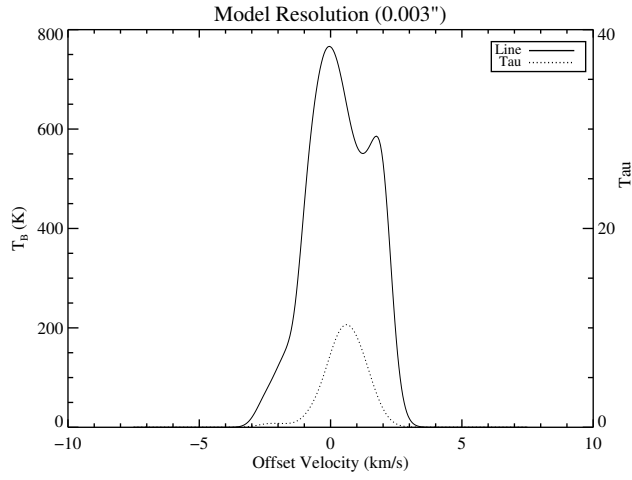


Figure 3.7 HCO^+ $J=7-6$ spectral line profile at model resolution through the dense clump at position $x = 5$ AU, $y = -3$ AU (for reference with Figure 3.5). The central density of the clump is $\sim 10^{15} \text{ cm}^{-3}$. Some emission from the central regions escapes, and the line is not completely self-absorbed.

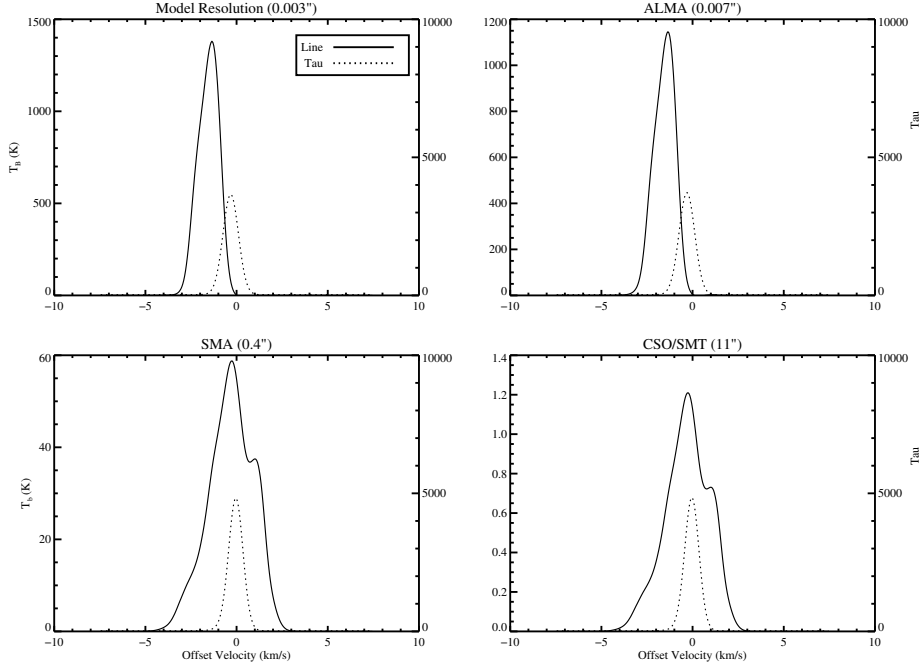


Figure 3.8 HCO^+ J=7-6 spectral line profile of proto-GGP, convolved to the beam of different telescopes. The assumed abundance is $1 \times 10^{-9}/\text{H}_2$ (0.5 depletion from standard ISM values, Lee, Bettens & Herbst 1996). In all cases, the simulated telescope is pointed directly at the proto-GGP. The telescopes simulated are ALMA, the SMA and a 10m class single dish. The corresponding optical depth, τ , is overplotted, with values on the right side of each box. The disk is face-on.

3.4.3 Abundances

We have modeled the HCO^+ abundances as uniform, modulo depletion factors (§ 3.3.4). In Figure 3.5, we present face-on images of the protoplanetary disk at 0.5, 0.1 and 0.01 depletion factors from standard ISM abundances. The proto-GGP is no longer visible at lower abundances. This holds for all inclinations, as well as all lower HCO^+ transitions. With less emitting molecules along the line of sight, the proto-GGP emission is no longer able to dominate over the other dense clumps in the disk. However, the proto-GGP does, in fact, emit similar peak line temperatures as other dense clumps in the cloud. Why, then, does the protoplanet not appear to emit brightly in the image? The image shows velocity integrated line intensity - the total area under the emission spectrum. Much of the emission from the proto-GGP is self absorbed, and the majority of the emission comes from radiatively pumped gas in the outer layers at low velocity dispersion (§ 3.5.1). This effect reduces the velocity integrated intensity.

3.5 Line Profiles

3.5.1 Non-LTE Effects: Radiative Pumping in the Vicinity of Dense Gas Clumps

In Figure 3.6, we have plotted the HCO^+ ($J=7-6$) emission spectrum through the proto-GGP in the model with 0.5 depletion factor. The large optical depths cause the line flux to be ~ 0 K at line center. The emission from the proto-GGP does not originate at the core of the dense clump of gas, but rather in the more diffuse outer layers. While the gas in the dense core of the proto-GGP is in LTE, the emission from this gas suffers heavy extinction owing to the high optical depths at line center. However, the density through the proto-GGP drops off quickly with radius allowing gas in the outer layers (where $\tau \lesssim 1$) to be radiatively pumped by ~ 1500

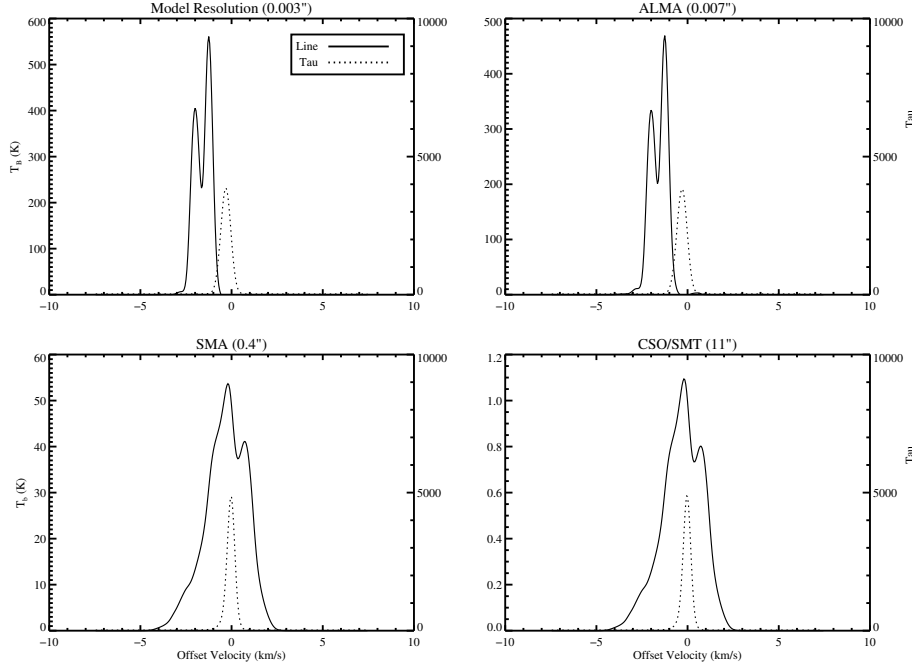


Figure 3.9 HCO^+ J=7-6 spectral line profile of proto-GGP, convolved to the beam of different telescopes. The assumed abundance is $5 \times 10^{-10}/\text{H}_2$ (0.1 depletion from standard ISM values, Lee, Bettens & Herbst, 1996). In all cases, the simulated telescope is pointed directly at the proto-GGP. The telescopes simulated are ALMA, the SMA and a 10m class single dish. The corresponding optical depth, τ , is overplotted, with values on the right side of each box. The disk is face-on.

K gas near the protostar. The strong emission line temperatures, then, originate in radiative excitation of lower density non-LTE gas, rather than from the core of the cold proto-GGP, and consequently does not reflect the kinetic temperature of the emitting gas.

The emission pattern of heavy self-absorption at line center, and radiatively pumped gas at the surface is characteristic only of the densest clump of gas in our models, e.g., the self-gravitating proto-GGP with central density $\sim 10^{15} \text{ cm}^{-3}$. As it is these densest clumps that serve as antecedents to GGPs, the line profile of heavy self absorption at line center combined with offset emission may be characteristic of GGPs in formation. The optical depth in other dense clumps in the circumstellar disk is sufficient to produce self-absorption in the line profiles, but not to the same degree as seen toward the proto-GGP. As an example, in Figure 3.7, we plot the emergent HCO^+ J=7-6 spectra at model resolution and depletion factor 0.5 from a clump in the face-on disk (located at $x = 5 \text{ AU}$, $y = -3 \text{ AU}$ for reference with Figure 3.5) with central density $\sim 1.75 \times 10^{11} \text{ cm}^{-3}$. The optical depth at line center only reaches $\tau \approx 1$ near the dense core of the clump, allowing significant emission from both the LTE core, as well as the radiatively pumped outer layers of the dense clump to escape. In contrast, the optical depth at line center at the core of the proto-GGP reaches a total value of several thousand, rendering the majority of the proto-GGP optically thick.

The nature of emission from the proto-GGP has implications concerning the assumed chemistry in these models. High optical depths through the densest regions of the proto-GGP prevents radiation from emerging. For example, even in the model with lowest optical depths (0.01 depletion factor), only $\sim 5\%$ of the emission at the line peak originating from the center of the proto-GGP reaches the observer. This pales in comparison to the emission from the radiatively pumped

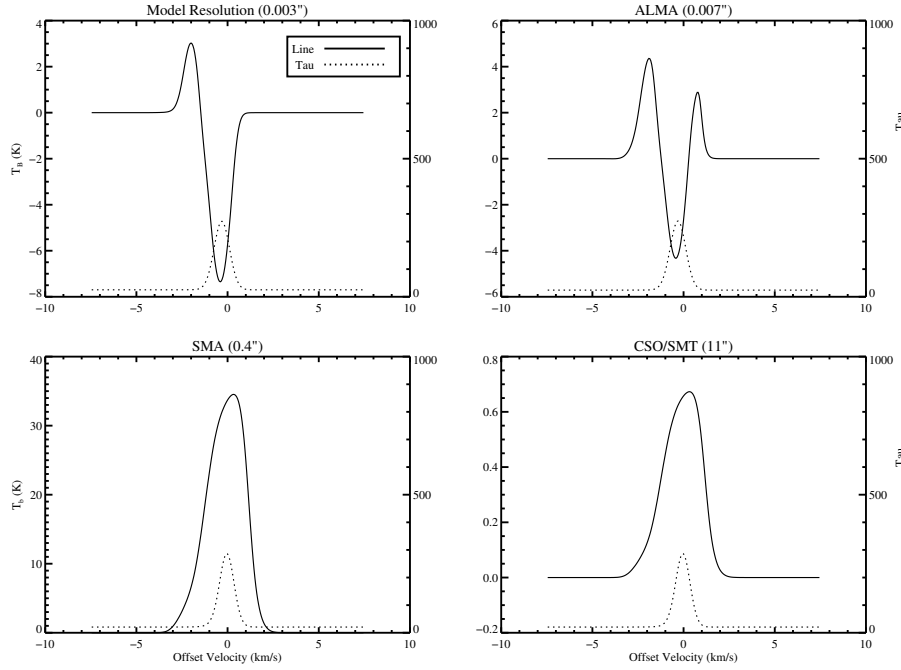


Figure 3.10 HCO^+ $J=7-6$ spectral line profile of proto-GGP, convolved to the beam of different telescopes. The assumed abundance is $5 \times 10^{-11} / \text{H}_2$ (0.01 depletion from standard ISM values, Lee, Bettens & Herbst, 1996). In all cases, the simulated telescope is pointed directly at the proto-GGP. The telescopes simulated are ALMA, the SMA and the 10m class single dish. The corresponding optical depth, τ , is overplotted, with values on the right side of each box. The disk is face-on.

gas in the outer layers of the proto-GGP which has an order of magnitude higher source function than the LTE gas at the core. The emission due to radiative pumping of the less dense gas in the outer layers of the proto-GGP will tend to mask more complex chemistry that may be occurring in the denser regions.

3.5.2 Effects of Abundance and Resolution

In order to further quantify the effect dense clumps have on the emission line profiles, we have convolved the model results with circular Gaussian telescope

beams of different sizes (corresponding to the diameter of the telescope and the frequency of interest) and plotted the synthesized emission line spectra for three different HCO^+ abundances.

In Figure 3.8, 3.9 and 3.10, we have plotted the model emission line profile as viewed by ALMA, the SMA and 10m class single-dish telescopes [e.g., Caltech Submillimeter Observatory (CSO) or the Heinrich Hertz Submillimeter Telescope (SMT)]. With each spectral line, we have overplotted the optical depth (τ) as a function of velocity. The model disks are viewed face on. The line profiles are found to change significantly as a function of abundance. However, in each instance the line profiles through the proto-GGP are heavily self-absorbed.

In the model with a 0.5 depletion factor, the emission line through the proto-GGP, both at model resolution and that of ALMA, is self-absorbed to zero flux at line center. This is evident from the location of the peak in the optical depth profile. The asymmetry in the line profile ($\sim 1\text{-}2 \text{ km s}^{-1}$ of line center) is due to motion along the line of sight of the emitting atmosphere. As the beam size gets larger, more emission from the disk is included, and the effects of self-absorption begin to be washed out. The model with 0.1 depletion factor is qualitatively very similar to the 0.5 depletion factor case. There are minor differences involving the emission of different velocity components in the proto-GGP, but generally the results are the same. It is notable, however, that the peak line temperature has dropped by a factor of 2-3. Self-absorption features become more pronounced in the model with 0.01 depletion where an inverse p-cygni profile is observed. In this lowest abundance model, the column of emitting molecules is low enough that the emission can no longer fill in the absorption trough. The absorption is washed out for angular resolutions $\gtrsim 0.1''$. The emission from the rest of the disk, once folded into the beam, quickly counteracts the self-absorption feature and a

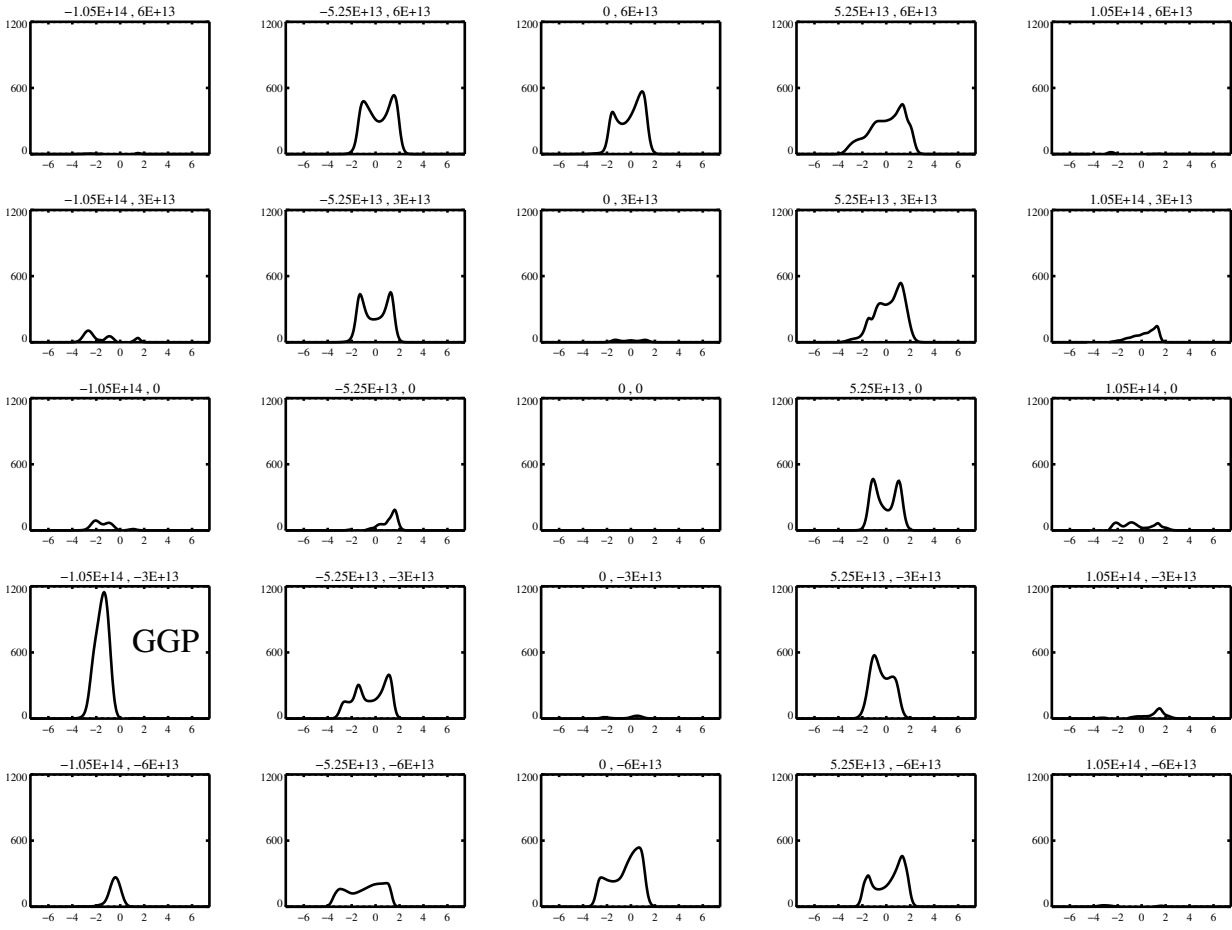


Figure 3.11 Spectral map of model with $1 \times 10^{-9} / \text{H}_2$ abundance. The disk is face on, and the beam is $0.007''$, corresponding to the longest ALMA baseline. The x-axis in each plot is offset velocity (km s^{-1}) and the y-axis in Rayleigh-Jeans Temperature (K). The title in each panel refers to the offset position in cm. The map is made from the mirror image of the density contours presented in Figure 3.1.

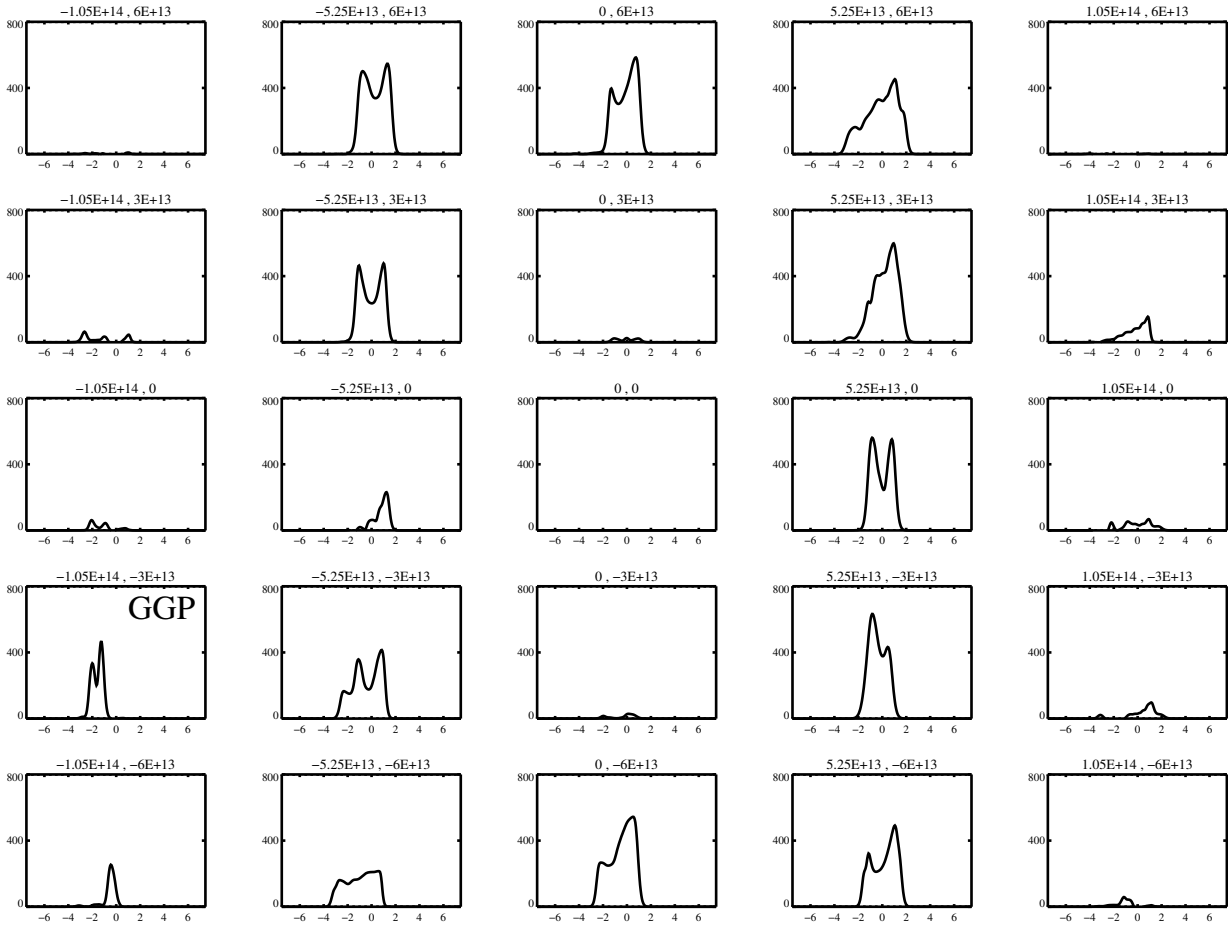


Figure 3.12 Spectral map of model with $5 \times 10^{-10} \text{ H}_2$ abundance. The disk is face on, and the beam is $0.007''$, corresponding to the longest ALMA baseline. The x-axis in each plot is offset velocity (km s^{-1}) and the y-axis in Rayleigh-Jeans Temperature (K). The title in each panel refers to the offset position in cm. The map is made from the mirror image of the density contours presented in Figure 3.1.

single peaked Gaussian line is observed.

At all abundances in our models, the self absorption through the proto-GGP reduces the flux at line center to 0 or negative values. Conversely, non self-gravitating dense clumps in our models only show moderate self-absorption. It may be that complete self-absorption to zero or negative flux is a signature of GGP formation discernible by ALMA. As the disk becomes more inclined, the self-absorption features become less discernible as the emission line broadens.

3.6 Spectral Maps

In Figure 3.11, we have taken spectra along various lines of sight through the face on protoplanetary disk with 0.5 depletion, convolved to a $0.007''$ ALMA beam. The proto-GGP stands out in emission quite high above the rest of the disk. This was evident as well in the contour emission map (Figure 3.2).

Spectral mosaics are particularly useful for identifying GGPs at low HCO^+ abundance levels (e.g., Figure 3.12) where the proto-GGP may make itself evident through its bright emission line and self-absorbed profile. This type of emission is missed in a velocity integrated intensity contour map, however, owing to self-absorption in the line.

3.7 Chapter Conclusions

In this chapter, we have presented non-LTE radiative transfer calculations of HCO^+ rotational line emission in a gravitationally unstable protoplanetary disk. Our models suggest the following:

1. Dense gas clumps associated with proto-GGPs formed via disk instabilities may be observable with interferometers (e.g., ALMA) in molecular transitions with high critical density (e.g., HCO^+ $J=7-6$). The emission is domi-

nated by radiatively pumped gas in the outer layers of dense clumps, and thus does not necessarily reflect the physical temperature of the emitting gas.

2. The emission lines arising from the densest self-gravitating gas clumps in the protoplanetary disk are completely self-absorbed to zero or negative flux. The line profiles from other dense gas clumps are self absorbed, as well, although to a lesser degree.
3. Proto-GGPs often appear as bright peaks in spectral line maps, making them easier to identify in the presence of extended disk emission.
4. ALMA will have the angular resolution and sensitivity necessary to directly image proto-GGPs in formation in nearby circumstellar disks.

More complete chemical models and reaction networks will be incorporated in our models in future works. Additionally, a thorough investigation as to the variation of spectral line profiles as a function of disk evolution is underway.

CHAPTER 4

THE ROLE OF GALACTIC WINDS ON MOLECULAR GAS EMISSION FROM
GALAXY MERGERS

Those images look pretty dope

-T.J. Cox, on model CO images of galaxy merger during quasar phase

4.1 Chapter Abstract

Galactic winds from starbursts and Active Galactic Nuclei (AGN) are thought to play an important role in driving galaxy evolution. Here, we assess the impact of these winds on the CO emission from galaxy mergers, and, in particular, search for signatures of starburst and AGN-feedback driven winds in the simulated CO morphologies and emission line profiles. We do so by combining a 3D non-LTE molecular line radiative transfer code with smoothed particle hydrodynamics (SPH) simulations of galaxy mergers that include prescriptions for star formation, black hole growth, a multiphase interstellar medium (ISM), and the winds associated with star formation and black hole growth. Our main results are: (1) Galactic winds can drive outflows of masses $\sim 10^8$ - $10^9 M_\odot$ which may be imaged via CO emission line mapping. (2) AGN feedback-driven winds are able to drive imageable CO outflows for longer periods of time than starburst-driven winds owing to the greater amount of energy imparted to the ISM by AGN feedback compared to star formation. (3) Galactic winds can control the spatial extent of the CO emission in post-merger galaxies, and may serve as a physical motivation for the sub-kiloparsec scale CO emission radii observed in local advanced mergers. (4) Secondary emission peaks at velocities greater than the circular ve-

locity are seen in the CO emission lines in all models, regardless of the associated wind model. In models with winds, however, these high velocity peaks are seen to preferentially correspond to outflowing gas entrained in winds, which is not the case in the model without winds. The high velocity peaks seen in models without winds are typically confined to velocity offsets (from the systemic) $\lesssim 1.7$ times the circular velocity, whereas the models with AGN feedback-driven winds can drive high velocity peaks to ~ 2.5 times the circular velocity.

4.2 Chapter Introduction

Observed relationships in galaxies between central black hole mass and stellar mass (e.g., Magorrian et al. 1998), velocity dispersion (i.e. the $M_B H$ - σ relation; e.g., Gebhardt et al. 2000; Ferrarese & Merritt 2000), or galaxy structural properties (e.g., the black hole fundamental plane: Hopkins et al. 2007a,b) indicate a co-eval nature in supermassive black hole growth and star formation in galaxies. These results have prompted a number of investigations in recent years to quantify this apparent self-regulation in star formation and black hole growth in galaxies, and their relationship to the formation and evolutionary history of the host system (e.g., Kauffmann & Haehnelt, 2000; Hopkins et al. 2006a,b; 2007c,d).

Over the last two decades, observations of local galaxies have painted a compelling picture in which galaxy mergers provide the link between massive starbursts and central black hole growth and activity. ULIRGs (Ultraluminous Infrared Galaxies), for example, are a class of starburst galaxies with elevated infrared luminosities ($L_{\text{IR}} \geq 10^{12} L_{\odot}$) which typically show signs of interactions (e.g., Downes & Solomon, 1998; Sanders et al. 1988a; Scoville et al. 2000). While the intense infrared luminosity in these sources certainly owes in large part to the merger induced starbursts (e.g., Sanders et al. 1988a,b; Sanders & Mirabel

1996), in some cases a contribution from a buried active galactic nucleus (AGN) may be non-negligible. For example, many ULIRGs show spectral energy distributions (SEDs), infrared color ratios (e.g., $F[25]/F[60]\mu\text{m}$), polycyclic aromatic hydrocarbon emission (PAH) deficits, and emission line fluxes (e.g., [Ne V] at $14.3\mu\text{m}$) consistent with central AGN activity (e.g., Armus et al. 2004, 2006; Farrah et al. 2003; de Grijp et al. 1985). Indeed, 35-50% of ULIRGs with luminosity above L_{IR} of $10^{12.3} L_{\odot}$ show optical and NIR spectra consistent with AGN activity (Kim, Veilleux & Sanders, 2002; Tran et al. 2001; Veilleux, Kim & Sanders, 1998). These results suggest that these merging systems are simultaneously undergoing a massive star formation and central black hole growth phase.

Observed similarities such as these between starburst galaxies, ULIRGs and quasars prompted Soifer et al. (1987) and Sanders et al. (1988a,b) to propose an empirically derived evolutionary sequence which connects galactic starbursts to quasars through galaxy mergers. In this picture, the fueling of the central black hole and AGN growth phase is realized during the major merger when gaseous inflows trigger nuclear starbursts as well as central black hole growth. The dusty galaxy transitions from a cold, starburst dominated ULIRG, to a warm, AGN-dominated ULIRG (where 'cold' and 'warm' refer to $F[25/60\mu\text{m}]$ ratios), and, as supernovae and stellar winds clear the obscuring gas and dust, to an optical quasar. In this sense, galaxy mergers provide a unique laboratory for studying the possible co-evolution of starbursts, black hole growth and activity, and spheroid formation.

Recent models have provided a theoretical foundation and further evidence for a merger-driven starburst-AGN connection in galaxies. Specifically, simulations by Springel, Di Matteo & Hernquist (2005a) have shown that galaxy mergers can fuel large-scale gaseous inflows (e.g., Barnes & Hernquist 1991, 1996) which

trigger nuclear starbursts (Mihos & Hernquist 1996; Springel et al. 2005a) as well as promote central black hole growth (Di Matteo, Springel & Hernquist 2005). Subsequent winds associated with the growth of central black holes can lift the veil of obscuring gas and dust, and along several sightlines produce a quasar with comparable lifetimes, luminosity functions, and observed B -band and X-ray properties to those observed (Cox et al., 2006b; Hopkins et al. 2005a-d; 2006a-d). The merger remnants quickly redden owing to gas depletion and the impact of feedback from star formation and black hole growth (e.g., Springel et al. 2005b) and resemble elliptical galaxies in their kinematic and structural properties. Indeed, the population of stars formed during the starbursts accounts for the central “excess light” seen in ongoing mergers (e.g., Rothberg & Joseph 2004, 2006) and provides a detailed explanation for the luminosity profiles of old ellipticals (e.g., Kormendy et al. 2007; see Mihos & Hernquist 1994a; Hopkins et al. 2007e,f,g).

A consensus picture has thus been borne out from these observations and simulations over the last two decades in which so called ‘feedback’ processes associated with winds from star formation and black holes act to self-regulate the growth of both the stellar and black hole masses in galaxies (e.g., Fabian 1999; Silk & Rees 1998). Indeed, the effects of starburst and AGN feedback-driven winds have been observed in local galaxies (e.g., Heckman et al. 2000; Martin 2005; Rupke, Veilleux & Sanders 2005a-c; Rupke & Veilleux 2005; Tremonti, Moustakas & Diamond-Stanic 2007), as well as those at high- z (e.g., Narayanan et al. 2004; Pettini et al. 2002; Shapley et al. 2003) by way of absorption line outflows. However, the direct effect of feedback processes (especially from the highly efficient central AGN) on the emission properties of galaxies is not yet well characterized (see Veilleux, Cecil & Bland-Hawthorn 2005 for an extensive review and associated references). In this sense, it is important to relate theories of galaxy forma-

tion and evolution which incorporate physically motivated models of feedback processes to observational signatures of winds across the electromagnetic spectrum.

In particular, observations of molecular gas in galaxies have proven valuable in characterizing the physics related to nuclear star formation and central AGN fueling in galaxy mergers as the molecular gas serves as fuel for both star formation and the central black hole(s). For example, interferometric observations of molecular gas in ULIRGs show that most typically harbor $\sim 10^{10} M_{\odot}$ of molecular gas within the central 1.5 kpc (Scoville et al. 1986; Bryant & Scoville 1999). Moreover, high resolution maps of dense molecular gas at submillimeter wavelengths in ULIRGs have revealed kinematic structures of double nuclei in mergers (Scoville, Yun & Bryant 1997), bar-driven inflows (Sakamoto et al. 2004), and the density structure of gas fueling the central AGN (Iono et al. 2004).

With the increased spatial resolution and sensitivity afforded by the latest generation of (sub)mm-wave interferometers (e.g., the SMA, CARMA, PdBI), a number of recent observations have been able to pioneer investigations as to the effects of galactic winds on molecular gas emission in galaxies (e.g., Iono et al. 2007; Sakamoto, Ho & Peck 2006; Walter, Weiß & Scoville 2002). Detections such as these are expected to become more routine in upcoming years as the ALMA interferometer becomes available. An important complement to these current and forthcoming observations of molecular line emission from starburst galaxies and AGN are physical models which directly relate CO emission properties to galactic scale winds.

In this context, it is our aim to investigate the role that galactic winds can play on CO emission properties from starburst galaxies and AGN via numerical simulations. In particular, we focus on specific signatures imprinted by winds

on imageable CO morphologies and emission line profiles. In this chapter, we present self-consistent radiative transfer calculations for the emission properties of CO molecular gas in gas-rich galaxy mergers which account for the winds associated with both star formation and black hole growth.

In § 4.3, we describe the hydrodynamic simulations. In § 4.4 we provide an example of our methods by applying our radiative transfer calculations to a model of a star-forming disk galaxy. In § 4.5, we discuss the effect of winds on observed CO morphologies. We explore the response of emission line profiles to winds in § 4.6, present a broader discussion of these results with respect to observations in § 4.7, and summarize in § 4.8. Throughout this paper, we assume a Λ CDM cosmology with $h=0.7$, $\Omega_\Lambda=0.7$, $\Omega_M=0.3$.

4.3 Numerical Methods

4.3.1 Hydrodynamics

The hydrodynamic simulations used for this study employed a modified version of the publicly available N -body/SPH code, GADGET-2 (Springel, 2005), adopting the fully conservative formulation of SPH developed by Springel & Hernquist (2002). The methods used to construct the progenitor galaxies, as well as a detailed description of the algorithms used to simulate the physics of feedback from star formation and accreting black holes is detailed in Springel, Di Matteo & Hernquist (2005a), and we direct the reader toward this work for further information. Here, we briefly summarize these methods, and describe the specifics of the modeling most pertinent to this chapter.

The interstellar medium (ISM) is modeled as a multi-phase medium in which pressure feedback from supernovae heating is treated through an effective equation of state (EOS) (Springel, Di Matteo & Hernquist, 2005a). The disk galaxies

used as progenitors in these simulations employed a softened EOS with softening parameter $q_{\text{EOS}}=0.25$ (see Figure 4 of Springel et al. 2005a). The ISM is modeled to include cold, dense gas surrounded by a hot ISM, and is realized numerically through “hybrid” SPH particles (Springel & Hernquist, 2003b). In this formulation, cold ISM is allowed to grow through radiative cooling of the hot ISM, and conversely feedback associated with star formation can evaporate cold clouds into diffuse, hot gas. Star formation follows the prescription of Springel & Hernquist (2003b) and is constrained to fit the Schmidt/Kennicutt observed star formation laws (Kennicutt, 1998a,b; Schmidt, 1959).

In order to explore the effects of galactic winds on the molecular ISM, we include a formulation for both accreting black holes, and winds associated with massive starbursts. In our SPH formalism, the black holes are included as sink particles which accrete gas from the surrounding ISM. The accretion is treated with a Bondi-Lyttleton-Hoyle parametrization (Bondi & Hoyle, 1944, Hoyle & Lyttleton, 1939) with a fixed maximum rate corresponding to the Eddington limit. The black hole radiates such that its bolometric luminosity is given by $L=\epsilon\dot{M}c^2$ with accretion efficiency $\epsilon=0.1$. We further assume that 5% of this energy couples to the surrounding ISM such that 0.5% of the accreted mass energy in our simulations is reinjected isotropically into the ISM as thermal energy (a parameter choice which allows the merged galaxy to reproduce the local $M_B H$ - σ normalization [Di Matteo, Springel & Hernquist, 2005]). Hence, the black hole energy deposition rate into the ISM may be expressed as

$$\dot{E}_{\text{BH}} = \epsilon_{\text{effective}}\dot{M}_{\text{BH}}c^2 \quad (4.1)$$

where $\epsilon_{\text{effective}}=0.005$ (Cox et al. 2007; Springel, Di Matteo & Hernquist. 2005a).

Starburst winds are treated utilizing the constant wind models of Springel &

Hernquist (2003b). In this formulation, the mass loss rate (denoted by \dot{M}_w) is assumed to be proportional to the star formation rate (denoted by \dot{M}_\star), such that:

$$\dot{M}_w = \eta \dot{M}_\star \quad (4.2)$$

where η quantifies the wind efficiency. The wind is assumed to have a speed constrained by a fraction of the supernova energy (χ):

$$\frac{1}{2} \dot{M}_w v_w^2 = \chi \epsilon_{\text{SN}} \dot{M}_\star \quad (4.3)$$

In a recent study of galactic winds in galaxy mergers, Cox et al. (2007) found that highly efficient, high velocity winds ($\eta \geq 1$) may be unphysical in that they tend to prevent any starburst after the major merger. We thus choose a moderate wind efficiency of $\eta=0.5$, and constant wind velocity $v_w=837 \text{ km s}^{-1}$ for this study. These numbers are consistent with the favored momentum-driven wind scalings for the galaxy masses we simulate found by Oppenheimer & Davé (2006). For more details concerning constraints on wind velocities and efficiencies in galactic scale simulations, we refer the reader to Cox et al. (2007).

The energy input rate into the ISM from star formation may be expressed as

$$\dot{E}_{\text{sb}} = \epsilon_{\text{SN}} \dot{M}_\star \quad (4.4)$$

where ϵ_{SN} is the energy imparted by supernovae, per solar mass, taken here to be $1.4 \times 10^{49} \text{ ergs } M_\odot^{-1}$ (Springel & Hernquist 2003b).

The progenitor galaxies in our models contain a dark matter halo initialized with a Hernquist (1990) profile, concentration index $c=9$, spin parameter $\lambda=0.033$ and circular velocity $V_{200}=160 \text{ km s}^{-1}$. The galaxy's exponential disk is rotationally supported and comprises 4.1% of the total mass. We utilize 120,000 dark matter particles, and 80,000 total disk particles, 40% of which are gaseous in nature, the remainder serving as collisionless star particles. The total masses of the

progenitor galaxies were $1.4 \times 10^{12} M_{\odot}$, and the final merger produced a central black hole with mass $\sim 5 \times 10^7 M_{\odot}$. The softening lengths were 100 pc for baryons, and 200 pc for dark matter.

We have conducted five binary merger simulations. Each of the progenitor galaxies in our simulations was constructed with the aforementioned physical parameters, and the varied parameters include initial orbit, V_{200} , gas fraction and types of wind included (e.g., starburst and/or AGN). Identical progenitor galaxies were used in each simulation, save for the single model with an increased gas fraction. The initial conditions for the merger simulations are summarized in Table 5.1, and we will henceforth refer to the simulations by their model name listed in Column 1 of Table 5.1. In order to simplify analysis and limit the number of free parameters, throughout this paper we will largely analyze the properties of the four simulations which share the same merger orientation and have 40% initial gas fraction, and utilize the coplanar simulations (model co-BH) for only specific comparisons.

4.3.2 Overview of A Major Merger

In the binary merger simulations presented here, after the initial passage of the merging galaxies, gas is driven into the nuclear regions owing to tidal torquing (Barnes & Hernquist, 1991, 1996). This begins a major black hole growth phase. While the galaxies approach toward and undergo final coalescence¹ (hereafter defined as the in-spiral stage) they go through a massive starburst and LIRG/ULIRG phase while the central black hole grows as an enshrouded AGN following the

¹Nuclear Coalescence is defined for the purposes of this paper as when the progenitor BH particles are separated by less than a smoothing length, and are thus no longer distinguishable. BH particles are included for all models in this paper, although they do not accrete in model no-winds. Coalescence could equivalently be defined as when the stellar bulges of the progenitors are no longer distinguishable, though in practice the choice of a definition for nuclear coalescence is somewhat arbitrary and makes little difference in the results. The time of coalescence is typically $T \sim 1.6$ Gyr, though varies slightly from model to model.

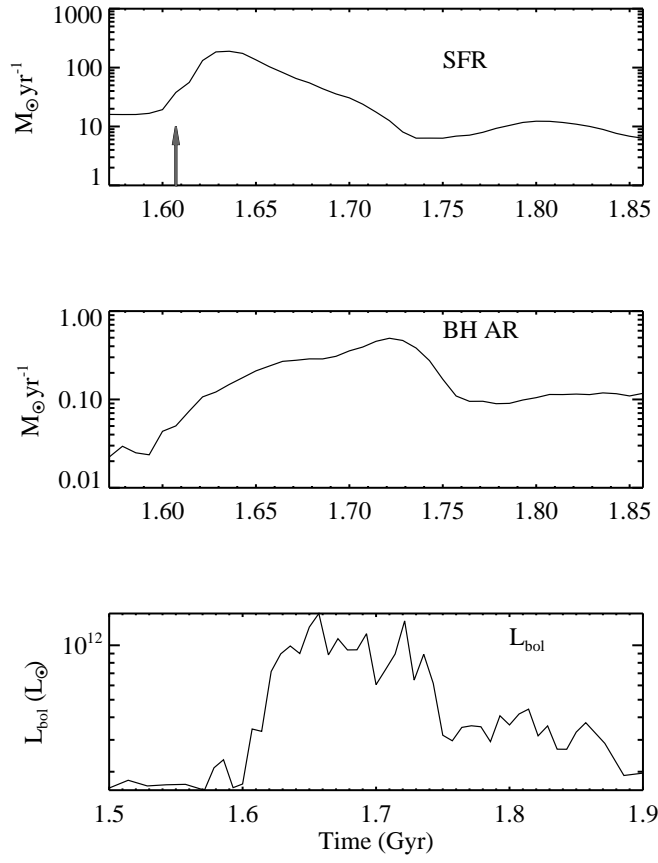


Figure 4.1 SFR, black hole accretion rate and bolometric luminosity as a function of time for model BH. The arrow in the top panel denotes the point of nuclear coalescence.

Table 4.1. Progenitor Galaxies and Wind Models

Run	Other Names Used	θ_1	ϕ_1	θ_2	ϕ_2	V_{vir} (km s^{-1})	Gas Frac	BH	SNe
BH	e	30	60	-30	45	160	0.4	yes	no
no-winds	e-no	30	60	-30	45	160	0.4	no	no
sb	–	30	60	-30	45	160	0.4	no	yes
sbBH	–	30	60	-30	45	160	0.4	yes	yes
co-BH	h	0	0	0	0	160	0.4	yes	no

¹Column 1 is the name of the model used in this chapter. Column 2 lists alternative names for these models used by Chakrabarti et al. (2007a,b), Cox et al. (2006a,b; 2007), Hopkins et al. (2005a-d; 2006a-d; 2007h), and Robertson et al. (2006a-c), for comparison. Columns 3 & 4 are initial orientations for disk 1, Columns 5 & 6 are for disk 2. Column 7 gives the virial velocity of the progenitors and Column 8 gives their initial gas fractions. Columns 9 and 10 describe the types of winds (optionally) included in each model.

methodology developed by Springel et al. (2005a). In the models which include AGN feedback-driven winds, after nuclear coalescence, the thermal energy associated with the black hole accretion drives a powerful wind into the surrounding ISM and strongly reduces the star formation rate. During much of this time, along several sightlines, the object may be viewed as an optical quasar (Hopkins et al. 2005a-d; 2006a-d; 2007h). The galaxy then proceeds to evolve passively into a red elliptical galaxy (Springel, Di Matteo & Hernquist, 2005b). In Figure 4.1, we show as a reference the SFR, black hole accretion rate, and bolometric luminosity of model BH throughout the time period considered in this chapter.

The galaxies and quasars formed via this formulation for AGN feedback in galaxy merger simulations have proven consistent with observed quasar luminosity functions and lifetimes (Hopkins et al. 2006a-d, 2006a,c,d; though see Richards et al. 2006), as well as the locally observed $M_{\text{BH}}-M_{\text{bulge}}$ relation (Di Mat-

teo et al. 2005; Hopkins et al. 2007a,b; Robertson et al. 2006a,c). These simulations have also shown successes in reproducing observed X-ray, IR and CO patterns characteristic of ULIRGs and quasars (Cox et al. 2006b Chakrabarti et al. 2007a,b; Narayanan et al. 2006a, respectively), the bimodal galaxy color distribution (Springel, Di Matteo & Hernquist, 2005b; Hopkins et al. 2006b), Seyfert galaxy luminosity functions (Hopkins & Hernquist, 2006), the kinematic structure of merger remnants (Cox et al. 2006a), and observed properties of $z \sim 6$ quasars (Li et al. 2007a,b; Narayanan et al. 2007a).

4.3.3 General Wind Properties in the Simulations

In principle, there are three mechanisms for driving winds in our major merger simulations: via shock heated gas (Cox et al. 2004, 2007), starburst (Cox et al. 2006c, 2007) and AGN-feedback (Cox et al. 2007; Hopkins et al. 2005a-d; Springel, Di Matteo & Hernquist 2005a,b). In practice, however, outflow rates in the simulations are dominated by winds driven by starbursts and AGN feedback. This was explicitly shown by Cox et al. (2007) who found that during the active phase, the outflow rate owing to shock heated gas was at most an order of magnitude less than that from starbursts and/or AGN. Thus for the rest of this chapter, we will focus primarily on the effects of winds from star formation and AGN-feedback, and rely on the model without these winds (though with shock-heated winds) as the fiducial comparative model. We note that Table 1 refers to this model as ‘no-winds’ though in practice winds owing to shock heated gas do exist, albeit with minimal impact on the molecular ISM.

We next review some of the broader physical effects generated by AGN feedback driven and supernovae-driven winds. In a recent comprehensive study of galactic winds in mergers utilizing (among others) identical models to those presented here, Cox et al. (2007) analyzed the decoupled properties of starburst and

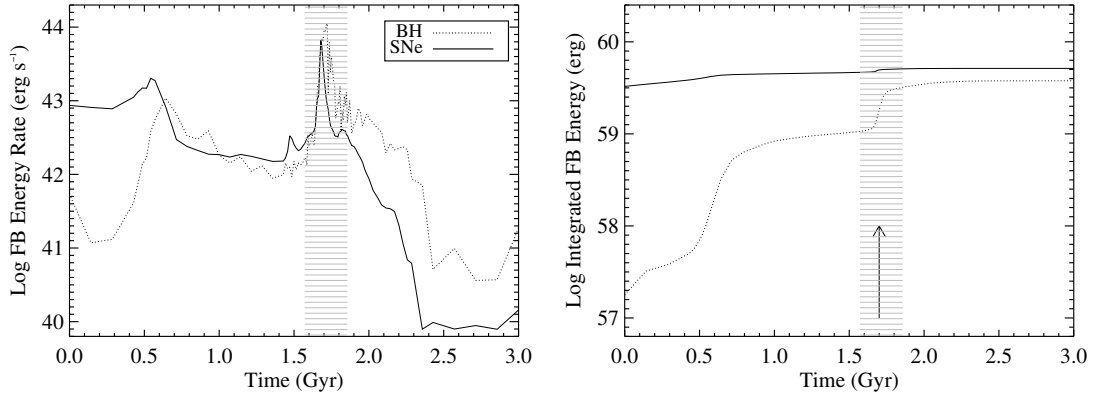


Figure 4.2 Instantaneous feedback energy rate (*left*) and integrated feedback energy (*right*) input into the ISM by black holes (dotted line) and starburst winds (solid line) for model sbBH. The hatched region is the ~ 0.3 Gyr period of peak starburst and black hole activity which will be considered for the remainder of this paper. While the integrated feedback from star formation and black holes is roughly equivalent, the starburst delivers its energy in a slow and steady manner from simulation time $T=0$ spread out over much of the galaxy, in contrast to the near point explosion characteristic of the black hole winds. The arrow in the bottom panel denotes the point of nuclear coalescence. Model results first published in Cox et al. (2007).

AGN feedback-driven winds in galaxy merger simulations. We refer the reader to this work for a thorough analysis of these effects, and highlight here the wind properties most relevant to the discussion of this paper.

As a reference, we first show the instantaneous and integrated feedback energies for model sbBH in Figure 4.2 (e.g., Equations 4.1; model results first published in Cox et al. 2007). We highlight (hatched area) the period of peak starburst and AGN activity which we will focus on for the remainder of this study, and denote as the “active phase”. We focus on this period as the models exhibit their peak wind activity during this time.

The first passage of the galaxies triggers a starburst event, fueling star formation rates to $\sim 50 M_{\odot} \text{yr}^{-1}$, irrespective of the presence of a central black hole. At this point, starburst-driven winds begin to disrupt the central cold gas supplies, limiting to some degree (dependent on the wind efficiency and speed) the magnitude of the starburst. In the simulations presented here, during the in-spiral stage, prior to nuclear coalescence, $\sim 90\%$ of the stellar mass (and thus $\sim 90\%$ of the starburst generated wind mass) is produced (Cox et al. 2007).

The growth of the central AGN and associated feedback winds develops along a markedly different story line. While the initial passage and in-spiral stage of the galaxy merger fuels central black hole growth, the majority of black hole growth occurs during the active phase highlighted in Figure 4.2, typically around nuclear coalescence. The exact percentage of black hole growth that occurs during the active phase is dependent on galaxy mass (Cox et al. 2007), but the generic trends are robust.

After the active phase, the total integrated feedback energy deposited into the ISM from star formation and black holes is roughly the same. However, the instantaneous properties are different. While the energy input from star formation

winds is spread out over the entire in-spiral and active phase, the black hole offers a relatively short impulse of energy. The result of the slow buildup of the stellar mass and relatively rapid black hole growth phase results in black holes contributing over five times the energy input to the ISM as stars during the active phase (Cox et al. 2007). This will have important consequences on the relative impact of winds on CO emission from starbursts and AGN. Throughout this chapter, we will focus on the rough peak of the active phase, specifically $T \sim 1.6-1.8$ Gyr.

4.4 Isolated Disk Galaxy

To illustrate the generic properties of our methods, we have allowed a fiducial 40% gas fraction progenitor disk galaxy to evolve as outlined in Springel et al. (2005a). For reference, in Figure 4.3, we plot the H_2 column density map through the model disk galaxy. In Figure 4.4 we present the CO (J=1-0) through (J=10-9) intensity contours for comparison with observations where the intensity units are $K \cdot km \ s^{-1}$ where the temperature unit is a Rayleigh-Jeans temperature.

The CO (J=1-0) emission traces the star forming molecular gas through the spiral arms and becomes more intense near the starbursting nuclear region. Additionally visible are individual concentrations of cold gas and star forming regions emitting as discrete pockets of CO (J=1-0) emission throughout the spiral arms. Higher density CO transitions probe gas of a higher critical density. Thus the higher-lying transitions probe the higher density peaks, and become more centrally concentrated, following the density distribution in the galaxy.

At first glance, the emission contours from e.g., the CO (J=1-0) image appear to peak at higher temperatures (T_B) than are typically recorded from observations of local star forming spirals. This effect owes to the spatial resolution of the radia-

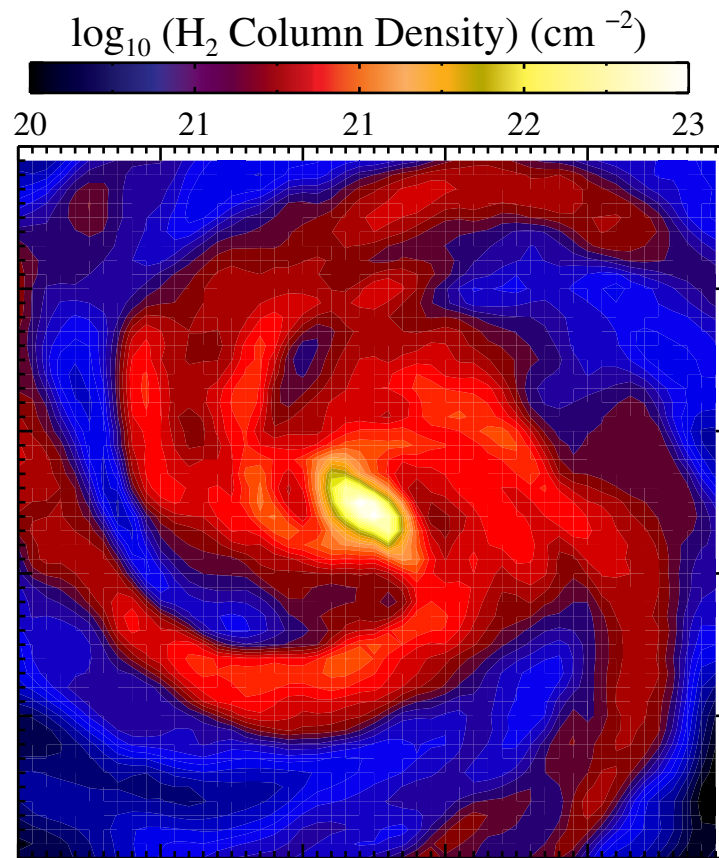


Figure 4.3 H_2 column density for fiducial progenitor disk galaxy (CO contours shown in Figure 4.4). The panel is 12 kpc on a side, and the scale is on top.

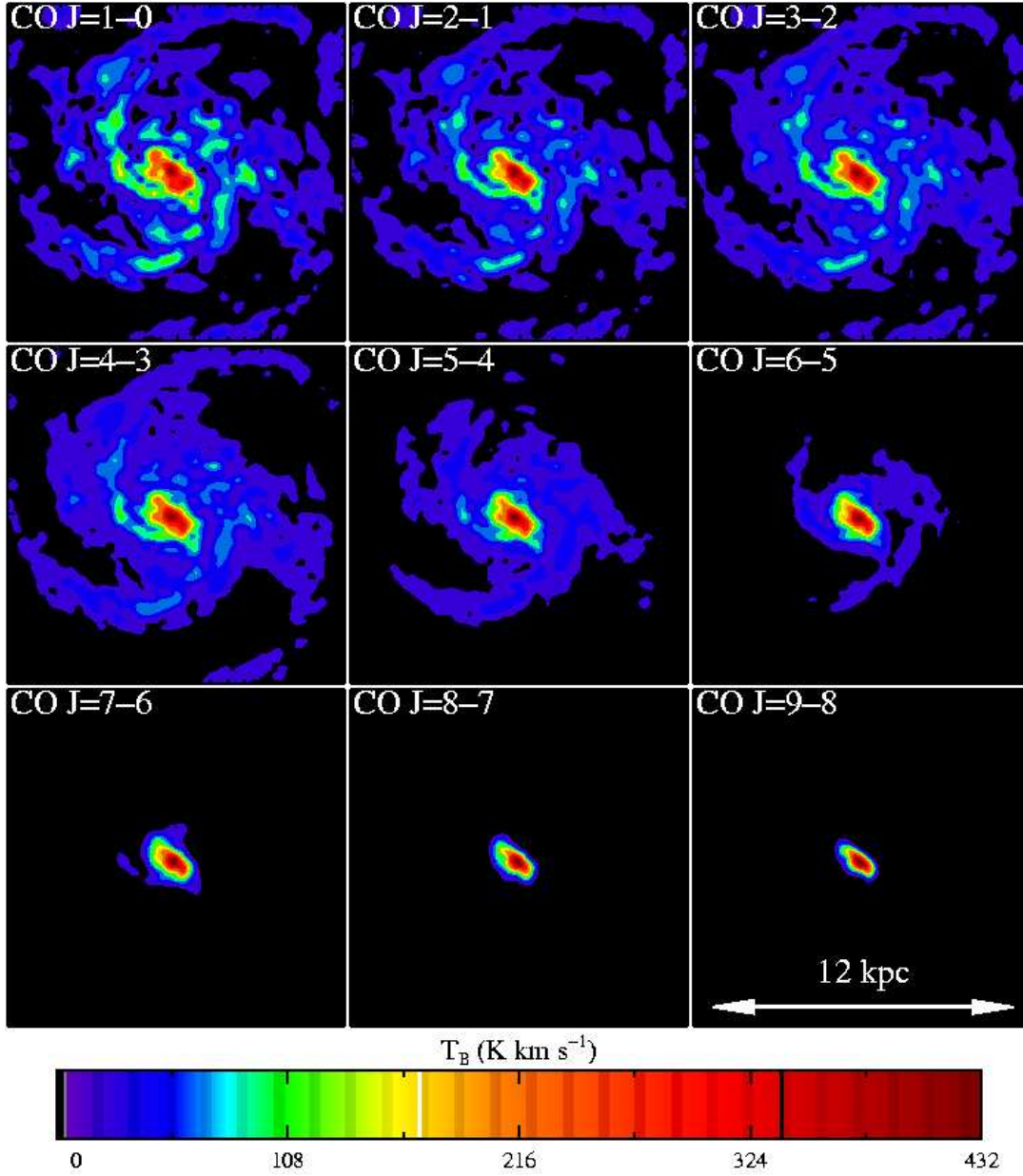


Figure 4.4 Simulated CO (J=1-0) through (J=9-8) emission contours for progenitor disk galaxy. While lower CO transitions trace the bulk of the molecular gas, higher lying transitions with relatively high critical densities probe only the nuclear star forming regions. Panels are 12 kpc on a side, and scale on bottom is in units of K km s^{-1} .

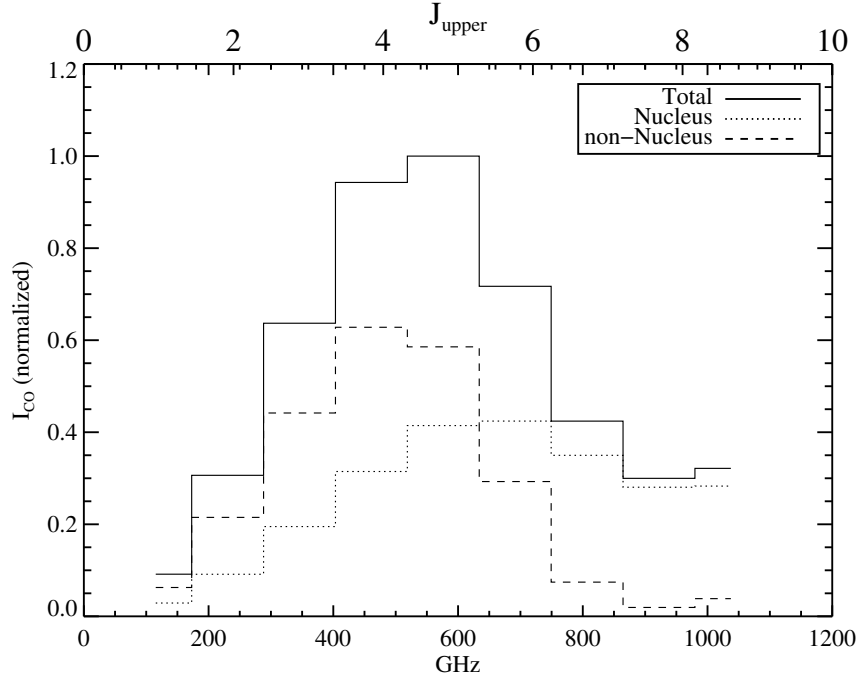


Figure 4.5 Normalized CO SED of a representative progenitor disk galaxy. The CO SED is decomposed into contribution from the nuclear (central kpc) region and the rest of the galaxy. The CO SED shows the relative flux density for different CO transitions, and plots the frequency of the transition on the bottom axis and upper J state on the top axis. The peak in the total CO SED as well as that just from the starbursting nucleus is consistent with results derived from local starburst galaxies, supporting our methodology for deriving CO excitation patterns in galaxy simulations (Bradford et al. 2005; Weiß et al. 2005b).

tive transfer models (~ 250 pc). When simulating more practical observing conditions, the results from our modeling are quite comparable to observations of local universe spirals. As an example, we compare our models to $50''$ observations by Scoville & Young (1983) of CO ($J=1-0$) emission from M51. When our model disk galaxy was scaled to be at the distance of M51 and the CO ($J=1-0$) emission convolved to the same resolution as the Scoville & Young observations, the integrated intensity in our model was comparable to the ~ 60 K-km s $^{-1}$ observed in M51 (Scoville & Young, 1983).

In Figure 5.2 we present the normalized CO line spectral energy distribution (SED) of the model face-on disk galaxy. The CO SED represents the total integrated flux density emitted from each line and serves as a diagnostic for the excitation conditions in the molecular gas. These are plotted as the CO integrated flux density versus the upper rotational quantum number of the transition. CO SEDs are particularly useful in studies of unresolved high- z sources (e.g., Narayanan et al. 2007a; Weiß et al. 2005a, 2007). We have also decomposed the CO SED by plotting the contribution to the flux from the starbursting nucleus (central kpc) and from the rest of the galaxy.

The CO flux density rises up to the CO ($J=5-4$) transition, and then drops toward higher excitation lines. The intensity from the highly excited component of the CO gas (e.g., $J>6$) comes primarily from the warm and dense conditions in the nuclear starburst regions whereas the outer regions of the galaxy (e.g., radius=1-6 kpc) contribute less to the total flux density from high lying lines. This is in good agreement with observations of local starbursts. For example, in a CO SED decomposition of M82, Weiß et al. (2005b) found that the central regions peak at the CO ($J=6-5$) transition whereas the total SED peaks near the CO ($J=4-3$) transition. Similarly, the CO line SED from the nuclear region of NGC 253 peaks near $J=7$ or

$J=8$ (Bayet et al. 2004; Bradford et al. 2003, 2005)

4.5 CO Morphology in Mergers with Winds

Our approach in combining non-LTE radiative transfer calculations with SPH simulations allows us to uniquely explore, for the first time, a variety of the decoupled effects of starburst and AGN feedback-driven winds on the molecular gas emission from galaxy mergers. In particular, a powerful tool for understanding the spatial distribution of molecular gas in local mergers is through high resolution velocity-integrated intensity contour maps. These can serve to describe the morphology and kinematics of the star-forming molecular gas, as well as characterize the nature of star-forming regions through observations of multiple excitation levels (e.g., Iono et al. 2004). Indeed, such maps have revealed, for example, the compact nature of molecular emission in mergers (Bryant & Scoville, 1999), the double-nucleus in the central regions of Arp 220 (Sakamoto et al. 1999), and the large scale distribution of atomic and molecular gas in colliding galaxy systems (Iono, Yun & Ho, 2005). In this section, we build on the current understanding of CO morphologies in interacting systems by describing the response of the CO morphology to starburst and AGN feedback-driven winds. We first discuss general properties of the CO morphology in mergers, and then continue with a discussion of signatures of galactic winds apparent in CO emission maps via imageable outflows. We conclude the section with a brief discussion of secondary effects of galactic winds in affecting the spatial extent of CO gas.

4.5.1 General Properties of CO Morphology

In Figure 4.6, we show the evolution of the CO ($J=1-0$) emission during a major merger of two disk galaxies simulated in run sbBH (model with starburst and black hole winds). The properties discussed in this subsection (§ 4.5.1) are generic

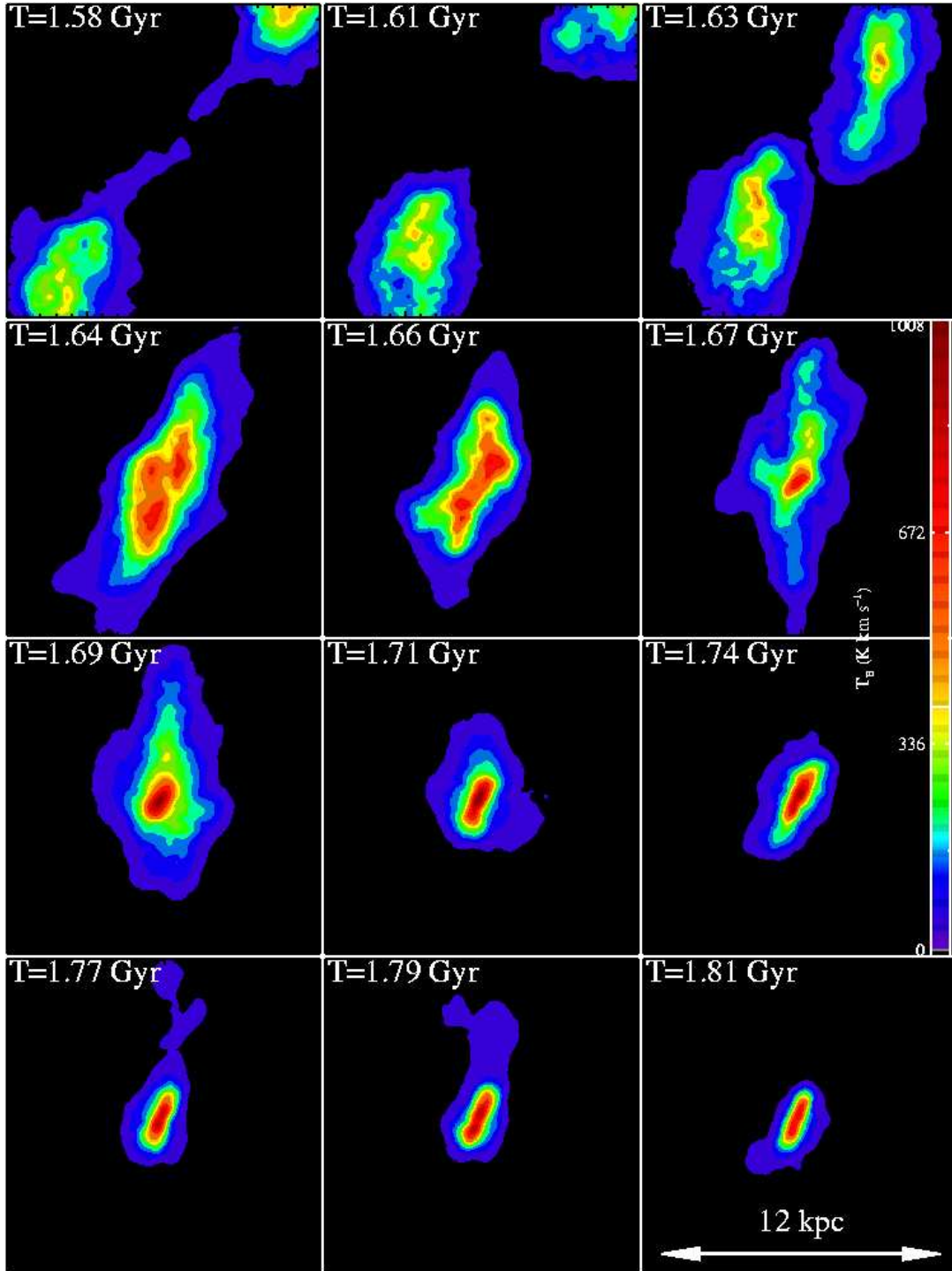


Figure 4.6 Contours of velocity-integrated CO ($J=1-0$) emission at various snapshots through evolution of merger model sbBH, with both starburst and AGN feedback-driven winds. The results discussed here are generic for all wind models. Upon nuclear coalescence ($T=1.7$ Gyr) a burst of star formation drives the CO luminosity to near peak values. The CO luminosity then fades as star formation

to each of our models, regardless of wind parameter choice. The images in Figure 4.6 start after the first passage of the galaxies, when they are approaching for their final coalescence. The tidal interaction of the first passing of the galaxies causes ‘streamer’ gas to emit in the intergalactic space between the two galaxies. The CO morphologies are disturbed by the first passage itself, and the CO emission is extended in nature until the nuclei have fully merged. The first passage of the galaxies induces a burst of star formation, peaking in the nuclear regions of each galaxy. This is reflected in the luminous CO emission at the center of each galaxy.

Because the CO (J=1-0) can be thermalized at relatively low critical densities, and lies only ~ 5 K above ground, it serves as a good tracer for total molecular gas content. Both diffuse envelopes of clouds as well as dense cores can emit CO (J=1-0) flux. Conversely, emission from higher lying lines of CO, and high dipole moment molecules (e.g., HCO+, HCN, CS) arises primarily from dense cloud cores. Thus, higher lying CO lines (e.g., CO J=3-2) from the merger broadly follow the distribution of the CO (J=1-0) line, but remain more compact in nature, generally emitting only from the dense starbursting nucleus. This was explicitly seen in the disk galaxy in Figure 4.4 as well.

The total CO intensity peaks soon after the progenitor galaxies lose individual identity, and there is only one surface brightness peak. During this time, stars formed in the merger-induced starburst heat up the molecular gas such that collisions readily excite the CO in the warm ($T \sim 50$ K) and dense ($n \sim 10^4 \text{ cm}^{-3}$) gas. The columns are still quite large through the nucleus as the starburst has not had time to consume the available molecular gas.

The velocity-integrated CO intensity across all transitions drops through the evolution of the merger. This can be attributed to global consumption of cold

molecular gas by star formation over time. This result is consistent with observations by Gao & Solomon (1999) who found from CO (J=1-0) emission that the total molecular gas content of a merger decreases as a function of projected nuclear separation in galaxy mergers.

4.5.2 Molecular Outflows

Starburst and AGN feedback-driven winds can leave an imprint on the molecular line emission via large scale imageable molecular outflows. These winds are seen to entrain large masses of molecular gas in outflows which appear prominently as a secondary surface brightness peak in velocity-integrated emission contour maps (Narayanan et al. 2006a).

In this section, we discuss the properties of the CO morphology in the context of these outflows. The outflows discussed here are only those which are large enough to be visible via CO (J=1-0) emission maps. For the purposes of understanding general trends of imageable outflows in this section, we will find it convenient to define an imageable outflow as any CO emission peak at least 50% of the nuclear emission maximum, with a projected distance at least 1.5 kpc away from the galactic nucleus. The molecular outflows are defined only after nuclear coalescence, and thus also follow the requirement that the CO emission peak be separate from the stellar surface density peak.

Before continuing, we note that the simulations chosen here are not extreme in any way (Figure 4.1). The peak B-band luminosity during the quasar phase is $\sim 10^{11} L_{\odot}$. Similarly, the peak IR luminosity is $\sim 10^{12} L_{\odot}$, allowing the galaxy to be just visible as a ULIRG. More massive mergers (e.g., Cox et al. 2007), and, as will be discussed in § 4.5.2.3, more coplanar mergers will drive stronger winds, leaving the simulations in this section representative of lower limits.

4.5.2.1 Outflow General Properties

Here, we discuss the general properties of both starburst and AGN feedback-driven outflows which appear in CO emission maps. While there are differences in some specific properties of the outflows based on the type or strength of the driving wind, we defer those comparisons to later subsections and focus this subsection on the outflow properties shared by all the simulations presented here.

In Figure 4.7, we show an example of molecular gas entrained in the outflow from model BH (AGN winds only; outflow first described in Narayanan et al. 2006a). The cold gas in the outflow is not completely ablated by starburst and AGN heating. While the CO emission from cold gas in the outflows closest to the nucleus is faint owing to lower columns of cold molecular gas, clouds which remain more deeply embedded in the outflow continue to exhibit active star formation. During short (~ 5 Myr) time intervals, the CO ($J=1-0$) velocity-integrated intensity from galactic outflows can be seen to be comparable (within a factor of ~ 2) to the galaxy's nuclear emission.

The imageable outflows typically correspond to entrainments of mass $\sim 10^8$ - $10^9 M_\odot$, with peak H_2 column of $\sim 10^{22}$ - 10^{23} cm^{-2} (within the constraints of our definition of an imageable outflow, § 4.5.2). The more massive outflows in this mass range tend to be seen closer to the point of nuclear coalescence, with a trend toward decreasing outflow mass as the merger progresses. This owes to more loosely bound gas near the time of coalescence, as well as the feedback energy rate being near its peak (Figure 4.2). These outflow masses are typically 5-15% of the total molecular gas mass. In the mergers e, sb, and sbBH, with random disk orientation angles, the outflows do not occur in any preferred direction. As we will discuss later, this is not the case for the coplanar model.

The entrained clouds can be relatively excited, allowing outflows to be image-

able at higher-lying CO transitions (e.g., $J \gtrsim 4$). In Figure 4.8, we show the outflow from the first panel of Figure 4.7 in CO transitions $J=1-0$, $J=3-2$ and $J=4-3$. The latter two transitions have a relatively high critical density of $\gtrsim 10^5 \text{ cm}^{-3}$ meaning they are typically thermalized only in the dense cores of GMCs, and may rely on radiative pumping for excitation in other parts of the ISM. The warm and dense gas heated by active star formation in the deeply embedded clouds in the outflows collisionally excite the CO gas into higher levels. In fact, the CO flux density in the outflow peaks at $J=4$, consistent with actively star-forming gas and multi-line measurements of excitation patterns in starburst-driven outflow of M82 (Walter, Weiß & Scoville, 2002). It should be noted that the relative visible lifetimes of outflows in higher-lying transitions may be much smaller than at CO ($J=1-0$). For example, the outflow presented in Figure 4.7 appears as a unique secondary surface brightness peak $\sim 35 \text{ Myr}$ at CO ($J=1-0$). In the CO ($J=3-2$) transition, the same outflow is distinguishable from the background for only $\sim 20 \text{ Myr}$.

4.5.2.2 Relative Role of AGN and Starbursts in Powering Imageable Outflows

As an illustrative point demonstrating the relative contributions of starburst and AGN winds in driving imageable molecular outflows, in Figure 4.9 we plot three snapshots during the period of nuclear coalescence for models no-winds, BH, sb, and sbBH (thus varying only the form of winds included, and not geometry of the merging galaxies). The wind-dependent morphological differences in the models are typically minimal near the point of nuclear coalescence, and thus the outflows imaged at this time serve as a reasonable comparison for the capacity of different wind models to drive outflows. Here, loosely bound gas near the inner regions is seen to be entrained in nuclear galactic winds. For reference, these outflows are the same as those shown in Figures 4.7 and 4.8.

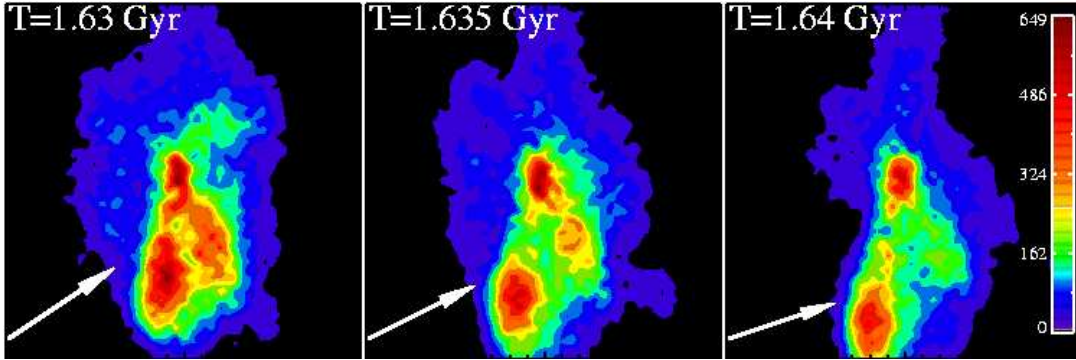


Figure 4.7 Velocity-integrated CO ($J=1-0$) emission map of imageable molecular outflows (shown by arrow) seen in the model with black hole winds only (see also Narayanan et al. 2006a). Thermally driven winds associated with black hole growth can entrain large masses ($\sim 10^8 - 10^9 M_\odot$) of molecular gas, resulting in directly imageable outflows. For reference, nuclear coalescence is at $T=1.6$ Gyr. The units are K-km s^{-1} (scale on right), and the panels are 12 kpc each.

Model BH is able to drive strong, imageable outflows (4th row, Figure 4.9) with properties described generally in § 4.5.2.1. The black hole feedback is tightly associated with the accretion rate, and thus the AGN wind is produced over a very short period of time and peaks soon after nuclear coalescence. Relative to the evolution of the galaxy, the AGN wind generically acts like a point explosion, and the bulk of the energy is imparted to the ISM nearly instantaneously. Indeed, Hopkins et al. (2006c) and Hopkins & Hernquist (2006) have shown explicitly that these AGN-driven winds are well-characterized by generalized Sedov-Taylor solutions for point explosions. The imageable outflows in model BH are primarily seen soon after the major merger, when the gas is still highly dynamical and loosely bound. They are also seen near the height of quasar activity, when the AGN feedback-driven winds are strongest.

The starburst driven winds are also able to power outflows (2nd row, Fig-

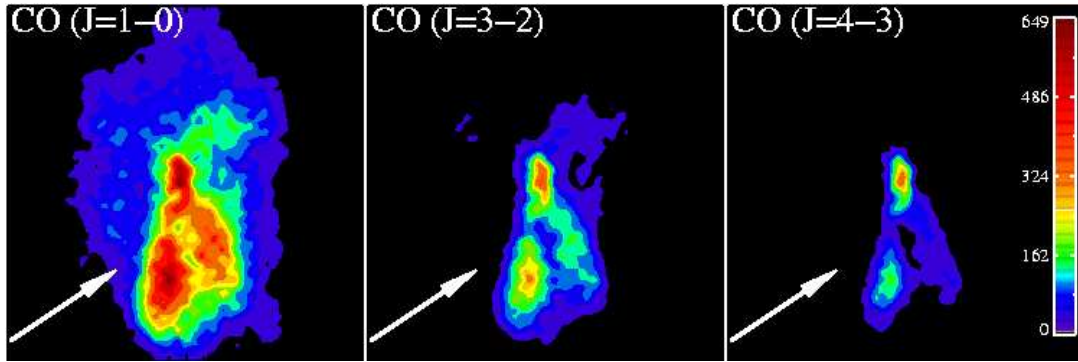


Figure 4.8 First panel of Figure 4.7 in commonly observed CO transitions $J=1-0$, $J=3-2$, and $J=4-3$. The massive and dense outflows entrain numerous GMCs, and continue to actively form stars. Dense cores in entrained GMCs emit strongly in higher-lying CO transitions, and can be imaged in $J=3-2$ and $J=4-3$, at submillimeter wavelengths. The outflow lifetime typically drops with transition as the outflows become more diffuse further from the nuclear regions (see text). For reference, nuclear coalescence is at $T=1.6$ Gyr. The intensity scale in K-km s^{-1} , and the scale is on the right. Each panel is 12 kpc on a side.

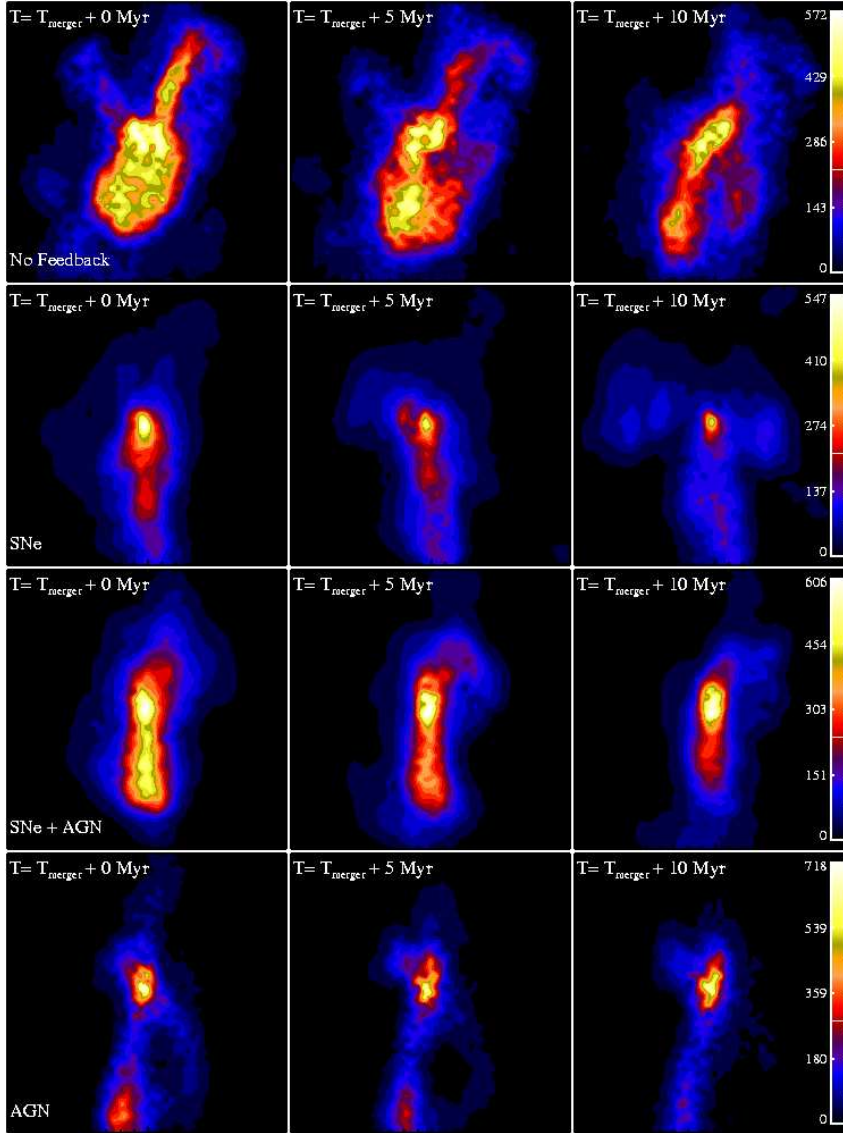


Figure 4.9 CO ($J=1-0$) emission contours in snapshots of models no-winds, sb, sbBH and BH (thus varying only wind models) near nuclear coalescence. The first snapshot in each row is the point of nuclear coalescence, and the timestamps at the top left refer to the length of time after coalescence. Loosely bound gas soon after the merger is visible in the nuclear regions of the model without winds (no-winds, top row). As the strength of the winds increases (second through fourth rows), this gas is entrained and can be imaged in outflow. The wind with the strongest instantaneous impact is the AGN-only simulation (model BH) as the presence of starburst winds can slow accretion onto the central black hole. Thus, the outflows in the AGN-only wind model are the most dramatic. Each panel is

ure 4.9), albeit less strongly than in the AGN-wind models; consequently, these outflows are detectable via emission mapping for shorter periods of time. The typical lifetime of an outflow such that it is detectable in CO (J=1-0) in the sb simulation (with only starburst winds) is $\sim 20\text{-}25$ Myr (compared with ~ 35 Myr in the AGN only model). On average, $3\text{-}5 \times 10^8 M_\odot$ are entrained, although outflows as small as $\sim 10^7 M_\odot$ are seen to occur, consistent with observations of starburst driven outflows by Sakamoto et al. (2005) and Walter et al. (2002). It should be noted that these values are derived within the constraints of the parameters chosen for our starburst winds ($\eta=0.5$, $v_w=837 \text{ km s}^{-1}$; § 4.3). In principle, a more efficient wind might increase the mass outflow rate, but, as discussed in Cox et al. (2007), such parameter choices were found to quench merger-induced starbursts, and are thus probably not representative of e.g., ULIRGs.

The relative weakness of starburst-driven outflows compared to the AGN only model is a direct consequence of the lower peak energy input from the starburst-driven winds, and hence lower power. During the active phase, the feedback from black holes inputs more than five times the energy as that imparted by star formation. This can be attributed to two causes. First, black hole growth is far more efficient at converting accreted mass into thermal energy than star formation. For example, by utilizing Equations (4.1) and (4.4), Cox et al. (2007) noted that the relative efficiency of black holes to star formation in converting gas mass to energy deposited into the ISM was of order ~ 640 . (See, also, Lidz et al. 2007.) Second, during the active phase, the relative black hole growth rate is much larger than the concomitant SFR. During this time, while the BH grows by a factor of ~ 4 , only $\sim 8\%$ of the final stellar mass is formed (Cox et al. 2007). In contrast, $\sim 90\%$ of the stellar mass (and consequently, stellar winds) is produced during the in-spiral stage, prior to the active phase.

The effect of including both starburst and AGN winds is demonstrated in the third row of Figure 4.9. The outflows produced are more massive and longer lived than the starburst-only wind models, but less so than the AGN-only wind models. The greater capacity to drive outflows over the starburst winds only model (sb) can be attributed to the extra energy input given by the accreting black hole(s). However, the outflows in Figure 4.9 are seen to be less powerful than those in the black hole only model. This effect owes to the starburst winds that occur prior to nuclear coalescence. As shown explicitly by Cox et al. (2007), starburst winds lower the amount of rotationally supported gas early during the in-spiral stage, which limits the amount of gas available for immediate funneling into the central nucleus via tidal torquing (Hernquist, 1989; Mihos & Hernquist, 1994b, 1996). This gas does eventually rain into the nuclear potential, fueling black hole growth and producing a black hole with the same mass as in the AGN wind only model (BH) and a galaxy that lies on the $M_{\text{BH}}-\sigma_v$ line (Cox et al. 2007; Di Matteo, Springel & Hernquist, 2005; Robertson et al. 2006a), as well as the black hole fundamental plane (Hopkins et al. 2007a,b). However, the black hole growth is integrated over significantly longer time, and thus the impact of the associated winds on molecular gas emission is diminished from the AGN-only model.

The relative effects of AGN feedback and starburst-driven winds on powering imageable molecular outflows can be summarized in Figure 4.10, where we plot the mass of imageable outflows as a function of time for models BH, sb and sbBH. The masses of gas each model is able to drive in an outflow is comparable to within a factor of $\sim 2-3$. AGN feedback-driven winds drive imageable outflows clustered primarily around nuclear coalescence and the peak period of black hole accretion. In comparison, the models with starburst driven winds (sb and sbBH)

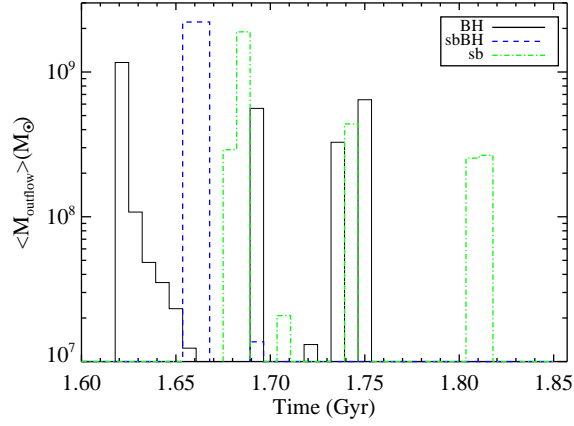


Figure 4.10 Masses of imageable outflows as a function of time for model BH, averaged over three orthogonal sightlines for models BH, sb and sbBH. The masses of a typical imageable outflow are comparable between models, though the AGN-only model is able to drive outflows for longer periods of time than the simulations with starburst winds. For reference, the times of nuclear coalescence are $T=1.6$ Gyr for model BH and $T=1.7$ Gyr for models sbBH and sb.

power imageable outflows for relatively shorter periods.

4.5.2.3 Merger Orbit Dependence

The strength of outflows in merger models depends on the initial orientation of the merging galaxies. In models where the disks are aligned, strong tidal torquing can cause a rapid inflow of gas thus providing a sudden burst of AGN feedback energy injected into the ISM. Alternatively, geometries such as those in the BH and no-winds models by comparison experience less tidal torquing on the gas, causing the major black hole accretion phase to be longer lived. In order to investigate the dependence of CO outflows on merger orbit, we have run simulation co-BH (Table 5.1) in which the progenitor galaxies are coplanar with the orbital plane ($\phi_1=\theta_1=\phi_2=\theta_2=0$). The stronger tidal torquing in the coplanar configuration

results in a more efficient blow-out of material. The H_2 gas in the galaxy remains confined in a thin configuration in the plane of the merger, consistent with previous simulations which showed the possibility of disk formation from major mergers (Springel, & Hernquist, 2005; Robertson et al. 2006b).

In Figure 4.11, we show a typical outflow from the coplanar model. Similar to the other models in Table 5.1, the primary molecular outflows occur at or near the point of nuclear coalescence. Unlike models sb/sbBH/BH, which showed no preferred direction for outflows, the outflows in coplanar model co-BH are seen to occur almost exclusively in the plane of the merger with an expanding shell-like structure.² The apparent lifetime of the outflows is dramatically increased as well in this merger model. In the sb/sbBH/BH models, the outflows typically involve loosely bound gas entrained in AGN winds which fall back into the nuclear potential, tending the emission toward a centrally concentrated morphology. Conversely, the outflows in the coplanar model appear to continue expanding within a 6 kpc (radius) region, resulting in an increasing half light radius throughout the evolution of the post-merger galaxy. The continued presence of imageable outflows in the coplanar model is seen explicitly in Figure 4.12, where we show the mass of imageable outflows for models BH and co-BH (thus varying only the orientation angle) as a function of time.

The imageable outflows are most dramatic for face on viewing angles as the outflows are preferentially within the plane of the merger. While at some inclined angles outflows continue to be visible, broadly, the more edge-on the viewing angle becomes, the more difficult imageable outflows become to detect against

²We caution that the outflows seen here are unrelated to the “shells” and “ripples” seen around many merger remnants and ordinary ellipticals. These features are stellar-dynamical in origin and are caused by “phase-wrapping” of stars (e.g., Quinn 1984; Hernquist & Quinn 1987) as tidal debris falls into the potential well of the remnant (Hernquist & Spergel 1992). Indeed, gas associated with these shells is on self-intersecting trajectories and will collect at the center of the remnant (e.g., Weil & Hernquist 1992, 1993).

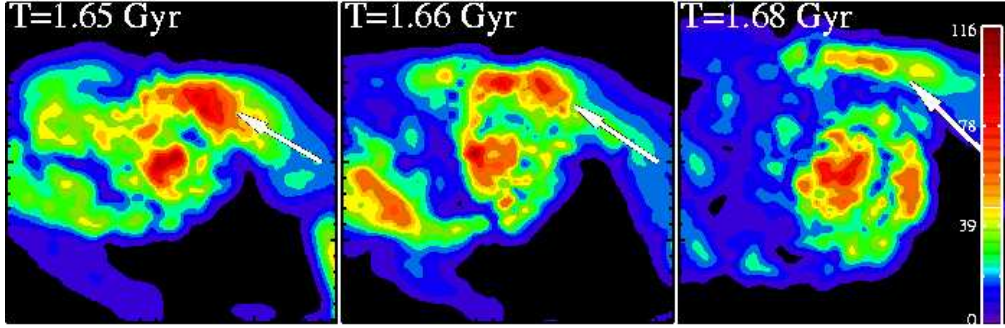


Figure 4.11 Coplanar merger simulation, co-BH, soon after nuclear coalescence. The imageable molecular outflows occur preferentially in the plane of the merger in a shell-like structure. An emergent outflow is visible near the top of the nuclear region, as well as the remnant of an older outflow in the bottom right of the first two panels. For reference, the point of coalescence for model co-BH is $T=1.5$ Gyr. Scale of panels are 12 kpc.

nuclear emission. That said, outflows may be preferentially detectable along these sightlines via spectral line signatures which we will discuss further in § 4.6. Within the plane of the merger, outflows can be viewed in outflow, or falling back into the nucleus throughout the entire ~ 200 Myr during the peak of the active phase investigated here.

The peak black hole accretion rate and integrated energy deposited into the ISM are similar for both the coplanar model and model BH. Consequently, the typical physical conditions of the AGN feedback-driven outflows are roughly the same in the two simulations. In the coplanar model discussed in this section, the typical mass of an outflow is a few $\times 10^8 M_{\odot}$, similar to the outflows observed in model BH which had a more generic inclination angle for the progenitor galaxies.

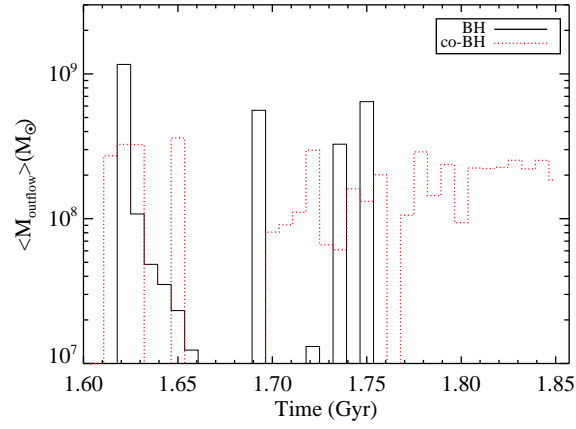


Figure 4.12 Masses of imageable outflows as a function of time for model BH and co-BH (thus varying only merger orbit angle) averaged over three orthogonal sightlines. The masses of a typical imageable outflow are comparable between models, though the coplanar model drives imageable outflows for longer periods of time.

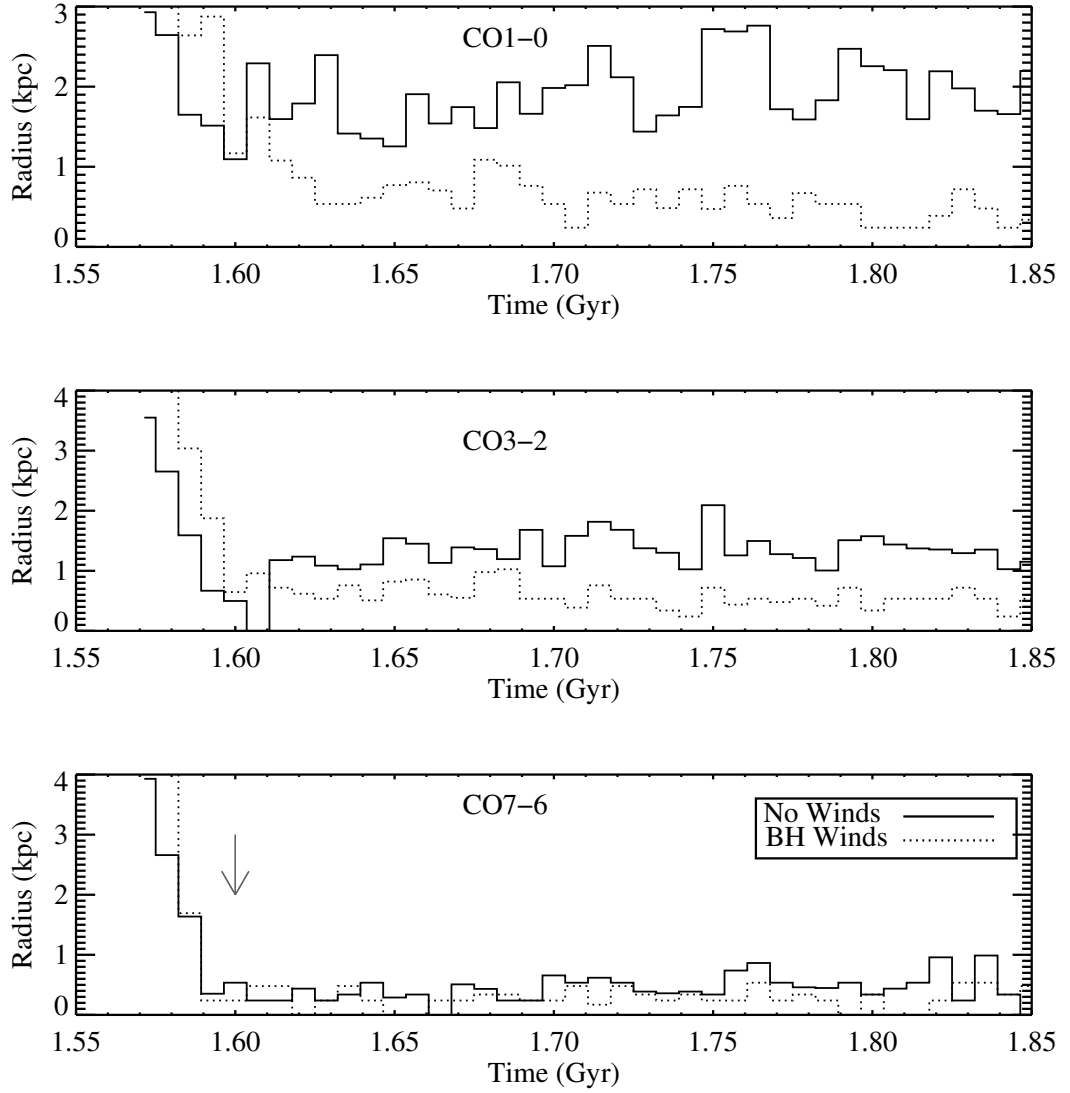


Figure 4.13 CO halflight radius as a function of time for models with AGN winds only (model BH) and with no winds (model no-winds) for observable CO transitions CO ($J=1-0$), CO ($J=3-2$) and CO ($J=7-6$). The emission from model BH with winds is uniformly compact in all CO transitions, typically confined to a region of a few hundred pc. The emission from model no-winds, without winds, is stratified, with a characteristic CO ($J=1-0$) scale of $\sim 1.5-2$ kpc, and becoming more compact at higher lying transitions. The arrow in the third panel denotes the point of nuclear coalescence. (See text for details.)

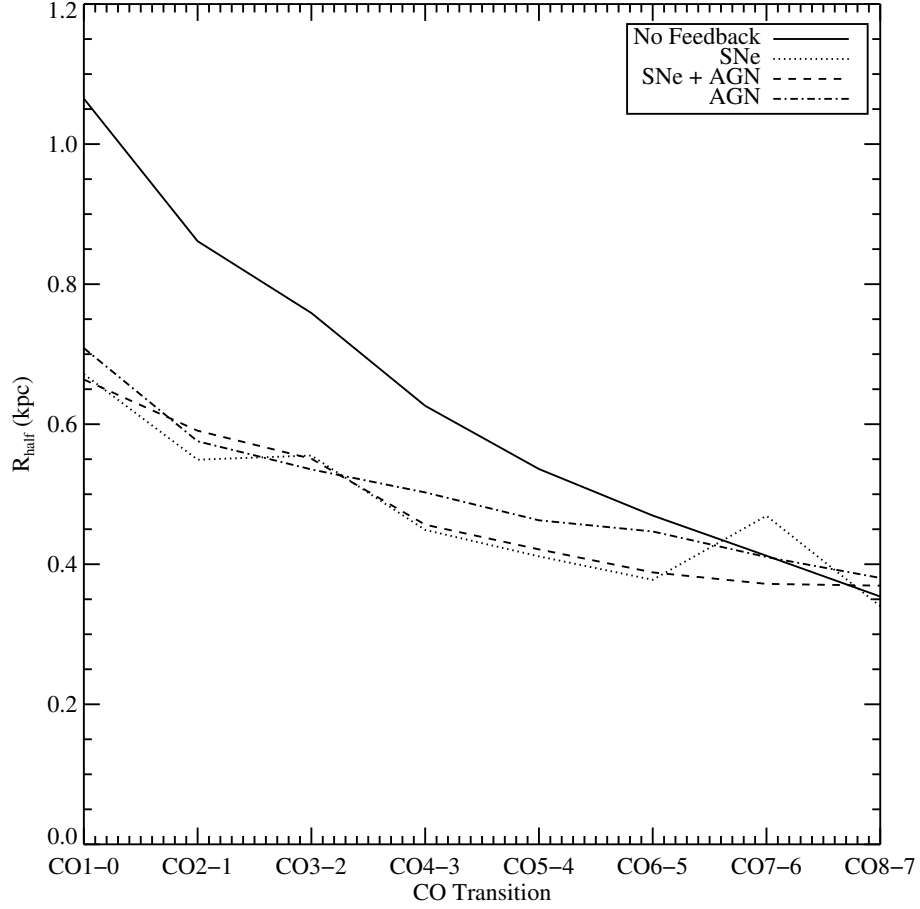


Figure 4.14 Sightline averaged half-light radius as a function of transition for models BH, no-winds, sb and sbBH (thus varying only wind parameters). The average half-light radius is calculated after nuclear coalescence. The emission from the model without winds is relatively stratified, with emission becoming more compact at higher transitions. The models with winds also exhibit stratification, though the half-light radius for the lowest transitions is about a factor of two smaller than the models without winds. The dispersion in these trends across various sightlines is small.

4.5.3 CO Half-Light Radius

Galactic winds can play a role in the spatial extent of CO emission in galaxy mergers. After nuclear coalescence, the CO ($J=1-0$) emission in the simulation without winds (model no-winds) is seen to be more spatially extended than the emission from mergers with winds by a factor of ~ 2 . The CO ($J=1-0$) emission from model no-winds has a typical half-light radius of 1-2 kpc (Figure 4.13, top panel). The CO emission remains on these extended scales throughout the evolution of the merger, and star formation simply consumes the available molecular gas as fuel.

The predicted lack of extended CO ($J=1-0$) emission in galaxy mergers with winds is consistent with observations. In a high resolution CO survey of five mergers, Bryant & Scoville (1999) found the primary CO emission to be compact and concentrated within a 300-400 pc radius of the nucleus in three sources, and within 1.6 kpc in all of the objects in the sample. Moreover, high resolution observations and radiative transfer modeling of local mergers have confirmed the compact nature of CO emission in mergers (Downes & Solomon, 1998). Winds associated with growing black holes and/or starbursts may help to explain this.

In the models with winds, as the galaxies merge, the sudden inflow of gas into the nucleus rapidly drives up the nuclear star formation rate, as well as the accretion rate of the black hole(s). The feedback associated with star formation and the central AGN is effective at heating the gas in the nuclear regions, and dispersing lower density CO ($J=1-0$) gas, leaving behind only a dense core of cool gas in the central regions in the winds models. The average CO ($J=1-0$) half light radius after the nuclei have coalesced for the models with SNe and/or AGN is ~ 700 pc. This was also seen in Figure 4.6 where we showed that the major CO ($J=1-0$) intensity for the model with SNe and AGN winds originates in a compact region, in agreement with observations of local ULIRGs (Bryant & Scoville 1999;

Downes & Solomon 1998).

In principle, these model results can be directly tested through observations of higher lying CO lines from local galaxies. The middle and bottom panels of Figure 4.13 show the halflight radius as a function of time for models BH and no-winds for the CO (J=3-2) and CO (J=7-6) transitions. These transitions probe denser gas than CO (J=1-0), and have a critical density of $\gtrsim 10^5 \text{ cm}^{-3}$. Figure 4.13 shows that the emission from the model with no winds is stratified such that tracers of dense gas [e.g., CO (J=7-6)] are more compact by nearly an order of magnitude than tracers of lower density gas [e.g., CO (J=1-0)]. In Figure 4.14 we show the mean half light radius for each model plotted as a function of CO transition. Here, we have averaged the half light radius after nuclear coalescence in each simulation. The CO emission in the model without winds becomes more compact in higher lying transitions (e.g., those with higher critical densities). In the models with SNe and/or AGN winds, the CO emission shows a similar behavior, but the halfflight radius for the lowest transitions is about a factor of two smaller than in the models without winds.

With these predictions, we caution that specific values quoted here are dependent on a number of assumptions included in parameter choices (such as, for example, the specific multi-phase ISM breakdown (e.g., Springel & Hernquist, 2003b) or constant CO abundances), and thus the normalization of the plots presented are to be taken within those confines. However, the general trends are likely to be more robust. In this sense, the relatively shallow slope in half-light radius versus transition (Figure 4.14) remains a valid observational test for the role of galactic winds in shaping observed CO spatial extents. Finally, it is important to note that the weak trend in average halfflight radius as a function of transition in Figure 4.14 is an ensemble-averaged trend over three orthogonal

sightlines and numerous points in the post-coalescence evolution of the galaxies. Thus, observations examining this relationship must select samples of galaxies after the progenitors have coalesced - in other words, after the merger has only a single nuclear emission peak in the CO morphology.

4.6 Signatures of Winds in CO Line Profiles

4.6.1 Overview

Generically, when the nuclei of the progenitor galaxies are still resolvable, prior to coalescence, the unresolved CO emission line exhibits multiple emission peaks corresponding to the nuclear regions of each galaxy (e.g., Greve & Sommer-Larsen, 2006). When the molecular gas in galaxy mergers becomes dynamically relaxed, the CO emission line is reasonably well represented by a single broad Gaussian. Alongside this general trend, at various times throughout the evolution of the merger, secondary (and potentially, though less commonly, tertiary and quaternary) peaks can be seen superposed on the broad CO Gaussian-like line. In Figure 4.15, we show a representative evolution of CO spectral lines, and how they correspond to the CO morphology. These secondary peaks superposed on the broad Gaussian originate in massive CO gas clumps moving along the line of sight. In Figure 4.15, the secondary peak in the third panel represents emission from the outflowing clump visible in the corresponding CO contour image.

While these superposed secondary emission peaks are a general feature of all models in our simulations, the physical origin of these peaks is dependent on the strength of the winds included in a given merger model. In particular, secondary emission peaks with velocities greater than the circular velocity typically represent loosely bound gas which has not virialized (peaks at velocities lower than the circular velocity may also be loosely bound gas, though they may also repre-

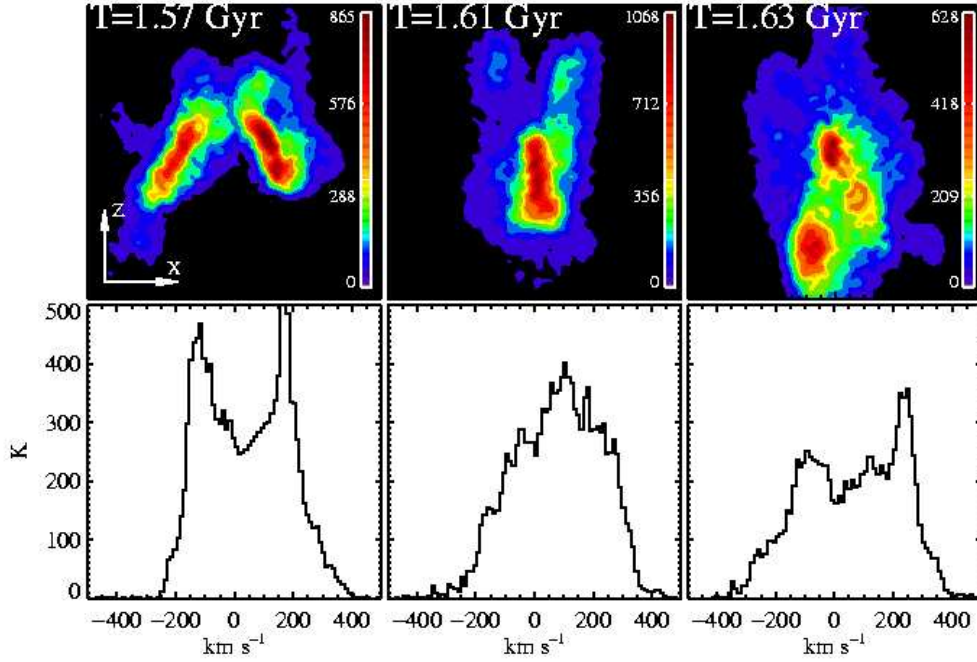


Figure 4.15 *top*: CO ($J=1-0$) emission contours of three snapshots during the merger simulation with winds from black holes (model BH). *bottom*: CO ($J=1-0$) spectra of snapshots, viewing the emission from the $-\hat{z}$ direction (coordinate axes in top left panel). The CO emission lines early in the merger are characteristically double-peaked, where each peak corresponds to emission from the individual nuclear regions of the progenitor galaxies (first column). As the merger advances, the emission lines are typically well-described by a single Gaussian (middle column). There are excursions from this trend, however, as outflowing gas can give rise to a secondary peak in the emission line red or blueshifted from the systemic velocity of the galaxy (third column; this outflow and line profile was also presented in Narayanan et al. 2006a). The emission contours each have their own scale on the right, to facilitate color contrasts. For reference, the time of nuclear coalescence is $T=1.6$ Gyr. The units of emission are in velocity-integrated intensity (K-km s^{-1}). The panels are 12 kpc on a side.

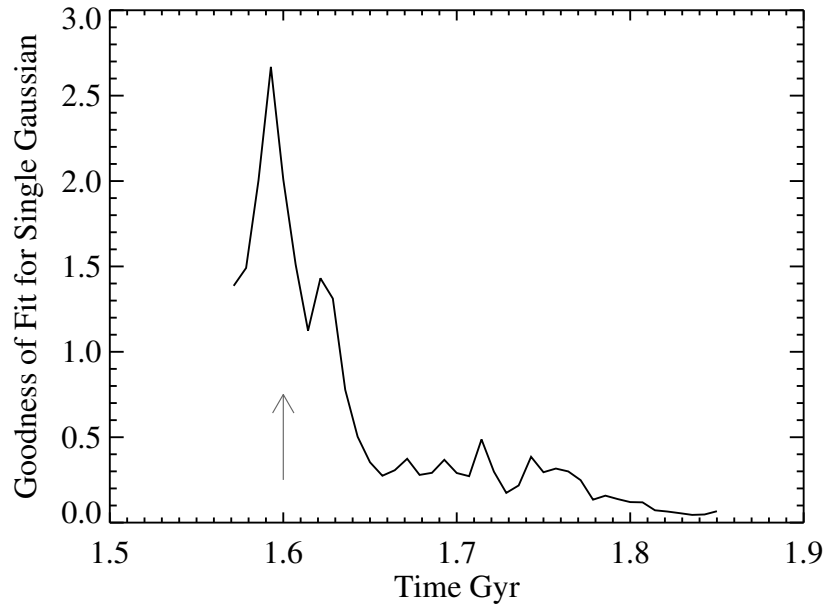


Figure 4.16 Goodness of fit for a single Gaussian fit to spectra from model BH as a function of time. When the merger is prior to and near coalescence, and the gas is highly dynamical, and a single Gaussian provide a relatively poor description of the emission line profile. As the gas virializes after coalescence, a single Gaussian better represents the emission line profile. The goodness of fit is taken here as the median of the square of the residuals. The arrow denotes the time of nuclear coalescence.

sent gas in rotational support; for brevity we hereafter refer to secondary peaks at velocities greater than the circular velocity as ‘high velocity peaks’). As we will show more quantitatively, in models which include winds, this high velocity gas is typically entrained in outflow during periods of activity (e.g., elevated star formation rate or black hole growth), and thus give rise to high velocity peaks in the emission line representative of outflowing gas. This is analogous to the situation seen in the CO morphologies presented in Figure 4.9 when loosely bound gas simply fell into the central potential in the model without winds, but was entrained in outflow in models with winds (here, models sb, sbBH and BH). This effect of winds on CO emission profiles was first shown explicitly in similar calculations by Narayanan et al. (2006a). This work demonstrated that once the galaxies merged, large columns of gas outflowing along the line of sight can leave their imprint on the broad single-Gaussian emission line characteristic of galactic CO emission by introducing an additional superposed emission peak, red or blueshifted at the line of sight velocity of the outflow.

The relative significance of high velocity peaks compared to the main emission line decreases as the gas virializes in the merger. To illustrate this, in Figure 4.16 we plot the evolution of the goodness of fit (taken here as the median of the square of the residuals) for a single Gaussian fit to the emission lines from model BH, although the results are common across all models. The impact of winds in driving high velocity peaks decreases as the merger progresses.

In our models, high velocity peaks in CO emission lines are typically representative of clumps of gas moving along the line of sight with masses $\gtrsim 5 \times 10^7 M_{\odot}$. Gas clumps with masses much less than this are typically not able to emit strongly enough to be seen in the emission spectrum over the main Gaussian. In the remainder of § 4.6, when we discuss clumps of outflowing and infalling gas, we

will be referring to those above this minimum mass that are able to impact the emission line profile.

Because high velocity peaks appear in our simulations even in spatially unresolved observations, they may be a powerful diagnostic for AGN and starburst induced outflows both in the local Universe and at earlier epochs. However, at this point in the discussion, there are open questions regarding the uniqueness of this line profile, as well as how these secondary peaks specifically relate to starburst and AGN activity. In the remainder of this section, we attempt to quantify the use of molecular emission line profiles as a diagnostic for outflowing gas in galaxy mergers.

4.6.2 The Driving Force Behind High Velocity Peaks in CO Emission Profiles

Emission lines representing gas with a strong line of sight velocity component can originate from either outflowing or infalling gas. As demonstrated by Narayanan et al. (2006a), AGN feedback-driven molecular outflows can generate high velocity secondary peaks in the CO emission lines when the outflow has a significant line of sight velocity component. Any gas falling into the central potential with a negative radial velocity with respect to the center of mass of the system (e.g gas that is in infall, or pre-coalescence mergers) may also drive high velocity peaks in the CO emission lines, and are thus degenerate with high velocity peaks that originate in outflows. It is therefore necessary to establish the uniqueness of high velocity peaks in CO emission lines with respect to an actual outflow or infall origin. Any attempt to break this degeneracy requires a more detailed knowledge of the physical properties and observational characteristics of the galaxy during periods when high velocity peaks are observable.

In order to assess how the evolutionary state of the galaxy merger may determine the origin of high velocity peaks (i.e. whether they owe to outflowing

or infalling gas), we investigate the physical conditions during times when the galaxy exhibits high velocity peaks. To this end, we created synthetic CO ($J=1-0$) spectra along three orthogonal sightlines for the models in Table 5.1. To identify candidate emission lines with high velocity peaks driven by winds (as opposed to rotation), we require the emission line to have a peak near the systemic velocity of the galaxy, and an additional peak with velocity greater than $\pm 160 \text{ km s}^{-1}$. This fiducial requirement is set in place to filter out multiple emission peaks that arise from rotation as $\sim 160 \text{ km s}^{-1}$ is the circular velocity of the post-merger galaxy at the spatial extent of the H_2 gas, and thus the maximum velocity of rotating gas. We consider all high velocity peaks whose peak intensity is at least 20% the peak line intensity.

Upon identifying a line with a high velocity peak, we then determine whether the clump of gas generating the high velocity peak is outflowing or infalling. In order to simplify the analysis, in the few cases with multiple high velocity peaks, we focused on the peak with highest velocity. In Figure 4.17, we plot a histogram of the number of high velocity peaks seen as a function of time in the simulation with black hole winds only (model BH), summed over 3 orthogonal lines of sight. We have further broken the line profiles down into having an outflow or infall origin. As a reference for the evolutionary state of the merger, we have overplotted the SFR, black hole accretion rate, and bolometric luminosity.

Figure 4.17 demonstrates that while the number of high velocity peaks is roughly constant after the major merger, the origin of these line profiles is a function of the evolutionary state of the galaxy. During phases of heavy black hole growth, the majority of the high velocity peaks owe to outflowing gas. Towards the end of the quasar phase, when much of the blowout has already occurred, gas raining from outer parts of the galaxy give rise to multi-peaked profiles with an

infall origin. Conversely, similar analysis from the model without winds shows a more random origin for high velocity peaks in the emission profiles, reflecting the more randomly oriented velocity vectors of loosely bound clumps. This is explicitly shown in Figure 4.18, where we show the origin of high velocity peaks in a merger without winds compared with the bolometric and IR luminosity.

Another way of saying this is that the winds in model BH do not *cause* the high velocity peaks to exist in the CO spectra. Rather winds typically entrain the clumps of gas behind the high velocity peaks in outflow, thus giving physical significance to secondary peaks. This is not the case in the model with no winds, where the molecular gas representative of the high velocity peaks has random radial velocities with no preferred direction (Figure 4.18). *High velocity peaks are seen in models both with and without winds; in wind models, though, these peaks preferentially owe to outflowing gas during peaks of starburst activity and black hole growth.*

Observationally, many of the criteria that are used in creating samples of local galaxy mergers may select galaxies which are at the peak of their starburst or AGN activity. High velocity peaks in the emission profiles (e.g., higher than the circular velocity of the host) observed in these galaxies may be likely, then, to owe to outflowing clumps of gas (Figure 4.17). For example, the extreme bolometric and IR luminosities trace not only the prodigious star formation owing to the merger induced starburst, but also reflect a large contribution from the growing supermassive black hole. The winds associated with this black hole growth are behind much of the outflowing molecular gas during the most luminous phase of the galaxy's evolution. Similarly, IR colors which select objects with embedded AGN, such as the $25\mu\text{m}/60\mu\text{m}$ flux ratio, may preferentially show objects which owe their outflow profile to outflows as opposed to infalling gas clumps. Finally, the hard X-ray flux is dominated by the central AGN, and thus traces the general

growth of the central black hole. Our models suggest that the phase during which the X-ray luminosity is at its greatest will be marked by high velocity peaks in the CO emission originating in outflowing molecular gas.

4.6.3 Distinguishing Characteristics

A natural question is whether or not one can observationally infer the nature of high velocity peaks in CO emission lines as discussed in § 4.6.1. Distinguishing characteristics between the various origins for high velocity peaks may be evident when considering limiting velocities for the high velocity peak much greater than the virial velocity. Figures 4.17 and 4.18 showed the presence of all high velocity peaks beyond a limiting velocity being set at the virial velocity of the galaxy (here, $\sim 160 \text{ km s}^{-1}$). Because high velocity peaks in the simulations without winds are driven by dynamical effects, rather than winds, few emitting clumps of gas are able to regularly sustain velocities much greater than the escape velocity of the galaxy (or $\sqrt{2} \times V_c$). In contrast, when included, winds are able to drive outflows at higher speeds.

We show this effect quantitatively in Figure 4.19 where we plot the number of high velocity peaks as a function of limiting velocity for both two models with AGN winds (models BH and co-BH) and the model with no winds. At velocities greater than ~ 1.7 times the virial velocity, the number of high velocity peaks driven by purely dynamical effects in model no-winds drops rapidly while winds from the AGN in model BH and co-BH are still able to drive clumps in outflow at these velocities. The range of the numbers of high velocity peaks in the models with AGN winds owes to a merger-orientation dependent range in instantaneous black hole feedback energies. More efficient fueling of the central AGN in the coplanar model allows for a stronger impact of the winds on the molecular line profiles (cf. § 4.5.2.3). In either case, both models which consider AGN feedback

show that AGN feedback-driven winds can drive high velocity peaks at larger velocities than dynamical effects can typically account for. In this sense, one may be able to discriminate between high velocity peaks with an outflow origin versus random kinematics when restricting the limiting velocity of the peaks to $\gtrsim 1.7$ times the virial velocity of the galaxy.

The dispersion seen between the no winds model and the models with AGN winds (BH and co-BH) in Figure 4.19 is in principle a lower limit. The galaxies in Figure 4.19 are relatively low mass - $M_{\star} \sim 10^{11} M_{\odot}$. Cox et al. (2007) found that the energy input by accreting black holes in galaxy mergers increases as a function of galaxy mass for a variety of progenitor gas fractions (ranging from 0.05 to 0.8) and initial merger angles. Specifically, these authors found $E_{\text{BH}}/f_g \propto M_{\star}^{1.13}$, suggesting that higher mass galaxies have the capacity to drive CO peaks at even higher speeds compared to their virial velocity. As an example, a merger with similar gas fraction and orientation angle as model BH, though with final stellar mass $\sim 10^{12}$ would have roughly an order of magnitude greater black hole energy input (Cox et al. 2007).

Figure 4.19 suggests that the effect of AGN feedback-driven winds on CO emission line profiles should be discernable by comparing a merger's virial velocity to observed high velocity features in the CO line profile. A comparably clear (and observationally more tractable) test may be an analysis of the velocity offset of high velocity peaks with respect to the centroid velocity of the emission line. When examining high velocity peaks defined with respect to the centroid velocity, we find the curves presented in Figure 4.19 are robust. This owes to a narrow distribution of centroid velocities in all the models, with a typical standard deviation in the distribution $\sigma \sim 20 \text{ km s}^{-1}$.

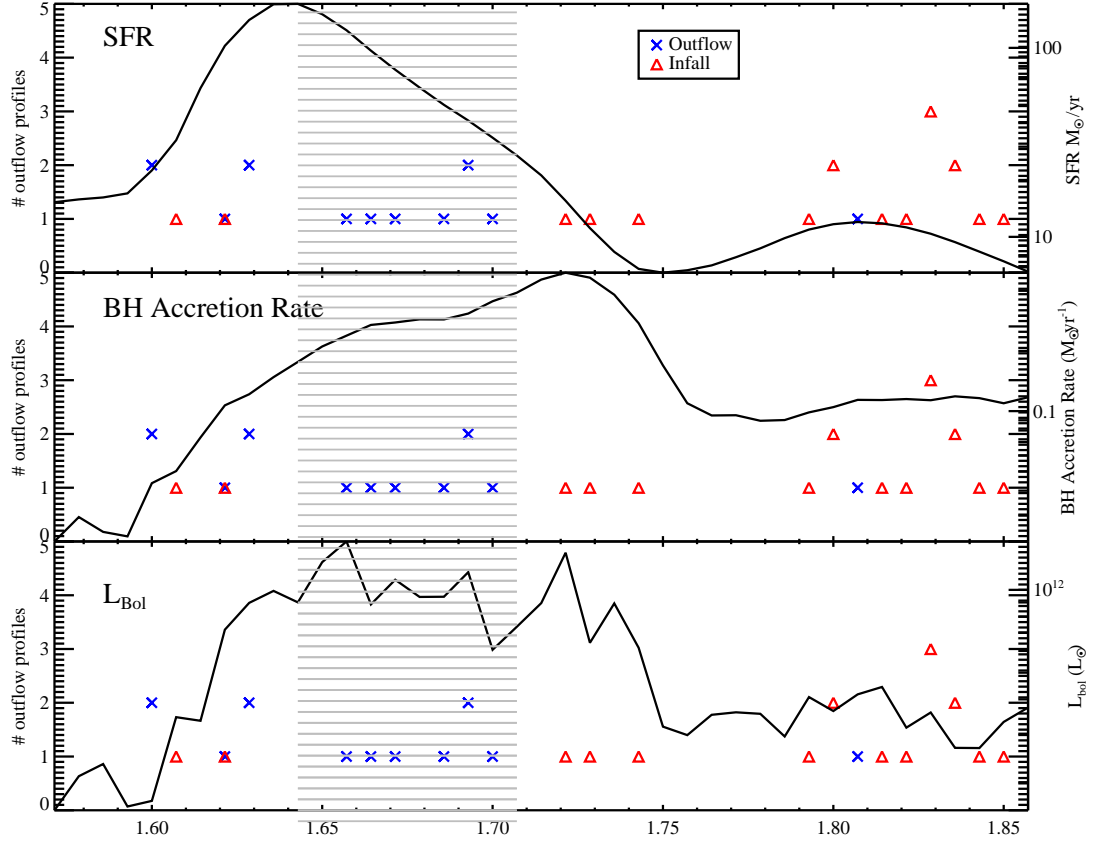


Figure 4.17 Physical and observable properties of model BH (model with BH winds) as a function of simulation time. Additionally plotted are a histogram of the number of secondary high velocity peaks seen, and the physical origin of the peak. The blue crosses are number of high velocity peaks associated with an outflow (summed over 3 orthogonal viewing angles), and the red triangles are number of high velocity peaks originating from infalling gas. Infalling gas is seen both early and late in the merger's evolution. During periods of elevated activity (e.g., increased SFR or black hole accretion), most of the high velocity peaks owe to outflowing gas (hatched region). The left axis is associated with the histogram of high velocity peaks, and the right axis with the physical or observable quantity overplotted in that panel. For reference, the time of coalescence is $T=1.6$ Gyr.

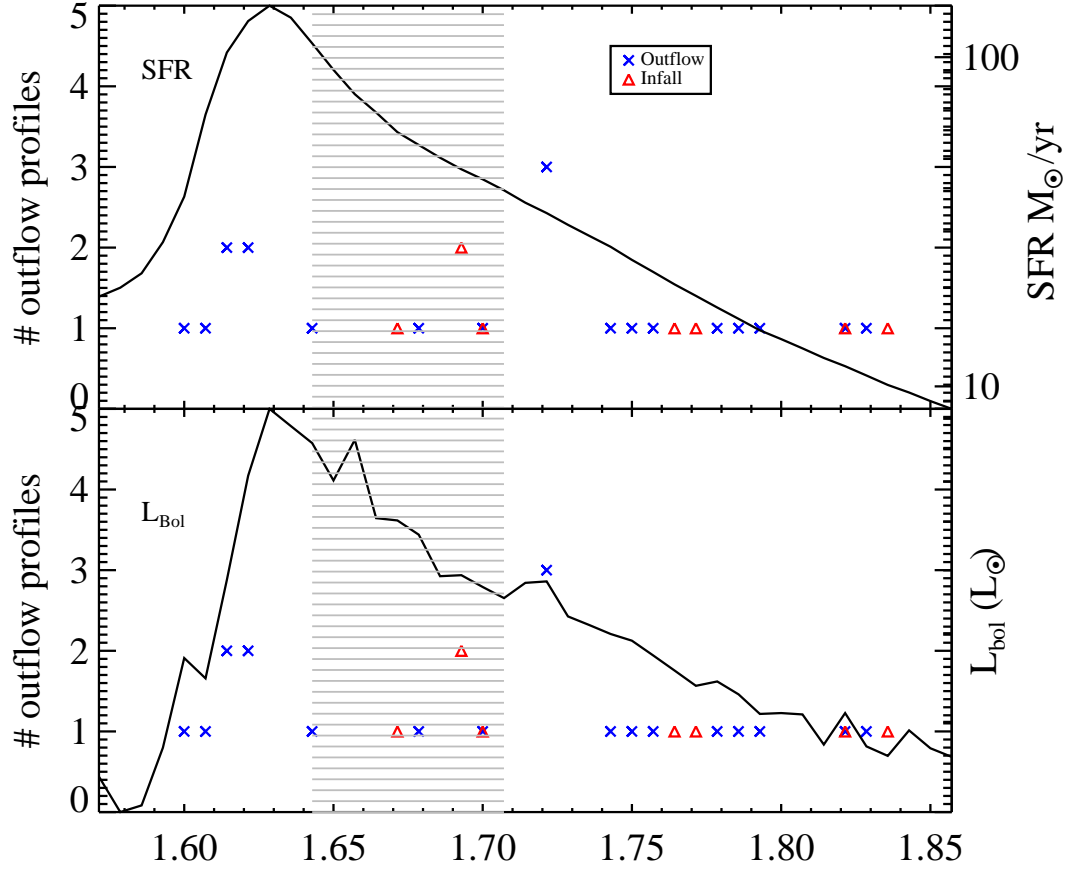


Figure 4.18 SFR and bolometric luminosity from model no-winds as a function of simulation time. Additionally plotted are a histogram of the number of secondary high velocity peaks seen, and the physical origin of the peak. The blue crosses are number of high velocity peaks associated with an outflow (summed over 3 orthogonal viewing angles), and the red triangles are number of high velocity peaks originating from infalling gas. No apparent trends are seen reflecting the randomly oriented radial velocity vectors driving the high velocity peaks in the no-winds model. The hatched region covers the same time period as that in Figure 4.17 just as a comparative reference with that plot. The left axis is associated with the histogram of high velocity peaks, and the right axis with the physical or observable quantity overplotted in that panel. For reference, the time of coalescence is $T=1.6$ Gyr.

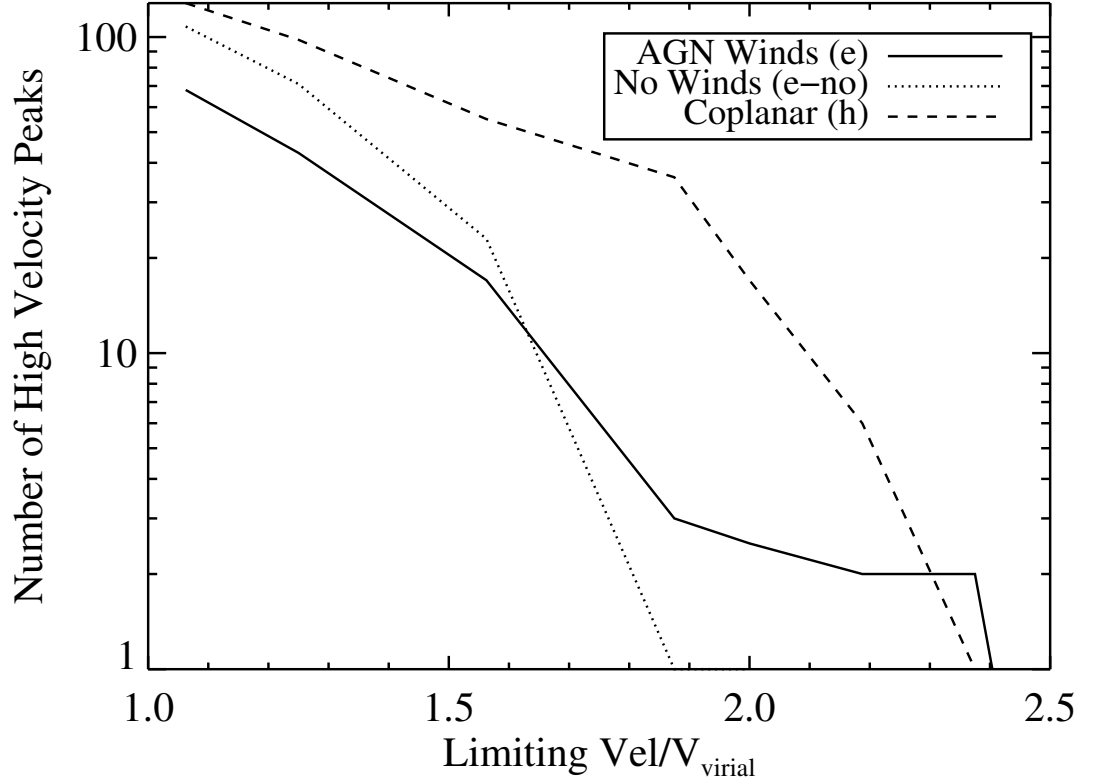


Figure 4.19 Number of high velocity peaks as a function of minimum velocity for the high velocity peak summed over three orthogonal sightlines. Solid line is model with AGN winds (model BH) and dashed line is model with no winds. High velocity peaks in model without winds are driven by random dynamics of clumps of gas, and thus are unable to sustain velocities much greater than the virial velocity of the host galaxy. In contrast, clumps of gas entrained in AGN winds are seen at higher velocities, giving rise to more high velocity peaks at the highest velocities. One may be able to discriminate between high velocity peaks with an outflow origin versus random kinematics when restricting the limiting velocity $\gtrsim 1.7$ times the virial velocity.

4.7 Discussion

Many of the model results presented in this chapter have the potential to be directly tested in the near future, either with existing datasets, or with observations from millimeter wave interferometers such as CARMA and PdBI, and high resolution submillimeter telescopes such as the Submillimeter Array (SMA) or Atacama Large Millimeter Array (ALMA).

First, it is worth briefly revisiting the evolutionary status of the galaxies studied here, and placing them into a larger context. In a merger-driven scenario for quasar formation, gaseous inflows fueled by tidal torquing on the gas (Barnes & Hernquist 1991, 1996; Hernquist, 1989) fuel nuclear starbursts (Mihos & Hernquist 1996), allowing the galaxy to be viewed as a dusty starburst system similar to local ULIRGs (Chakrabarti et al. 2007a). The gaseous inflows fuel central black hole growth (Hopkins et al. 2005a-d; 2006a-d; 2007h; Di Matteo et al. 2005; Springel et al. 2005a) which makes the galaxy first visible as a ULIRG with warm infrared colors (Chakrabarti et al. 2007a), and then as an optically selected quasar (Hopkins et al. 2005a-d; 2006a-d; 2007h). A key physical process in driving the host galaxy along this sequence is galactic winds. Namely, winds driven by AGN feedback (as well as nuclear starbursts) contribute to clearing the veil of obscuring gas and dust surrounding the central black hole, and allow the quasar to become visible across numerous sightlines (Hopkins et al. 2005a). These winds are most prominent during the ~ 200 Myr associated with major black hole growth. The models presented in this chapter therefore examine simulated galaxy mergers during this time period of heightened wind activity, starting near nuclear coalescence, and ending slightly after the quasar light curve has declined. During this time, the galaxy is seen to have increased IR, X-ray and B -band luminosities, indicative of the starburst event and central black hole growth (Figure 4.17). In

this sense, these simulations are designed to provide analysis for local galaxies selected for nuclear activity via elevated X-ray and IR fluxes (e.g., ULIRGs).

Second, we have shown that the effects of winds can shape the molecular morphology of galaxy mergers. For example, distinct differences are seen in the simulations with winds versus without when considering the spatial extent of the CO emitting gas (§ 4.5.3). The predicted weak evolution of average half-light radius as a function of transition for evolved mergers can be tested in the CO ($J=1-0$), ($J=2-1$), ($J=3-2$) and ($J=7-6$) transitions with current technology using a millimeter-wave interferometer (e.g., CARMA, PdBI) and the SMA.

Perhaps the most dramatic effects of galactic winds on the CO morphology lie in imageable signatures of entrained molecular outflows. CO outflows driven by starburst-dominated winds have been imaged in a handful of nearby galaxies. Recent mapping of starburst galaxies M82 and NGC 3256 have shown that molecular gas can indeed survive in outflows entrained in starburst-driven winds (Walter et al, 2002; Sakamoto et al. 2006). Both galaxies are known to be interacting systems, the latter a major merger. The outflow masses are recorded to be $\sim 10^7$ - $10^8 M_{\odot}$, consistent with the model results presented in § 4.5. The outflows have been detected in CO ($J=2-1$) emission (peaking at CO $J \sim 3$ or 4; Weiß et al. 2005b), and are thought to be actively forming stars, again consistent with these models. The outflow observed in M82 appears to be distributed in a roughly spherical halo with radius ~ 1.5 kpc. This outflow may correspond with an $H\alpha$ outflow, as well as M82's dust halo (Alton, Davies & Bianchi, 1999; Walter et al. 2002). This type of morphology is seen along some sightlines in the models BH and co-BH, alongside the more collimated outflows characteristic of e.g., Figure 4.9.

Outflows which are thought to be driven by a central AGN have been imaged in local galaxies as well. Recent SMA observations of NGC 6240 by Iono et al.

(2007) have revealed an outflow in CO (J=3-2) morphologically similar to the outflow seen in Figure 4.7. NGC 6240 is a major merger near final coalescence with two central X-ray sources, which *Chandra* observations have suggested are a binary AGN (Komossa et al, 2003). In this sense, the outflow imaged in NGC 6240 occurs when our models suggest the most massive outflows may be imageable (§ 4.5.2.2). The mass of the outflow in this system is estimated to be $\sim 5 \times 10^8 M_{\odot}$, consistent with the typical masses entrained in AGN winds in our simulations. Similar morphological features to those associated with molecular outflows have been detected in local LIRG/ULIRG NGC 985, though the interpretation of these features is still uncertain (Appleton et al. 2002).

While the number of outflows directly imaged in CO remains small and limited to only relatively recent observations, outflows traced in absorption (e.g., Na I D lines) have a much more extensive detection history and associated literature. Absorption line outflows have been detected in the UV and optical in both nearby starburst galaxies/AGN (Heckman et al. 2000; Martin 2005; Rupke & Veilleux 2005; Rupke, Veilleux & Sanders 2005a-c), as well as high-redshift galaxies (Pettini et al. 2002; Shapley et al. 2003) and quasars (Ganguly et al. 2006; Hamann, Barlow & Junkkarinen 1997; Misawa et al. 2005, 2007a,b; Narayanan et al. 2004; Trump et al. 2006; Wise et al. 2004). HI has also been seen in outflow in active galaxies via absorption lines (Morganti, Tadhunter & Oosterloo 2005). In addition to the neutral absorption line outflows detected, many outflows are relatively high ionization lines (e.g., CIV, NV; Hamann et al. 1997; Narayanan et al. 2004). In this sense, it appears as though these may be different populations of outflows from the cold, neutral emission line outflows discussed in this chapter. Interestingly, in the few systems with CO outflow candidates (as evidenced by their morphology), there is an apparent coincidence between the velocity off-

sets in the molecular outflows and absorption line outflows. For example, the starburst-driven outflow observed in local merger NGC 3256 by Sakamoto et al. (2006) has a velocity offset (from the systemic, which in the case of CO, typically corresponds to the nuclear emission) of ~ 300 km/s, while Heckman et al. (2000) showed a blueshifted Na I D absorption line of velocity ~ 300 km/s. Similarly, Appleton et al. (2002) found two Ly α and NV absorbers in NGC 985 at coincident velocities as those which CO gas is seen projected against the nucleus. The data bring up the interesting speculative suggestion that perhaps the absorption line outflows seen in these systems are physically associated with the CO emitting outflows. If so, it may be that the neutral and ionized outflows exist more toward the outer envelopes of the entrained complexes of molecular clouds as the conditions toward the central regions of these flows are extremely cold and dense (~ 10 -30 K, $\sim 10^5$ - 10^6 cm $^{-3}$; Figure 4.7). A full investigation into the potential relationship between UV and optical absorbers and CO outflows is beyond the scope of the material in this chapter, but studies into possible physical motivations for absorption line outflows within the context of these models are underway.

In principle, unresolved emission line profiles from galaxies are more easily obtainable in large numbers than the high-resolution maps necessary to directly image outflows. Brief inspection by eye suggests that at least some local galaxies appear to espouse the high velocity peaks discussed in § 4.6 (e.g., Narayanan et al. 2005; Sanders Scoville & Soifer, 1991; Solomon, Downes & Radford, 1992; Yao et al. 2003). As previously discussed, robustly determining the physical mechanism driving high velocity peaks is difficult, although tests similar to Figure 4.19 may be possible with some prior knowledge of the host circular velocity. It is interesting to note that absorption line outflows, which have been attributed to starburst-driven winds, have been detected in many of the ULIRGs in the afore-

mentioned CO samples (Martin, 2005; Rupke et al. 2005a-c).

Apparent high velocity peaks appear prodigiously in $z \sim 2$ submillimeter galaxies (SMGs; Greve et al. 2005; Tacconi et al. 2006; see Blain et al. 2002 and Solomon & Vanden Bout 2006 for recent reviews). The high velocity peaks in SMGs may be explained by the prodigious star formation rates in these galaxies, in combination with a contribution from an embedded AGN. If the extreme luminosities owe solely to starbursts, then massive star formation rates of order $\sim 1000 \text{ M}_{\odot} \text{ yr}^{-1}$ are typical of these sources (e.g., Blain et al. 1999). The relative role of AGN energy input in SMGs is a debated topic, as well as whether they are currently undergoing, or are soon to undergo a heavy black hole accretion phase (e.g., Alexander et al. 2005a,b; Borys et al, 2005; Chakrabarti et al. 2007b). In either case, powerful winds produced by the intense $\sim 10^3 \text{ M}_{\odot} \text{ yr}^{-1}$ SFR and/or the central black hole could potentially drive high velocity peaks. That said, we caution against a direct application of these model results toward SMGs. For one thing, the virial properties of the progenitor galaxies in these models have not been explicitly scaled for $z \sim 2$ (Robertson et al. 2006a), and it is not clear how that will affect merger-induced star formation rates and black hole growth during the active period. Moreover, it is not completely clear that SMGs are the product of binary mergers as this chapter has focused on. Models appropriate for $z \sim 2$ mergers (e.g., Chakrabarti et al. 2007b; Robertson et al. 2006a) will have to be studied in the context of galactic winds in order to assess the potential relationship between these results and SMGs.

4.8 Chapter Conclusions and Summary

We have combined 3D non-LTE radiative transfer calculations with SPH simulations of galaxy mergers in order to investigate the effects of galactic-scale winds

on the molecular line emission in starburst galaxies and AGN. We find that galactic winds are a natural result of merger-induced star formation and black hole growth. These winds can entrain molecular gas of order $\sim 10^8\text{-}10^9 M_\odot$ which imprints generic signatures in both the CO morphology as well as unresolved emission line profiles. The specifics of the morphological and emission line indicators of molecular outflows depend on physical parameter choices within the galaxy merger models. In particular, the energy source (i.e. BH accretion or star formation), as well as the merger orientation can vary the strength, direction, and duration of imageable molecular outflows, as well as the velocity separation of high velocity peaks in multi-component emission lines. Many of the results including the half-light radius as a function of excitation, or the velocity offsets of high velocity peaks in the emission lines vary enough between physical parameter choices such that these models may be used to constrain physical origins for observed CO morphologies and line profiles. In detail, we find the following:

1. Molecular outflows entrained in winds driven by AGN feedback are typically longer lived than those entrained in starburst driven winds. This owes to the relative strength of AGN feedback-driven winds versus starburst driven winds. These types of imageable outflows have been recorded in at least some local systems (e.g., Iono et al. 2007).
2. Winds from AGN feedback in coplanar merger models are typically more powerful than mergers which occur at more random orientations. This results in imageable outflows being visible for the majority of the ~ 200 Myr 'active period' studied here.
3. The spatial extent of CO emission can be controlled by the presence of galactic winds. The emission is seen to be stratified with transition in all mod-

els such that the CO (J=1-0) half-light radius is larger than the radius from higher lying transitions (e.g., CO J=7-6), though the degree of stratification depends on the inclusion of winds. The relatively compact nature of observed CO emission in local mergers ($R_{1/2}$ typically confined to the central kpc; Scoville & Bryant, 1999) may be a consequence of AGN feedback or starburst-driven winds.

4. In all models, high velocity peaks (peaks at velocities greater than the circular velocity) can exist superposed on the post-merger galaxy's broad CO emission line. In models without winds, these peaks owe to random kinematics of molecular gas. In models with winds, these peaks are seen to originate primarily from gas entrained in outflow, at least during the period of peak black hole accretion/star formation.
5. High velocity peaks driven by random kinematics do not typically appear at velocity offsets (from systemic) greater than ~ 1.7 times the circular velocity of the post-merger galaxy. In contrast, peaks entrained in AGN feedback-powered winds can be driven to velocities near 2.5 times the circular velocity. The centroid velocities of the simulated lines are typically (1σ) within $\sim 20 \text{ km s}^{-1}$ of the true systemic velocity, and can generally be used as a reliable substitute for the systemic velocity. Thus in general the above results hold true when measuring the velocity offsets of high velocity peaks with respect to line centroids as well.

CHAPTER 5

THE NATURE OF CO EMISSION FROM $z \sim 6$ QUASARS

I'd just observe a plain old galaxy at $z \sim 6$

Me at my thesis defense, as recorded by committee member Arjun Dey

5.1 Chapter Preface

As of the time of the writing of this thesis, there had only been a single detection of CO at $z \sim 6$, in quasar J1148+5251 (Walter et al. 2004). Since that time, there have been two subsequent detections between $z=5-6$ (Carilli et al. 2007; Maiolino et al. 2007), both of which exhibit CO emission properties highly consistent with the models presented in this chapter (specifically, the observed line widths). I defer comparisons to a full sample of $z \sim 6$ quasars to a future work as more detections become published, and focus the presented comparisons for this chapter to observations to J1148+5251 .

5.2 Chapter Abstract

We investigate the nature of molecular gas emission from $z \sim 6$ quasars via the commonly observed tracer of H_2 , carbon monoxide (CO). We achieve these means by combining non-local thermodynamic equilibrium (LTE) radiative transfer calculations with merger-driven models of $z \sim 6$ quasar formation that arise naturally in Λ -cold dark matter (Λ CDM) structure formation simulations. Motivated by observational constraints, we consider four representative $z \sim 6$ quasars formed in the halo mass range $\sim 10^{12} - 10^{13} M_\odot$ from different merging histories. The main results follow. We find that, owing to massive starbursts and funneling

of dense gas into the nuclear regions of merging galaxies, the CO is highly excited during both the hierarchical buildup of the host galaxy and the quasar phase and the CO flux density peaks between $J=5-8$. The CO morphology of $z \sim 6$ quasars often exhibits multiple CO emission peaks which arise from molecular gas concentrations which have not yet fully coalesced. Both of these results are found to be consistent with the sole CO detection at $z \sim 6$ (as of the time of the writing of this thesis), in quasar J1148+5251. Quasars which form at $z \sim 6$ display a large range of sightline-dependent line widths. The sightline dependencies are such that the narrowest line widths occur when the rotating molecular gas associated with the quasar is viewed face-on (when the L_B is largest), and broadest when the quasar is seen edge on (and the L_B is lowest). Thus, we find that for all models, selection effects exist such that quasars selected for optical luminosity are preferentially seen to be face-on which may result in CO detections of optically luminous quasars at $z \sim 6$ having line widths narrower than the median. The mean sightline-averaged line width is found to be reflective of the circular velocity of the host halo, and thus scales with halo mass. For example, the mean line width for the $\sim 10^{12} M_\odot$ halo is $\sigma \sim 300 \text{ km s}^{-1}$, while the median for the $\sim 10^{13} M_\odot$ quasar host is $\sigma \sim 650 \text{ km s}^{-1}$. Depending on the host halo mass, approximately 2-10% of sightlines in our modeled quasars are found to have narrow line widths compatible with observations of J1148+5251. When considering the aforementioned selection effects, these percentages increase to 10-25% for quasars selected for optical luminosity. When accounting for both temporal evolution of CO line widths in galaxies, as well as the redshift evolution of halo circular velocities, these models can self-consistently account for the observed line widths of both submillimeter galaxies and quasars at $z \sim 2$. Finally, we find that the dynamical mass derived from the *mean* sightline-averaged line widths

provide a good estimate of the total mass, and allows for a massive molecular reservoir, supermassive black hole, and stellar bulge, consistent with the local $M_{\text{BH}}\text{-}M_{\text{bulge}}$ relation.

5.3 Chapter Introduction

The discovery of extremely luminous quasars at $z \gtrsim 6$ via novel color selection techniques demonstrates that massive galaxies and supermassive black holes formed very early in the Universe (Fan et al. 2002, 2003, 2004). Observations of the dusty and molecular interstellar medium (ISM) in $z \sim 6$ galaxies can serve as a unique probe into the star formation process in the first collapsed objects, and help quantify the relationship between star formation and black hole growth when the Universe was less than a billion years old (e.g., Wang et al. 2007; for a recent review, see Solomon & Vanden Bout 2005). Serving as a proxy for observationally elusive molecular hydrogen (H_2), rotational transitions in tracer molecules such as ^{12}CO (hereafter, CO), HCN and HCO^+ can provide diagnostics for the physical conditions in the star-forming giant molecular clouds (GMCs) of high redshift galaxies (e.g., Bertoldi et al. 2003a,b; Carilli et al. 2005; Riechers et al. 2006a; Walter et al. 2003).

The highest redshift quasar that has been found, SDSS J1148+5251 (hereafter J1148+5251) at $z=6.42$ (Fan et al. 2003) is an extremely bright object with bolometric luminosity $\sim 10^{14} L_{\odot}$, and is thought to be powered by accretion onto a supermassive black hole of mass $\sim 10^9 M_{\odot}$ (Willott, McLure, & Jarvis 2003). Bertoldi et al. (2003b) measured a far infrared luminosity of $1.3 \times 10^{13} L_{\odot}$, which, if powered solely by starburst-heated dust, corresponds to an exceptional star formation rate of $\sim 3000 M_{\odot}\text{yr}^{-1}$.

Pioneering CO observations of J1148+5251 have revealed a great deal con-

cerning the molecular ISM in the host galaxy of this $z \sim 6$ quasar. Through multi-line observations and large velocity gradient (LVG) radiative transfer modeling, Bertoldi et al. (2003a) found that the CO flux density peaks at the J=6 level of CO, indicative of the warm and dense conditions characteristic of vigorous star formation. A measured molecular gas mass of $M_{\text{H}_2} \approx 10^{10} M_{\odot}$ shows that J1148+5251 plays host to a large reservoir of molecular gas (Bertoldi et al. 2003a; Walter et al. 2003). Subsequent high resolution observations with the Very Large Array (VLA) by Walter et al. (2004) discovered that the CO emission in this galaxy is extended on scales of 2.5 kpc and is resolvable into two emission peaks separated by 1.7 kpc, with each peak tracing $\sim 5 \times 10^9 M_{\odot}$ of molecular gas. These observations suggest that J1148+5251 is a merger product (Walter et al. 2004; Solomon & Vanden Bout 2005).

CO observations of J1148+5251 have presented challenges for models of galaxy formation as well. For example, dynamical mass estimates from observed CO line widths are not able to account for the presence of a $\sim 10^{12} M_{\odot}$ stellar bulge as would be predicted by the present-day $M_{\text{BH}}\text{-}M_{\text{bulge}}$ relation, suggesting that the central supermassive black hole could have grown in part before the host galaxy (Walter et al. 2004). In contrast, the presence of heavy elements (Barth et al. 2003), and significant CO emission (Bertoldi et al. 2003a; Walter et al. 2003, 2004) imply that the ISM has been significantly enriched with metals from early and abundant star formation. Recent theoretical arguments have additionally proposed that a relation between black hole mass and stellar bulge mass is a natural consequence of AGN feedback in galaxies (Di Matteo et al. 2005, 2007; Hopkins et al. 2007a; Sijacki et al. 2007), and that this relation shows only weak ($\sim 0.3 - 0.5$ dex) evolution in galaxies from redshifts $z=0\text{-}6$ (Robertson et al. 2006a,c; Hopkins et al. 2007a).

Numerical simulations can offer complementary information to observations of $z \sim 6$ quasars by providing a framework for the formation and evolution of $z \sim 6$ quasars and the relationship between the star forming ISM in these galaxies and observed CO emission. Calculations by Springel, Di Matteo & Hernquist (2005a,b) have found that galaxy mergers serve as a viable precursor for quasar formation. Strong gaseous inflows driven by tidal torques on the gas (e.g., Barnes & Hernquist 1991, 1996) can fuel nuclear starbursts (e.g., Mihos & Hernquist 1994c, 1996) and feed the growth of central, supermassive black holes (Di Matteo et al. 2005); subsequent feedback from the AGN can lift the veil of obscuring gas and dust and, along numerous sight lines, reveal an optically bright quasar (Hopkins et al. 2005a,b).

More recently, Li et al. (2007a) have proposed a merger driven model for quasar formation at $z \sim 6$ which fits naturally into a Λ CDM framework. By performing numerical simulations which simultaneously account for black hole growth, star formation, quasar activity, and host spheroid formation, these authors found that galaxy mergers in early $\sim 10^{13} M_{\odot}$ halos can result in the formation of bright quasars at $z \sim 6$. The quasars in these simulations exhibit many properties similar to the most luminous quasars at $z \sim 6$, including both observables, such as the rest-frame B -band luminosity, and inferred characteristics (e.g., the central black hole mass and bolometric luminosity). These simulations can thus serve as a laboratory for investigating the properties of the interstellar medium in the first quasars, as well as the relation between CO emission and star formation at early epochs.

In order to quantitatively couple these models with CO observations, molecular line radiative transfer calculations are necessary. Recent works by Narayanan et al. (2006a,b, 2007b) have developed a methodology for simulating molecu-

lar line transfer on galaxy-wide scales. In this chapter, we aim to investigate the plausibility of $z \sim 6$ quasar formation in massive $\sim 10^{12} - 10^{13} M_{\odot}$ halos in a hierarchical structure formation scenario by modeling the observed CO emission from these high redshift sources. We achieve these means by coupling the non-LTE radiative transfer codes of Narayanan et al. (2006a,b, 2007b) with the hierarchical $z \sim 6$ quasar formation models of Li et al. (2007a). We make quantitative predictions for $z \sim 6$ quasars which form in halos with masses ranging from $\sim 10^{12} - 10^{13} M_{\odot}$, and provide interpretation for existing and future CO observations of $z \gtrsim 6$ quasars.

In § 5.4 we describe the numerical models employed. In § 5.5, we present the modeled CO excitation characteristics and luminosities. In § 5.6, we discuss the morphology of the CO gas. In § 5.7 we describe the derived emission line profiles and compare our models to observations of the only detected CO measurement in a $z \sim 6$ quasar, J1148+5251. In § 5.8, we use the model CO lines to investigate the usage of CO observations as dynamical mass indicators in the highest redshift quasars. We conclude with a discussion comparing the CO emission properties of our simulated quasar with other high- z galaxy populations in § 5.9 and summarize in § 5.10. Throughout this paper we assume a cosmology with $h=0.7$, $\Omega_{\Lambda}=0.7$, $\Omega_M=0.3$.

5.4 Numerical Methods

In order to capture the physics of early Universe quasar formation, simulations must have the dynamic range to faithfully track the evolution of the most massive halos within which these quasars reside (e.g., Haiman & Loeb 2001), as well as follow the stars, dark matter, ISM and black holes in the progenitors of the quasar host galaxy. We have performed multi-scale calculations which include cosmo-

logical dark matter simulations in a volume of 3 Gpc^3 to identify the most massive halos, and subsequent hydrodynamic galaxy merger computations within these halos at higher resolution. The cosmological and galaxy merger simulations were implemented using the parallel, N -body/Smoothed Particle Hydrodynamics (SPH) code GADGET-2 (Springel 2005). We then applied the non-LTE radiative transfer code, *Turtlebeach* (Narayanan et al. 2006a,b), to the outputs of the hydrodynamic galaxy merger simulations to investigate the emission properties of the CO molecular gas in the resultant quasar. The quasar formation simulations and radiative transfer algorithms are described in detail in Li et al. (2007a) and Narayanan et al. (2006a,b, 2007b), respectively, and we refer the reader to those works for more detail; here, we briefly summarize, and focus on the aspects of the calculations directly relevant to this chapter.

5.4.1 Cosmological Simulations

Observational evidence suggests that quasars at $z \sim 6$ likely form in very massive ($\sim 10^{13} M_\odot$) halos. For example, quasars at $z \sim 6$ have an extremely low comoving space density of $n \approx 10^{-9} \text{ Mpc}^{-3}$ (e.g., Fan et al. 2003), comparable to the rarity of massive $\sim 10^{13} M_\odot$ halos at $z \sim 6$. Further evidence comes from black hole mass-halo mass correlations, and theoretical arguments relating quasar luminosity and halo mass (Lidz et al. 2006). In addition, recent numerical simulations by Pelupessy, Di Matteo & Ciardi (2007) have suggested that the buildup of supermassive $\sim 10^9 M_\odot$ black holes by $z \sim 6$ may require galaxy mergers in extremely rare $\gtrsim 10^{13} M_\odot$ halos. The strongest evidence for high redshift quasar formation in massive halos comes from recent Sloan Digital Sky Survey (SDSS) clustering measurements by Shen et al. (2007) which indicate that the minimum mass for high redshift quasar hosts is $\sim 6 - 9 \times 10^{12} M_\odot$. While these arguments are suggestive, they are not conclusive. Thus, one major goal of this work is to

further investigate the hypothesis that $z \sim 6$ quasars live in high mass halos and constrain the range of host halo masses for these sources by comparing their simulated CO emission to observations. To this end, we have simulated 4 quasars which form hierarchically through numerous mergers in massive halos ranging in mass from $\sim 10^{12} - 10^{13} M_{\odot}$.

In order to simulate the large subvolume of the Universe necessary to track the evolution of massive halos and formation of $z \sim 6$ quasars, as well as achieve a reasonable mass resolution at the same time, we performed the structure formation simulation with a multi-grid procedure similar to Gao et al. (2005). We first ran a uniform resolution simulation of a 3 Gpc^3 volume, with an effective mass and spatial resolution of $m_{\text{dm}} \sim 1.3 \times 10^{12} M_{\odot}$ and $\epsilon \sim 125 h^{-1} \text{ kpc}$ (comoving softening length), respectively, with initial conditions generated by CMBFAST (Seljak & Zaldarriaga 1996). We assumed a σ_8 of 0.9 (though see Li et al. [2007a] for a discussion of the implications of other choices for the cosmological parameters).

We then used a friends-of-friends group finder in order to seek out candidate massive halos within which early quasars form. Anticipating that these rare quasars will be progenitors of massive objects today, we identified the most massive halos at $z=0$, and then resimulated the evolution of these objects and their immediate environment at a much higher mass and force resolution assuming an initial redshift of $z=69$. The final effective resolutions of the halo evolution simulations were $m_{\text{dm}} \sim 2.8 \times 10^8 M_{\odot}$ and $\epsilon \sim 5 h^{-1} \text{ kpc}$.

The merger tree of the halos was extracted from the simulations in order to provide information concerning the masses of the largest contributing progenitors to the halo mass and allow us to reconstruct the hierarchical buildup of the quasar host galaxy. We considered groups that contribute at least 10% of the halo mass as progenitors in the merger history resulting in e.g., seven progenitors for

Table 5.1. $z \sim 6$ Quasar Models

Name ^a	z^b	M_{vir}^c [$10^{12} M_{\odot}$]	V_{vir}^d [km s^{-1}]	M_{BH}^e [$10^9 M_{\odot}$]	$L_{\text{bol}}(\text{peak})^f$ [$10^{13} L_{\odot}$]	$\tau_{QSO}(L_{\text{bol}} \geq 10^{13} L_{\odot})^g$ [Myr]
Q1	6.5	7.7	626.4	2.0	2.0	55.5
Q2	5.6	3.8	467.9	1.0	5.0	22.3
Q3	7.2	1.5	340.7	0.2	1.5	4.0
Q4	5.5	8.1	593.2	0.4	1.1	21.9

^aName of quasar model.

^bRedshift of the quasar at peak accretion activity.

^cVirial mass of the quasar host halo, assuming overdensity $\Delta = 200$.

^dVirial velocity of the quasar host halo, assuming overdensity $\Delta = 200$.

^eBlack hole mass of the quasar.

^fPeak bolometric luminosity of the quasar.

^gQuasar lifetime for $L_{\text{bol}} \geq 10^{13} L_{\odot}$.

the most massive halo simulated. Table 5.1 lists the properties of all the resultant quasars.

The discussion throughout this paper will largely focus on quasars Q1-Q3 which formed hierarchically in the cosmological simulations. Quasar Q4 is a binary coplanar merger specially simulated for studying the dependence of the CO emission properties on merger history, and will be discussed only in § 5.7.2.

5.4.2 Galaxy Merger Simulations

To derive the physical properties of the $z \sim 6$ quasar host galaxies, we resimulated their merger trees hydrodynamically using GADGET-2. GADGET-2 utilizes a fully conservative SPH formulation which allows for an accurate handling of discontinuities (Springel & Hernquist 2002). The code accounts for radiative cool-

ing of the gas (Katz et al. 1996; Davé et al. 1999), and a multiphase description of the ISM that includes cold clouds in pressure equilibrium with a hot, diffuse gas (e.g., McKee & Ostriker 1977; see also Springel & Hernquist 2003a). Star formation is constrained by observations of local galaxies, and follows the Kennicutt-Schmidt laws (Kennicutt, 1998a; Schmidt 1959; Springel & Hernquist 2003b). The progenitor galaxies had dark matter halos initialized to follow a Hernquist (1990) profile, and the virial properties are scaled to be appropriate for cosmological redshifts (Robertson et al. 2006a).

Black holes in the simulations are realized through sink particles that accrete gas following a Bondi-Hoyle-Lyttleton parameterization (Bondi & Hoyle 1944; Bondi 1952; Hoyle & Lyttleton 1939). To model feedback from central black holes, we assume that 0.5% of the accreted mass energy is reinjected into the ISM as thermal energy (Di Matteo et al. 2005; Springel, Di Matteo & Hernquist 2005a,b). This formulation for AGN feedback in galactic scale simulations has been shown to successfully reproduce X-ray emission patterns in galaxy mergers (Cox et al. 2006b), observed quasar luminosity functions and lifetimes (Hopkins et al. 2005a-d, 2006a,c,d, 2007b), the Seyfert galaxy luminosity function (Hopkins & Hernquist 2006), the $M_{\text{BH}}-\sigma_v$ relation (Di Matteo et al. 2005; Hopkins et al. 2007a; Robertson et al. 2006a), the bimodal galaxy color distribution (Springel et al. 2005b, Hopkins et al. 2006b,e, 2007d), characteristic CO emission patterns in ultraluminous infrared galaxies (ULIRGs; Narayanan et al. 2006a), infrared colors of ULIRGs and $z \sim 2$ Submillimeter Galaxies with embedded AGN (Chakrabarti et al. 2007a,b), and the kinematic structure of merger remnants (Cox et al. 2006a).

We assume that the black holes in these simulations formed from the first stars (e.g., Abel, Bryan & Norman 2002; Bromm & Larson 2004; Yoshida et al. 2006), and that the seed masses for the black holes are $200 M_{\odot}$ at $z=30$. Before

the first progenitor galaxies entered the merger tree, their black holes grew at the Eddington limit, resulting in seed black hole masses of $\sim 10^4 M_\odot$ at the time of the first merger. The black holes in the simulations are assumed to merge when their separation is less than a gravitational softening length ($30 h^{-1} \text{pc}$).

We model evolution of the CO emission in the quasars from $z \sim 8$ to $z \sim 5$, noting that the peak of the quasar activity is roughly $7 \gtrsim z \gtrsim 5.5$. The black hole luminosity outshines the stellar luminosity for a large range of redshifts, and it is this time that we refer to as the 'quasar phase' for any given galaxy.

5.4.3 Evolution of Model Quasars

To aid in the discussion in the remainder of this work, we qualitatively describe the evolution of the most massive ($\sim 10^{13} M_\odot$; halo mass) quasar host, though the results are general for all models considered in Table 5.1. The quasar host galaxy builds hierarchically, through seven major mergers between $z = 14.4$ -8.5. Strong gravitational torques on the gas drive massive gaseous inflows, causing heavy accretion onto the central black hole(s), and triggering intense starbursts that typically form stars at a rate between $\sim 10^3 - 10^4 M_\odot \text{yr}^{-1}$. The black holes accrete heavily as gas is funneled in toward the nuclear regions. Feedback from the most massive central black hole then drives a powerful wind, creating numerous lines of sight along which the central quasar is no longer obscured, and the black hole luminosity outshines the stellar luminosity. The central supermassive black hole can be visible as an optically bright quasar ($L_{\text{bol}} > 10^{13} L_\odot$) for ~ 50 Myr (though less for lower mass quasar host galaxies; Table 5.1). The powerful quasar wind quenches the starburst, and self-regulates the black hole growth. In the post quasar phase, the luminosity of the galaxy subsides, and it eventually evolves into a cD-like galaxy. More details concerning the evolution of the models presented here are discussed in Li et al. (2007a).

5.5 Excitation and Luminosity of CO

The CO spectral energy distribution (SED) is the CO flux density emitted per rotational J state and thus provides a direct measure of the excitation characteristics of molecular gas (e.g., Weiß et al. 2005a). The shape and peak of the CO SED describe the relative number of molecules in a given rotational J state, and serve as observable diagnostics of the underlying temperature and density of the emitting molecular gas. Here, we describe in detail the excitation characteristics of the most massive quasar host (Q1, $M \sim 10^{13} M_{\odot}$), and explicitly note when the lower mass models exhibit different properties. In Figure 5.1, we show the redshift evolution of the peak in the CO SED. Moreover, in Figure 5.2, we show representative CO SEDs for quasar Q1 at three redshifts during the quasar phase. The CO SEDs are averaged over three orthogonal viewing angles, though the SEDs derived from each individual angle are nearly identical.

Strong gravitational torques exerted on the gas by the multiple mergers drive massive amounts of cold gas into the central kiloparsec, giving rise to densities as high as $\sim 10^7 \text{ cm}^{-3}$ in GMC cores at the beginning of the quasar phase ($z \sim 7$). The combination of these dense conditions and heating associated with the continued starburst cause the CO molecular gas to become highly excited. During this time, the peak of the CO SED rises to J=8. Molecular gas in the central \sim kiloparsec dominates the high-lying excitation. To place this in the context of active star forming regions in the local Universe, Weiß, Walter & Scoville (2005b) found the CO SED to peak at J=6 in the nuclear region of starburst galaxy M82.

As energy input from the quasar begins to quench the starburst and dispel gas from the central regions, the star formation rate drops to $\sim 10^2 M_{\odot} \text{ yr}^{-1}$. Consequently, the peak excitation in the molecular gas rapidly drops to values more similar to local starbursts. During most of the quasar phase, the CO flux density

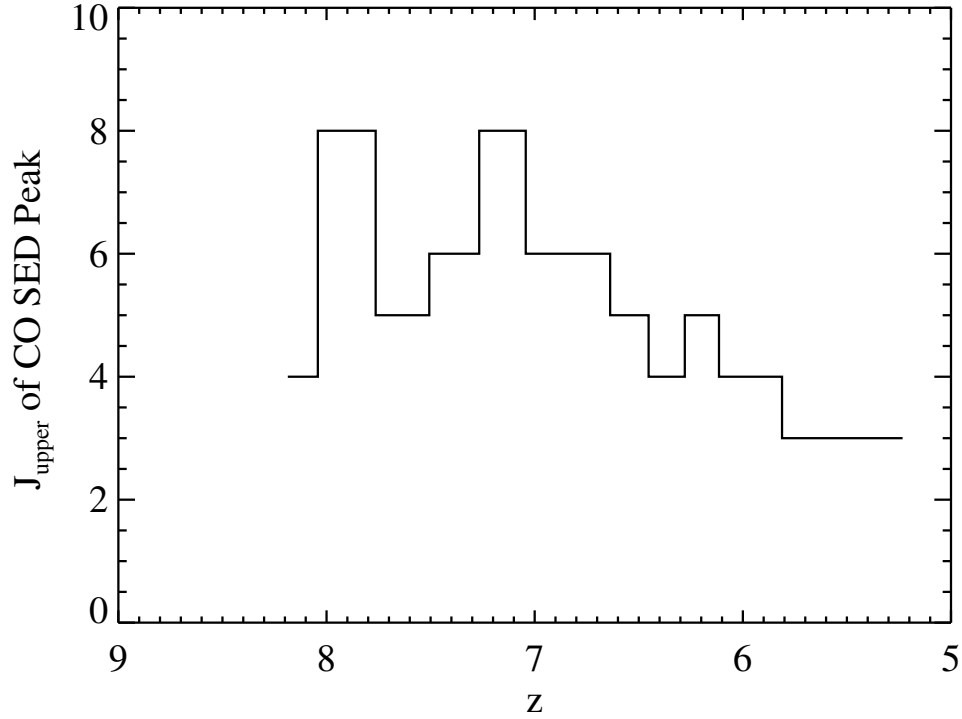


Figure 5.1 Upper rotational state (J_{upper}) of CO SED peak as a function of redshift for most massive quasar host, model Q1 (see Table 5.1). During the early, massive starburst, most of the CO is highly excited. During the height of the quasar phase, the peak in the CO excitation in our simulated galaxy ranges from $J=8$ in the beginning of the quasar phase to $J=5$ near the end. This is broadly consistent with observations of excited molecular gas in the sole CO detection at $z \sim 6$ (Bertoldi et al. 2003a). As the starburst subsides in the post-quasar phase, lower temperatures and densities drive the peak in the CO SED down to $J \sim 3$.

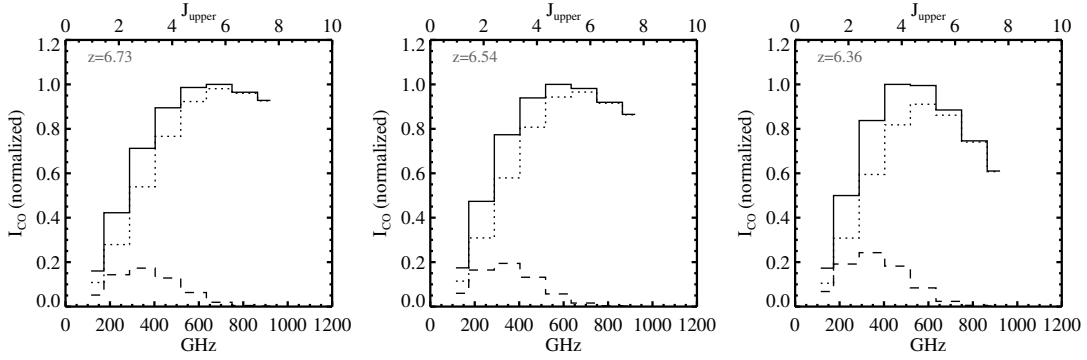


Figure 5.2 The CO SED (solid line) at three points during the peak of the quasar phase of our most massive simulated galaxy ($M \sim 10^{13} M_{\odot}$; model Q1). Massive starbursts and dense conditions in the central kiloparsec cause the CO flux density to peak at $J=8$ prior to and at the beginning of the quasar phase (not shown). During the bulk of the quasar phase, the CO SED peak drops to $J=6$ owing to quenching of the starburst by black hole feedback, and remains roughly constant for the remainder of the quasar's life. As the central AGN quenches the nuclear starburst, less gas is in highly excited ($J \gtrsim 6$) states, and the slope on the blue end of the peak becomes much steeper. The dotted line is the CO SED from just the central kpc, and the dashed line is the contribution from radius=1-4 kpc). The upper level of each transition is listed on the top axis.

in the simulated galaxy peaks at $J=6$. This is consistent with the multi-line observations and CO SED derivations by Bertoldi et al. (2003a), who find the CO flux density in J1148+5251 to peak at $J=6$. In a merger-driven model for high- z quasars, the interplay between massive starbursts and feedback from central black holes is important in determining the observed CO excitation characteristics in galaxies like J1148+5251.

The peak of the CO flux density remains roughly constant through the height of the quasar phase. As feedback from the central black holes further extinguishes the nuclear starburst, fewer molecules are highly excited, and consequently, the relative flux density from higher J levels begins to drop. In Figure 5.2, the slope of the CO SED at levels higher than the turnover point is seen to become steeper as the quasar evolves. When the accretion onto the central supermassive black hole subsides in the post-quasar phase ($z \lesssim 6$), the star formation rate (SFR) drops to $\lesssim 50 M_{\odot} \text{ yr}^{-1}$. The bulk of the molecular gas in this late stage of the galaxy's evolution is only moderately excited, and the peak in the CO SED declines to $J \approx 3-4$.

The trends discussed above are similar in models Q2 and Q3 (Table 5.1), though the overall normalization is slightly different. The CO SED of both the intermediate mass and low mass models (Q2 and Q3) peaks at $J=6$ at the beginning of the quasar phase, and settles at $J=4$ as the starburst subsides. The lower excitation values in the lowest mass model owe to overall lower densities and star formation rates. For example, during the quasar phase, the SFR from model Q3 is $\sim 30 M_{\odot} \text{ yr}^{-1}$.

Another way to view the excitation characteristics of the molecular gas is through the velocity-integrated CO luminosity (in units of K-km s^{-1} , where the K is the Rayleigh-Jeans temperature). In Figure 5.3, we show the normalized

velocity integrated CO ($J=1-0$, $J=3-2$, $J=6-5$ and $J=9-8$) intensity as a function of redshift. We additionally plot the SFR, stellar, and black hole luminosity. The CO luminosity across all transitions decreases as the merger activity progresses, and the starburst reaches its peak. This is especially true of the high- J states which are typically excited by collisions in the starburst-heated gas. All CO transitions peak in integrated intensity early on, when the starburst has not consumed most of the available star-forming gas, and collisions help to sustain molecular excitation. As the starburst fades owing to a diminishing fuel supply, the intensity from the high lying CO transitions (e.g., 6-5, 9-8) falls off rapidly while the lower- J transitions experience a more moderate decline. In part, this owes to the fact that the lowering of gas temperatures and densities does not heavily affect the molecular excitation at $J=1$. De-excitation of warm, dense star forming gas additionally contributes to populating the lower J states. While the CO luminosity is only about half of its maximum value during the quasar phase, the bolometric luminosity of the galaxy peaks here as the central quasar becomes visible (Figure 5.3, *bottom panel*).

5.6 Molecular Gas Morphology

In this section, we discuss the CO morphology of the model quasar host galaxies through their evolution. The discussion is again focused on the most massive simulation (Q1), though the results are generic for each of the models studied here. In Figure 5.4, we show the evolution of the central 2 kpc of the CO ($J=1-0$) emission in the most massive halo, Q1, during the hierarchical buildup of the host galaxy and quasar phase. Individual concentrations in the molecular gas density which have not fully coalesced appear during the buildup of the quasar host galaxy, and through parts of the quasar phase (e.g., $z=6.73$, Figure 5.4), giving

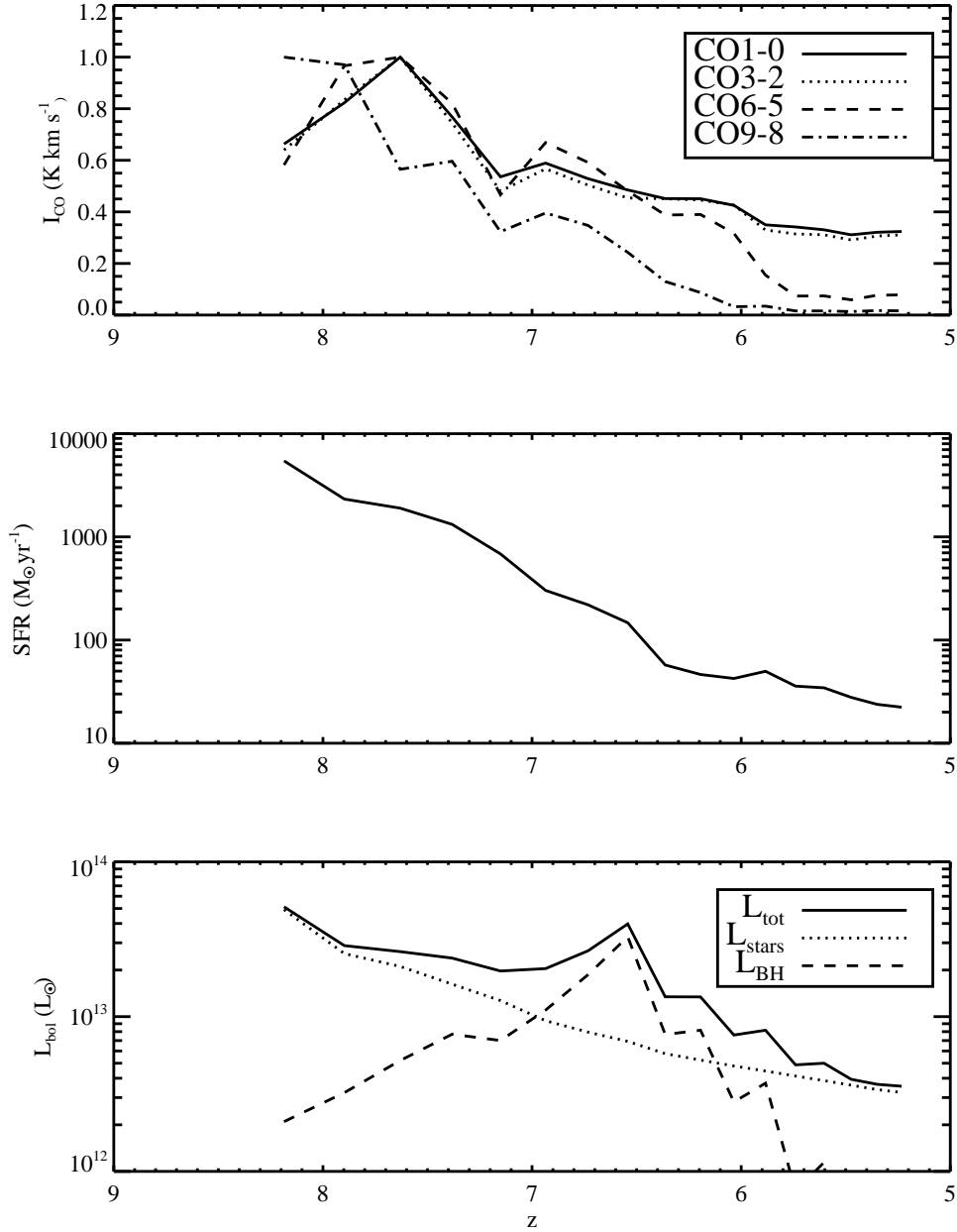


Figure 5.3 *Top*: Velocity-integrated CO Intensity (K km s^{-1}) as a function of redshift for various CO transitions for quasar Q1. Each transition is normalized at its peak value. *Middle*: Star formation rate and *Bottom*: Quasar bolometric luminosity as a function of redshift. The bolometric luminosity is broken up into contribution by stars and black holes. The bright CO emission in high J transitions during the quasar phase is representative of massive star formation, though the bulk of the spheroid formed during the hierarchical buildup of the quasar host galaxy, prior to the active quasar phase.

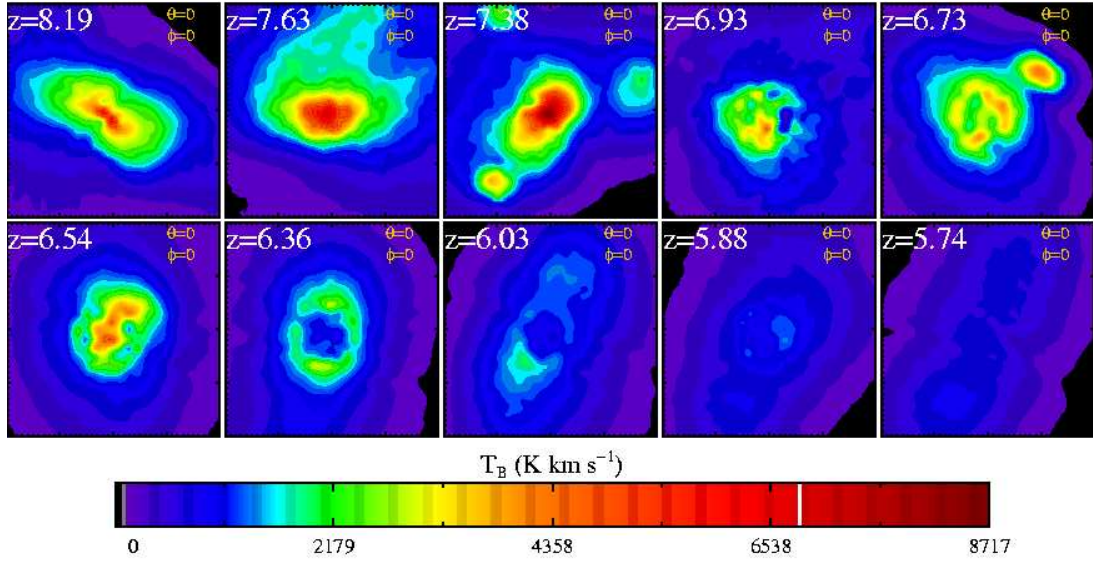


Figure 5.4 Evolution of CO (J=1-0) emission contours from $z=8.2$ - 5.7 in most massive halo, model Q1 ($M \sim 10^{13} M_{\odot}$). Multiple emission peaks are visible as cold gas falls in toward the nucleus, similar to observations of J1148+5251. As the starburst and quasar activity subsides, the CO intensity fades. Each panel is four kpc on a side. The emission is in terms of velocity-integrated intensity (K-km s^{-1}), and the scale is at the bottom. The viewing angle of each panel is listed in the top right corner, and is always $\theta = 0, \phi = 0$ for this figure.

rise to multiple CO ($J=1-0$) emission peaks. Near the end of the quasar's lifetime, the molecular gas settles into a nuclear disk, with the densest gas in the central ~ 500 pc.

The morphological features of our simulated quasar agree reasonably well with observations. Observations of J1148+5251 have revealed two CO ($J=3-2$) emission peaks in the central 2 kpc (Walter et al. 2004), similar to the multiple surface CO surface brightness peaks seen at many points in our models (e.g., Figure 5.4). This suggests that the observed multiple surface brightness peaks in the CO morphology of J1148+5251 may owe to separated peaks of high density emission in the nucleus that have not yet coalesced. To further illustrate this point, in Figure 5.5, we have plotted the CO ($J=3-2$) emission contours at $z=6.73$ over three orthogonal viewing angles, and six random ones. Most viewing angles exhibit two surface brightness peaks, suggesting that a merger origin for the formation of J1148+5251 is viable.

Within the constraints of our numerical simulations, multiple density peaks in the cold gas appear to be the most plausible explanation for the observed morphology of J1148+5251. Multiple emission peaks in the CO morphology of galaxy mergers have also been noted to arise from large entrainments of molecular clouds in AGN-driven winds (Narayanan et al. 2006a; Chapter 4). In the current simulations, however, the characteristic outflow morphologies of Chapter 4 are not seen during the active quasar phase. Emission from the nuclei of progenitor galaxies can additionally cause multiple CO surface brightness peaks. However, by the time the simulated host galaxy reaches the height of the quasar phase, the most massive nuclei have all merged into the central potential (Li et al. 2007a).

The excitation characteristics in the vicinity of massive starbursts can cause

transition-dependent CO morphologies. In Figure 5.6, we show the CO ($J=1-0$), ($J=3-2$), and ($J=6-5$) emission contours for the central 2 kpc of the most massive host during the quasar phase. The multiple emission peaks which owe to merging clumps of dense gas ($z=6.73$ in this plot) appear in all transitions. When the cold gas has coalesced in the nucleus, emission from the lowest excitation gas traced by CO ($J=1-0$) exhibits discrete pockets of emission whereas higher-lying emission originating from denser gas is centrally concentrated. As seen in Figure 5.2, the warm and dense conditions in the starbursting nucleus of the quasar ensure that the CO remains excited, with the peak flux density at $J=5-8$. The CO gas in the nucleus is typically excited out of the $J=1$ level, resulting in discrete pockets of emission in the circumnuclear molecular gas. The higher-lying emission, which originates in the warmer, denser cores of GMCs, is more prevalent in the central 500 pc of the quasar, resulting in a smoother distribution.

Owing to the violent nature of the quasar's formation process, the spatial extent of the CO emission has a large dynamic range, and varies from ~ 2 kpc to ~ 300 pc (half-light radius) throughout the evolution of the host galaxy. The more extended morphologies are representative of times when gas is falling into the central potential, and in the post quasar phase when winds have produced an extended morphology. More compact CO emission is seen primarily when the cold gas has completely coalesced, and the quasar is most active.

The starburst is centrally concentrated in the central ~ 250 pc of the quasar host galaxy during the majority of the simulation presented here. Conversely, the CO morphology is not always so compact. The CO emission through $J=10$ is extended during the buildup of the host galaxy (prior to the quasar phase) owing to merging gas clumps. This implies that CO may not always serve as an adequate tracer of the starburst during the major merger phase of the quasar's formation.

During the active quasar phase, when most of the gas has fallen into the nucleus, emission from higher CO transitions (e.g., $J \gtrsim 6$) tends to become compact, and faithfully trace the active starburst.

5.7 CO Emission Lines

The simulated properties of the CO emission lines show variations among the models presented in Table 5.1. In this section we discuss the CO emission lines in terms of the CO ($J=6-5$) lines as the CO SED peaks near $J=6$ for most of the quasar phase, and thus this transition best traces the properties of the bulk of the molecular gas. Unless otherwise specified, the nature of the CO line profile as described in the remainder of this section is not seen to vary significantly with observed transition.

5.7.1 General Nature of Modeled Line Profiles

In Figure 5.7, we show a sample of 3 random CO ($J=6-5$) emission lines from the simulated quasars Q1, Q2 and Q3 at the peak of their respective quasar phases. The first noteworthy point regarding the CO emission lines from the $z \sim 6$ quasar models is that they are characteristically featured, with a significant amount of substructure. Along many lines of sight, several smaller emission spikes (with $\sigma \sim 50 - 100 \text{ km s}^{-1}$) originating in dense CO clumps in the central 2 kpc sit superposed on the broader emission line. These emitting clumps are centrally concentrated in the quasar, and similar emission features are seen in higher spatial resolution spectra.

Another clear feature of Figure 5.7 is the apparent trend of narrowing line width with decreasing halo circular velocity. The CO linewidths are reflective of the circular velocity, and are thus strongly dependent on the mass of the quasar host galaxy. To further illustrate this, in Figure 5.8, we show the mean sightline-

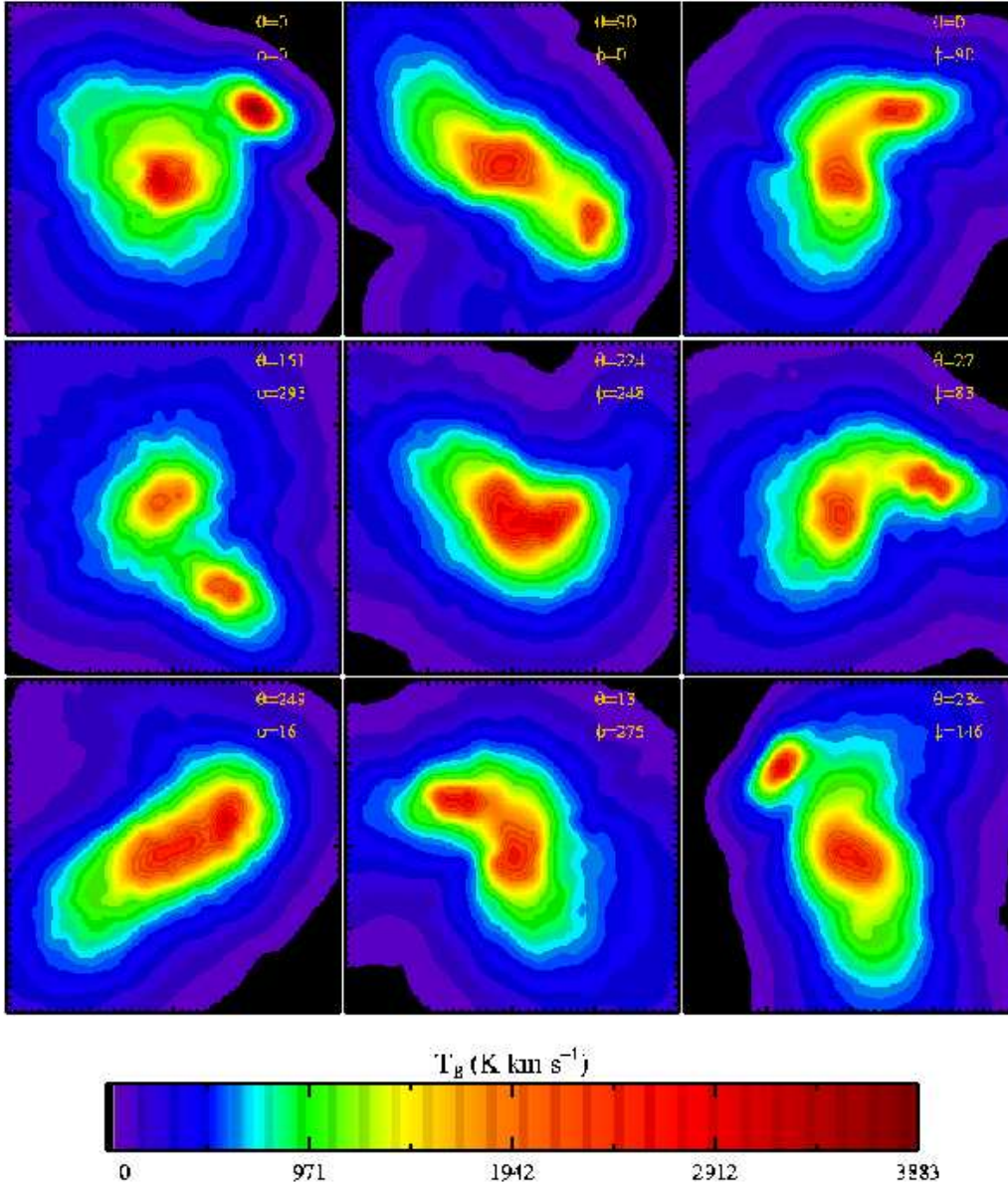


Figure 5.5 CO ($J=3-2$) emission from most massive quasar host (Q1) at $z=6.73$, while cold gas from the merger is still infalling. Top three panels are three orthogonal viewing angles, and the bottom six viewing angles are randomly drawn. The orientation for the line of sight is in the top right corner of each panel. Along many different viewing angles, multiple CO components are visible, similar to the observed morphology of J1148+5251 (Walter et al. 2003), indicating a viable merger origin for J1148+5251. Each panel is four kpc on a side. The emission is in terms of velocity-integrated intensity (K-km s^{-1}), and the scale is at the bottom.

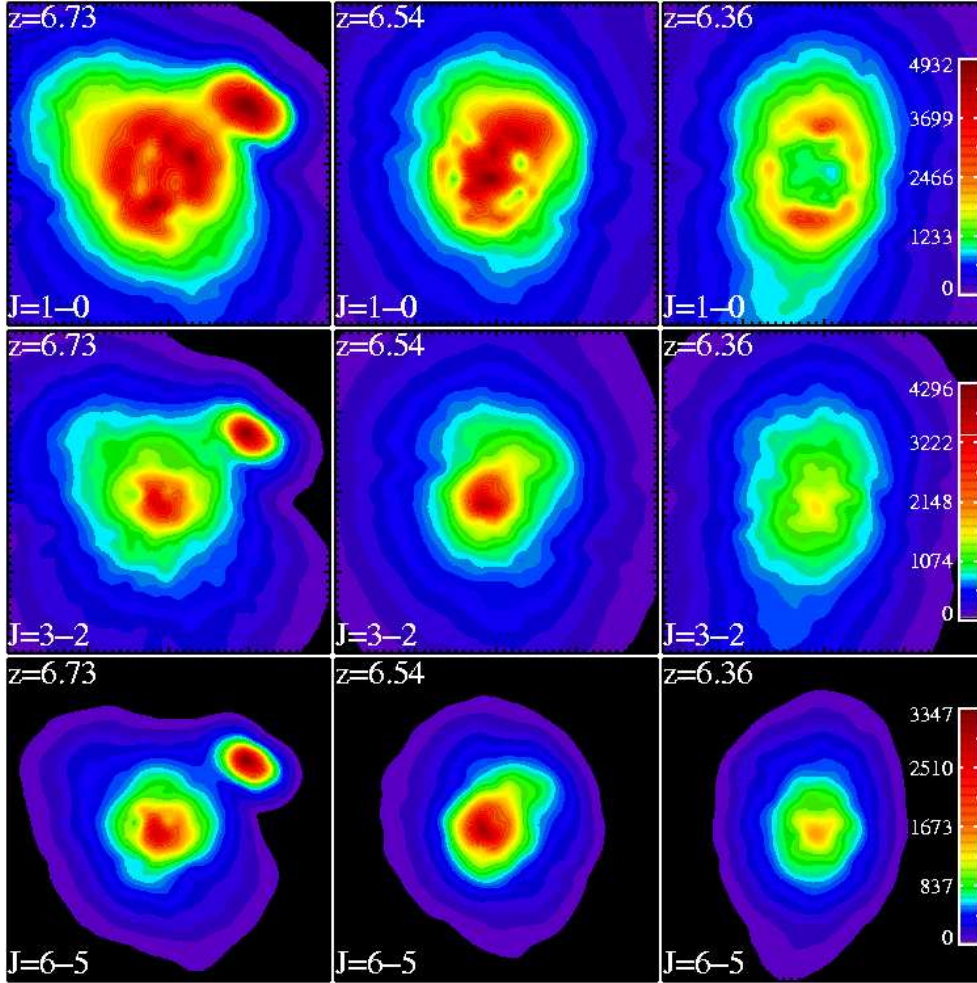


Figure 5.6 Excitation dependent CO morphologies: CO ($J=1-0$), ($J=3-2$) and ($J=6-5$) emission contours from most massive quasar host (Q1) during the peak of the quasar phase. Columns are constant in redshift, and rows are constant in transition. Multiple CO emission peaks are seen arising from merging cold clumps of gas, as well as circumnuclear gas in the ($J=1-0$) case. The gas in the central \sim kpc is highly excited, and thus does not show prominent ($J=1-0$) emission, but causes the ($J=3-2$) and ($J=6-5$) emission to be centrally concentrated. Multiple CO emission peaks are seen in higher lying transitions owing only to merging gas as the bulk of the gas in the central \sim kpc is highly excited. These results are robust across all modeled viewing angles. The viewing angle for each panel is the same, and is $\theta = 0, \phi = 0$, for comparison with Figures 5.4 and 5.5. Each panel is four kpc on a side, and each row (transition) is on its own scale to facilitate interpretation. The scales are on the right, and the units are in terms of velocity integrated

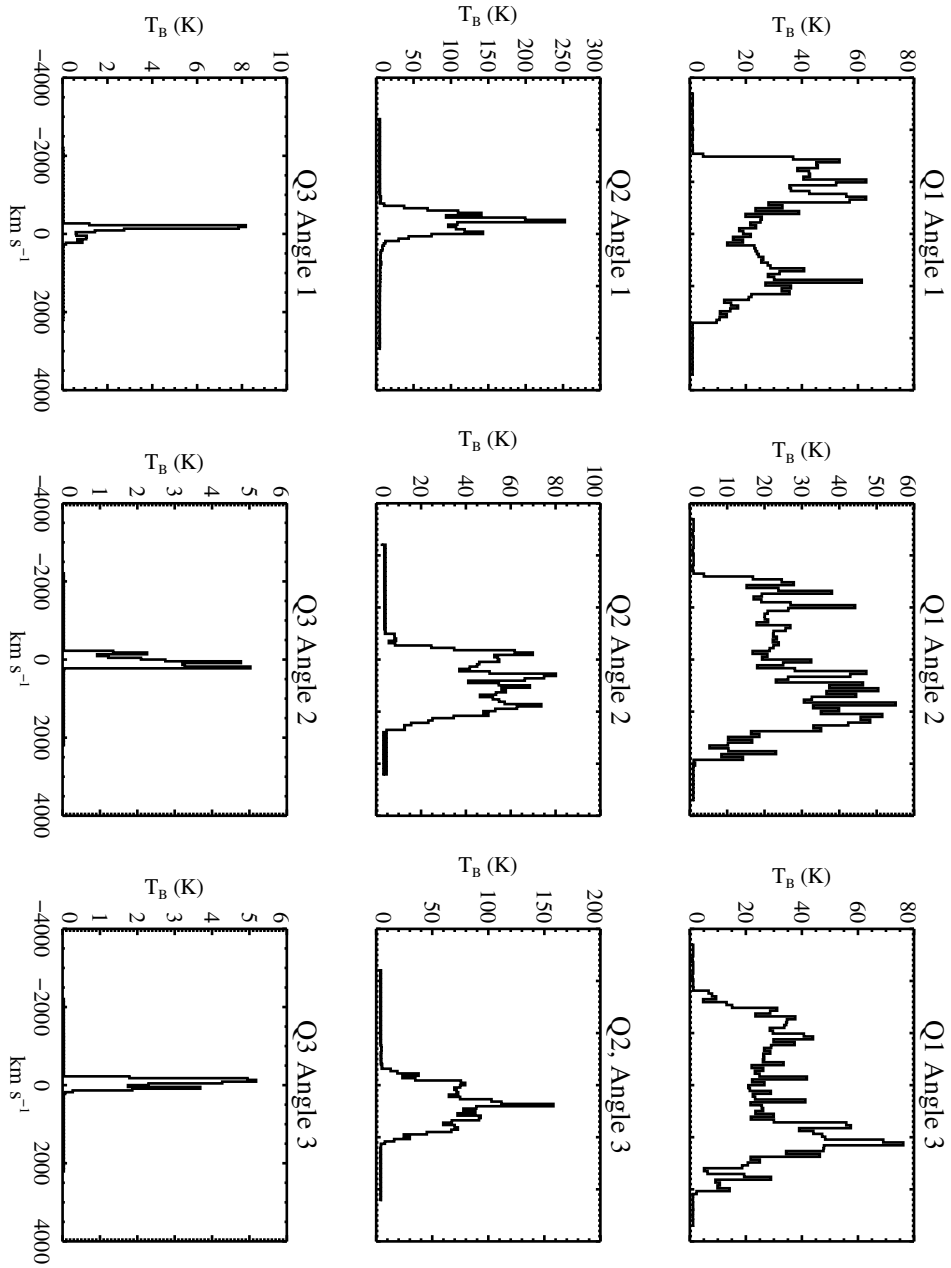


Figure 5.7 CO ($J=6-5$) emission lines from model quasars Q1, Q2 and Q3 at peak of their quasar phases viewed from three random sightlines. The first row corresponds to quasar Q1, the second to Q2 and third row to Q3, The characteristic emission line widths drop with halo mass, though remain featured in each model with several substructure spikes superposed on broader lines. Spectra have been convolved with a circular $5''$ Gaussian beam, and modeled at an angular diameter distance of 1 Gpc.

averaged CO (J=6-5) line width during the hierarchical buildup and quasar phase of the quasars formed in the halos of Q1-Q3. We additionally show the range of sightline-dependent observed line width values. The multiple mergers involved in the formation of the simulated $z \sim 6$ quasars give rise to large velocity dispersions along a number of sightlines during the buildup of the quasar host galaxies. During this time, much of the molecular gas is not virialized, and thus the typical line widths exhibited represent about twice the expected circular velocity at the spatial extents of the molecular gas. In the quasar phase, as the gas virializes into a molecular disk, the CO line widths drop to values more consistent with the virial velocity of the host. In the most massive ($\sim 10^{13} M_{\odot}$, model Q1; Table 5.1) halo, this is manifested in broad ($\langle \sigma \rangle \sim 500 - 800 \text{ km s}^{-1}$) predicted CO emission line widths, whereas in the halos with lower circular velocity (quasars Q2, Q3), the mean CO line width is ~ 450 and $\sim 300 \text{ km s}^{-1}$, respectively. It is important to note that in all cases, while the aforementioned trends hold, a large range of line widths is permitted at all points as they are strongly sightline-dependent. Another way to view this is through the detailed distribution of line widths themselves. In Figure 5.9, we show a histogram of the sightline-dependent line widths during the quasar phase for models Q1-Q3.

These derived linewidths are a natural consequence of our initial assumptions of quasar formation in massive halos, and that half the cold gas mass is in molecular phase. Within the confines of our initial assumptions, these results are consistent with virial arguments. Thus, for example, the broad emission lines seen in the massive $\sim 10^{13} M_{\odot}$ halo simply reflects the virial velocity of the host galaxy at the radial extent of the molecular gas distribution, which is of order $\sim 550 \text{ km s}^{-1}$.

CO line measurements of J1148+5251 by Bertoldi et al. (2003a), and Walter et

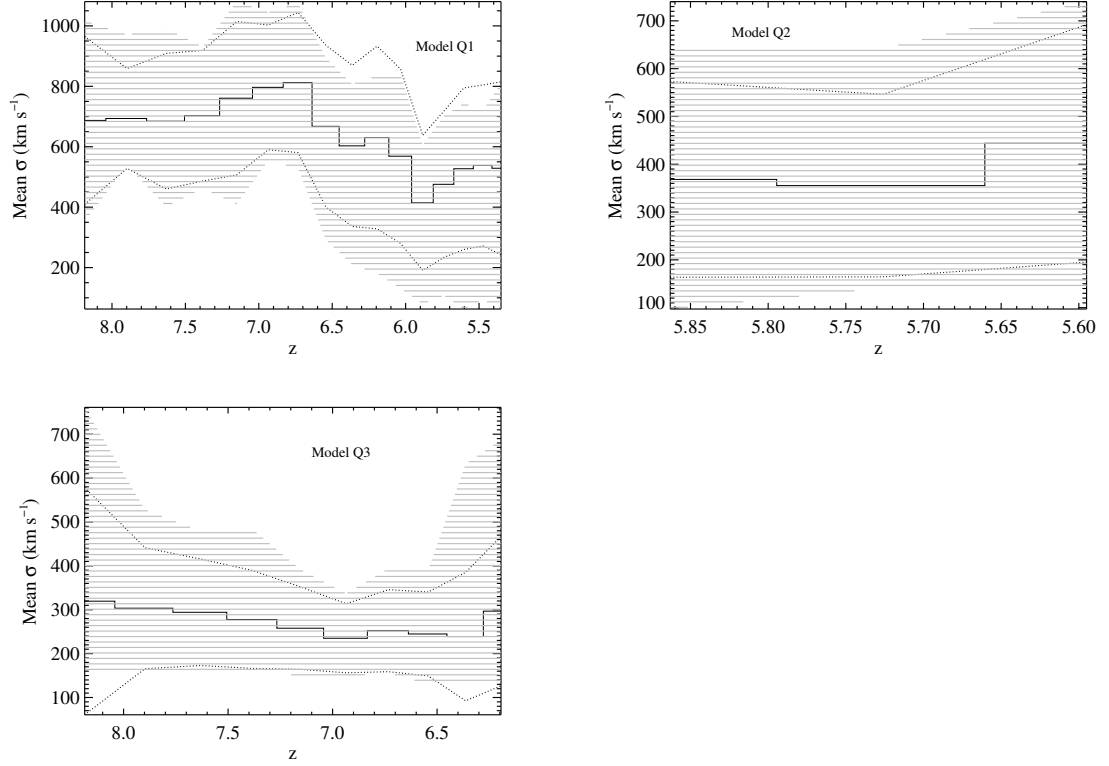


Figure 5.8 Sightline-averaged velocity dispersion (σ) of CO ($J=6-5$) emission lines (solid line, middle) as a function of redshift for quasar models Q1-Q3. The shaded area shows the range of derived σ over 250 randomly sampled sightlines, and the upper and lower dotted lines show the 2σ linewidths for each snapshot. The spectra have been convolved with a circular $5''$ Gaussian beam, and binned to 50 km s^{-1} . During the hierarchical buildup of the host galaxy, the H_2 gas is highly dynamical, and the typical line widths are broader than the virial velocity of the host galaxy by a factor of $\sim 1.5 - 2$. As the gas virializes during the quasar phase, the line widths drop, and roughly trace the virial velocity of the galaxy. A range of line widths are permitted throughout the evolution of the host galaxy, with larger numbers of sightlines being compatible with the narrow ($\sigma \sim 120 \text{ km s}^{-1}$) detected line in J1148+5251 near the end of the quasar phase. The number of sightlines compatible with observations naturally increases in the lower mass halos (Q2 and Q3) as the CO lines faithfully trace the virial velocity of the galaxy during the quasar phase.

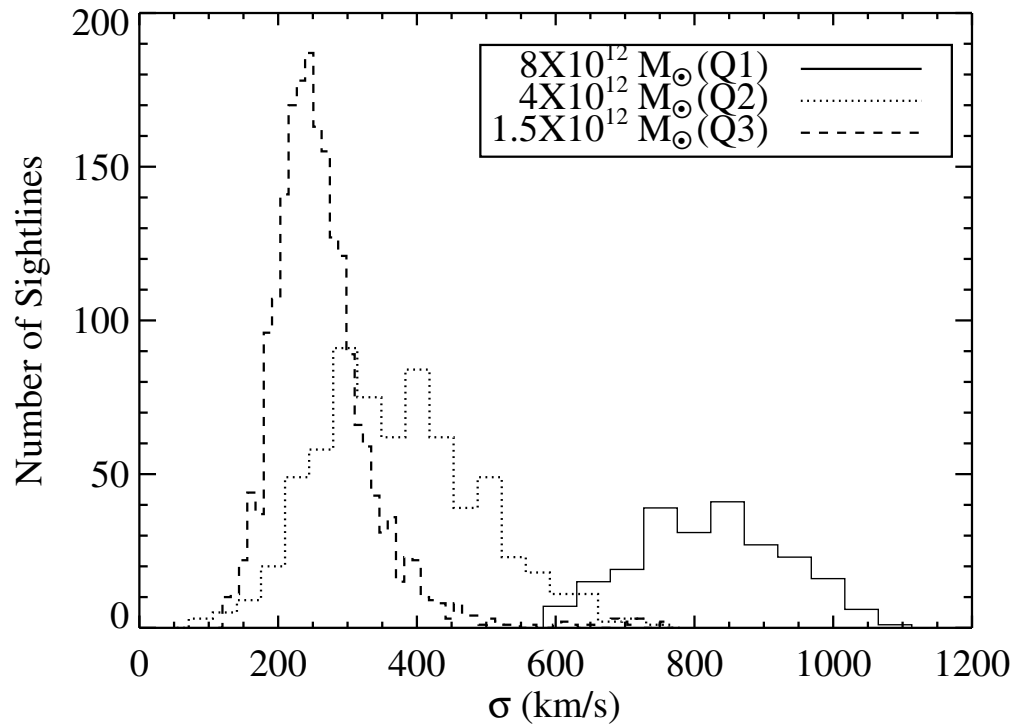


Figure 5.9 Histogram of sightline-dependent line widths during quasar phase for three halo mass models. The mean line width traces the virial velocity of the host galaxy, and thus become narrower in lower mass galaxies. In all cases, a broad range in linewidths is observable.

al. (2003, 2004) showed CO (J=3-2, J=6-5 and J=7-6) emission lines with width $\sim 280 \pm 140 \text{ km s}^{-1}$ (FWHM; corresponding to $\sigma \sim 120 \pm 60 \text{ km s}^{-1}$ for a Gaussian line). While this is a factor of 2-5 narrower than the median line width predicted in our models (Figure 5.8 and 5.9), it is worthwhile to note the non-negligible fraction of sightlines for each of the quasar models that are compatible with the narrow observed line widths (Figure 5.9). Through the quasar phase and beginning of post-quasar phase, $\sim 2 - 3\%$ of sightlines in the most massive quasar host (Q1) have linewidths compatible with the line widths measured in J1148+5251 (Bertoldi et al. 2003a; Walter et al. 2003, 2004). The smaller virial velocity of the lower mass halos (Q2 and Q3) naturally produce more sightlines with narrow line widths compatible with observations. During the quasar phase, the quasar formed in the $4 \times 10^{12} M_{\odot}$ halo (model Q2) shows CO (J=6-5) emission line widths consistent with observations $\sim 5\%$ of the time, and the quasar formed in the $1.5 \times 10^{12} M_{\odot}$ halo (model Q3) reveals CO (J=6-5) line widths consistent with observations $\sim 10\%$ of the time.

In an effort to understand the relationship of these models to the measured CO line width of J1148+5251, it is of interest to explore the origin behind the particular percentages of sightlines that are compatible with observations, and possible trends which may tend observations toward particular sightlines. We thus focus the remainder of this section on this investigation. We conclude the section with a discussion as to what circumstances may bring agreement between our simulations and observations, and the implications of these results with respect to potential observable tests motivated by these models.

5.7.2 Effect of Merger Remnant Structure and Disk Formation on Line Widths

We have thus far considered the formation of quasars hierarchically through multiple mergers whose physical conditions were derived self-consistently from cos-

mological simulations. It is possible that not all quasars at $z \sim 6$ form via numerous violent merging events, but rather through a more 'ordered' merger. It is thus worth quantifying the potential dependence of line width on merger history, and in particular, how a more ordered merger remnant may affect the observed line widths. To provide a limiting example, we have conducted a test simulation of a coplanar binary merger in a halo of $\sim 10^{13} M_{\odot}$ (model Q4; Table 5.1). The progenitors were initialized with a Hernquist (1990) profile, spin parameter $\lambda=0.033$ and circular velocity $V_{200} \sim 600 \text{ km s}^{-1}$. The disks had an initial gas fraction of 0.99, and the virial properties were scaled to be appropriate for $z=6$ (Robertson et al. 2006a).

In Figure 5.10, we show the CO (J=3-2) morphology for the resultant quasar over two orthogonal viewing angles, and their corresponding unresolved emission spectra. The remnant forms a strong disk-like morphology, consistent with the findings of Robertson et al. (2006b) and Springel & Hernquist (2005c). As expected, the CO line width and profile are a sharp function of the viewing angle of the disk. Averaged over 250 random sightlines, we find that the predicted CO (J=6-5) emission line width from this source is consistent with the observed line width J1148+5251 $\sim 4\%$ of the time, comparable to the more massive quasar hosts (Q1 and Q2) which formed from multiple mergers.

The percentage of sightlines compatible with observations in the binary merger Q4 arises from a limited range of angles a disk can be from face on to keep line widths within a particular limit. Specifically, if one considers an inclined toy disk of pure gas with velocity dispersion σ_{virial} , then in order for observed velocity dispersions to fall below a particular value, σ_{obs} , the inclination angle from face on is limited by:

$$\theta < \sin^{-1} \left(\frac{\sigma_{\text{obs}}}{\sigma_{\text{virial}}} \right). \quad (5.1)$$

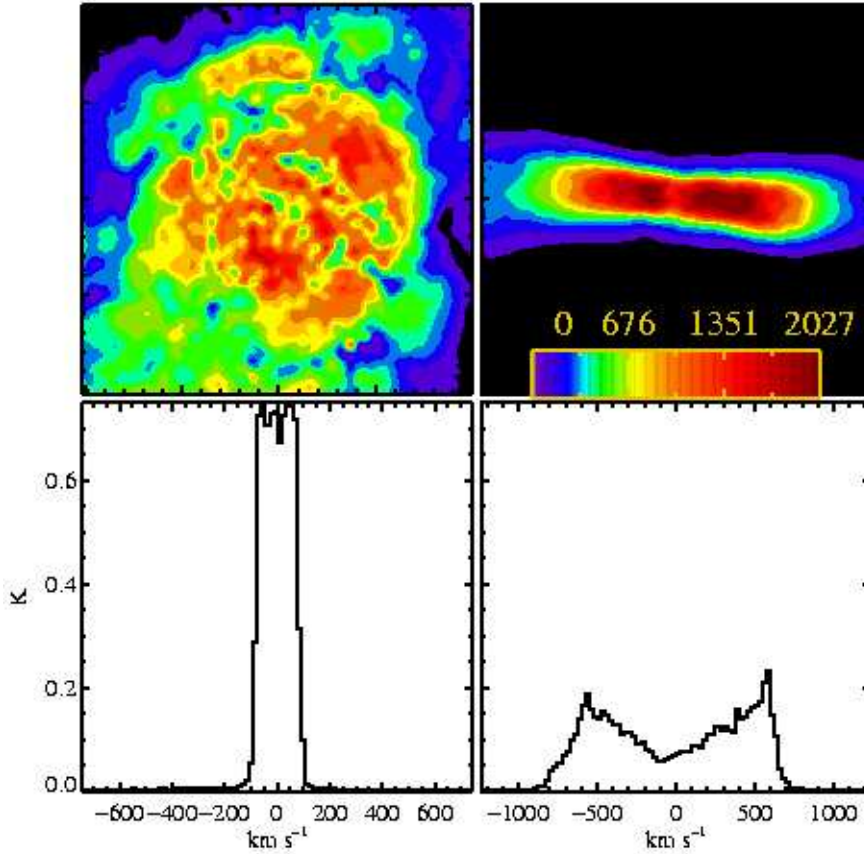


Figure 5.10 CO ($J=1-0$) morphology and unresolved line profiles of the remnant formed from a binary merger simulation (model Q4) across two orthogonal sightlines (face-on and edge-on). The progenitors were initialized on a coplanar orbit in a $\sim 10^{13} M_{\odot}$ halo. The resultant quasar host galaxy has large rotating molecular disk, resulting in narrow observed emission lines in face-on viewing angles, and broad lines in edge-on viewing angles. Approximately 4-5% of sightlines show narrow line widths compatible with observations of J1148+5251 (see Equation 5.2). The maps are 12 kpc across, and the scale is in units of $K\text{-km s}^{-1}$.

However, inclinations along both the polar (θ) and azimuthal (ϕ) axes have to be within this limit of a face-on configuration to keep the line of sight velocity dispersion below observed line widths. As such, the probability of having both θ and ϕ randomly drawn such that they both fall below a critical value to match an observed line width is

$$P(\theta < \theta_{\text{crit}}, \phi < \phi_{\text{crit}}) = \frac{4}{\pi^2} \left(\sin^{-1} \left[\frac{\sigma_{\text{obs}}}{\sigma_{\text{virial}}} \right] \right)^2, \quad (5.2)$$

where $P \approx 4\%$ for $\sigma_{\text{obs}} = 180 \text{ km s}^{-1}$ (the upper limit σ of the observed line in J1148+5251), and $\sigma_{\text{virial}} = 600 \text{ km s}^{-1}$. This probability then represents the upper limit of fraction of sightlines that will be compatible with the observed CO line width in J1148+5251 for disks with circular velocity $\sim 500 \text{ km s}^{-1}$.

This clarifies why the percentage of sightlines compatible with observations in the massive multiple-merger models (Q1-Q3) is relatively small. The cold gas in the three quasars which formed out of multiple non-idealized mergers (Q1-Q3) settles into rotating nuclear disks. As an aside, it is interesting to note that the amount of rotationally supported gas is seen to be dependent on the mass of the galaxy. Namely, the lower mass halos show a larger percentage of gas in stable rotation. To illustrate this, in Figure 5.11 we show the fraction of rotationally supported gas for quasars Q1-Q3 as a function of redshift, noting in particular the points of peak quasar activity. When the most massive galaxy (Q1) is seen as a quasar, roughly 50% of the H_2 gas is rotationally supported. Conversely, in the lowest mass model (Q3), $\sim 90\%$ of the gas is rotationally supported. This may be a direct result of the amount of energy input from the central quasar during these times. Cox et al. (2007) demonstrated that the amount of rotationally supported gas in galaxy mergers decreases with increasingly efficient winds. During the peak of the quasar phase, the black hole luminosity is over an order of magnitude brighter in model Q1 than in Q3.

In either case, though, large percentages of the gas in all of the quasars (Q1-Q3) are seen to be rotationally supported during the quasar phase. Because of this, the number of sightlines compatible with observations is roughly characterized by Equation 5.2. Thus, the most massive model (Q1) shows line widths compatible with observations $\sim 2 - 3\%$ of the time, consistent with a predicted upper limit of $\sim 4\%$ for $\sim 10^{13} M_{\odot}$ halos. Similarly, in the lowest mass model (Q3), where $\sim 90\%$ of the gas is rotationally supported, the 10% of sightlines seen to be compatible with observed line widths is compatible with the predicted upper limit of $\sim 13\%$. The fact that the modeled fraction of sightlines is always slightly smaller than the toy model in Equation (5.2) owes to the fact that some of the gas in the galaxy is still highly dynamical and not virialized.

5.7.3 CO Line Width-Quasar Luminosity Relation: Potential Selection Effects

Given the dispersion of CO (J=6-5) line widths along different lines of sight, an interesting relation to explore is one between the optical quasar luminosity and CO emission line width in search of potential observational selection effects which may bias observations of $z \sim 6$ quasars toward smaller line widths. In Figure 5.12, we plot the σ from the CO (J=6-5) line width as a function of the attenuated rest-frame *B*-band luminosity over 5000 lines of sight throughout the quasar phase for the most massive model, Q1. We utilize the methodology of Hopkins et al. (2005a) in computing the dust-attenuated quasar luminosity, and include contributions from both the stellar component, as well as the central AGN.

There is a general trend for sightlines which show the brightest rest-frame *B*-band luminosity to have smaller CO line widths. This can be understood via decomposition of the quasar luminosity into its stellar and AGN components. Specifically, while the stellar luminosity does not vary much with viewing angle, the contribution of the central black hole to the total luminosity is strongly depen-

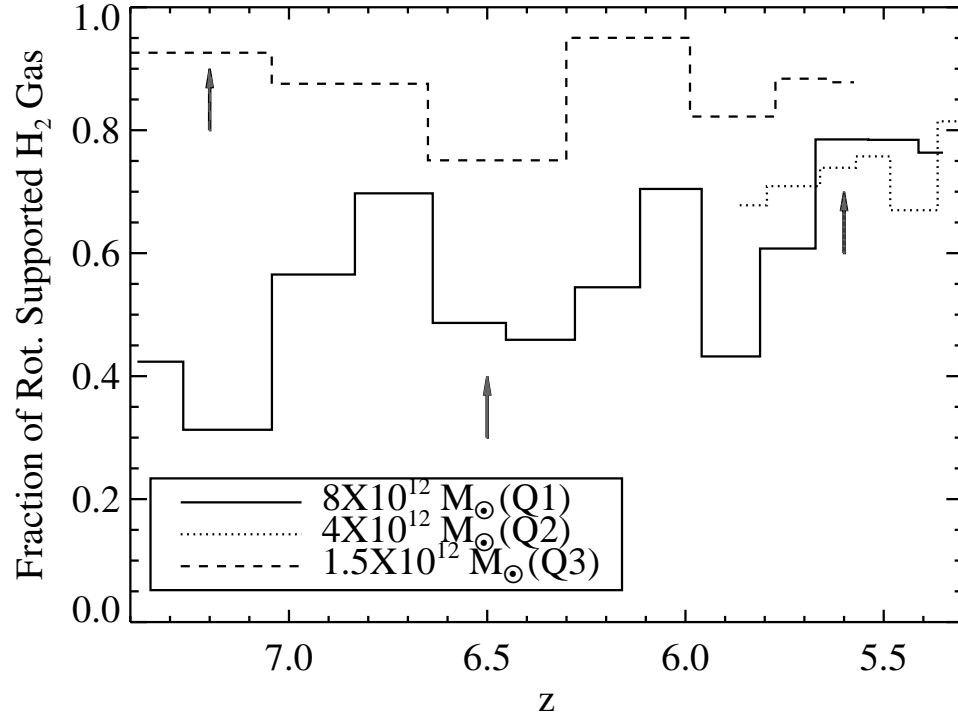


Figure 5.11 Fraction of rotationally supported molecular gas in quasars Q1-Q3. Gas is considered to be in rotational support if its rotational velocity is at least 80% the expected circular velocity at that radius. Arrows point to redshift of peak quasar activity (also listed in Table 5.1). Gas is seen to more easily settle into a stable rotational configuration in the lower mass quasar hosts, though all quasars naturally form relatively strong disks during the quasar phase.

dent on the viewing angle with respect to the rotating molecular gas. Directions which view the molecular disk in an edge-on configuration result in a heavily obscured central AGN. Along these sightlines, the emergent CO emission line is typically broad (e.g., bottom right panel, Figure 5.10). Conversely, when the molecular disk is seen in a more face-on viewing angle (and thus has narrower CO emission lines), the central AGN can be viewed relatively unobscured, and the attenuated rest-frame B -band luminosity is consequently higher. This effect is typical during the quasar phase, and only rarely is the black hole relatively unattenuated through an edge-on sightline, which causes broad CO lines to be visible when the rest-frame B -band luminosity peaks.

The results of this relationship between bolometric luminosity and line width suggest a potential selection effect which may cause quasars selected for optical luminosity to have systematically lower CO line widths, owing to the preferred face-on viewing angle for the molecular disk. In Figure 5.13, we plot the percentage of sightlines with line widths compatible with observations as a function of limiting rest-frame B -band luminosity. For the highest flux cuts, the fraction of sightlines with narrow line widths increases from 2-3% to $\sim 10\%$. This selection effect is robust across both the lower mass halo models as well. In models Q2 and Q3, the fraction of sightlines compatible with observations increases to ~ 15 and 25% respectively, for the highest luminosity cuts.

Finally, we note that the viewing angles corresponding to the smallest (2σ) line widths in our simulations typically fall within a 25° range in polar and azimuthal angle from face-on. This range of angles is consistent with recent observational studies which have suggested that the commonly observed narrow CO line widths of high- z quasars may correspond to a preferred viewing angle of $10 - 15^\circ$ from face-on (Carilli & Wang 2006; Wu 2007).

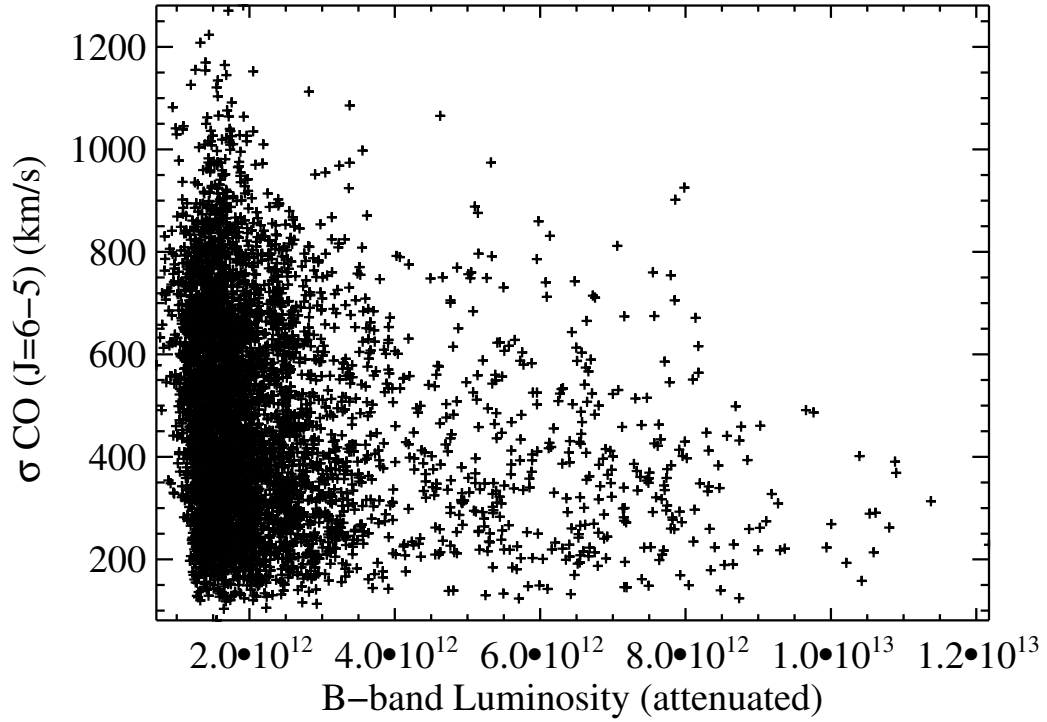


Figure 5.12 CO (J=6-5) emission line width (σ) versus attenuated rest-frame B -band luminosity. The brightest quasar luminosities correspond to face-on molecular disk configurations where the central AGN is the least obscured. These face-on sightlines additionally show narrow CO line widths. Thus, surveys which select quasars for optical luminosity may preferentially select objects that have narrow CO line widths. This may have important consequences for using CO as a dynamical mass indicator in quasars.

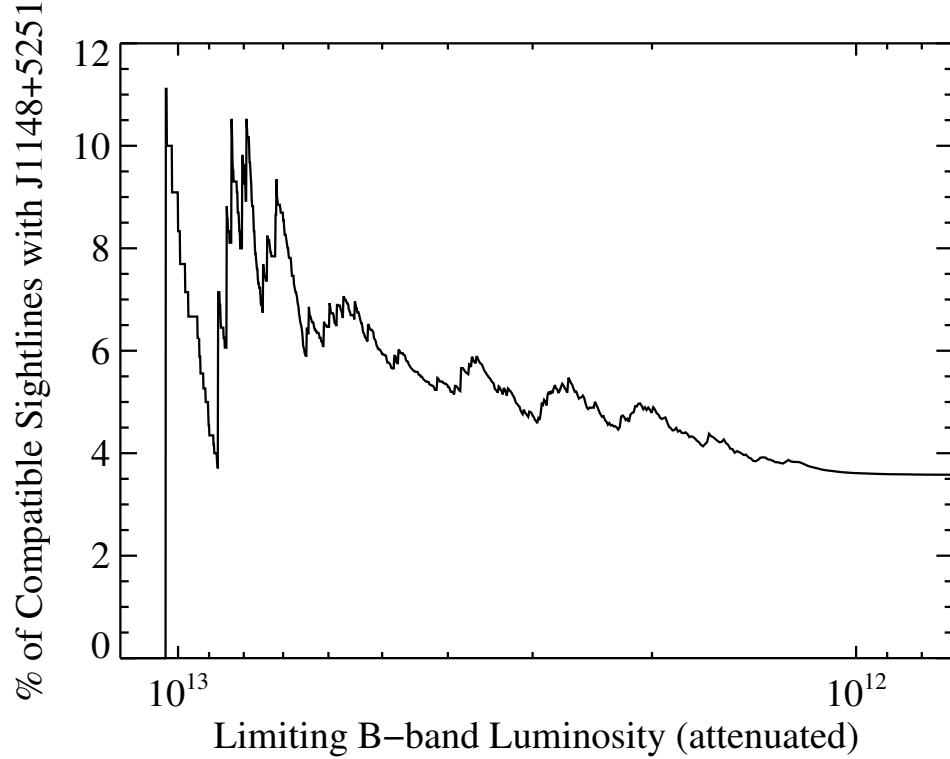


Figure 5.13 Percent of sightlines of $\sim 10^{13} M_{\odot}$ quasar over which line widths are compatible with observations versus limiting rest-frame *B*-band luminosity. Natural molecular disk formation in the quasar host galaxy gives rise to a selection effect which enhances the likelihood that flux-limited optical surveys will view the quasar in a face-on configuration. These viewing angles also typically have narrower CO line widths, and thus may increase the chances of viewing a narrow emission line in quasars which is not necessarily characteristic of the true sightline-averaged mean line width. Line widths are derived from CO (J=6-5) line profiles, and compared to upper limit of sole CO detection at $z \sim 6$, J1148+5251. Rest-frame *B*-band luminosities are dust attenuated, and calculated using the methodology of Hopkins et al. (2005a).

5.7.4 Interpretation of $z \sim 6$ Quasar Observations

Our simulations show that $z \sim 6$ quasars which form in massive halos will characteristically have broad mean line widths, consistent with simple virial arguments. The mean simulated line widths are in apparent contradiction to observed narrow ($\sigma \sim 120 \pm 60 \text{ km s}^{-1}$) line widths of the sole CO detection at $z \sim 6$ (Walter et al. 2004), though a non-negligible fraction of sightlines (ranging from 2-3% for the most massive model to $\sim 10\%$ in the lowest mass model) are compatible with this observation. Potential selection effects owing to molecular disk formation in these galaxies will increase the probability of narrow-line detection when selecting quasars for optical luminosity, ranging from $\sim 10\%$ in the most massive quasar host to 25% in less massive ones. The full dispersion in line widths is predicted to become more apparent at lower optical luminosities (Figure 5.12).

Our models find that quasars which form in the lower end of our halo mass range at $z \sim 6$ (e.g., quasars Q2 and Q3) may have similar rates of detection as those which form in the most massive $\sim 10^{13} M_{\odot}$ halos (e.g., quasar Q1). This owes to the competing effects of smaller quasar lifetimes in the lower mass halos, but more lower mass halos in the simulated cosmological volume. Specifically, the quasars formed in the $4 \times 10^{12}(1.5 \times 10^{12}) M_{\odot}$ halos have luminosities $\gtrsim 10^{13} L_{\odot}$ for a factor of $\sim 2.5(14)$ less time than the quasar formed in the $10^{13} M_{\odot}$ halo (Table 5.1). However, standard halo mass functions predict more low mass halos than massive $\sim 10^{13} M_{\odot}$ halos (Press & Schechter 1974; Sheth & Tormen 2002; Springel et al. 2005). The cosmological simulations of Li et al. (2007a) (which were used in this work) found approximately 3(7) times as many halos of mass $5 \times 10^{12}(2 \times 10^{12}) M_{\odot}$, compared to the single $\sim 10^{13} M_{\odot}$ halo identified in the simulation box at $z \sim 6$ (Li et al. 2007a, Figure 14). In this sense, quasars which form in lower mass halos may be identified at similar rates as those which form

in $\sim 10^{13} M_{\odot}$ halos.

One result of this work is to motivate observational tests of these models. A direct prediction of these simulations is that a CO survey from a large sample of quasars at $z \sim 6$ which probes lower on the optical luminosity function may directly constrain the range of potential line widths which originate from high redshift quasars. At the median rest-frame B -band luminosity, our models predict that a large range of line widths should be observed (Figure 5.12). A potential caution associated with this test is that physical processes on scales below the resolution of our simulations may limit optical detections of quasars with edge-on disks at $z \sim 6$. For example, if a dusty molecular torus exists on scales smaller than ~ 100 pc and provides high levels of obscuration along sightlines other than face-on, then the variation of optical luminosity with inclination angle will be steeper than suggested by Figure 5.12. It is thus not a straightforward assumption that optical surveys will need to probe only an order of magnitude lower in rest-frame B -band luminosity to test these models as Figure 5.12 suggests, but rather it is in the limit that quasars with relatively inclined disks at $z \sim 6$ can be detected that these models predict a broad range of CO line widths at lower optical luminosities.

A more clear test may come from observations of the progenitors of $z \sim 6$ quasars themselves. For example, a direct prediction from these models is that CO observations of either the most massive progenitor galaxies prior to the merger (e.g., at $z \sim 8$; see Table 1 of Li et al. 2007a), or the ongoing mergers themselves may exhibit a large dispersion in CO line widths, with median velocity dispersion reflective of the halo virial velocity (Figure 5.8). The identification of potential progenitors at $z \gtrsim 7$ is predicted to be feasible through z -band dropouts (Robertson et al. 2007).

In either case, these models suggest that surveys at $z \sim 6$ which observe either the most massive progenitors of quasar host galaxies, or highly inclined disks (closer to edge-on, and likely lower luminosity) associated with $z \sim 6$ quasars will see a broader dispersion of CO line widths. The model halos presented here reflect the range of halo masses in our cosmological simulation which were feasibly able to create a $z \sim 6$ quasar. As such, based on the line widths seen in our lowest mass host galaxy (Q3), samples of CO detections at $z \sim 6$ which probe quasars with a range of disk inclination angles should find a median line width at least \sim twice the value of the sole detection. Surveys which observe quasars with inclined molecular disks and still find consistently narrow line widths may reflect an inability of our radiative transfer simulations to fully capture the appropriate physics necessary to predict accurate CO line widths from these early Universe galaxies. If, for example, our assumptions regarding molecular gas content or CO abundances are incorrect, it could be that CO emission is preferentially seen in lower velocity gas in the host galaxy. Alternative possibilities may include super-Eddington accretion for the central black hole which may allow for luminous quasars at $z \sim 6$ in less massive halos than those adopted here (e.g., Volonteri & Rees 2005). It is, however, attractive that the simulations presented here do provide a model for the CO emission from the earliest quasars which are consistent with observations of the CO excitation and morphology of J1148+5251. More observations to fully determine the nature of CO line widths in $z \sim 6$ quasars will be necessary to assess the validity of this aspect of our modeling.

5.8 Spheroid, Black Hole, and Dynamical Mass

Because submillimeter-wave radiation typically does not suffer the heavy extinction characteristic of optical emission, CO lines are often used as dynamical mass

indicators in dusty starburst galaxies. Dynamical masses are derived assuming that the emitting gas is rotationally supported, and that the line width provides a measure of the rotational velocity. Here we assess the usage of CO-derived dynamical masses in $z \sim 6$ quasars. As a case study, we will focus on the most massive simulation ($\sim 10^{13} M_{\odot}$; model Q1), though the trends are generic for all quasars presented in this work.

Generally, theoretical arguments have predicted that the $M_{\text{BH}}-\sigma_v$ and black hole mass-bulge mass relations show only weak evolution with redshift (Robertson et al. 2006a). Using numerical simulations of galaxy mergers by Cox et al. (2006a) and Robertson et al. (2006a) that include black hole feedback, Hopkins et al. (2007a) found that the normalization of the $M_{\text{BH}}-M_{\text{bulge}}$ relation shows weak ($\sim 0.3 - 0.5$ dex) trends toward larger $M_{\text{BH}}/M_{\text{bulge}}$ from $z=0$ - 6. The simulations presented here provide additional support for a scenario in which the stellar bulge and central black hole grow coevally in the earliest galaxies.

In the most massive galaxy presented here, the supermassive black hole grows rapidly during the hierarchical buildup of the quasar host galaxy, and reaches a total mass of $\sim 2 \times 10^9 M_{\odot}$ during the peak quasar phase, similar to black hole mass estimates in J1148+5251 (Willott et al. 2003). Owing to the extreme star formation rates which can be as large as $\sim 10^4 M_{\odot}\text{yr}^{-1}$ between redshifts $z=9$ and $z=8$ during the final violent mergers (e.g, Figure 5.3), the bulge reaches a total mass of $\sim 10^{12} M_{\odot}$ by the quasar phase. The black hole and stellar bulge masses are related such that $M_{\text{BH}} = 0.002 \times M_{\text{bulge}}$ during the quasar phase, roughly consistent with the local $M_{\text{BH}}-M_{\text{bulge}}$ relation (Li et al 2007a; Magorrian et al. 1998; Marconi & Hunt 2003). We note, though, that during the peak of the quasar activity, the $M_{\text{BH}} - \sigma_v$ relation is not necessarily obeyed as the stellar bulge is not dynamically relaxed.

The massive starburst at $z \gtrsim 7$ results in an ISM highly enriched with metals, consistent with the observed FeII/MgII abundances, [CII] emission, CO emission, and dust masses for $z \sim 6$ quasars (Barth et al. 2003; Bertoldi et al. 2003b; Dietrich et al. 2003a,; Freudling et al. 2003; Jiang et al. 2006; Maiolino et al. 2005; Walter et al. 2003, 2004). Li et al. (2007a) have found that the metallicity in the simulated $\sim 10^{13} M_{\odot}$ quasar presented here is solar to supersolar during the quasar phase, owing to the $\sim 10^4 M_{\odot} \text{yr}^{-1}$ starburst during the hierarchical merging process of the quasar formation. These findings are consistent with the mean abundances of ~ 4 times solar in a sample of $4 < z < 5$ quasars observed by Dietrich et al. (2003b) and imply that black hole growth and stellar bulge formation are correlated at high redshifts. These simulations support findings that the relationship is regulated by feedback from supermassive black holes (e.g., Di Matteo, Springel & Hernquist 2005c; Robertson et al. 2006a; Hopkins et al. 2007a).

CO observations of high- z quasars have suggested that central black hole masses may be excessively large compared to the stellar bulge mass as predicted by the present day $M_{\text{BH}}\text{-}M_{\text{bulge}}$ relation. Dynamical mass estimates of J1148+5251 using CO line measurements have indicated that the stellar bulge may be under-massive by a factor of $\sim 10 - 50$ if the present day $M_{\text{BH}}\text{-}M_{\text{bulge}}$ relation holds at $z \sim 6$ (Walter et al. 2004). Studies of other quasars at $z \gtrsim 3$ using CO line widths as a proxy for enclosed mass have arrived at similar conclusions (Shields et al. 2006).

In order to investigate the usage of CO as a dynamical mass indicator, in Figure 5.14, we plot the evolution of the median dynamical mass of the quasar host galaxy from the most massive simulation (Q1) derived from the CO (J=6-5) emission line over 250 random lines of sight, as well as 3σ contours for the observed

range of linewidths. In particular, we show

$$M_{\text{dyn}} = k \frac{\sigma^2 R}{G \sin(i)} \quad (5.3)$$

where we use an adopted k of 8/3 and assume an average inclination angle of 30° . We plot the total mass of the host galaxy (within the central 2 kpc) throughout its evolution, including the multi-phase ISM, dark matter, stars, and black holes. We additionally plot the ratio of the median derived dynamical mass to the total mass enclosed. The dynamical mass is derived from the width of the CO (J=6-5) line as the CO excitation peaks at the J=6 level, and this transition thus best trace the bulk of the molecular gas during the quasar phase of our simulated galaxy. We note, however, that the line widths from lower transition lines do not deviate much from these trends.

During the hierarchical buildup of the host galaxy (pre-quasar phase), the gas is still highly dynamical, and not completely virialized. This results in large CO line widths, and consequently derived dynamical masses which largely overestimate the true mass. During this time, the typical derived dynamical mass results in an overestimate of the true mass by a factor of $\sim 2 - 5$. As the gas becomes more rotationally supported during the quasar phase, the CO (J=6-5) line width serves as a better tracer of the mass enclosed. These results are consistent with similar derivations by Greve & Sommer-Larsen (2006) who found that CO can serve as an accurate dynamical mass tracer in merger simulations to within 20%.

An important point from Figure 5.14 is that a large sightline-dependent range of values are possible for derived dynamical masses. While the median line widths provide reasonable estimates of the true mass, many lines of sight permit significant underestimates. The radiative transfer simulations presented here may then bring some resolution between CO observations which are suggestive of a strong evolution in the $M_{\text{BH}}-M_{\text{bulge}}$ relation at high redshift, and models

which imply a lesser evolution between present epochs and early times. Figure 5.14 shows that a large range of dynamical masses may be inferred simply based on observed viewing angle. While the median CO line widths accurately traces the enclosed mass for the bulk of the quasar phase, potential selection effects (Figures 5.12 and 5.13) may bias masses derived from CO line widths from quasars toward an underestimate of the true mass. These model results are consistent with the recent study by Wu (2007) who found that CO line widths provided a particularly poor estimate of bulge velocity dispersion for local Seyferts with line widths narrower than $\sim 400 \text{ km s}^{-1}$ (FWHM; $\sigma \sim 170 \text{ km s}^{-1}$). In contrast, the inclination-corrected CO line width was found to correspond well with the bulge velocity dispersion.

5.9 Comparisons to Other High Redshift Populations

A natural question which arises from this work is, how do the CO properties of these extreme $z \sim 6$ objects relate to other known starburst and AGN populations? Two extreme high redshift galaxy populations which may serve as interesting comparisons are: 1. Optically selected quasars; and 2. Dusty submillimeter selected galaxies at $z \sim 2$ (see respective reviews by Solomon & Vanden Bout, 2005, and Blain et al. 2002).

5.9.1 Quasars

Only a handful of quasars have been detected in molecular line emission owing to beam dilution and limited sensitivity at millimeter and submillimeter wavelengths. As of the writing of the recent review by Solomon & Vanden Bout (2005), there have been about 16 quasars at $z \gtrsim 1$ for which molecular gas emission properties have been published.

Deciphering the molecular gas morphology remains an issue for most quasars

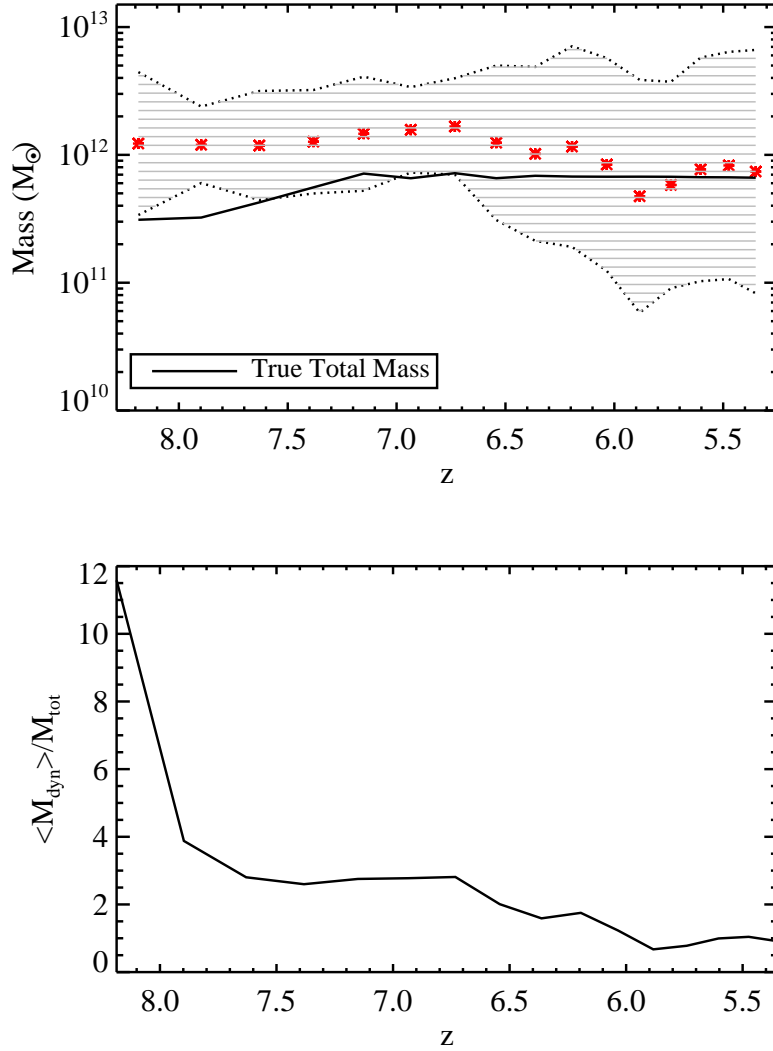


Figure 5.14 *Top*: Median dynamical masses derived from line widths over 250 random sightlines through the hierarchical buildup and evolution of quasar host galaxy (red crosses). The shaded region represents the 3σ range of sightline-dependent derived dynamical masses, and the solid line the true total mass within the central 2 kpc. The dynamical masses are derived assuming an inclination angle of 30° , and a molecular spatial extent of 2 kpc. *Bottom*: Ratio of median derived dynamical mass to total mass. During the hierarchical buildup and early quasar phase, much of the gas is highly dynamical; consequently, derived dynamical masses from CO line widths do a poor job representing the true enclosed mass, typically overestimating by factors of 2-5. As the gas virializes the inclination angle and CO line widths both flatten out, and the derived mass becomes a

since the majority of them have been detected in molecular line emission with the help of gravitational lensing, resulting in multiple imaging. The spatial extent of the molecular emission in most quasars appears to range from $\sim 1 - 5$ kpc (Solomon & Vanden Bout, 2005), similar to the simulations presented here as well as observations of J1148+5251. Multiple CO emission peaks are detected less often, though it is not clear whether or not this is a spatial resolution issue. Of seven imaged quasars listed in the recent review by Solomon & Vanden Bout (2005), three have clear CO companions (including J1148+5251), with distances in the emission peaks ranging from 1.7-8.7 kpc (e.g., Carilli et al. 2002). The more sensitive, and higher spatial resolution observations that will be routinely achieved with ALMA will clarify the CO morphology of quasars.

The CO excitation conditions that have been measured in quasars have primarily been at $z \sim 2$. Barvainis et al. (1997) find that the CO is substantially excited in the Cloverleaf quasar (H1413+117, $z \sim 2.5$) through the J=7 level. High spatial resolution observations of two $z \sim 4$ quasars by Carilli et al. (2002) find similar excitation conditions in CO, both of which have multiple CO emission peaks in their morphology. More recent large velocity gradient modeling of $z \sim 4.7$ quasar BR 1202-0725 also found a CO SED that peaks at J=7 (Riechers et al. 2006b). The high excitation conditions observed in quasars are indicative of extremely warm and dense molecular gas heated by ongoing star formation, and are consistent with active star formation during the quasar phase.

The quasar sample of Solomon & Vanden Bout reports CO line widths in high- z quasars ranging from roughly $\sigma \sim 100 - 250 \text{ km s}^{-1}$ (Carilli & Wang 2006). Large bandwidth observations with the 4GHz COBRA correlator on OVRO by Hainline et al. (2004) of a sample of three $z=2-3$ quasars showed similarly narrow CO line width.

While these are in apparent contrast to the large mean line widths in $z \sim 6$ quasars reported here, the narrower line widths of quasars from $2 \leq z \leq 5$ may be simply explained by the evolution of V_c with decreasing redshift. Namely, while quasars from $2 \leq z \leq 5$ appear to form in halos of comparable mass to those at $z \sim 6$ (Croom et al. 2005; Shen et al. 2007), the expected circular velocity will naturally be lower than their $z \sim 6$ analogs by a factor of $\sqrt{(1+z)/(1+6)}$. As a result, the circular velocity for these halos at $z \sim 2$ would be of order $\sigma \sim 300\text{--}350 \text{ km s}^{-1}$, consistent with clustering measurements of $z \sim 2$ quasars (e.g., Croom et al. 2005; Porciani & Norberg 2006; Myers et al. 2006; Hopkins et al. 2007i) and studies of the quasar proximity effect (e.g., Faucher-Giguere et al. 2007; Kim & Croft 2007; Nascimento Guimaraes et al. 2007), and slightly larger than measured CO line widths (Solomon & Vanden Bout, 2005), though it is possible that there is a potential selection bias toward quasars with narrow line widths (§ 5.7.3) at lower redshifts as well.

In this context, we emphasize that the simulations presented here *do not* predict large ($\sigma \sim 500\text{--}800 \text{ km s}^{-1}$) line widths for quasars which form at lower (e.g., $z \sim 2$) redshift, even if they form in halos of comparable mass to luminous sources at $z \sim 6$. To illustrate this, we examine the predicted CO line widths of the binary merger simulation of Narayanan et al. (2006a; also presented in Robertson et al. 2006a). The circular velocity of the progenitor galaxies was $V_c=160 \text{ km s}^{-1}$. The total masses of the progenitor galaxies in this example was $4.8 \times 10^{11} h^{-1} M_\odot$, and the final merger produced a central black hole mass of $\sim 5 \times 10^7 h^{-1} M_\odot$. The σ of the unresolved CO (J=1-0) line profile ranges from 100-150 km s^{-1} during the peak of the quasar phase, over three orthogonal viewing angles, consistent with CO line width measurements of $z \sim 2$ quasars, and reflective of the host virial velocity.

These models then suggest a self-consistent picture which naturally explains the evolution of CO line widths as function of redshift in terms of the circular velocity of the quasar host galaxy halo. Future modeling will need to quantify the extent of potential molecular disk-driven selection effects (e.g., § 5.7.3) for quasars at lower redshifts ($z \sim 2-4$). Indeed other works have suggested that quasars in this redshift range may be observed at a preferred shallow range of viewing angles as evidenced by their CO line widths (e.g., Carilli & Wang 2006).

5.9.2 Submillimeter Galaxies

Submillimeter galaxies (SMGs) represent a class of massive, dusty starbursts at $z \sim 2$ largely detected by blind surveys with the SCUBA and MAMBO bolometers. Typical infrared luminosities in these sources of $\sim 10^{13} L_{\odot}$ correspond to a SFR of $\gtrsim 1000 M_{\odot} \text{yr}^{-1}$, assuming an insignificant AGN contribution (Smail 2006). X-ray and IR studies have shown that these galaxies are known to contain embedded AGN, although their relative contribution to the bolometric luminosity is uncertain (Alexander et al. 2005a,b; Donley et al. 2005; Polletta et al. 2006). Optical morphologies of SMGs indicate that many are interacting and/or mergers (Chapman et al. 2004). Recent CO morphologies and emission line profiles have furthered this scenario (Greve et al. 2005; Tacconi et al. 2006). Many studies have pointed to a picture in which SMGs may be ongoing mergers at $z \sim 2$, though in a pre-quasar phase (e.g., Blain et al. 2002). This combined with the fact that SMGs are the most massive and actively star forming galaxy population at $z \sim 2$ make SMGs an interesting comparative for our simulated $z \sim 6$ quasar.

The excitation characteristics have been observed in multiple CO emission lines for only one case: $z=2.5$ SMG SMM J16359+6612. In this galaxy, the CO flux density peaks at $J=5$ (Weiß et al. 2005a), consistent with highly excited gas. The excitation conditions are similar to those seen in our simulations when the SFRs

are comparable.

The molecular morphology in SMGs closely resembles the extended CO emission seen in simulations and observations of J1148+5251, as well as in the pre-quasar phase galaxy in our simulations at $z=7-10$. The average CO FWHM radius in the recent Tacconi et al. (2006) sample is 2 kpc. The large spatial extent of CO emission in SMGs combined with an apparent lack of strong quasar activity has been interpreted as being the consequence of extremely massive and gas rich galaxy mergers early in the evolution of the galaxy, and prior to the quasar phase (e.g., Tacconi et al. 2006). Indeed, if SMGs form through hierarchical mergers, then the models presented here suggest that the spatially extended and disturbed CO morphologies seen in SMGs further indicate that these galaxies may be mergers prior to an optical quasar phase (e.g., Figure 5.4).

The CO line widths of SMGs are more enigmatic. The average CO emission line from an SMG is typically about double the width of that from a quasar of similar redshifts (e.g., Carilli & Wang 2006; Greve et al. 2005; Tacconi et al. 2006). The average line width in SMGs is $\sigma \sim 330 \text{ km s}^{-1}$ (FWHM $\sim 780 \text{ km s}^{-1}$), compared to a mean σ of 130 km s^{-1} seen in $z \sim 2$ quasars (Greve et al. 2005). Within the context of the models presented in this work, a number of physical motivations for these differing line widths may be at play.

First, in our models the mean line widths from galaxies with virialized cold gas are seen to roughly correspond with the circular velocity of a host halo. When comparing galaxies of similar redshifts, if SMGs are dynamically relaxed, this would imply that SMGs may originate in more massive halos than quasars. Indeed, clustering measurements made by Blain et al. (2004) have suggested that SMGs are hosted by halos slightly larger than quasars at comparable redshifts. If SMGs reside in halos $\gtrsim 4$ times more massive than typical quasar host galaxies,

the difference in CO line widths may be accounted for.

An alternative explanation for the line widths may arise from an evolutionary standpoint. Specifically, as Figure 5.8 shows, there is a typical drop in CO line width by a factor of ~ 2 close to the quasar phase of a merging galaxy system. This owes to gas in the violent environs of a galaxy merger becoming rotationally supported late in the evolution of the merger. If SMGs are a class of objects hosted by halos of similar mass to their quasar counterparts, then it may be that SMGs are simply massive mergers at $z \sim 2$ prior to their active quasar phase. Certainly CO line profiles and morphologies from SMGs are consistent with merging activity (Greve et al. 2005; Tacconi et al. 2006; Narayanan et al. 2006a, 2007b). Moreover, numerical simulations of merging galaxies coupled with self-consistent radiative transfer solutions have pointed to a picture in which SMGs may be mergers caught in a phase of massive black hole growth, though prior to an optical quasar phase (Chakrabarti et al. 2007b).

Other authors have suggested that SMGs may be similar to quasars in their place in galaxy evolution, but simply viewed more edge-on. Carilli & Wang (2004) suggested that if these $z \sim 2$ galaxy populations are truly of the same class, then one can infer a mean viewing angle of $\sim 13^\circ$ for quasars, whereas SMGs are more likely randomly oriented.

Finally, it may be that the CO emission properties of SMGs are not explained by physical models such as those presented in this work. If, for example, the massive star formation rates are fueled at least in part by accretion of gas from the host halo (which is seen to occur for at least some galaxies in cosmological simulations; see e.g., Finlator et al. 2006), the CO line widths may not reflect the circular velocity of the system, at least during phases of elevated star formation, as they do in merging galaxies.

In summary, correspondence between some observed trends of molecular line emission in the models of hierarchical $z \sim 6$ quasar formation and SMGs which form at later times suggest that it is plausible that SMGs fall naturally into a merger-driven evolutionary sequence, though, at least from molecular line diagnostics alone, its location on this sequence is not completely clear. Of course, alternative scenarios cannot be ruled out here. Further models of hierarchical galaxy mergers appropriate for $z \sim 2$ will have to be examined in order to further quantify the relation of CO emission properties to the evolution of SMGs.

5.10 Chapter Summary and Conclusions

We have applied non-LTE radiative transfer simulations to cosmological and hydrodynamic galaxy formation simulations to predict the CO emission from representative $z \sim 6$ quasars that are modeled to form hierarchically in massive $10^{12} - 10^{13} M_{\odot}$ halos. We made predictions concerning the CO excitation patterns, morphologies, and line widths in this extreme class of objects. We further made broad comparisons to the only current CO detection at $z \gtrsim 6$, J1148+5251 at $z=6.42$. Our main results are the following:

1. Owing to very warm and dense conditions in the molecular ISM, the CO flux density is predicted to peak at the J=8 level during the early, hierarchical formation process of the quasar host galaxy ($z \sim 8$), when the SFR can be as high as $\sim 10^4 M_{\odot} \text{yr}^{-1}$. During the peak quasar phase, the central AGN reduces the nuclear starburst, and the SFR drops to $\sim 10^2 M_{\odot} \text{yr}^{-1}$. Consequently, the CO flux density peaks at the J=5-6 level. These excitation conditions are indicative of an ongoing starburst, and are consistent with observations of J1148+5251. As the gas becomes more diffuse and the starburst dies down in the post-quasar phase ($z \lesssim 6$), the peak in the CO flux is

predicted to drop to $J \approx 3$.

2. The CO morphologies of $z \sim 6$ quasars may exhibit multiple emission peaks during the active quasar phase, owing to separated peaks of high density emission that have not yet coalesced. The multiple emission peaks in the morphology of the CO ($J=3-2$) gas during the quasar phase of our simulations are very similar to observations of J1148+5251, and are robust along many viewing angles. These results imply that a merger-driven formation scenario for $z \sim 6$ quasars produces CO morphologies consistent with that of J1148+5251.
3. On average, the CO line widths from quasars at $z \sim 6$ are reflective of the virial velocity of the host halo, though there exists a large sightline dependent dispersion in line widths. During the hierarchical buildup of the host galaxy, the median line widths are roughly twice the virial velocity, and settle to the virial velocity during the quasar phase. During the quasar phase, the sightline-averaged line width for the $\sim 10^{13} M_{\odot}$ halo is $\sim 500 - 800 \text{ km s}^{-1}$. In the lowest mass halo ($\sim 10^{12} M_{\odot}$) the sightline averaged line width is $\sim 300 \text{ km s}^{-1}$.
4. A fraction of sightlines in each model is compatible with observations, and is a strong function of halo mass. Specifically, the number of sightlines with narrow line widths compatible with observations increases with decreasing halo mass. The most massive $\sim 10^{13} M_{\odot}$ halo shows $\sim 2 - 3\%$ of sightlines compatible with observations. The $\sim 10^{12} M_{\odot}$ halo has line widths similar to observations of J1148+5251 $\sim 10\%$ of the time. The percentage of sightlines compatible with observations increase owing to selection effects (next point).

5. Quasars at $z \sim 6$ selected for optical luminosity may preferentially be in a face-on configuration as this provides the least obscuration of the central black hole. In these configurations, the CO line widths are narrower, thus causing quasars selected for optical luminosity to preferentially have narrower line widths than their sightline averaged values. The fraction of sightlines with line widths compatible with observations increases to 10-25% when considering quasars selected for optical luminosity. This suggests that these models may be in agreement with observations if J1148+5251 is being observed in a face-on configuration. A direct consequence of these selection effects is that in order to observe the full dispersion in CO line widths in $z \sim 6$ quasars, observations must probe quasars with edge-on molecular disks (which are typically lower on the optical luminosity function).
6. Because of the evolution of V_c with redshift of halos of similar mass, quasars which form in $\sim 10^{12} - 10^{13} M_\odot$ halos (as they are thought to; see e.g., Croom et al. 2005; Shen et al. 2007) at lower redshift will naturally have smaller line widths, compatible with observations. We explicitly show this by examining the line widths of a binary merger simulation appropriate for present epochs. In this light, the simulations presented here *do not* predict large ($\sigma \sim 500 - 800 \text{ km s}^{-1}$) CO line widths for quasars which form at lower redshifts, but rather a suggestive self-consistent model for the potential origin of CO line widths in quasars at both low and high redshift.
7. Our merger-driven model for quasar formation predicts a host galaxy that lies on the $M_{\text{BH}}-M_{\text{bulge}}$ relation during the active quasar phase (Li et al. 2007a; Robertson et al 2006a; Hopkins et al. 2007a). During the hierarchi-

cal buildup of the host galaxy, the median CO line width tends to typically overestimate the dynamical mass by a factor of 2-5 as much of the gas is highly dynamical, and not virialized. During the quasar phase, dynamical masses derived from the median line widths are a better representation of the true mass. There is a large range in derived dynamical masses coincident with the large sightline-dependent range of line widths seen at a given time. If selection effects are in place such that molecular disks in observed high- z quasars are typically close to face-on, CO-derived dynamical masses will preferentially underestimate the true mass unless the shallow viewing angle is accounted for.

CHAPTER 6

WARM-DENSE MOLECULAR GAS IN THE ISM OF GALAXIES

I think maybe you should be an observer instead...

-Fred Lo after hearing my talk on models of CO emission in $z \sim 6$ quasars

6.1 Chapter Abstract

The role of star formation in luminous and ultraluminous infrared galaxies (LIRGs, $L_{\text{IR}} \geq 10^{11} L_{\odot}$; ULIRGs $L_{\text{IR}} \geq 10^{12} L_{\odot}$) is a hotly debated issue: while it is clear that starbursts play a large role in powering the IR luminosity in these galaxies, the relative importance of possible enshrouded AGNs is unknown. It is therefore important to better understand the role of star forming gas in contributing to the infrared luminosity in IR-bright galaxies. The J=3 level of ^{12}CO lies 33K above ground and has a critical density of $\sim 10^4 \text{ cm}^{-3}$. The $^{12}\text{CO}(J=3-2)$ line thus serves as an effective tracer for warm-dense molecular gas heated by active star formation. Here we report on $^{12}\text{CO}(J=3-2)$ observations of 17 starburst spirals, LIRGs and ULIRGs which we obtained with the Heinrich Hertz Submillimeter Telescope on Mt. Graham, Arizona. Our main results are the following: 1. We find a nearly linear relation between the infrared luminosity and warm-dense molecular gas such that the infrared luminosity increases as the warm-dense molecular gas to the power 0.92; We interpret this to be roughly consistent with the recent results of Gao & Solomon (2004a,b). 2. We find $L_{\text{IR}}/M_{\text{H}_2\text{warm-dense}}$ ratios ranging from ~ 38 to $\sim 482 L_{\odot}/M_{\odot}$ using a modified CO-H₂ conversion factor of $8.3 \times 10^{19} \text{ cm}^{-2} (\text{K km s}^{-1})^{-1}$ derived in this paper.

6.2 Chapter Introduction

An important result from the *IRAS* observatory was the discovery of large numbers of galaxies which emit prodigiously in the infrared. The *IRAS* Bright Galaxy Survey (*BGS*, flux limited, $f_{60\mu m} \geq 5.4$ Jy; Soifer et al 1987, 1989) reported on infrared fluxes of 330 galaxies.

An interesting subset of these objects, coined Luminous Infrared Galaxies (LIRGs, $L_{\text{IR}} \geq 10^{11} L_{\odot}$), and Ultraluminous Infrared Galaxies (ULIRGs, $L_{\text{IR}} \geq 10^{12} L_{\odot}$), serve as a unique tool to better understand the temporal evolution of starburst phenomena (the field is reviewed by Sanders & Mirabel, 1996). As evidenced by morphological studies, ULIRGs are likely the product of galaxy mergers, or strongly interacting galaxies (Sanders et al. 1988a, Lawrence et al. 1991, Leech et al. 1994). While many LIRGs are also merger remnants, they can also be gas and/or dust-rich spirals.

The source of infrared luminosity in ULIRGs and high luminosity LIRGs has been under contention for quite some time. The luminous activity from the central regions in LIRGs and ULIRGs suggests either a massive starburst, dust enshrouded AGN, or some combination of the two. High resolution ($\sim 1''$) millimeter observations have shown large amounts of molecular gas concentrated in the nuclear regions of these galaxies (e.g. Scoville et al., 1989, Bryant & Scoville 1999). Numerical simulations have shown that galaxy mergers can efficiently drive gas toward the nuclear regions of the remnants (Barnes & Hernquist 1992, Mihos & Hernquist 1996). Nearly all bright *IRAS* galaxies have been found to be rich in molecular gas (Tinney et al. 1990, Sanders, Scoville & Soifer 1991, hereafter SSS91). This molecular gas is not only the nascent birthplace for massive star formation, but may also act as fuel for a hidden AGN. Additionally, the processes may be linked. Several authors have suggested that the large amounts of gas may

lead to the buildup of large nuclear star clusters which may augment the formation for a central AGN (Scoville et al. 1989, Surace et al. 1998, Evans et al. 1999, Scoville et al. 2000).

Strong constraints must be placed on the interstellar medium (ISM) in LIRGs and ULIRGs in order to better understand the source of luminosity and their role in the evolutionary sequence of galaxies. Rotational transitions in carbon monoxide are often used as a tracer for molecular gas in the ISM. The first extensive studies of the molecular gas in (U)LIRGs via ^{12}CO (hereafter, CO) line emission were presented by Tinney et al. (1990), and SSS91. These authors analyzed CO (J=1-0) emission from a sample galaxies with $L_{\text{IR}} \gtrsim 10^{10} L_{\odot}$.

Of particular interest in the ISM is the properties of warm, dense gas, as it is this gas that directly traces star formation. Because CO (J=1-0) can be excited at relatively low temperatures (~ 5 K above ground) and densities ($\sim 10^2$ - 10^3 cm^{-3}), it serves as a good tracer for total molecular gas, but is relatively insensitive to the warmer, denser gas directly involved in the star formation process. In contrast, high lying rotational transitions of CO directly trace warm, dense gas. The J=3 level of CO lies 33K above ground and has a relatively high critical density of $1.5 \times 10^4 \text{ cm}^{-3}$. The CO (J=3-2) transition can serve as a tracer of dense molecular gas heated by active star formation, and thus as a diagnostic for the starburst phenomena in these galaxies. Sensitivity to the presence of dense gas is important in determining the evolutionary state of LIRGs/ULIRGs. For example, in the well studied galaxy, Arp 220, Solomon, Downes & Radford (1992) presented single dish data taken in CO (J=1-0), HCO^+ (J=1-0), and HCN (J=1-0). The CO (J=1-0) spectra shows a single peak while the emission lines from the high-density tracers HCO^+ and HCN each showed two peaks. Taniguchi & Shioya (1998) discussed the double-horned profile seen in the high-density tracers HCO^+ and HCN as

corresponding to the starburst regions associated with two separate nuclei in this galaxy. This model was further supported by high resolution observations by Sakamoto et al. (1999). It is therefore evident that high-density gas tracers are vital to the understanding of molecular gas in LIRGs and ULIRGs.

Several previous surveys of LIRGs and ULIRGs have relied on millimeter-wave studies of HCN ($J=1-0$) in order to probe the properties of the dense molecular component of these objects (e.g. Solomon, Downes & Radford, 1992, Gao & Solomon 2004b, and references therein). However, the low lying levels of HCN do not necessarily trace gas that is both *warm and dense*. For example, the $J=1-0$ emission of HCN traces densities of $n(\text{H}_2) \gtrsim 3 \times 10^4 \text{cm}^{-3}$; however, it only lies at a temperature of $\sim 4.25\text{K}$ above the ground state. Thus, while observations of this transition will reveal the physical conditions of dense molecular gas, both cool and warm, it does not necessarily probe the gas heated by active star formation. In order to study properties of the gas *directly involved in star formation*, one must look toward lines that have a high excitation temperature, as well as a high critical density.

While there have been numerous studies of CO ($J=1-0$) emission (Sanders & Mirabel, 1996 and references therein), there are relatively few studies of LIRGs and ULIRGs in higher lying CO transitions. Rigopoulou et al (1996) reported a CO ($J=2-1$) survey of 6 ULIRGs, and Yao et al. (2003) presented the first survey of CO($J=3-2$) emission of LIRGs and ULIRGs from the Scuba Local Universe Galaxy Survey (SLUGS). Recent high-resolution studies of warm-dense molecular gas in individual LIRGs have been performed by Iono et al. (2004) and Wang et al. (2004).

In order to better understand the role of star formation in LIRGs and ULIRGs, and how it varies with infrared luminosity, we have conducted a survey of CO

(J=3-2) emission as a tracer for warm-dense molecular gas in 17 normal starburst spirals, LIRGs and ULIRGs detected by the *IRAS BGS* survey. We made these observations at the 10m Heinrich Hertz Submillimeter Telescope (HHSMT) on Mt. Graham. A similar study has been recently performed by Gao & Solomon (2004a,b), using HCN (J=1-0) as a tracer for dense molecular gas. In § 6.3 we present the observations and data; in § 6.4 we discuss the excitation conditions via the CO (J=3-2)/CO(J=1-0) line ratio; in § 6.5 we interpret the line profiles; in § 6.6 we discuss the data with respect to the dominant source of infrared luminosity (starburst vs. AGN), and in § 6.7 we summarize.

6.3 Selection and Observations

The galaxies in this study were selected from the *IRAS BGS* sample which was flux limited at $f_{60\mu m} \geq 5.4$ Jy. All but two of the objects observed here have previously shown strong CO (J=1-0) emission (Mirabel et al. 1990, Tinney et al. 1990, SSS91, Yao et al. 2004) and were therefore known to be rich in molecular gas. The galaxies were originally selected in their respective CO (J=1-0) surveys from the *IRAS BGS* surveys, and in the case of Yao et al. (2004), the SLUGS survey. The galaxies in these papers were chosen for position on the sky, and thus not biased for any particular galaxy properties. Our goal was to observe a number of galaxies over a wide IR luminosity range: we observed 17 galaxies ranging in IR luminosity from $10.41 < \log(L_{\text{IR}}) < 12.39$, spanning from starburst spiral galaxies to ULIRGs. The infrared luminosities and $60\mu m$ fluxes may be found in Table 1. All of the galaxies were chosen such that they were not redshifted out of the atmospheric transmission windows near 345 GHz. We additionally took care to observe objects whose CO emitting region would be unresolved within the 23'' HHSMT beam (see also §3). We selected objects with a declination greater than

-1°. The full list of objects observed can be found in Table 1.

We observed our sample of 17 galaxies on the HHSMT over three runs in November 2003, March 2004 and January 2005. We used the facility 345 GHz SIS receiver utilizing both polarizations. The acousto-optical spectrometer (AOS) was used as the backend, with a usable bandwidth of 1GHz, and velocity resolution of 0.85 km s^{-1} . For calibration sources, we observed Orion, W3OH and IRC10216. Telescope pointing was checked every hour with observations of planets. The observations were made in beam switching mode with a throw of $60''$, and a chopping frequency of 4 Hz. Typical integration time was ~ 4 hours which yielded signal to noise ratios of about 10 in most sources. Note, that due to time constraints, we were not able to achieve this level of S/N for every object. Additionally, some of the higher luminosity objects fell at a redshift such that their observed frequencies were near atmospheric water lines, decreasing the S/N. The weather conditions were good with a typical τ at 225 GHz of ~ 0.1 . We detected CO (J=3-2) emission in 15 out of the 17 galaxies in our sample¹.

The data reduction was performed using the GILDAS CLASS package. We subtracted a linear baseline from the data, excluding points in the emission line from the fit. The data were then co-added, weighted by the rms noise of each spectrum. We smoothed the data to a resolution between 3.2 km s^{-1} and 25.6 km s^{-1} , depending on the noise levels. We converted from an antenna temperature, T_A , to main beam temperature, T_{MB} , by scaling by the main beam efficiency, η_{mb} , using $T_{MB} = T_A / \eta_{mb}$. Main beam efficiencies were measured to be ~ 0.50 at the CO (J=3-2) line frequency during the March 2004 observing run. Observing parameters may be found in Table 1.

¹Please note that while we did not detect emission in NGC 3583, Yao et al. (2003) detected emission with peak temperature of $\sim 0.1 \text{ K}$. Baseline problems in our data prevented us from ascertaining if we saw a line or simply baseline ripple.

While the galaxies were all resolved within our 23'' beam, the primary nuclear gas and dust emitting regions were not. In Figure 6.1-Figure 6.4, we show the HHSMT beamprint overlaid on the optical images taken from the *Digitized Sky Survey*² and the 2MASS images taken from the *2-Micron All Sky Survey*. In the same Figures we show the CO (J=3-2) spectrum we obtained for each object in this study. The objects are arranged in order of increasing L_{IR} .

6.4 CO (J=3-2)/(J=1-0) Line Ratio

The ratio of intensities (K km s^{-1}) of the CO (J=3-2) line to the CO (J=1-0) line, R_3 , serves as a probe of the excitation temperature and optical depth of the emitting gas. A high ratio ($\gtrsim 1$) indicates the gas is warm, and optically thin.

Because the CO (J=3-2) and (J=1-0) observations were taken at different telescopes with different beam sizes, certain considerations must be taken into account when comparing the line intensities. Both the beam size, b , and angular extent of the sources on the sky, s , play a role in determining the ratio:

$$R_3 = \frac{I_{32}(s^2 + b_{32}^2)}{I_{10}(s^2 + b_{10}^2)} \quad (6.1)$$

Where I is the intensity (K km s^{-1}):

$$I_{\text{CO}} = \int T_{\text{mb}}(\text{CO}) dV \quad (6.2)$$

In recent high resolution (2''-3'') millimeter-wave observations of 7 LIRGs, Bryant & Scoville (1999) find that nearly all of the detected CO (J=1-0) emission is concentrated within the central 1.6 kpc in 6 of the 7 objects. Because it is unlikely that

²The Digitized Sky Surveys were produced at the Space Telescope Science Institute under U.S. Government grant NAG W-2166. The images of these surveys are based on photographic data obtained using the Oschin Schmidt Telescope on Palomar Mountain and the UK Schmidt Telescope. The plates were processed into the present compressed digital form with the permission of these institutions.

there will be significant CO (J=3-2) emission where there is no CO (J=1-0), we assume that all of the emitting gas in our sample is confined within the same region, and, with the distances to each object, compute the angular extent of emitting gas for each object.

The CO (J=1-0) data were taken at the IRAM 30m, Kitt Peak 12m, the Nobeyama Radio Observatory, and the Swedish-European Submillimeter Telescope (SEST) (Mirabel et al. 1990, Tinney et al. 1990, SSS91, Yao et al. 2003). The beam size of the 10m HHSMT at 345 GHz is $\sim 23''$.

The R_3 ratios are presented in Table 2. Our mean value of R_3 is 0.50. In a survey of CO (J=3-2) emission in 28 nearby galaxies, Mauersberger et al. (1999) found a mean value of R_3 of 0.63. Similarly, Yao et al. (2003) found a mean R_3 of 0.66 in their survey of 60 LIRGs/ULIRGs. The average R_3 for our objects is larger than the average value seen in Galactic molecular clouds of 0.4 (Sanders et al. 1993). The spread in the ratios in Table 2 suggest a variety of excitation conditions in the molecular gas in our sample of galaxies. As we will show, this will become quite important in Chapter 7.

6.5 Line Profiles

The observed line profiles allow us to gain a better understanding of the kinematics of the emitting molecular gas. Krugel et al. (1990) examined simple models of galaxies in order to explain their line profiles. They assumed the gas was distributed in a disk, and constructed isothermal models of galaxies gridded in radius and azimuth. They allowed the clouds to rotate around the center like a rigid body out to a distance, R_R , set as a free parameter, and then forced the velocity to 200 km s^{-1} . We use the results of these models to illustrate possible kinematic signatures found in our observed line profiles. The line profiles of the objects in our

sample tend to fall into three general categories: single Gaussian (e.g. NGC 2276), double-peaked (e.g. Arp220), and three component (e.g. NGC3079). These can all be explained by models in which the beam is larger than the emitting region, and a part of the flat rotation curve is included. While it is clear from Figures 6.1-6.4 that we have resolved the optical emitting region of all of the galaxies in this sample, as described in § 6.4, the bulk of the CO-emitting gas likely remains unresolved within the $23''$ beam. Here, we discuss the line profiles of the objects in this study, and how they relate to other observations from the literature.

Single-Gaussian Profiles: The single Gaussian line profile has a width which varies based on viewing angle: if the galaxy is face on, then the line width is dominated by the turbulent velocity among the emitting clouds. If, however, there is an inclination angle of $i < 90^\circ$, then the effects of the rotation of the galaxy are evident in the line width.

NGC 7817: The optical and 2MASS images (Figures 6.1-6.4) indicate our observations of the circumnuclear star-forming region are unresolved in this spiral galaxy. The CO (J=1-0) line profile appears to have a possible double-peak which would be consistent with the fact that we are viewing this galaxy slightly edge-on (SSS91).

NGC 2276, NGC6701: The narrow single-Gaussian line profiles for these galaxies are likely due to viewing these spirals \sim face on.

NGC 834: The CO (J=1-0) profile in this spiral (Chini, Krugel & Lemke 1996, Hattori et al. 2004) is difficult to interpret due to noise (SSS91, Young et al. 1995). It appears to be double-horned in CO (J=1-0). A large ring of star forming gas is seen in $H\alpha$ maps by Hattori et al. (2004): this ring may be the origin of the 1-0 double peak. This double peak may emerge in a CO (J=3-2) spectrum with a higher signal to noise ratio.

IRAS 23436+5257, IRAS 07251-0248: The emission lines presented here for these galaxies are the first to be published. The objects appear to be disturbed and/or interacting galaxies (Figures 6.1-6.4).

UGC 5101: The CO (J=3-2) spectrum presented here has an asymmetric profile with a high-velocity bulge. The HCN (J=1-0) line appears to be a more symmetric Gaussian (Gao & Solomon, 2004b). The CO (J=1-0) spectrum, in contrast has a clear double-horned profile (Solomon et al. 1997). Armus et al. (2004), discuss the presence of a buried AGN in this galaxy through the detection of [Ne V] 14.3 μ m line. Farrah et al. (2003) describe this object as having an enshrouded AGN which plays a large role in contributing to the near-IR flux, but becoming more negligible at longer wavelengths. Many other authors have discussed the possibility of an enshrouded AGN in this object (e.g. Imanishi, Dudley & Maloney, 2001, Imanishi et al. 2003, and references therein). Sanders et al. (1988) interpret the morphology as a late-stage merger. NICMOS images show only a single nucleus (Scoville et al. 2000), making it unlikely that the possible double-peak is due to individual nuclei from progenitor galaxies in a merger. High resolution mapping will help to interpret this line profile better.

IRAS 17208-0014: Gao & Solomon (2004a) present HCN (J=1-0) observations of this object, and Rigopoulou et al.(1996) present CO (J=2-1) observations of this object. Our profile appears consistent with both sets of data. The object has the optical spectrum of an HII region (Veilleux, Sanders & Kim. 1999). Scoville et al. (2000) and Farrah et al. (2003) classify IRAS 17208-0014 as being powered by a pure starburst, with little to no AGN component. NICMOS images show this galaxy to have a disturbed outer disk (Scoville et al. 2000).

Double Horned Profiles: The double-horned profile was evident in many of our objects as well. There are two distinct sub-categories: those with symmetric

peaks (e.g. NGC 3094 and Arp 220), and those where one peak is higher than the other (e.g. NGC 992). Krugel et al. model the symmetrical double-peaked objects as galaxies that are unresolved, with the bulk of the emitting gas confined to a circumnuclear ring. However, as was discussed in §1, and below, there may be alternative explanations for NGC 828 and Arp 220. The asymmetric double peak profile is more enigmatic. Krugel et al. suggest that if the gas is distributed symmetrically in the galaxy's disk, such profiles might arise if the observation is centered off the center of the disk. Alternatively, this profile may arise if the LIRG/ULIRG has two distinct nuclei from a merger, and the emitting molecular gas from one has a larger velocity dispersion than the other. A third scenario may arise from molecular outflows/dynamics (cf. Chapter 4), though we do not explore this possibility here.

NGC 3094: While our data for this object are sufficiently noisy that a double peak is not clear, higher resolution data from Yao et al. (2003) show the double peak to be evident. Imanishi (2000) classifies this object as having a highly obscured AGN.

NGC 992: While the CO (J=3-2) spectrum shows an asymmetric double-horned profile, the CO (J=1-0) profile is inconclusive. The general shape is similar, but noise dominates the features enough to make it difficult to ascertain whether or not there are two individual peaks in the 1-0 profile (SSS91). The galaxy appears to be a spiral (Chini, Krugel & Lemke 1996) undergoing a starburst (Ashby, Houck & Matthews, 1995). It is likely, following the modeling of Krugel et al., that the asymmetric line profile arises from a telescope pointing offset from the center of the CO disk.

NGC 828: Hattori et al. (2004) observed H α in this object, and describe it as a disturbed spiral galaxy. Kinematic evidence from high-resolution CO (J=1-

0) mapping suggest that this galaxy is an ongoing merger (Wang, Scoville & Sanders, 1991). CO (J=1-0) spectra (SSS91, Young et al. 1995) appear to display two peaks, although the double-horn is significantly more asymmetric than is seen in the two major peaks in the 3-2 spectra presented in this study.

NGC 7771: The observation may be slightly off from the optical center (*DSS* images, Figures 6.1-6.4), although the entire gas emitting region appears to remain unresolved within the beam (*2MASS* images, Figures 6.1-6.4). The CO (J=1-0) profile looks single-Gaussian. The double peak is likely due to the rotational structure of the galaxy.

Arp 220: This object is well studied in the literature, and we will only briefly discuss the line profile. As discussed in §1, the CO (J=1-0) spectrum of Arp 220 shows a single Gaussian peak, while the spectrum from high-density tracers (e.g. HCN J=1-0, CO J=3-2) reveal a double peak. The double peaks are interpreted to belong to each nuclei of the progenitor galaxies (Taniguchi & Shioya, 1998).

Triple-Peaked Profiles: Of our sample, NGC 3079 and NGC 6286 were best fit by three Gaussians; When fit to a single Gaussian, the FWHM's of these objects are $\sim 450 \text{ km s}^{-1}$. Krugel et al. observed a similar feature in the starburst galaxy, Mrk 1034, and modeled this as the spectral signature of a resolved galaxy where the inclination was such that both the central core, and extended gas with a flat rotation curve were being observed. This type of model produces the symmetric spectra seen in some of our observations, with the height of the central peak rising with respect to the two outer peaks as the inclination angle of the galaxy drops.

NGC 3079: This galaxy appears to fit the Krugel et al. model. Indeed the *2MASS* image shows that the beam extends significantly beyond the nuclear dust and gas emitting region. Tinney et al. (1990) presented a CO (J=1-0) spectrum of NGC 3079 compiled from a map; the profile appears to be an asymmetric double-

horn.

NGC 6286: The optical and 2MASS images reveal this observation to be of an edge on spiral. The asymmetric line profile was best fit by three Gaussians, although it is likely to simply be a double-horned spectrum that was observed off of the CO emission center. Indeed, the CO (J=1-0) line profile appears more symmetric, although the presence of more than one peak is difficult to determine given the noise (SSS91).

6.6 Source of IR Luminosity

The search for the driving source of high luminosity LIRGs and ULIRGs has been the subject of numerous observational and theoretical studies. While it is clear that there is active star formation in these objects, there remains evidence that dust-enshrouded active nuclei may play an important role as well (e.g. Yun & Scoville, 1998). In this section, we investigate the source of IR luminosity in the high-luminosity LIRGs and ULIRGs in our sample.

6.6.1 L_{IR} versus $L_{\text{CO J=3-2}}$

Correlations between infrared luminosity, and the luminosity due to high critical density tracers such as HCN have been discussed extensively (Solomon et al. 1992, Gao & Solomon 2004a,b). In a recent survey of normal (spiral) galaxies, LIRGs and ULIRGs, Gao & Solomon (2004b) found a linear relationship between L_{IR} and L_{HCN} over three orders of magnitude in infrared luminosity; this suggests that over the IR luminosity range spanned ($\log(L_{\text{IR}}) \lesssim 12.36$) the dense molecular gas (and thus, high mass star formation) is the dominant form of IR emission in both the LIRGs and ULIRGs. Additionally, Carilli et al. (2004) have shown for high redshift ULIRGs that the correlation between IR luminosity and HCN luminosity is nearly linear as well. These correlations suggest that at some level,

the dense interstellar medium and infrared luminosity in these objects are intertwined. Since CO (J=3-2) is an indicator of warm-dense gas, we use our dataset combined with those of other works to further test this hypothesis. Similar to the Gao & Solomon study, we probe infrared luminosities up to $\log(L_{\text{IR}})=12.39$.

We obtained values for L_{IR} from SSS91 and the *IRAS Revised Bright Galaxy Survey* (Sanders et al. 2003). We calculated L_{CO} using

$$L_{\text{CO}} \approx \pi / (4 \ln 2) \theta_{\text{mb}}^2 I_{32} d_L^2 (1+z)^{-3} \quad (6.3)$$

where θ_{mb} is the FWHM of the telescope Gaussian beam, and d_L is the luminosity distance. The data for L_{CO} are presented in Table 2. So that we may increase the number of objects in our analysis, we included 14 objects which we detected (please see caption of Figure 6.5 concerning exclusions), as well as 40 objects³ studied by Yao et al. (2003). In order to account for calibration differences in the data sets, we used Arp 220 as a common calibrator, and scaled our L_{CO} values such that the Arp 220 CO luminosities matched. This scaling factor was 0.26.

We present L_{IR} vs. $L_{\text{CO J=3-2}}$ in Figure 6.5. We fit the data using a linear χ^2 minimization routine, and recovered for the fit:

$$\log(L_{\text{IR}}) = 0.92(\pm 0.07) \times \log(L_{\text{CO J=3-2}}) + 3.28(\pm 0.60) \quad (6.4)$$

We interpret this result as consistent with the linear slope found by Gao & Solomon (2004a,b).

If the observed FIR emission is produced primarily by heating from massive stars, the star formation rate (SFR) can be given as a function of L_{IR} (Kennicutt, 1998):

$$\text{SFR}(\text{M}_{\odot} \text{ yr}^{-1}) \approx 2 \times 10^{-10} (L_{\text{IR}} / \text{L}_{\odot}) \quad (6.5)$$

³All the objects for which Sanders et al. 2003 reported an infrared luminosity

Previous studies of the relationship between L_{IR} and $L_{\text{CO } J=1-0}$ have found a non-linear relationship such that the infrared luminosity increases as the CO ($J=1-0$) luminosity to the ~ 1.25 . Because $L_{\text{CO } J=1-0}$ is proportional to the total molecular gas mass (Appendix A of SSS91), this has been interpreted as an increase in star formation efficiency (SFE), defined as the SFR over the total molecular gas mass, as a function of SFR (e.g. Solomon et al. 1992). $L_{\text{IR}}/\text{CO}(J=1-0)$ serves as a tracer for star formation efficiency as a function of all available molecular gas. $L_{\text{IR}}/\text{HCN}(J=1-0)$ is canonically interpreted as a tracer for SFE as a function of all available *dense, star-forming gas* (e.g. Gao & Solomon, 2004b). In contrast, CO($J=3-2$) traces warm, dense gas heated by embedded stars (§ 6.2) and thus $L_{\text{IR}}/\text{CO}(J=3-2)$ probes the infrared luminosity as a function of *recent star formation*. In light of these standard interpretations, it follows then, that the linear relationship seen between L_{IR} and L_{HCN} implies that the SFR per unit *dense* molecular gas mass remains constant through $\log(L_{\text{IR}}) \lesssim 12.3$; this result is confirmed by our observed relationship between L_{IR} and $L_{\text{CO } J=3-2}$ which shows a nearly constant SFR as a function of warm-dense molecular gas heated by active star formation. These observations strengthen the conclusion of Gao & Solomon (2004b) that the IR luminosity in LIRGs and ULIRGs up to an IR luminosity of at least $\log(L_{\text{IR}}) \sim 12.3$ is primarily driven by heating from O and B stars.

The observed linear relationships suggest that star formation does play an important role in powering the infrared luminosity in LIRGs and ULIRGs. However, it may be that this relationship breaks down at higher IR luminosities as possible AGN contribution becomes more important. As an example, we extrapolate our fit to observations of Hyperluminous Infrared Galaxies (HLIRGs). Extrapolating from our fit, a galaxy with $\log(L_{\text{IR}}) \sim 13$ would require $\sim 4 \times 10^{11} M_{\odot}$ of warm-dense molecular gas in the nuclear regions. For comparison, the HLIRG

FSC 10214+4274 has $L_{\text{FIR}}=1.8\times10^{14}L_{\odot}$ and CO (J=3-2)-traced warm-dense gas mass of $M_{\text{H}_2}=2.2\times10^{11}M_{\odot}$ (an upper limit as the luminosity may have been enhanced by gravitational lensing, Close et al. (1995)); similarly, HLIRG FSC 15307+3252 has $L_{\text{FIR}}=1.3\times10^{13}L_{\odot}$ and has an upper limit of warm-dense gas mass (as measured from CO J=4-3 observations) of $M_{\text{H}_2}\lesssim10^{10}M_{\odot}$. Both are believed to have central AGN as their main source for infrared luminosity (Yun & Scoville 1998).

The disparity in the measured versus predicted amount of warm-dense gas in these HLIRGs suggests that at higher infrared luminosities, there may exist a strong deviation from the fit described by Equation 4 which may be evident from the higher luminosity points in Figure 6.5. This implies that the infrared emission may grow non-linearly with increasing emission from warm-dense molecular gas.

It may be that there is an interplay between an AGN and star formation contribution to L_{IR} . The case has been mounting for an evolutionary sequence between hierarchical mergers and AGN formation (e.g. Scoville, 2003). It has recently become clear that most galaxies contain supermassive black holes (Kormendy & Richstone, 1995, and references therein). There is also evidence that there is a connection between black hole growth and central ISM physics in the remnants of galaxy mergers. Recent SPH simulations have shown that AGN feedback in galaxy merger remnants can rapidly quench star formation after the initial merger-induced starburst (Springel, Di Matteo & Hernquist 2004a,b). Starbursts may be the dominant source of IR luminosity in less IR-luminous galaxies, while the AGN contribution becomes more important in higher luminosity objects. Quenching of star formation owing to AGN feedback may be responsible for a steepening of the slope in the L_{IR} versus L_{CO} plot for the galaxies with

$\log(L_{\text{IR}}) \gtrsim 12.3 \text{ L}_{\odot}$. Indeed, some 35%-50% of ULIRGs with $L_{\text{IR}} \geq 10^{12.3} \text{ L}_{\odot}$ show AGN activity from optical and NIR spectra (Tran et al. 2001; Veilleux, Kim & Sanders, 2002). This luminosity is approximately where our sample of LIRGs and ULIRGs ends, and a location for a possible deviation from the fit in Figure 6.5. Additionally, Farrah et al. (2002) discuss coeval starburst and AGN activity in a sample of SCUBA HLIRG sources.

6.6.2 L_{IR} versus Mass of Star-Forming Molecular Gas

One of the main arguments for the existence of a dust enshrouded AGN as the main power source in luminous infrared galaxies is a SFE ($L_{\text{IR}}/M_{\text{H}_2}$) larger than that seen in normal spiral galaxies. If the sole source of energy is a nuclear starburst, then, assuming a reasonable initial mass function, there should be an Eddington-like limit on the star formation efficiency given by $\text{SFE} \sim 500 \text{ L}_{\odot} / M_{\odot}$: objects with ratios significantly higher than this are likely to require an additional source of energy (Scoville, Yun & Bryant 1997; Scoville, 2003).

The warm-dense gas mass is obtained using a modified version of the linear relation between the CO luminosity and M_{H_2} (Young & Scoville, 1982; Tinney et al., 1990; SSS91). Following Gao & Solomon (2004b), we employ a Large Velocity Gradient (LVG) model in order to derive a CO (J=3-2)-H₂ conversion factor. For a kinetic temperature of 35K, the model provides curves of $n(\text{H}_2)$ and $N(\text{H}_2)$ as a function of $I_{\text{CO}3-2}$ and $I_{\text{CO}1-0}$. For our galaxy sample, the curves yield an average $N(\text{H}_2)/I_{\text{CO}3-2}$ of $8.3 \times 10^{19} \text{ cm}^{-2} (\text{K km s}^{-1})^{-1}$. We then find

$$M_{\text{H2warm-dense}} = 1.33 \times L_{\text{COJ=3-2}} M_{\odot} (\text{K km s}^{-1} \text{pc}^2)^{-1} \quad (6.6)$$

While the ratio of infrared luminosity to total gas mass may be a strong indicator as to the source of infrared luminosity, it is the *dense* gas mass that is expected to more directly trace star formation. Thus, a prudent test is to examine the ra-

ratio of L_{IR} to $M_{\text{H2,dense}}$. Gao & Solomon (2004a,b), found that this ratio remains between ~ 20 and ~ 200 , independent of total IR luminosity for normal spirals, LIRGs and ULIRGs. They additionally reported that the average L_{IR} to $M_{\text{H2,dense}}$ in their sample was $\sim 90 L_{\odot} / M_{\odot}$, comparable to molecular cloud cores (Mooney & Solomon 1988). These ratios were found through analysis of HCN ($J=1-0$). We find an average $L_{\text{IR}} / M_{\text{H2,warm-dense}}$ of $\sim 160 L_{\odot} / M_{\odot}$.

We present the ratio $L_{\text{IR}} / M_{\text{H2,warm-dense}}$ for our sample of LIRGs in Table 2. As is evident, none of the objects have a ratio $L_{\text{IR}} / M_{\text{H2}} > 500 L_{\odot} / M_{\odot}$. It is important to note the sensitive dependency of this number on the CO-H₂ conversion factor. Additionally, it is not clear that the CO-to-H₂ conversion factor is the same in all galaxies. Better constraints on variations in the conversion factor are necessary in order to use this method to make a robust statement concerning the source of IR luminosity.

6.7 Chapter Summary

We have presented single-dish CO ($J=3-2$) observations of a sample of starbursts, LIRGs and ULIRGs in order to study properties of the warm-dense, star forming gas. We detected emission in 15 out of 17 galaxies within our noise limits. We have found a nearly-linear relationship between the infrared luminosity and amount of warm-dense gas, confirming the recent results by Gao & Solomon for galaxies with $\log(L_{\text{IR}}) \lesssim 12.3$. We have derived a CO-H₂ conversion factor for CO($J=3-2$) in LIRGs/ULIRGs of $8.3 \times 10^{19} \text{ cm}^{-2} (\text{K km s}^{-1})^{-1}$.

Table 6.1. Observation Information

Object	RA (J2000)	Dec (J2000)	cz	Distance ²	Date Observed	Reference ³	$\log L_{\text{IR}}$ ⁴	$f_{60\mu m}$ ⁴	Detection?
			km s^{-1}	Mpc			L_{\odot}	Jy	
NGC 7817	0:04:10.1	20:46:30.6	2315	31.9	11/03	1	10.41	*	Yes
NGC 3583	11:14:28.0	48:17:38.5	2168	35.09	11/03	3	10.54	7.43	No
NGC 3079	10:02:16.3	55:39:46.9	1142	18.19	03/04	3	10.73	50.67	Yes
NGC 3094	10:01:38.3	15:45:10.3	2404	37.04	11/03	3	10.73	10.88	Yes
NGC 2276	7:28:27.8	85:45:09.8	2380	35.83	03/04	2	10.81	14.29	Yes
NGC 834	2:11:14.4	37:41:11.2	4687	61.48	03/04	1	10.94	6.65	Yes
NGC 992	02:37:25.4	21:05:47	4136	53.83	03/04	1	11.02	11.40	Yes
NGC 6701	18:43:14.9	60:38:58.1	3933	56.64	03/04	1	11.05	10.05	Yes
NGC 6621	18:12:54.9	68:21:27.0	6234	86.42	03/04	1	11.23	6.78	No
NGC 828	02:10:09.42	39:11:26.29	5371	70.37	11/03	1	11.31	11.46	Yes
NGC 6286	16:58:36.6	58:55:25.7	5637	79.78	11/03	1	11.32	9.24	Yes
NGC 7771	23:51:36.2	20:08:00.4	4336	57.11	11/03	1	11.34	19.67	Yes
IR23436+5257	23:46:05.8	53:14:00	10233	134.78	01/05	*	11.51	5.66	Yes
UGC 5101	09:32:10.5	61:21:22	11785	158.61	01/05	5	11.95	11.68	Yes
Arp 220	15:35:05.2	23:29:22.7	5450	79.90	11/03	3	12.21	104.09	Yes
IR07251-0248	07:27:37.5	-02:54:55	26257	343.74	01/05	*	12.32	6.49	Yes
IR17208-0014	17:23:21.4	-00:17:00	12852	175.68	01/05	4	12.39	32.13	Yes

¹ All objects are in order of increasing L_{IR} .² Distances given are proper distances, and are taken from Sanders et al. 2003 except for NGC 7817 which is from SSS91. Values for cz taken from the same references.³ References are for J=1-0 data: 1: Sanders et al. 1991, 2: Tinney et al. 1990, 3: Yao et al. 2003, 4: Mirabel et al. 1990, 5: Gao & Solomon, 2004b. An asterisk denotes no CO (J=1-0) observations that we could find.⁴ L_{IR} and $60\mu\text{m}$ flux from Sanders et al. 2003, except for NGC 7817 which was not given.

Table 6.2. Physical Properties of Observed Galaxies

Object	Intensity	\pm	R_3 ¹	L_{CO}	\pm	M_{H_2} CO(3-2)	\pm	$L_{IR}/M_{H_2 \text{ warm,dense}}$
	$K \text{ km s}^{-1}$	$K \text{ km s}^{-1}$		$10^9 K \text{ km s}^{-1} \text{ pc}^2$	$10^9 K \text{ km s}^{-1} \text{ pc}^2$	$10^9 M_\odot$	$10^9 M_\odot$	L_\odot / M_\odot
NGC 7817	2.94	0.07	0.03	0.04	0.001	0.05	0.001	482
NGC 3079	183.46	3.18	0.51	0.852	0.01	1.13	0.01	47
NGC 3094	15.10	0.41	0.60	0.290	0.008	0.39	0.01	139
NGC 2276	12.23	0.20	0.12	0.219	0.004	0.29	0.005	221
NGC 834	11.15	0.37	0.28	0.585	0.02	0.78	0.02	112
NGC 992	21.16	1.25	0.34	0.852	0.05	1.13	0.06	92
NGC 6701	28.80	0.42	0.45	1.28	0.02	1.70	0.02	66
NGC 828	59.21	1.77	0.50	4.06	0.121	5.41	0.16	38
NGC 6286	42.61	0.13	0.65	3.75	0.01	5.00	0.01	42
NGC 7771	19.28	0.22	0.32	0.873	0.01	1.16	0.01	188
IR23436+5257	20.05	1.19	*	4.96	0.29	6.61	0.39	49
UGC 5101	7.17	1.1	0.50	2.45	0.38	3.27	0.50	273
Arp 220	89.96	1.91	1.60	7.95	0.17	10.61	0.23	153
IR07251-0248	7.70	0.31	*	11.79	0.47	15.72	0.63	133
IR17208-0014	10.49	1.11	0.42	4.37	0.46	5.82	0.61	421

¹ Asterisk denotes no CO (J=1-0) data available.

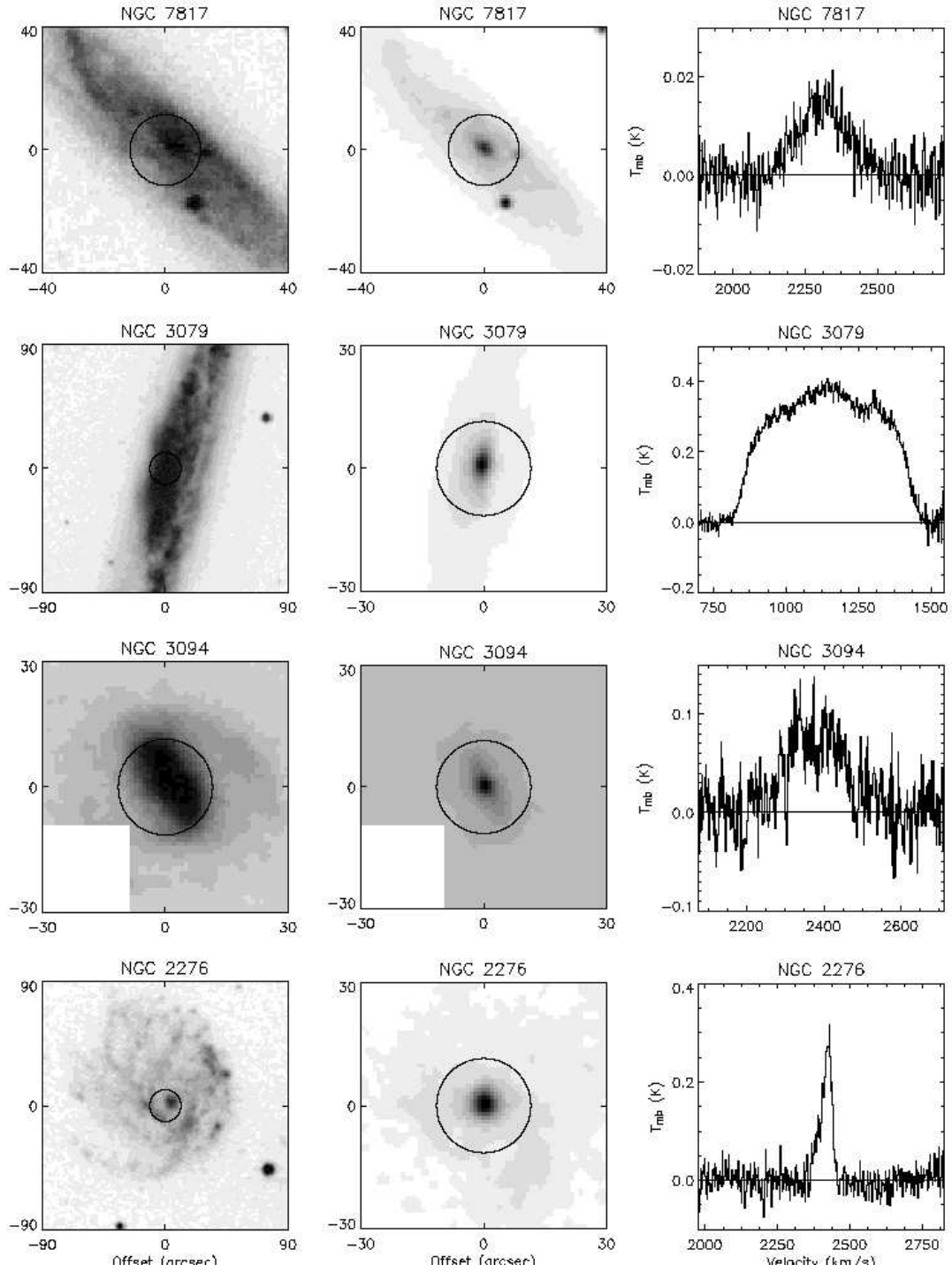


Figure 6.1 Each 3-panel row contains the following information from left to right: The *DSS* image with the 23'' HHSMT beam overlaid; The *2MASS* image with the 23'' HHSMT beam overlaid; The CO (J=3-2) emission line obtained at the HHSMT in this study.

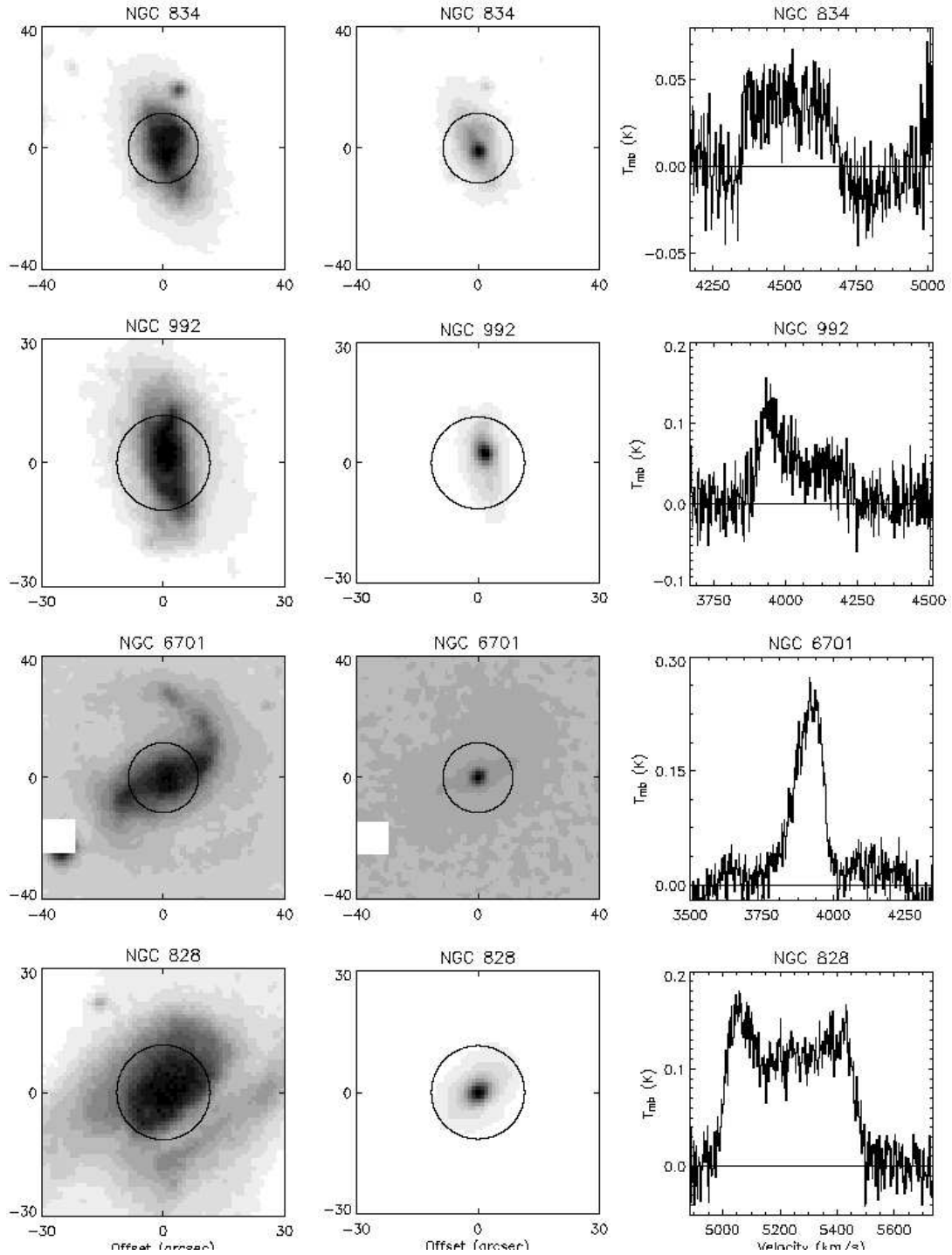


Figure 6.2 Each 3-panel row contains the following information from left to right: The *DSS* image with the 23'' HHSMT beam overlaid; The *2MASS* image with the 23'' HHSMT beam overlaid; The CO (J=3-2) emission line obtained at the HHSMT in this study.

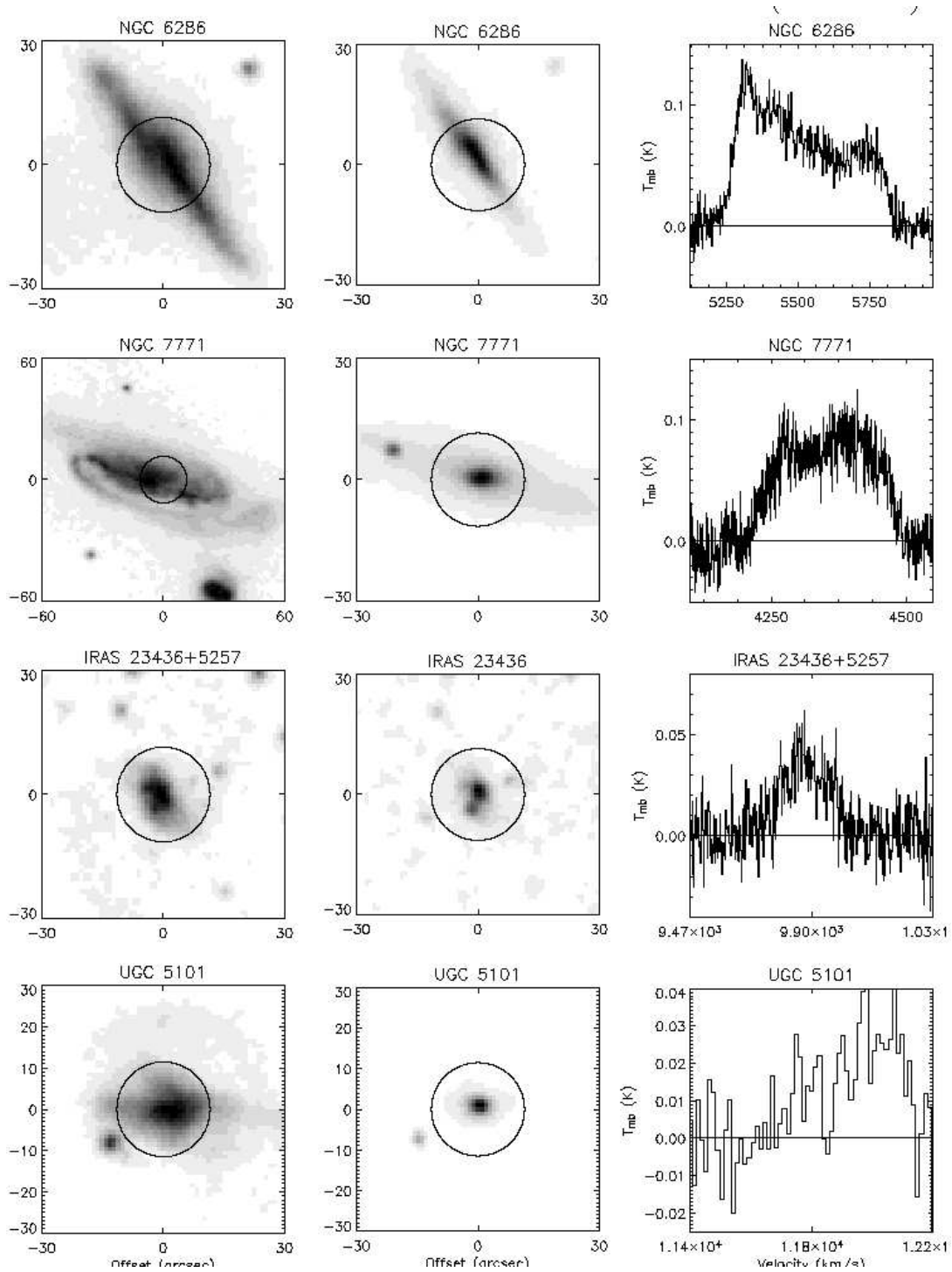


Figure 6.3 Each 3-panel row contains the following information from left to right: The *DSS* image with the 23'' HHSMT beam overlaid; The *2MASS* image with the 23'' HHSMT beam overlaid; The CO (J=3-2) emission line obtained at the HHSMT in this study.

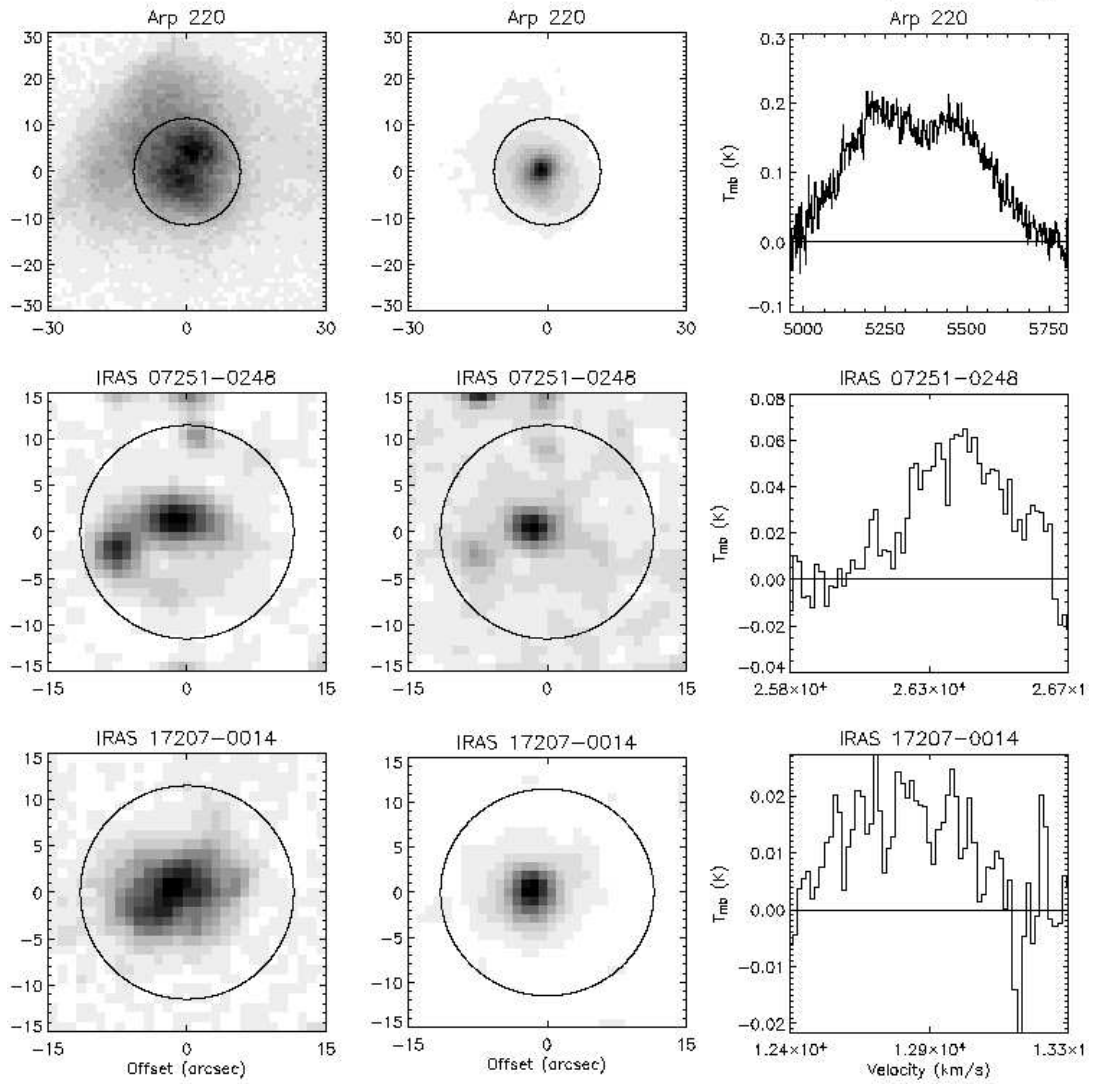


Figure 6.4 Each 3-panel row contains the following information from left to right: The *DSS* image with the 23'' HHSMT beam overlaid; The *2MASS* image with the 23'' HHSMT beam overlaid; The CO (J=3-2) emission line obtained at the HHSMT in this study.

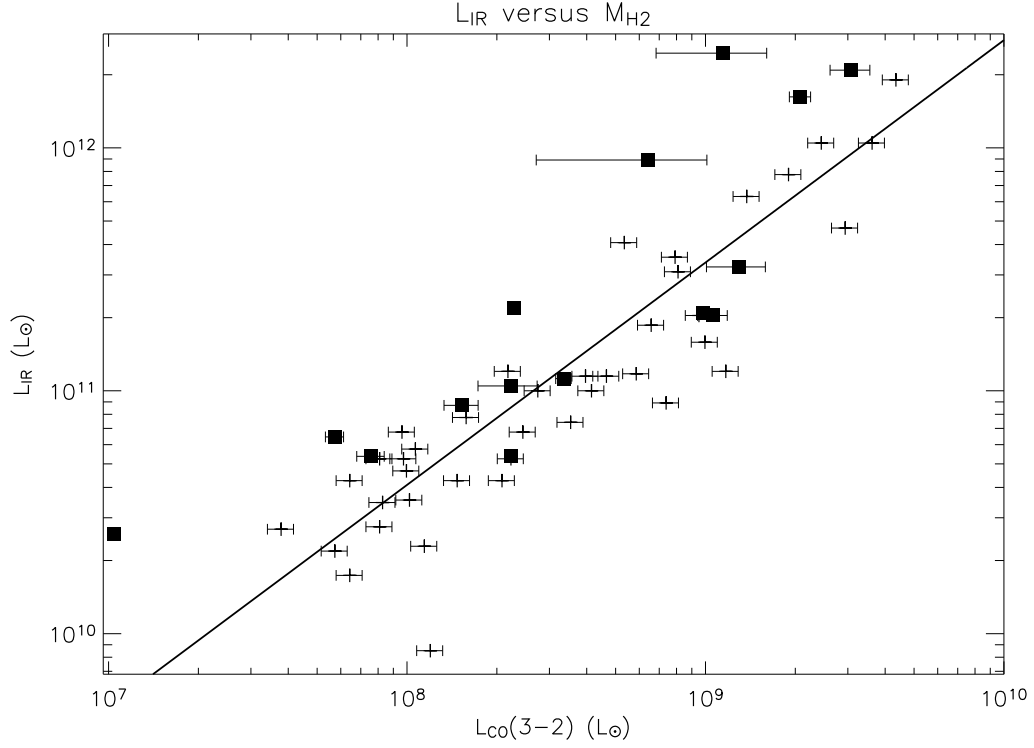


Figure 6.5 L_{IR} vs. $L_{\text{CO } 3-2}$. The slope of the fit is 0.92. Crosses are data points from Yao et al. (2003) while filled in squares are data taken in this study. Errors for objects from our sample derived from errors in intensity calculations. We estimate an error of 10% for the objects taken from the Yao et al. (2003) sample. No error bars are given for the L_{IR} data points. We have excluded NGC7817 from the fit (but left its point on the plot) as it has an extremely small L_{CO} with respect to the locus of objects we observed. When including this object, the slope changes to 0.85 ± 0.07

CHAPTER 7

MOLECULAR STAR FORMATION RATE LAW INDICATORS IN GALAXIES

All I know is I hope its not another molecular line talk...

Chuck Steidel to Chris Martin during the breakfast before my talk on this material at a conference.

7.1 Chapter Abstract

We derive a physical model for the observed relations between star formation rate (SFR) and molecular line (CO and HCN) emission in galaxies, and show how these observed relations are reflective of the underlying star formation law. We do this by combining self-consistent 3D non-LTE radiative transfer calculations with hydrodynamic simulations of isolated disk galaxies and galaxy mergers. We demonstrate that the observed SFR-molecular line relations are not necessarily representative of a more direct tracer of the SFR. Rather, they are driven by the relationship between molecular line emission and gas density, and anchored by the index of the Schmidt law controlling the SFR in the galaxy. Lines with low critical densities (e.g. CO J=1-0) are typically thermalized and trace the gas density faithfully. In these cases, the SFR will be related to line luminosity with an index similar to the Schmidt law index. Lines with critical densities greater than the mean density of most of the emitting clouds in a galaxy (e.g. CO J=3-2, HCN J=1-0) will exhibit significant emission driven by subthermally excited gas which owes its excitation to line trapping. The contribution to the total line luminosity from subthermally excited gas along the line of sight causes the line luminosity to increase with mean gas density superlinearly. Consequently the SFR-line lu-

minosity index is less than the Schmidt index. Our model for SFR-molecular line relations quantitatively reproduces the slopes of the observed SFR-CO (J=1-0), CO (J=3-2) and HCN (J=1-0) relations when a Schmidt law with index of ~ 1.5 describes the SFR. We use these results to make model distinguishing testable predictions for the SFR-molecular line relations of unobserved transitions.

7.2 Chapter Introduction

The rate at which stars form in galaxies has historically been parameterized in terms of “laws” relating the star formation rate (SFR) to the density of available gas. **(author?)** (Schmidt 1959) originally proposed a power-law form for the SFR such that $\text{SFR} \propto \rho^N$ (hereafter, referred to as a Schmidt Law).

Observed SFR relations typically come in two flavors. The first, relating surface SFR density to surface gas density takes the form:

$$\Sigma_{\text{SFR}} \propto \Sigma_{\text{gas}}^N . \quad (7.1)$$

Observations of local galaxies have constrained the surface density SFR index, N , to roughly $N=1.4 \pm 0.15$ (e.g. Kennicutt 1998a; Kennicutt 1998b? , and references therein).

The second varietal of SFR indicators relates the SFR to the mass of molecular gas above a given volumetric density. For example, local galaxy surveys have shown a relation exists between the SFR and molecular gas such that the SFR (as traced by the infrared luminosity - hereafter L_{IR}) is proportional to the ^{12}CO (J=1-0) luminosity to the 1.4-1.6 power (Sanders et al. 1991; Sanders & Mirabel 1996, and references therein). Because the J=1-0 transition of ^{12}CO (hereafter CO) can be excited at relatively low densities ($n \sim 10^2\text{-}10^3 \text{ cm}^{-3}$), and lies a modest ~ 5 K above ground, it serves as a valuable tracer of total molecular H_2 gas content

down to relatively low densities. These observed relations have been broadly interpreted as an increasing star formation efficiency (SFE; the SFR divided by M_{H_2}) as a function of molecular gas mass (Gao & Solomon 2004a; Gao & Solomon 2004b; Sanders et al. 1991).

Recent observations of HCN have suggested that a perhaps more fundamental volumetric SFR relation for galaxies exists in terms of the *dense* molecular gas. Because HCN (J=1-0) has a relatively high critical density ($n_{\text{crit}} \sim 10^5 \text{ cm}^{-3}$) compared to that of CO (J=1-0), HCN is typically only thermalized in the dense cores of molecular clouds. Thus, in the limit that the bulk of HCN luminosity originates from thermalized gas, HCN serves as a good tracer of the dense molecular gas that is actively involved in the star formation process. This is in contrast to CO (J=1-0) which tends to emit from both dense cores as well as diffuse molecular filaments and cloud atmospheres.

Pioneering millimeter-wave observations by **(author?)** (Gao & Solomon 2004a, Gao & Solomon 2004b) uncovered a tight linear correlation between the infrared luminosity and HCN luminosity in a sample of local galaxies, ranging from quiescent spirals to luminous and ultraluminous infrared galaxies (LIRGs and ULIRGs, respectively). This relationship was found by **(author?)** (Wu et al. 2005) to hold in individual star forming cores in the Milky Way as well. Observations of a roughly linear correlation between L_{IR} and CO (J=3-2) emission (with critical density $n_{\text{crit}} \sim 10^4 \text{ cm}^{-3}$) in a similar sample of galaxies further corroborated this result, and provided evidence against HCN-related chemistry driving the observed **(author?)** (Gao & Solomon 2004a, Gao & Solomon 2004b) relations (**(?)** Yao et al. 2003).

Despite a plethora of observations, a consensus physical interpretation of the seemingly disparate L_{IR} -HCN (J=1-0), L_{IR} -CO (J=1-0) and L_{IR} -CO (J=3-2) relations has yet to be borne out of the literature. **(author?)** (Gao & Solomon 2004a, Gao & Solomon 2004b)

suggest that the linear relationship between $L_{\text{IR}}\text{-HCN (J=1-0)}$ reflects a scenario in which the SFR in galaxies is directly proportional to the amount of dense molecular gas, and similarly, a constant star formation efficiency in terms of dense molecular gas. In this picture, LIRGs and ULIRGs simply have a higher fraction of their molecular gas in a dense gas phase which is reflected in the linear $L_{\text{IR}}\text{-HCN (J=1-0)}$ slope¹ and non-linear $L_{\text{IR}}\text{-CO (J=1-0)}$ slope. ?) suggest a similar interpretation for their observed relation of $L_{\text{IR}} \propto \text{CO (J=3-2)}^{0.92}$.

(author?) (Wu et al. 2005) extended these interpretations to include the observed linear $L_{\text{IR}}\text{-HCN (J=1-0)}$ relation within the Galaxy. These observations suggested that dense molecular cores may represent a fundamental unit of star formation. In this case, the only difference between a ULIRG like Arp 220 and a Galactic star forming region is the number of individual star forming units present. This leads to a natural linear relationship between the SFR and amount of dense molecular gas.

From the theoretical side, (author?) (Krumholz & Thompson 2007) made headway towards understanding the observed relations by providing a model which quantitatively reproduces the observed $L_{\text{IR}}\text{-CO (J=1-0)}$ and $L_{\text{IR}}\text{-HCN (J=1-0)}$ relations for star forming clouds. By combining 1D non-local thermodynamic equilibrium (LTE) radiative transfer calculations with models of giant molecular clouds (GMCs), these authors found that the relationship between the SFR and molecular line luminosity in star forming clouds depends on how the critical density of the molecule compares to the mean density of the observed source. Lines with critical densities which are typically below the mean density in a galaxy (e.g. CO J=1-0) probe the total molecular gas commonly from galaxy to galaxy. In this

¹Throughout this paper we use the term slope interchangeably with 'index' (as in the exponent in a given SFR relation - e.g. Equation 7.1). We do this as we are considering all relations in log-log space.

scenario, the SFR-molecular line exponent can be represented by the index that relates SFR to total volumetric gas density (i.e. the Schmidt index). Conversely, observations of molecules which typically trace densities well above the mean density of the galaxy (e.g. HCN J=1-0) trace similar conditions from galaxy to galaxy - i.e. the peaks in the density spectrum. In these cases, the molecular line luminosity rises faster than linearly with increasing gas density and the corresponding relation between SFR and line luminosity is near linear. A key direction forward beyond these models is understanding the effects of emitting GMCs on a galaxy-wide scale, with the potential effects of molecular line radiative transfer.

In this paper, we build on the body of observational and theoretical work by providing a self-consistent physical model for the origin of the observed molecular SFR indicators on galaxy-wide scales, and relating them to observed relations. We additionally make model-distinguishing testable predictions for how the SFR in galaxies relates to as yet unobserved transitions in CO and HCN. We do this by combining 3D non-LTE molecular line radiative transfer codes (Narayanan et al. 2006a; Narayanan et al. 2006b; Narayanan et al. 2007a; Narayanan et al. 2007b) with smoothed particle hydrodynamic (SPH) simulations of both isolated star forming galaxies and galaxy mergers. Our methodology includes the effects of both collisional and radiative molecular excitation and de-excitation, a multi-phase ISM, star formation, black hole growth, and the winds associated with latter two processes (Springel et al. 2005a).

The paper is outlined as follows. In § 7.3 we describe our hydrodynamic and radiative transfer simulations. In § 7.4 we quantitatively describe the origin for the observed SFR-CO and SFR-HCN slopes, and follow by making testable predictions for submillimeter-wave telescopes in § 7.5. In § 7.6 we compare our results to the body of observational work in this field, and in § 7.7, relate these

simulations to other models and interpretations for molecular SFR indicators. In § 7.8, we conclude with a summary. Throughout the work we assume a Λ CDM cosmology with $h=0.7$, $\Omega_\Lambda=0.7$, $\Omega_M=0.3$.

7.3 Numerical Methods

7.3.1 Hydrodynamics

For this work we have modeled both isolated disk galaxies and major mergers. We do this as the **(author?)** (Gao & Solomon 2004a, Gao & Solomon 2004b) and ?) samples include both disk galaxies as well as ongoing mergers. We note, however, that the results in this paper are not dependent on our usage of any particular combination of disk galaxies or mergers.

The hydrodynamic simulations were conducted with a modified version of the publicly available N -body/SPH code GADGET-2 (Springel et al. 2005b). The prescriptions used to generate the galaxies, as well as the algorithms involved in simulating the physics of the multi-phase ISM, star formation, and black hole growth are described fully in in **(author?)** (Springel et al. 2005a) and ? ?). We refer the reader to these works for further details though summarize the aspects most relevant to this study here.

GADGET-2 accounts for radiative cooling of the gas (Davé et al. 1999; Katz et al. 1996), and a multi-phase ISM which is considered to consist of cold clouds embedded in a hot, pressure confining ISM (e.g. McKee & Ostriker 1977). This is realized numerically through ‘hybrid’ SPH particles in which cold clouds are allowed to grow through radiative cooling of the hot ISM, and conversely star formation can evaporate the cold medium into diffuse, hot gas. Pressure feedback from supernovae heating is treated via an effective equation of state (EOS) (see Figure 4 of Springel et al. 2005a). Here we utilize an EOS softening parameter of $q_{\text{EOS}}=0.25$.

Star formation is constrained to fit the observed Kennicutt-Schmidt laws (Kennicutt 1998a; Kennicutt 1998b; Schmidt 1959) such that:

$$SFR \propto \rho_{\text{cold}}^{1.5} \quad (7.2)$$

It is important to note that our star formation prescription is based on volumetric conditions, and not surface density as in Equation (7.1). That said, a number of studies have found that a volumetric SFR law like this correlates well with the observed Kennicutt-Schmidt surface density SFR laws (Cox et al. 2006c; ? ? ; Springel 2000?).

Black holes are optionally included in our simulations which accrete via a Bondi-Lyttleton-Hoyle parameterization with a fixed maximum rate corresponding to the Eddington limit. The black hole radiates such that its bolometric luminosity is set by the accretion rate with $L = \epsilon \dot{M} c^2$ with accretion efficiency $\epsilon=0.1$. We further assume that 5% of this energy couples isotropically to the surrounding ISM as feedback energy (Di Matteo et al. 2005; Springel et al. 2005a), a number chosen to match the normalization of the locally observed $M_{\text{BH}}-M_{\text{bulge}}$ relation. We have run identical simulations both with and without black holes for this work, and found that the inclusion of black holes makes little difference on the final result. We note, however, that we focus our molecular line comparisons to the SFR, and not L_{IR} (which could, in principle, have a contribution from buried AGNs at the highest luminosities) as a complete treatment of modeling the infrared SED (e.g. Chakrabarti et al. 2007a; Chakrabarti et al. 2007b; Jonsson 2006?) is outside the scope of this study.

Simulations utilizing this methodology for a multi-phase ISM, star formation, and the associated feedback processes from black holes and SNe have reproduced characteristic X-ray, IR and CO emission patterns of ULIRGs and quasars (Cox et al. 2006b; Chakrabarti et al. 2007a; Chakrabarti et al. 2007b; Narayanan et al. 2006a;

Narayanan et al. 2007b), the bimodal galaxy color distribution (Springel et al. 2005b; Hopkins et al. 2006b) and observed properties of $z \sim 6$ quasars (Li et al. 2007a? ; Narayanan et al. 2007a; Robertson et al. 2007). Moreover, these simulations have proven consistent with observed quasar luminosity functions and lifetimes (Hopkins et al. 2005a, Hopkins et al. 2005b; Hopkins et al. 2005c; Hopkins et al. 2005d; Hopkins et al. 2006a; Hopkins et al. 2006c?), Seyfert galaxy luminosity functions (Hopkins & Hernquist 2006), the locally observed Magorrian relation (Di Matteo et al. 2005; Hopkins et al. 2007a; Hopkins et al. 2007b; Robertson et al. 2006a; Robertson et al. 2006b), the abundance and clustering of quasars and mergers (Hopkins et al. 2006d; Hopkins et al. 2007c; Hopkins et al. 2007d), and the kinematic (Cox et al. 2006a) and spatial structure (Hopkins et al. 2007e; Hopkins et al. 2007f) of elliptical galaxies.

We consider both isolated disk galaxies with varying gas fractions and masses, as well as two equal mass binary mergers. We utilized 15 isolated galaxies exploring a parameter space with gas fractions=[0.2, 0.4, 0.8] and virial velocities=[115, 160, 225, 320, 500 km s⁻¹]. All disk galaxies (including the progenitors for the merger simulations) were initialized with a **(author?)** (Hernquist 1990) dark matter profile, concentration index $c=9$, and spin parameter $\lambda=0.033$. For all galaxies we utilize 120,000 dark matter particles, and 80,000 total disk particles. The softening lengths were 100 pc for baryons and 200 pc for dark matter.

For the mergers, the progenitor galaxies were identical to the disk galaxies described here, with $V_{200}=160$ km s⁻¹, and 40% gas fraction. For reference, the mergers are simulations 'no-winds' and 'BH' as described in **(author?)** (Narayanan et al. 2006a). The first merger snapshots considered are when the molecular disks of the progenitors are overlapped as the galaxies approach final coalescence. We utilize multiple snapshots throughout the evolution of the merger simulations beyond this point to represent observed merging pairs caught in various stages of evo-

lution (e.g. close pairs such as the Antennae to more evolved mergers such as Arp 220 and NGC 6240). All merger snapshots are during the period of highest star formation activity, when the galaxy can be considered a LIRG/ULIRG (model IR luminosities for these merger simulations can be found in (author?) (Chakrabarti et al. 2007a)). Sample CO images of the merger simulations employed here, as well as some of the model disk galaxies can be found in (author?) (Narayanan et al. 2007b).

It is an important point to note that no particular choice or combination of models affects the presented results. While some of the disk galaxies used may nominally have larger circular velocities or gas fractions than galaxies observed in the local Universe, because the results are general, not including them does not change our results or interpretation. We include a wide range of model galaxies to increase the number statistics and dynamic range of our simulations. The generality of our results will be shown more explicitly in § 7.4 and § 7.5.

7.3.2 Non-LTE Radiative Transfer

The propagation of a line through a medium with lower density than the line's critical density requires a full non-LTE treatment. Specifically, in this regime, both collisions and radiative processes contribute to the excitation and de-excitation of molecules. This formalism for molecular line transfer has long been applied to interpretations of galaxy observations via large velocity gradient codes (e.g. Goldreich & Kwan 1974), though has only recently been incorporated in full 3 dimensions in galaxy-wide models (? Narayanan et al. 2006a; Narayanan et al. 2007a; Narayanan et al. 2007b? ; Yamada et al. 2007). We employ the radiative transfer methodology of (author?) (Narayanan et al. 2007b), and refer the reader to that work for full details. Here, we briefly summarize.

The radiative transfer is performed in two phases. First, the molecular level

populations (and consequently source functions) are explicitly calculated using the 3D non-LTE code, *Turtlebeach* (Narayanan et al. 2006a; Narayanan et al. 2007b). In this, a solution grid to the level populations is guessed at, and model photons are emitted isotropically in a Monte Carlo manner. The level populations are updated by assuming statistical equilibrium, and balancing radiative and collisional excitations, de-excitation and stimulated emission (Bernes 1979). A new series of model photons is emitted and the process is repeated until the level populations are converged.

Once the level populations and source functions are known, the model intensity can be found by integrating the equation of radiative transfer along various lines of sight. Formally:

$$I_\nu = \sum_{r_0}^r S_\nu(r) \left[1 - e^{-\tau_\nu(r)} \right] e^{-\tau_\nu(\text{tot})} \quad (7.3)$$

where I_ν is the frequency-dependent intensity, S_ν is the source function, r is the physical depth along the line of sight, and τ is the optical depth.

The SPH outputs are smoothed onto a grid with ~ 250 pc spatial resolution for the radiative transfer. In order to more accurately describe the strongly density-dependent collisional excitation and de-excitation rates, we model the gas in grid cells to be bound in a mass spectrum of GMCs constrained by observations of Milky Way clouds (Blitz et al. 2006). The GMCs are modeled as spheres with power-law density gradients, and radii given by the Galactic GMC mass-radius relation (e.g. Rosolowsky 2005; Rosolowsky 2007; Solomon et al. 1987).

Observational evidence suggests a range of power-law indices for GMCs, ranging from $n=1-2$ (Andre et al. 1996; Fuller & Myers 1992; Walker et al. 1990). Tests utilizing a number of cloud density power-law indices within this range show that the results in this work are not sensitive to this parameter choice. Similarly, in the study of (author?) (Blitz et al. 2006) and (author?) (Rosolowsky 2007),

GMC mass spectrum indices were found to range from $\gamma \approx -1.4$ to -2.8 . Again, tests of mass spectrum indices showed that the results of this paper are not sensitive to parameter choices within the range of observational constraints. We nominally employ indices of $n=1.5$ and $\gamma=-1.8$ for the cloud density and GMC mass spectrum power-laws (Rosolowsky 2007). This methodology allows us to faithfully capture the emission processes from both dense molecular cores and more diffuse GMC envelopes (Narayanan et al. 2007b).

We have benchmarked our radiative transfer codes against published non-LTE radiative transfer tests (van Zadelhoff et al. 2002), and present the results for these tests in (author?) (Narayanan et al. 2006b). Our methodology for applying 3D non-LTE molecular line radiative transfer has shown success in reproducing characteristic observed CO line widths, morphologies, excitation conditions and intensities in isolated disk galaxies, local ULIRGs and quasars from $z \sim 2-6$ (Narayanan et al. 2006a; Narayanan et al. 2007a; Narayanan et al. 2007b).

The molecular gas mass fraction is assumed to be half, as motivated by local volume surveys (e.g. Keres et al. 2003), and the molecular abundances set uniformly at Galactic values (Lee et al. 1996). In this work, typically $\sim 1 \times 10^7$ model photons were emitted in the non-LTE calculations per iteration, and we considered transitions across 11 molecular levels at a time. The mass spectrum of GMCs had a lower mass cutoff of $1 \times 10^4 M_\odot$ and an upper mass cutoff of $1 \times 10^6 M_\odot$. The collisional rate coefficients were taken from the *Leiden Atomic and Molecular Database* (Schoier et al. 2005).

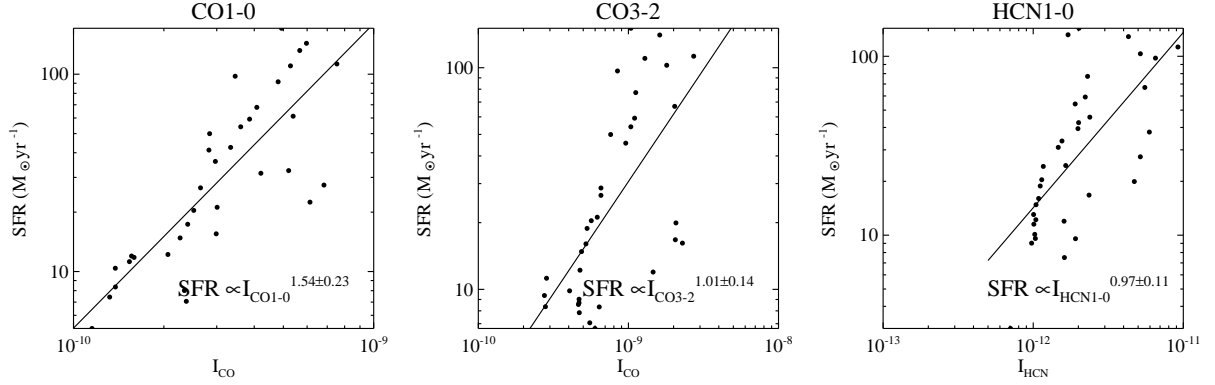


Figure 7.1 Model results showing the relationship between SFR and CO (J=1-0), CO (J=3-2) and HCN (J=1-0) emission. The molecular line emission is derived for a randomly drawn set of ~ 35 galaxy snapshots of our model sample of ~ 100 , and is a velocity-integrated intensity. The randomly drawn set is different for each plotted transition in order to illustrate the generality of our results. The solid lines are the least-squares fit to the plotted model results, and the exponent of the line in the bottom right corner of each panel. We randomly drew the sample of 35 galaxies 100 times, and quote the 1σ dispersion in the derived slopes as the ‘error’ values. The modeled relationships between SFR and molecular line luminosity are consistent with the observations of (author?) (Gao & Solomon 2004a, Gao & Solomon 2004b) and ?). The units of intensity are in $\text{erg s}^{-1} \text{cm}^{-2} \text{Hz}^{-1}$. We refrain from using traditional molecular line “luminosity” units as the discussion centers largely around the physical intensity associated with individual emitting gas cells in the simulations.

7.4 Origin of Observed SFR-CO and SFR-HCN Slopes

7.4.1 General Argument

In Figure 7.1 we plot the SFR-CO relations and SFR-HCN (J=1-0) relation as derived from our models of isolated disk galaxies and mergers with best fitting slopes overlaid. We plot the line intensities, though note that they are proportional to molecular line luminosity (L' , ?), the standard quantity reported in the observational literature. Included in the plot are a random sampling of 35 of the 15 disk galaxies and ~ 80 merger snapshots, spaced equally temporally with a sampling of 5 Myr. We first note the general agreement of the best fit slopes with observed relations by **(author?)** (Gao & Solomon 2004a, Gao & Solomon 2004b), ?), and **(author?)** (Sanders et al. 1991). Second, we note that we have utilized a randomly drawn sample of our simulated galaxies to demonstrate the generality of our results. From this, we see that any given combination of model disk galaxies and/or merger snapshots give roughly the same fits. We have quoted as “error” values the 1σ dispersion in 100 random draws of 35 model snapshots. The generality of these results occurs because the origin of the SFR-molecular line relations arise from the nature of the molecular emission from the individual galaxies themselves.

To see this, consider a galaxy which is forming stars at rate:

$$SFR \propto \rho^N \quad (7.4)$$

The relationship between the SFR and the luminosity of a molecular line

$$SFR \propto L_{\text{molecule}}^\alpha \quad (7.5)$$

is dependent on the relationship between the molecular line luminosity and the mean gas density in a cell of clouds:

$$L_{\text{molecule}} \propto \rho^\beta \quad (7.6)$$

where $\beta = N/\alpha$. Therefore, for a given Schmidt law index, N , the root issue in determining how the SFR relates to molecular line luminosity is understanding how the molecular line traces molecular gas of different densities (β). It is not trivial to simply attribute all luminosity of a given line transition to gas above its critical density as the potential contribution of subthermally excited gas is unknown, and can in some cases be non-negligible (e.g. Narayanan et al. 2006b). Thus, in order to solve for β , and thus α , we must consider the relationship between molecular line luminosity to gas of all densities from our model galaxies. We also note that the index α relating the SFR to molecular line luminosity is anchored by the assumed Schmidt-law index N .

A relationship between SFR and molecular line luminosity with exponent α that exceeds the Schmidt index, N , is indicative of a relationship in which the molecular line traces gas density in a sublinear manner ($\beta < 1$). Similarly, if the SFR-molecular luminosity index is less than the Schmidt index, N , then the line luminosity must globally trace the density of the emitting cells superlinearly ($\beta > 1$).

The global relationship between molecular line luminosity and mean gas density traced (β) is driven by how the critical density of the molecular line compares with the density of the bulk of the clouds across the galaxy. In short, lines which have critical density below the mean density of most of the emitting gas cells will be thermalized and rise linearly with increasing cloud density. These lines will consequently have SFR-line luminosity relations (α) similar to the Schmidt index controlling the SFR.

Lines which have critical densities far greater than the mean density of the bulk of the emitting gas will contain large amounts of subthermally (radiatively) excited gas which is excited owing to line trapping. Emission from subthermally

excited gas can be thought of as a scattering process in that the high critical density photon originates in dense, thermalized molecular gas, and is redistributed to more diffuse gas. Subthermal emission from radiatively excited cells tends to provide a significant contribution to the total luminosity from low density cells (Narayanan et al. 2006b), resulting in a situation where the line luminosity traces the sightline-averaged gas density superlinearly. In these cases, the SFR-line luminosity relation (α) has an index less than that of the underlying Schmidt law for the galaxy. In Figure 7.2, we show empirically how the line of sight velocity-integrated intensity from CO (J=1-0), CO (J=3-2) and HCN (J=1-0) relate to the sightline-averaged mean density along 50^2 sightlines for a fiducial disk galaxy. The solid line in each case shows linearity, with arbitrary normalization. Here, we see the expected result (from Equations 7.4-7.6) that the observed CO (J=1-0) emission traces the mean gas density along the line of sight roughly linearly, while the CO (J=3-2) and HCN (J=1-0) emission relate to the mean gas density superlinearly. There are details, of course, specific to the relationship between CO (J=1-0), CO (J=3-2) and HCN (J=1-0) luminosities and gas density traced which require a more in depth analysis, but these underlying themes are robust.

We devote the remainder of this section to examining the driving mechanisms behind the relationship between line luminosity and mean gas density (β), and utilize these to formulate a general model for observed SFR-molecular line luminosity relations in galaxies. As a reference point, we focus the following discussion on a 40% gas fraction disk galaxy with circular velocity of 160 km s^{-1} (though again note that the mean results are general - we discuss the dispersion in the model results and their relation to observational data sets in § 7.6). We plot the distribution of mean cell densities in this fiducial disk with the critical densities of a sample of CO lines overlaid in Figure 7.3 as an indica-

tor of the relative amounts of gas above given densities in the example galaxy. In order to account for the destruction of molecules in photodissociation regions (e.g. Hollenbach & Tielens 1999), we do not consider emission from regions with column density $\lesssim 1.5 \times 10^{21} \text{ cm}^{-2}$. This typically corresponds to cells with mean cloud density $\sim 50 \text{ cm}^{-3}$ in our simulations.

7.4.2 Quantitative Reasoning

We first note that a significant portion of the intrinsic luminosity in the galaxy escapes. While the optical depths can become large locally, velocity gradients across the galaxy serve to shift native absorption profiles out of resonance with the emission line on larger scales. Specifically, we see $\sim 60\%$ of the emission across most CO and HCN transitions escape the galaxy. The gas cells contributing to emission that escapes are of a fixed size, and distributed across the galaxy. These cells exhibit a wide range of mean cloud densities. We therefore focus on the properties of individual gas cells in our simulations (of all masses and densities) in order to build an understanding of how their summed properties drive the global line luminosities-gas density relation, and the consequent SFR-molecular line luminosity relation.

As discussed previously, the relationship between molecular line luminosity and gas density is controlled by how the critical density of the considered transition relates to the mean cloud density of the emitting cell. The observed SFR-molecular line relations (Gao & Solomon 2004a; Gao & Solomon 2004b?) are representative of three regimes: one in which the mean density of the bulk of the emitting clouds is higher than the line's critical density; one in which the mean density is lower than the line's critical density; and one in which the mean density is lower than the line's critical density and the line considered is a ground-state transition. We explore these three cases here. In Figure 7.4, we plot the line lumi-

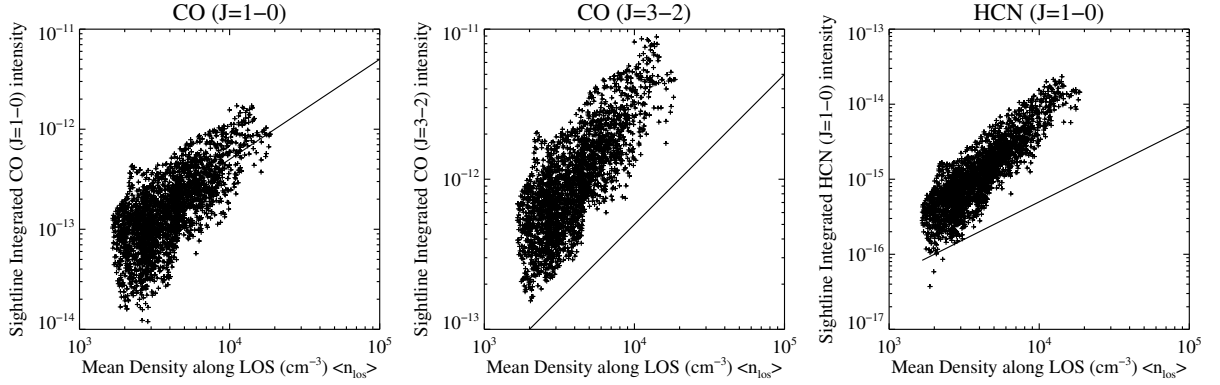


Figure 7.2 Velocity integrated molecular line intensities ($\text{erg s}^{-1} \text{ cm}^{-2} \text{ Hz}^{-1} - \text{km s}^{-1}$) along 50^2 sightlines for a fiducial disk galaxy versus mean density along the line of sight. The quoted mean density is the average along each sightline, and the velocity-integrated intensity is the emission that escapes along each sightline. The disk galaxy has a circular velocity of 160 km s^{-1} , and a gas fraction of 40% (though the results are general). The solid lines show linearity, and the normalization is arbitrary. The CO ($J=1-0$) emission traces the mean density along the line of sight roughly linearly, while the higher critical density tracers trace mean density superlinearly. These results are expected in order to recover the observed SFR-line luminosity relations (Equations 7.4-7.6).

osity versus mean density on a cell by cell basis for the CO ($J=1-0$), ($J=3-2$) and HCN ($J=1-0$) transitions from our fiducial disk galaxy. We will refer to this figure throughout the forthcoming discussion.

7.4.2.1 $n_{\text{crit}} \ll \bar{n}$

We first consider the regime in which the mean density of the bulk of the emitting clouds is typically higher than the line's critical density. At the critical density, the line is approaching thermalization and, in the limit that constant molecular abundances apply (with respect to H_2), the clouds are typically optically thick. In this

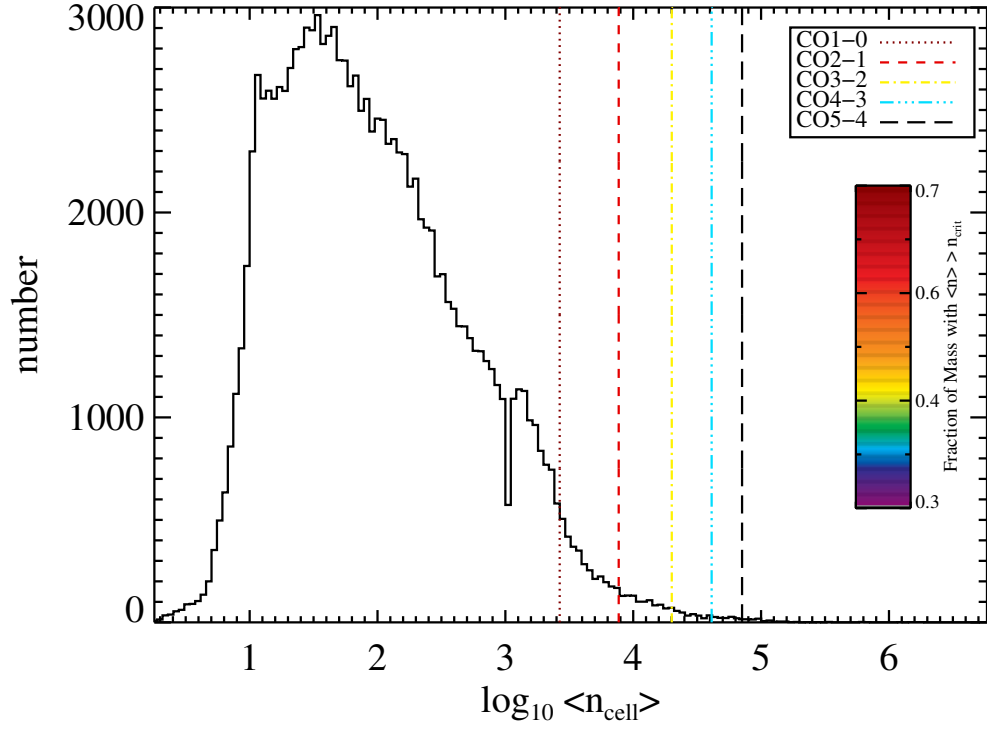


Figure 7.3 Distribution of mean cloud densities throughout our fiducial disk galaxy with circular velocity $v=160 \text{ km s}^{-1}$ and gas fraction $f=0.4$. The lines overlaid denote the location of critical densities of common CO transitions, and the color of each line indicates the fraction of gas mass with density above each critical density (with color scale on right). While most of the gas mass is above the critical density of the lowest lying transition, CO (J=1-0), higher lying transitions (e.g. CO J=3-2) may be subthermally populated through much of the galaxy.

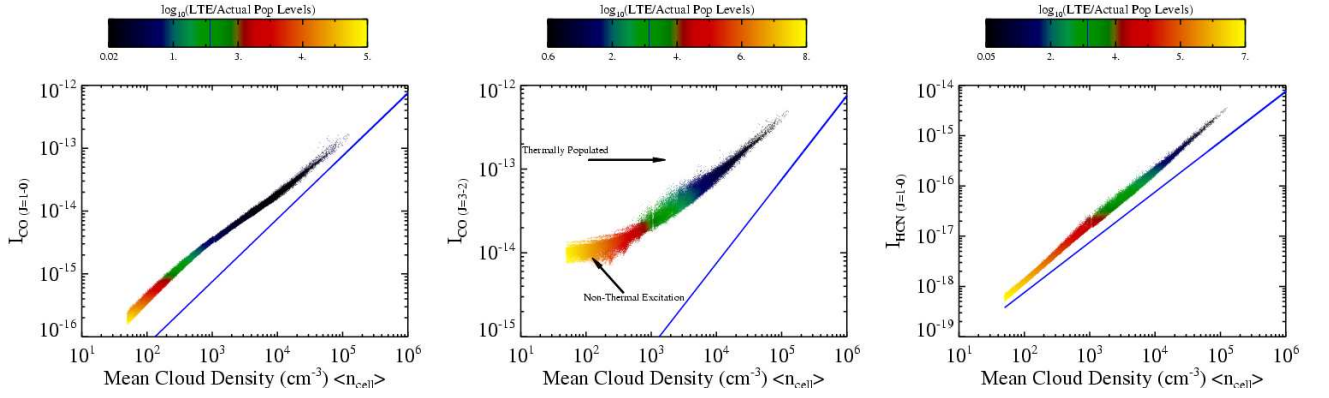


Figure 7.4 CO ($J=1-0$), ($J=3-2$) and HCN ($J=1-0$) intensity versus mean cloud density in our fiducial disk galaxy on a cell by cell basis. The quoted mean density is the mean density of the 50^3 cells in our sample grid. The blue line shows linearity, and the colors in the points show the ratio of LTE level populations to actual level populations for the upper J level of each transition. See text for details on how this drives the observed SFR-line luminosity relations. The units of intensity are in $\text{erg s}^{-1} \text{cm}^{-2} \text{Hz}^{-1}$ which are proportional to the standard observed L' molecular line luminosity units.

scenario, the emission arises primarily from the outer (lower column density) regions of clouds, and serves as a measure of the number of emitting clouds in a given cell. While groups of clouds are locally optically thick, on a galaxy-wide scale they are optically thin. Thus, the velocity dispersion of the bulk of clouds along a given line of sight has the effect of spreading the molecular line emission out in frequency space, permitting physically overlapping clouds to be counted. Because the mean cloud density increases with number of clouds in a given cell, in the optically thick limit, a roughly linear relation between molecular line emission and mean cloud density is natural.

In Figure 7.4 (left panel), we illustrate how these ideas translate into the effective molecular line luminosity-gas density relationship by showing the CO (J=1-0) intensity as a function of mean density in our fiducial disk galaxy. Overlaid in color is the level of thermalization. The bulk of the CO (J=1-0) emission comes from cells that are either in LTE or nearly thermalized. In this case, we can see how the relationship between CO (J=1-0) emission and gas density translates into the observed molecular SFR relation for CO (J=1-0). The observed SFR-CO (J=1-0) index of ~ 1.4 - 1.6 implies a roughly linear relationship between the observed CO (J=1-0) line luminosity and mean cloud density if a Schmidt-law index ~ 1.5 applies. We therefore arrive at the conclusion that transitions that have critical density well below the mean critical density of most emitting clouds will be roughly thermalized, and the SFR-line index will be similar to the underlying Schmidt-law index.

7.4.2.2 $n_{\text{crit}} \gg \bar{n}$

Let us now consider cases in which the gas density is in large part below the critical density of the emission line (which is not a ground state transition - e.g. CO J=3-2). In the lowest density cells, high critical density tracers such as CO

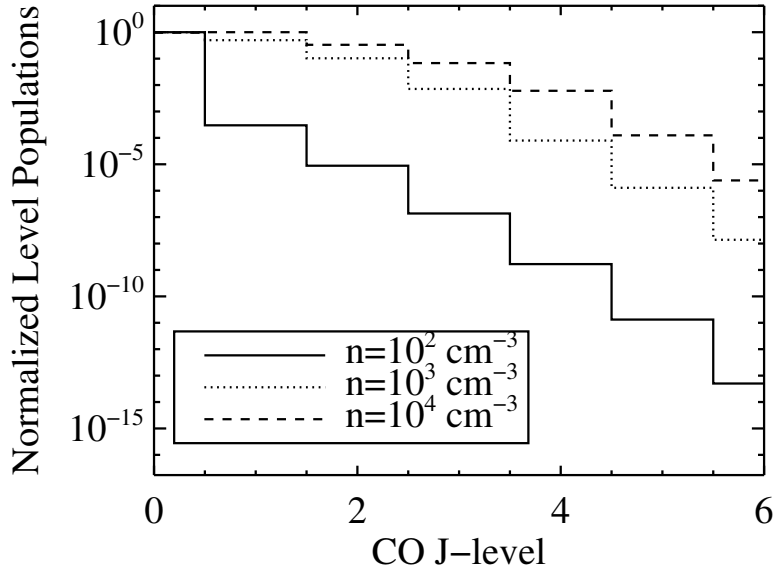


Figure 7.5 Normalized level population distributions for three gas cells of varying mean density in our sample disk galaxy. In the lowest density cell ($n_{\text{H}_2} \sim 10^2 \text{ cm}^{-3}$), all $J \geq 1$ states are subthermally populated, and rising with increasing density. The $J=1$ level is increasing with respect to roughly fixed $J=0$ populations with rising cloud density, resulting in increasing CO ($J=1-0$) flux with rising mean cloud density. Conversely, in the lower density curves, while the level populations from higher lying levels are also increasing with mean cloud density, they are not increasing *with respect* to each other (e.g. the relatively constant $J=3/J=2$ level population ratio from the $n_{\text{H}_2} \sim 10^2 \text{ cm}^{-3}$ cell through the $n_{\text{H}_2} \sim 10^3 \text{ cm}^{-3}$ cell). Here, the flux from e.g. the $J=3-2$ line will remain constant with increasing mean cloud density. This occurs until the $J=2$ level approaches thermalization and the $J=3$ populations begin to increase with respect to the $J=2$ populations.

($J=3-2$) are subthermally excited. Unlike the previous case, the emission from the lower mean density cells does not drop linearly with decreasing mean cloud density. Rather, the molecular excitation (and consequent emission) is supported by radiative excitation from neighboring cells with higher mean density.

The cells with the lowest mean density show a relatively constant flux level which is higher than would nominally be allowed if collisions alone drove the molecular excitation (Figure 7.4). To see this, consider the dependence of the cell's intensity on the molecular level populations:

$$I_\nu = \frac{n_u A_{ul}}{(n_l B_{lu} - n_u B_{ul})}, \quad (7.7)$$

where n_u and n_l are the upper and lower state level populations, and A_{ul} , B_{lu} and B_{ul} are the Einstein coefficients for spontaneous emission, absorption, and stimulated emission, respectively. In subthermally populated levels, $n_l \gg n_u$, and consequently $I_\nu \propto n_u/n_l$. When both l and u are subthermal, n_l and n_u increase in lock step superlinearly with increasing mean cloud density. This owes to a combination of the effects of collisional excitations (which increases linearly with density) and the additional contribution of radiative excitations. Because n_l and n_u both increase monotonically with gas density, there will be little change in the intensity as a function of increasing gas density. Consequently, the value of the intensity is roughly constant at $(n_u A_{ul})/(n_l B_{lu})$ where n_u and n_l are inflated (above the effects of collisional excitation alone) by line trapping.

At higher mean cloud densities, when the collisions begin to dominate the excitation processes for the l state, n_u continues to increase superlinearly with increasing density whereas n_l increases only linearly. Thus, n_u increases with respect to n_l with increasing mean cloud density, and the line intensity begins to rise with cloud density (Equation 7.7). At the highest mean cloud densities, the l and u states are both thermally populated, and the emission rises linearly with

increasing mean density as in § 7.4.2.1. In Figure 7.5, we plot an illustrative example of how the level populations evolve with increasing mean cloud density by showing the CO level population distributions for three cells with different mean densities in our fiducial disk galaxy. These rates of level population increase with increasing mean gas density translates to the relationship between I_{CO} and gas density for the CO (J=3-2) transition as shown in Figure 7.4 (middle panel).

At first glance, Figure 7.4 suggests that the CO (J=3-2) intensity traces the gas density (β) sublinearly, which is contradictory to what we would expect given the nearly linear SFR-CO (J=3-2) index (α ; Equations 7.4-7.6). However, the important quantity to consider is the total integrated intensity summed along sightlines through the galaxy (Figure 7.2). The gas in the low density subthermally populated regions along the line of sight is excited by emission from warmer, higher density gas, and thus has a characteristic intensity reflective of a higher brightness temperature than the meager densities in these gas cells would normally allow for via collisional excitation alone. Conversely, emission from higher density gas is more representative of the dense regions the photons originate from. If one could see directly into the thermalized nucleus, the CO (J=3-2) emission would be characteristic of the density of gas traced, and the consequent I_{CO} -gas density relation would be linear (e.g. § 7.4.2.1). However, the contribution to the emission from lower mean density regimes along the line of sight results in a total superlinear relation between intensity and gas density (β).

We show this more quantitatively in Figure 7.6, where we plot the relative light (line flux) to density ratios versus the mean density along a single sightline peering through the nucleus of our sample disk galaxy. We plot the light to density ratios for the CO (J=1-0) and CO (J=3-2) transitions, and normalize the ratios at the highest density cell. In Figure 7.6, it is evident that the lower density

gas along the line of sight toward the nucleus proportionally emits substantially more CO (J=3-2) intensity as a function of density than the thermalized gas². As shown in Figure 7.3, this lower density gas occupies a large fraction of the density spectrum in the galaxy, and is thus highly prevalent along the line of sight toward the dense nucleus. This translates to the CO (J=3-2) intensity tracing the sightline-integrated mean gas density superlinearly (Figure 7.2).

7.4.2.3 $n_{\text{crit}} \gg \bar{n}$; Ground State Transition

We now briefly turn our attention toward the SFR-HCN (J=1-0) relation as it represents an instructive combination of the phenomena driving the SFR-CO (J=1-0) and SFR-CO (J=3-2) relations. At its root, the characteristic emission pattern from HCN (J=1-0) falls into a similar category as that of CO (J=3-2). That is to say, it is dominated by subthermally excited gas, and the emission from these cells traces the gas density in a superlinear manner as it is representative of the radiation field from warmer, denser gas. Indeed, the result is expected as the critical densities from the two lines are only an order of magnitude different, and both are substantially higher than the mean density of most clouds in our model galaxies. The difference between HCN (J=1-0) emission and the CO (J=3-2) emission is that there is no flat portion of the line intensity-gas density curve as it is a ground state transition (Figure 7.4, right panel). The superlinear emission continues monotonically with cell density across the full range of densities in the example galaxy owing to nearly constant J=0 level populations and rising J=1 level populations (Equation 7.7). This was explicitly seen in Figure 7.5 for the case of CO (though qualitatively the case of HCN is similar). The intensity

²It is important to note that there is no “extra” photon production from subthermally excited gas. The emission from this diffuse gas is simply redistributed light which largely originated in thermalized cores. It is the increased relative light to density ratio (Figure 7.6) in this subthermally excited gas along the line of sight that causes the superlinear β index (Equation 7.6).

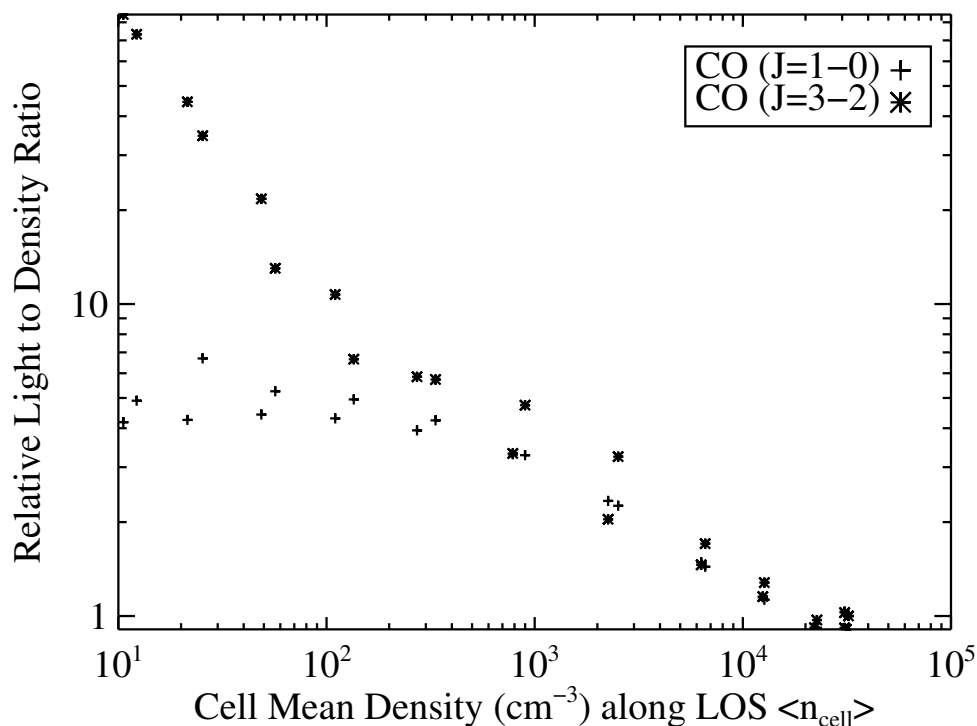


Figure 7.6 Ratio of intensity to gas density in gas cells along a line of sight that goes through the nucleus of the sample galaxy for the CO (J=1-0) and CO (J=3-2) transitions. Both the intensity and density curves are normalized to their respective maximum values (which both occur in the densest cell), so the expected light to density ratio is unity at the maximum density. For the CO (J=1-0) transition, most of the gas is thermalized along the line of sight, so the relative light to density ratio is nearly unity for most clouds. For the CO (J=3-2) transition, diffuse gas along the sightline contributes proportionally more luminosity than thermalized cells owing to radiative excitations by denser gas in the vicinity. When comparing to Figure 7.3, it is evident that these lower density clouds are numerous along a given sightline. The summed contribution of the intensity from these low density cells to the total integrated intensity causes the relationship between total luminosity and gas density to be superlinear. Consequently, the resultant SFR-molecular line relation has index of order unity.

risers superlinearly with increasing gas density because the excitation processes have a large contribution from both collisions and the molecular line radiation field. Collisional excitation rates (at a constant temperature) are proportional to the density. The substantial additional source of excitations from line trapping contributes to the superlinear excitation rates with density. This results in a nearly linear relationship between the SFR and HCN (J=1-0) luminosity in our models, consistent with the well established observational results of (author?) (Gao & Solomon 2004a, Gao & Solomon 2004b).

We therefore arrive at the following conclusions driving observed molecular line-SFR relations:

- For lines with critical densities well below the mean density of the clouds in the galaxy, the emission line will trace the total molecular content of the galaxy. In these cases, we find an SFR-molecular line luminosity index equivalent to the Schmidt-law index. This results in an SFR-CO (J=1-0) slope of ~ 1.5 when the SFR is constrained by $\text{SFR} \propto \rho^{1.5}$. Observationally, the SFR-CO (J=1-0) index is found to lie between 1.4-1.6.
- For lines with high critical densities, radiative excitation of gas with mean density well below the line's critical density allows this gas to contribute significantly to the emission. When the line is a ground state transition (e.g. HCN J=1-0), the intensity from gas cells rises monotonically with mean cloud density, though superlinearly owing to heavy contribution to the excitation from line trapping. When the line is a transition above the ground state (e.g. CO J=3-2), emission from the subthermally excited cells is roughly constant with increasing mean gas density until the level populations involved in the transition begin to approach LTE, at which point the intensity is roughly linear with mean cloud density. *In either case, for high*

critical density lines, line trapping by low density gas causes a sightline-integrated superlinear relationship between line luminosity and gas density (β). This results in an SFR-line luminosity index (α) lower than the Schmidt-law index. In the example of CO (J=3-2) and HCN (J=1-0) presented here, this results in SFR-line luminosity indices of ~ 1 , consistent with the measurements of ?) and (author?) (Gao & Solomon 2004a, Gao & Solomon 2004b).

7.4.3 Implications of Results

The results presented thus far are a natural solution to the observed SFR-CO and SFR-HCN relations. Without any special tuning of parameters, the same simulations are seen to additionally reproduce characteristic CO emission line morphologies, intensities, excitation conditions and effective radii of local disk galaxies and mergers (Narayanan et al. 2006a; Narayanan et al. 2007b), as well as quasars at $z \sim 6$ (Narayanan et al. 2007a). More broadly, the same galaxy evolution simulations have shown successes in reproducing a large body of characteristic observable features of starburst galaxies, ULIRGs and quasars from $z=0-6$ (§ 7.3.1, and references therein). In this sense, the modeled reproduction of the observed SFR-CO and SFR-HCN relations are a natural result of a self-consistent series of simulations.

Second, we re-emphasize that the relationship between SFR and CO/HCN emission is *built in* to the excitation mechanisms of both diffuse and dense gas in galaxies, though should be taken in an ensemble sense. Because the average excitation conditions of the disk galaxies and merger snapshots in our simulations result in molecular line-gas density relations compatible with the observed SFR-molecular line relations, no particular combination of disk galaxies and/or merger snapshots was necessary for the reproduction of observed relations in Figure 7.1.

It is important to note, however, that these simulations do not suggest that the particular excitation conditions presented in e.g. Figure 7.4 will apply to every galaxy in the (author?) (Gao & Solomon 2004a, Gao & Solomon 2004b) and ?) samples, but rather the average excitation conditions of these galaxies are such that the observed SFR-molecular line relations exist. To illustrate this point, in Figure 7.7, we plot the fractional photon production from subthermally populated gas (nominally defined here as gas with level population densities less than 100 times that of thermal) as a function of CO transition for ~ 40 snapshots of a merger simulation. The merger is characteristic of the dynamic range of excitation conditions seen in the galaxy simulations presented in this work, as well as the types of galaxies typically probed in SFR-molecular line studies. The solid line is the mean fractional photon production from subthermally excited gas, and the shaded region represents the 1σ contours of the dispersion across the snapshots. While the mean fractional emission from subthermally excited gas follows a trend that is somewhat expected given the plateau of critical densities with increasing CO excitation (Figure 7.7), the dispersion about the mean is nontrivial. Thus, any particular galaxy in the e.g. (author?) (Gao & Solomon 2004a, Gao & Solomon 2004b) samples may not exhibit the predicted I_{CO} -gas density relations predicted here. On average, however, the trends driving the SFR-molecular luminosity relations are robust.

A natural question is whether or not any given SFR-molecular luminosity relation holds particular significance as a physical SFR “law” relating the SFR to a property of the gas itself. The results in this section show that all SFR-molecular line relations are reflective of the underlying Schmidt law relating the star formation rate to gas density. That is, our models suggest that the observed linear SFR-molecular line luminosity relations (for high critical density

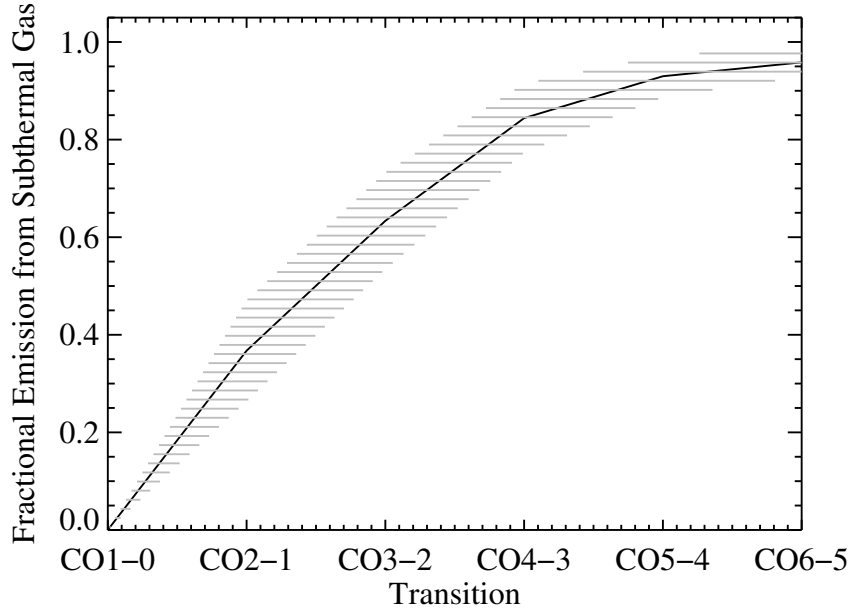


Figure 7.7 Fractional photon creation from subthermally excited gas as a function of CO transition for ~ 40 snapshots of a merger simulation. Note, this is not necessarily the same as the emission that escapes the galaxy. The solid line is the mean and the shaded regions show the 1σ dispersion seen across the snapshots. Gas is nominally considered to be subthermally excited if it has level populations $\lesssim 100$ times thermal. The trend remains constant regardless of our definition of subthermally excited gas though the normalization changes. The dispersion is evidence of varying excitation conditions between galaxies. The *average* excitation conditions are such that the line luminosity-gas density relations drive the observed SFR-line luminosity relations.

tracers) do not represent a fundamental indicator of the SFR, but are rather simply indicative of the underlying Schmidt law. Because we assumed that the $\text{SFR} \propto \rho^{1.5}$, the resultant SFR-molecular line relations from the models matched the observed relations rather well (Equations 7.4-7.6). To some degree, these models suggest that the observed SFR-CO and SFR-HCN relations reflect a physical SFR law similar to the ones assumed for this model (with index $N \approx 1.5$). Moreover, simulations have shown that this choice of an SFR law reproduces the observed surface density (author?) (Kennicutt 1998a, Kennicutt 1998b) SFR laws well (Cox et al. 2006c; Springel 2000). In this sense, the predicted molecular SFR relations in this section are simply reflective of the existing surface density SFR laws, as well as volumetric gas density SFR laws.

7.5 Testable Predictions

In Figure 7.1, we showed for a random drawing of our sample of ~ 100 disk galaxies and merger snapshots that our model results displayed consistent SFR-CO and SFR-HCN indices with observations of local galaxies (Gao & Solomon 2004a; Gao & Solomon 2004b? ; Yao et al. 2003). We can further extend these model results to make testable predictions for the indices of unobserved SFR-CO and SFR-HCN transitions.

We plot the predicted indices for the range of readily observable SFR-CO and SFR-HCN transitions in Figure 7.8. To derive these results, we randomly sampled 35 of our ~ 100 galaxies and took the best fitting slope between the SFR and molecular line luminosity. We did this for each transition 100 times, and in Figure 7.8 denote the mean of these results with the solid line, and the standard deviation in the dispersion with the hatched region. We additionally plot the observed data from the surveys of (author?) (Gao & Solomon 2004b) and ?) with associated er-

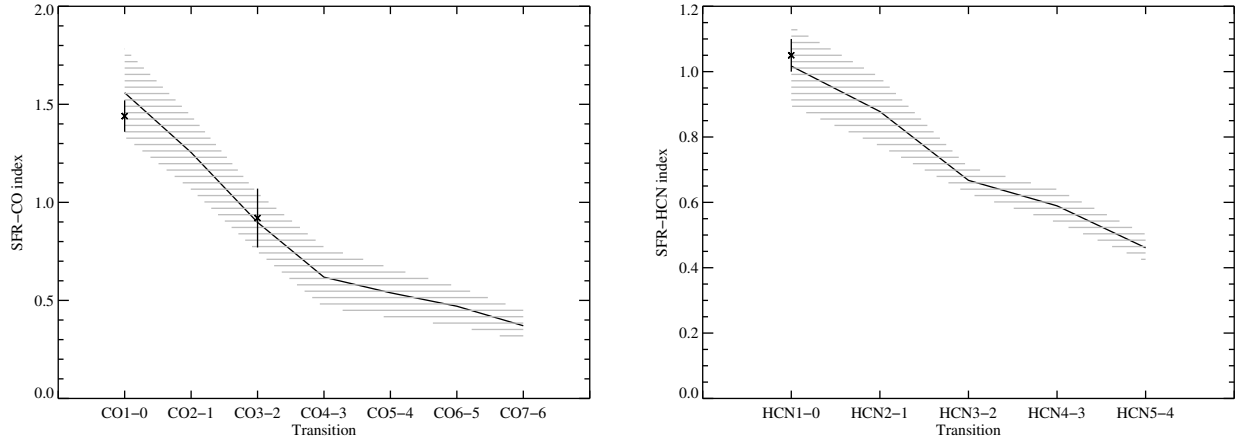


Figure 7.8 Predicted indices between SFR-CO and SFR-HCN relations for a series of molecular line transitions. The SFR-CO ($J=1-0$), SFR-CO ($J=3-2$) and SFR-HCN ($J=1-0$) indices are all consistent with the observations of (author?) (Gao & Solomon 2004a, Gao & Solomon 2004b) and ?). To simulate observational variance with particular galaxy samples, we randomly sampled 35 of our ~ 100 model galaxies 100 times. The solid line shows the mean derived slopes, and the shaded region the 1σ contours in the dispersion of slopes. Additionally plotted are the observed data from the surveys of (author?) (Gao & Solomon 2004b) and ?) with their quoted error bars. These predicted slopes serve as a direct observable test for these models.

ror bars. The model results are quite consistent with the three observational data points. Moreover, the dispersion in the prediction is consistent with the resultant dispersion in slopes of a random sampling of a comparable fraction of galaxies in the (author?) (Gao & Solomon 2004a, Gao & Solomon 2004b) sample.

The slope of the SFR-CO ($J=1-0$) relation roughly follows the assumed Schmidt law as the CO ($J=1-0$) serves as an accurate tracer of the total molecular gas. Higher lying transitions become shallower as the relationship between the transition and the gas density (globally) becomes superlinear. At higher e.g. CO transitions (e.g. CO $\gtrsim 4$), the decrease in the SFR- L_{CO} slope begins to flatten. Broadly, this owes to a relative plateau in the critical densities as a function of increasing rotational transition.

The predictions seen in Figure 7.8 may serve as model-distinguishing observational tests. That is, the standard interpretation of the linear relationship seen between L_{IR} and HCN ($J=1-0$) luminosity and CO ($J=3-2$) luminosity is that the molecular line emission traces dense gas more physically involved in the star formation process (e.g. $n \gtrsim 10^{4-5} \text{cm}^{-3}$). In that picture, observations of HCN and CO transitions with even higher critical densities ought to similarly show a linear relationship between L_{IR} and molecular line luminosity as they continue to probe dense star forming cores (e.g. Gao & Solomon 2004a; Gao & Solomon 2004b; Krumholz & Thompson 2004). In contrast, our models suggest that the observed relations between SFR and molecular line luminosity are driven by a substantial contribution to the line luminosity by subthermally excited (non-LTE) gas. In the limit that higher lying transitions have an even larger contribution from subthermally excited gas than e.g. HCN ($J=1-0$) or CO ($J=3-2$) (Figure 7.7) then the relationship between SFR and luminosity from these lines will be sublinear (Figure 7.8). Observations of alternative CO lines or higher lying HCN transitions in galaxies will provide a

direct test of these models (R.S. Bussmann et al. in prep).

7.6 Comparison with Observations

The model results presented here self-consistently reproduce the observed SFR-CO ($J=1-0$), SFR-CO ($J=3-2$), and SFR-HCN ($J=1-0$) indices for local galaxies. These are found to be reflective of the ensemble-averaged excitation conditions in these galaxies, and the manner in which the molecular line luminosity is related to mean cloud density.

Surveys of Galactic GMC cores have shown that high dipole moment molecules such as CS and HCN serve as an accurate tracer of dense gas mass (e.g. Shirley et al. 2003; Wu et al. 2005). However, the interpretation from extragalactic sources is mixed. Varying results have come from the observational literature regarding the origin of traditional tracers of dense gas (such as HCN) from extragalactic surveys. For example, (author?) (Greve et al. 2006) find the HCN emission in some systems to arise from dense, thermalized cores, whereas ?) cite Arp 193 as an example in which the bulk of the HCN emission arises from subthermally populated gas. More broadly, constraints on high lying transitions in CO, HCO^+ and HCN from the observational samples of (author?) (Greve et al. 2006), ?), ?), (author?) (Papadopoulos et al. 2007) and (author?) (Yao et al. 2003) among others evidence a wide range of molecular excitation conditions. In this regard, the models presented here are consistent with these observational results (Figure 7.7).

Sensitive observations of high redshift galaxies are beginning to measure sources in the early Universe in terms of their place on the SFR-molecular line relation as well (e.g Gao et al. 2007 ; Greve et al. 2005; Hainline et al. 2006; Riechers et al. 2006a; Wagg et al. 2005; Wagg et al. 2007; Weiß et al. 2007, for an extensive review, see Solomon & Vanden Bout 2005 and references therein). Owing to its relatively

high abundance, most detections at high- z have been in CO (with a smattering of HCN, HCO^+ and other molecules), and thus we focus our comparisons with high- z galaxies on CO. A summary of a nearly-current sample may be found in Figure 5 of (author?) (Riechers et al. 2006a).

In general, the interpretation of SFR-molecular line relations at high redshift are muddled by two factors. First, the increasing fraction of AGN in high redshift infrared luminous sources almost certainly contaminates the L_{IR} from the observed galaxies and quasars, thus causing a potentially significant overestimate in the SFR. Second, as the objects span a large range in redshifts, the rest frame transitions observed are typically quite diverse, and thus not always probing the same phase of gas. The cumulative L_{IR} -CO luminosity (over numerous transitions) index for sources from $z=0\sim6$ as reported by (author?) (Riechers et al. 2006a) is ~ 1.4 , similar to the local SFR-CO ($J=1-0$) relation. Certainly, at lower luminosities ($L_{\text{IR}} \lesssim 10^{12} L_{\odot}$), the molecular line data is dominated by CO ($J=1-0$) observations of local galaxies. The relationship between L_{IR} and CO luminosity for these sources then is consistent with the results of our simulations if the L_{IR} in the lower luminosity sources is dominated by dust heating by O and B stars. At higher luminosities ($L_{\text{IR}} \gtrsim 10^{12} L_{\odot}$) the sources are characteristically high redshift quasars, submillimeter galaxies and radio galaxies. While the observed CO transition in these sources is typically greater than the ground state transition, the relationship between L_{IR} and CO luminosity retains an index of ~ 1.4 . In contrast, our models (§ 7.4) would predict a slope less than $\sim 1.4-1.6$ if a Schmidt law index of $1.4-1.6$ was valid for these high redshift sources. One possible origin for this steeper slope is a contribution to the L_{IR} from embedded AGN.

Alternatively, the models presented here (as well as those of Krumholz & Thompson 2007) suggest that high critical density tracers such as HCN ($J=1-0$) and high lying

CO transitions may show a natural upturn from the SFR-line luminosity relation at the highest luminosities even without the contribution of embedded AGN. The galaxies at this end of the luminosity range are typically massive starbursts and/or advanced mergers with significant amounts of dense gas. As shown in Figure 7.4 in the high mean gas density regime, tracers of dense gas such as CO (J=3-2) and HCN (J=1-0) become thermalized. The galaxies in our simulations with the highest SFRs (typically recently coalesced mergers) contain a large amount of dense gas, and thus most of their e.g. CO (J=3-2) emission arises from thermalized cells. The luminosity from this gas rises linearly with increasing cloud density (β), and the consequent SFR-molecular line relation (α) will be superlinear (nearly equivalent to the Schmidt SFR index) for a sample of these galaxies. This is consistent with the modeling results of (author?) (Krumholz & Thompson 2007) who find a similar upturn in their SFR-molecular line relations when the mean cloud density is much greater than the critical density of the molecular line, as well as the observational results of (author?) (Gao et al. 2007).

We reiterate caution, however, that the SFR is typically derived from L_{IR} measurements, and at these high infrared luminosities, the L_{IR} may have a non-negligible contribution from a central AGN (e.g. Kim et al. 2002; Tran et al. 2001; Veilleux et al. 2002). While in principle our hydrodynamic simulations have the capability to investigate the potential contribution from growing black holes, a full calculation of the IR SED as well as relating it to inferred SFR properties is outside the scope of this work. The salient point of these models, as well as those of (author?) (Krumholz & Thompson 2007) regarding these high luminosity points is that *regardless of the potential contribution of embedded AGNs* these dense, star forming systems will systematically lie above the linear relation between L_{IR} and HCN (J=1-0)/CO (J=3-2) seen for lower luminosity ($L_{\text{IR}} \lesssim 10^{12} L_{\odot}$) systems.

7.7 Relationship to Other Models and Interpretations

We now turn our attention toward other models and interpretations for the observed SFR-molecular line relations, and how our solution compares to these works.

(author?) (Gao & Solomon 2004b) interpret the tight linear correlation between L_{IR} and HCN (J=1-0) luminosity as evidence for an increasing fraction of dense gas in the most luminous sources in their sample, as well as a constant star formation efficiency in terms of dense ($n \gtrsim 10^5 \text{ cm}^{-3}$) molecular gas mass. Because stars form in the dense cores of clouds, the linear relationship between L_{IR} (which is powered by star formation) and HCN (J=1-0) luminosity is interpreted as a natural one.

Our models find that the fraction of dense molecular gas naturally increases with star formation rate. This is true both for the mergers which funnel cold gas into the central kiloparsec (fueling starbursts of $\sim 100 \text{ M}_{\odot} \text{ yr}^{-1}$), as well as isolated disk galaxies. Indeed this is an expected result as the SFR in our simulations is parametrized in terms of the cold gas density. This results in a higher fraction of the gas being thermalized in high critical density tracers in the systems with the highest SFRs (and, by extension, highest infrared luminosities). Conversely, the quiescent star forming disk galaxies have a smaller fraction of their gas in a dense phase, and more of their HCN (J=1-0) and CO (J=3-2) emission driven by subthermal excitation. In this sense, then, the interpretation by **(author?)** (Gao & Solomon 2004b) is simply another way of describing the argument outlined in § 7.4. That is, galaxies with high SFRs have higher fractions of dense gas, and galaxies with lower SFRs have less. That said, we note that this is not the driving force behind the SFR-line luminosity relations in our models (§ 7.4), but rather a contribution from subthermal gas.

Utilizing observations of Galactic cloud cores, **(author?)** (Wu et al. 2005) found that the dense Galactic cloud cores showed a linear relationship between L_{IR} and HCN ($J=1-0$) emission. Using these results, they posited that the linear relationship between L_{IR} and HCN ($J=1-0$) emission arises from HCN tracing fundamental star forming units which scale self-similarly from star forming regions in the Galaxy to ULIRGs. In the context that even high critical density tracers such as HCN and CS are thermalized in star forming cores (a result supported by both observational and theoretical evidence, e.g. Shirley et al. 2003; Walker et al. 1994; Walker et al. 1994), the model results presented here are compatible with the observed results of **(author?)** (Wu et al. 2005). The simulations here show that when the mean cloud density approaches the critical density of a molecular line, the line luminosity faithfully traces the cloud density (e.g. Figure 7.4, left panel). Thus, we can speculate that our model results for gas of a high mean density is compatible with the findings of **(author?)** (Wu et al. 2005), though note that our simulations do not have the spatial resolution to robustly determine this.

An interesting question, in the context of these two sets of observations, arises in connecting the SFR-molecular line relation as seen in GMC cores to galaxy-wide scales. The observations of **(author?)** (Wu et al. 2005) focus on regions that are physically representative of the birthplace of stars, though it is not clear that they are not representative of the globally averaged conditions probed by **(author?)** (Gao & Solomon 2004a, Gao & Solomon 2004b). The models presented in this work do not have the spatial resolution to investigate the nature of emission from individual dense GMC cores. While our models can investigate observables from regions with high mean density, we are not able to decouple the emission from dense cores from the diffuse gas in GMC cloud envelopes (Narayanan et al. 2007b). However, a combination of the complementary mod-

eling results by **(author?)** (Krumholz & Thompson 2007) and this work may shed some light on to the connection between the works by **(author?)** (Wu et al. 2005) and **(author?)** (Gao & Solomon 2004a, Gao & Solomon 2004b).

The recent study by **(author?)** (Krumholz & Thompson 2007) utilized radiative transfer modeling coupled with physical models of GMCs (consistent with turbulence-regulated star formation) to derive a motivation for the observed SFR-molecular line relations. These authors found that for individual star forming clouds, the line luminosity from high critical density tracers such as HCN ($J=1-0$) increased superlinearly with mean gas density owing to an increase in the fraction of dense gas with increasing mean cloud density. This results in a linear relationship between SFR and HCN ($J=1-0$) luminosity. While the physical size scales probed are vastly different in this work as compared to that of **(author?)** (Krumholz & Thompson 2007), both works are able to self-consistently reproduce the observed relations between SFR, CO ($J=1-0$), and HCN ($J=1-0$) luminosity. The reasoning for this is a redistribution of light from dense cloud cores on a globally averaged scale. In our models, part of the emission from dense, thermalized regions escapes the galaxy while a fraction of the line luminosity is trapped by gas of a lower mean density, and then re-emitted. The emission patterns in individual clouds which are characterized by the observed SFR-line luminosity relations (e.g. Krumholz & Thompson 2007) scale naturally to galaxy-wide globally averaged measurements. This result is not unexpected from our simulations. Galaxies with higher SFRs have, on average, higher mean cloud densities than galaxies with lower SFRs. These systems are thus expected to follow comparable scaling relations as the model clouds investigated by **(author?)** (Krumholz & Thompson 2007) for GMCs of increasing mean cloud density. These model results may be directly tested as they predict that tracers of

higher critical density than HCN ($J=1-0$) or CO ($J=3-2$) will be thermalized in a small fraction of the galaxy's gas mass, and show a sublinear relationship between SFR and line luminosity (Figure 7.8).

Finally, we note that we include constant molecular abundances throughout our model galaxies, as a full chemical reaction network is both outside the scope of this work and not feasible given our spatial resolution limitations. In this sense, we are unable to evaluate these models in terms of potential HCN chemistry in the vicinity of a hard X-ray flux as has been argued by some authors. (e.g. ? Graciá-Carpio et al. 2006; Lintott & Viti 2006). We do note, though, that our models quantitatively reproduce the observed relations between SFR and CO ($J=1-0$), CO ($J=3-2$) and HCN ($J=1-0$) emission in local galaxies while utilizing constant fractional molecular abundances. This may imply that potential chemistry-related effects have a negligible effect on observed SFR-molecular line relations.

7.8 Conclusions and Summary

We have utilized a combination of self-consistent 3D non-LTE radiative transfer calculations with hydrodynamic simulations of isolated disk galaxies and galaxy mergers to derive a physical model for the observed SFR-molecular line relations. We specifically focus on the examples of the SFR-CO ($J=1-0$), CO ($J=3-2$) and HCN ($J=1-0$) relations as they are the best constrained observationally, and show that our model quantitatively reproduces the observed relations when a Schmidt index of ~ 1.5 is assumed.

While the linear relationship between SFR and high critical density tracers such as HCN ($J=1-0$) and CO ($J=3-2$) in galaxies have been interpreted as a fundamental SFR law owing to dense gas being the formation site of massive stars,

our models suggest that this is not the entire story. The linear relations of SFR and HCN ($J=1-0$) and CO ($J=3-2$) arise as a consequence of line trapping by diffuse molecular gas in the vicinity of dense cloud cores, resulting in significant emission from subthermally excited gas. The fundamental relation is instead the underlying Schmidt law which sets the way in which observed transitions trace the molecular gas.

Our model makes the prediction that for CO lines with $J_{\text{upper}} > 3$ and HCN lines with $J_{\text{upper}} > 2$, the SFR-line luminosity relationships will be sublinear (Figure 7.8). These predictions can directly be tested with existing submillimeter-wave technology, as well as with ALMA. Our models additionally provide specific interpretation regarding the existing observed SFR-molecular line relations:

1. The slope in a given SFR-molecular line luminosity relation is dependent on both the assumed Schmidt law controlling the SFR for the galaxy and the relationship between molecular line luminosity and density of emitting gas (the details of which are outlined in § 7.4). When line luminosity traces gas density linearly, the resultant SFR-line luminosity index is similar to the assumed Schmidt law index. In cases where the line luminosity increases with gas density superlinearly, the SFR is related to line luminosity with an index less than the Schmidt index. The relationship between line luminosity and gas density depends on how the critical density of the line compares with the mean density of the bulk of the emitting clouds. This directly affects the observed relations between SFR and CO ($J=1-0$), CO ($J=3-2$) and HCN ($J=1-0$) in the following way:
 - (a) Owing to its low critical density, the CO ($J=1-0$) line is roughly thermalized throughout most regions of the galaxies in our simulation sample.

This results in a linear rise in CO (J=1-0) luminosity with increasing gas density, and a consequent SFR-CO (J=1-0) relationship with index similar to the Schmidt index. For the case of a Schmidt index of ~ 1.5 , our simulations reproduce the observed relation between SFR and CO (J=1-0) luminosity.

- (b) The critical densities of CO (J=3=2) and HCN (J=1-0) are much higher than the mean density of the bulk of the clouds in our simulated galaxies. Because of this, significant amounts of emission can arise from subthermally excited diffuse gas in the vicinity of denser regions. This subthermally excited gas emits at intensities higher than its meager densities can account for owing to radiative pumping. A combination of emission from subthermally excited gas along with gas in LTE (whose emission traces increasing gas density linearly) along the line of sight results in a net superlinear relationship between intensity and gas density. The consequence of this is an SFR-line luminosity index less than the Schmidt index for high critical density tracers. For the case of a Schmidt index of ~ 1.5 , the observed relations between SFR and HCN (J=1-0) and CO (J=3-2) emission are recovered.
2. The emission processes driving the line luminosity-density relations (and consequently SFR-line luminosity relations) are variable such that some galaxies exhibit mostly thermalized gas for high critical density tracers whereas others are largely subthermally excited. Generally, the galaxies with higher SFRs have more of their gas thermalized which may drive the upturn in the L_{IR} -HCN (J=1-0) relationship for extremely high luminosity sources observed by **(author?)** (Gao et al. 2007).

CHAPTER 8

CONCLUDING REMARKS AND WAYS FORWARD

So...what are we supposed to have learned from this work?

-Juna Kollmeier, during the Q&A period after I gave a talk on the subject nature of Chapter 7.

In this thesis, I have explored emission from the molecular interstellar medium in environments ranging from protoplanetary disks to some of the earliest quasar host galaxies. In this, we saw that molecular line emission has the power to serve as a probe for interesting astrophysical effects. It can betray the presence of dense gas clumps which may form into gas giant planets, serve as a signature for galactic scale winds in galaxies, and provide a measure for the SFR in galaxies. Even more broadly, in this thesis I have attempted to provide *interpretation* for existing molecular line observations of varying astrophysical environments, and provide a sample of predictions for future observations. A key contribution from this thesis to the field has been (save for Chapter 6) mechanisms for interpreting existing and future observations.

There are, to some degree, a large number of avenues one could take with the existing tools regarding interpretation and predictions of molecular line emission from the cosmos. For example, as I alluded to in the discussion of Chapter 5, the CO line widths on average trace the virial velocity of galaxy host halos. By extending these line widths to $z \sim 2$ simulations, one might be able to make inferences regarding the evolutionary state of the intriguing submillimeter-luminous galaxies at this redshift based on their line widths. Further simulations of galaxy accretion and merging in $\sim 10^{13} M_{\odot}$ halos scaled for $z \sim 2$ would further solidify

this potential interpretation for the seemingly anomalously large line widths in these sources. Similarly, the methods presented in this thesis could be used to explore e.g. molecular disk formation in local ULIRGs (Scoville & Bryant, 1999), the effects of an ‘intracloud medium’ and the related molecular gas volume filling factor (Downes & Solomon, 1998), and CO luminosity functions in the local and distant Universe (e.g. Keres, Yun & Young, 2003).

From a theoretical standpoint, however, the methods presented in this thesis can only go so far. That is, the coarse resolution presented in these models forces our radiative transfer solutions to be dependent on a host of assumptions (Chapter 2) which limits the self-consistency of the models. In this regard, in the current state, the models will largely be limited to interpretive functions. The way forward is a mechanism for deriving concrete physical quantities from molecular line measurements. More specifically, the holy grail of potential contributions simulations have to offer to molecular astrophysics is a robust investigation into the conversion factor from molecular line luminosity to an H_2 gas mass - the so-called χ_{CO} factor.

Observational determinations suggest that the global conversion factor between CO luminosity and H_2 gas mass can vary by a factor of ~ 2 within the Galaxy, and by as much as a factor of ~ 5 when considering more extreme galaxies such as ULIRGs (e.g. Downes & Solomon, 1998; Gao & Solomon, 2004a). Moreover, using standard Galactic values, it is feasible to derive molecular gas masses larger than the dynamical mass in nearby galaxies (Downes & Solomon, 1998), highlighting the difficulty in using such a conversion factor given our current understanding of it. While observations have made at least some headway in constraining the range of possible CO- H_2 conversion factors, modeling has made little concomitant progress in narrowing these values, or understanding

how and why they may change in given astrophysical environments. In an era where galaxy formation models are relying on precision measurements of physical parameters, factors of ~ 5 uncertainty in mass measurements will quickly become a limiting factor in the analysis of forthcoming data sets.

So, what exactly will be necessary for simulations in forthcoming years to make a dent in this historically untractable problem? What has been lacking thus far is spatial resolution for the hydrodynamic and radiative transfer models. We have limited ourselves to ~ 100 - 250 pc resolution for the radiative transfer simulations in this work, though in principle achieving the ~ 40 pc resolution native to the hydrodynamic simulations is feasible with the available computing power. Load-balancing issues in the hydrodynamic simulations forced galaxy-scale simulations to the above quoted resolution, though newer existing algorithms will allow the spatial resolution to drop by a factor of ~ 4 (L. Hernquist, private communication).

Still, even at ~ 10 pc resolution, individual GMCs will only barely be resolved. In the next few years, as computing power allows for a subsequent increase in resolution by \sim an order of magnitude, models will be able to follow the pertinent physics concerning the star forming interstellar medium in galaxies. With a reasonable idea of the UV flux, cosmic ray flux, temperatures and densities throughout the galaxy, it will be feasible to calculate the H_2 mass fraction in the cold neutral medium, the CO/H_2 abundances, and subsequent emission patterns utilizing radiative transfer models such as those presented in this work. Curves of N_{H_2}/I_{CO} will lead to derivations of χ_{CO} under varied physical conditions.

As a note of encouragement, even radiative transfer simulations rife with assumptions (Chapter 2) can to zeroth order reproduce observed results. As an example of this, in Figure 8.1, I plot a distribution of the N_{H_2}/I_{CO} values for 50^2

lines of sight through a fiducial disk galaxy with 40% gas fraction and $v_{200} \sim 120$ km s⁻¹, utilizing the methods presented in this thesis. The mean derived ratio is $\sim 4.2 \times 10^{20} \text{ cm}^{-2} (\text{K-km s}^{-1})^{-1}$, consistent with the accepted Galactic value of $\sim 3 \times 10^{20} \text{ cm}^{-2} (\text{K-km s}^{-1})^{-1}$. This is, of course, somewhat circular as I have manifestly assumed molecular gas fractions and abundances consistent with local observations. However, it is promising that the methodology is largely in place to attack this fundamental problem, and understand its origins and variations with physical condition.

And with that note of encouragement, I conclude this thesis. It is my hope that the reader walks away having read this work with a feeling that much can be done by combining the existing tools of varied fields in astrophysics. Moreover, the promise of what lies on the horizon with increased computational ability and physical constraints motivated by ground-breaking observations is truly exciting.

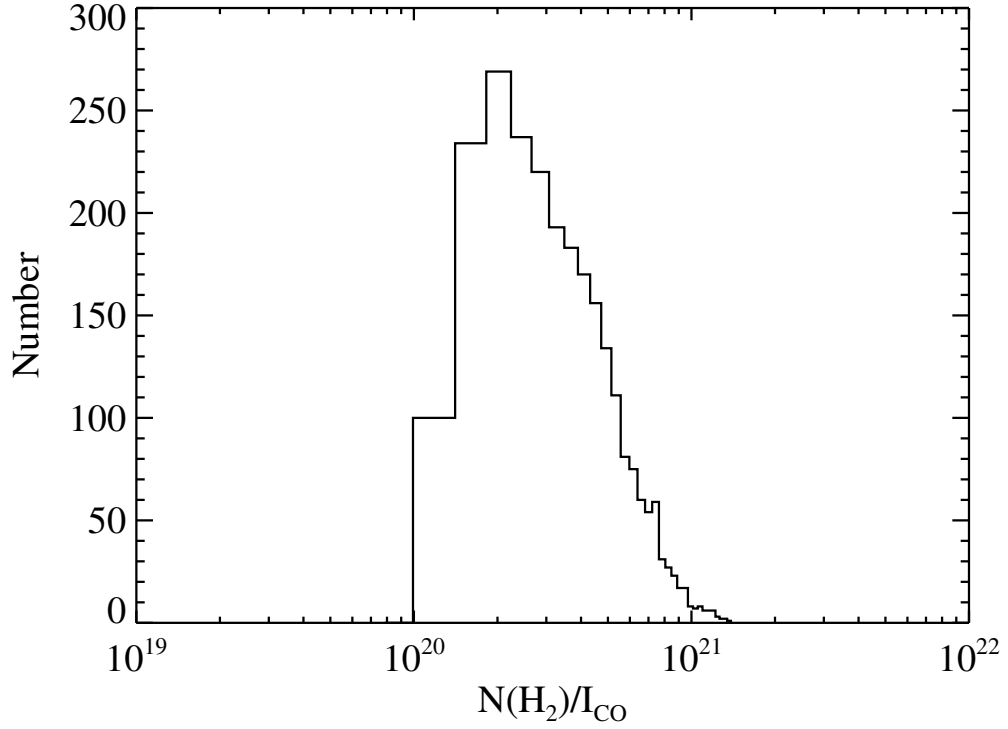


Figure 8.1 Distribution of N_{H_2}/I_{CO} values for 50² lines of sight through a fiducial disk galaxy. The galaxy has a 40% gas fraction, and circular velocity set at $\sim 120 \text{ km s}^{-1}$. The mean ratio is $\sim 4.2 \times 10^{20} \text{ cm}^{-2} (\text{K-km s}^{-1})^{-1}$, consistent with the accepted Galactic value of $\sim 3 \times 10^{20} \text{ cm}^{-2} (\text{K-km s}^{-1})^{-1}$.

REFERENCES

- [Abel et al. 2002] Abel, T., Bryan, G.L., Norman, M.L., 2002 *Science*, 295, 93
- [Aikawa & Herbst 1999] Aikawa, Y., Herbst, E., 1999, *A&A*, 351,233
- [Aikawa & Herbst 1999] Aikawa, Y., Herbst, E., 1999, *A&A*, 351,233
- [Alexander et al. 2005a] Alexander, D.M., Bauer, F.E., Chapman, S.C., Smail, I., Blain, A.W., Brandt, W.N., Ivison, R.J., 2005a, *ApJ*, 632, 736
- [Alexander et al. 2005b] Alexander, D.M., Smail, I., Bauer, F.E., Chapman, S.C., Blain, A.W., Brandt, W.N., Ivison, R.J., 2005b, *Nature*, 434, 38
- [Alton et al. 1999] Alton, P.B., Davies, J.I., Bianchi, S., 1999, *A&A*, 343, 51
- [Andre et al. 1996] Andre, P., Ward-Thompson, D., Motte, F., 1996, *A&A*, 314, 625
- [Andrews & Williams 2005] Andrews, S., Williams, J.P., 2005, *ApJ*, 619,175
- [Appleton et al. 2002] Appleton, P., Charmandaris, V., Gao, Y., Combes, F., Ghigo, F., Horellou, C., Mirabel, I.F., 2002, *ApJ*, 566, 682
- [Armus et al. 2004] Armus, L., et al., 2004, *ApJS*, 154, 178
- [Armus et al. 2006] Armus, L., Bernard-Salas, J., Spoon, H.W.W., Marshall, J.A., Charmandaris, V., Higdon, S.J.U., Desai, V., Hao, L., Teplitz, H.I., Devost, D., Brandl, B.R., Soifer, B.T., Houck, J.R., 2006, *ApJ*, 640, 204
- [Ashby et al. 1995] Ashby, M.L.N., Houck, J.R., Matthews, K., 1995, *ApJ*, 447,545
- [Barnes & Hernquist 1991] Barnes, J.E., Hernquist, L.E., 1991, *ApJ*, 370, L65
- [Barnes & Hernquist 1996] Barnes, J.E., Hernquist, L.E., 1996, *ApJ*, 471, 115

- [Barth et al. 2003] Barth, A.J., Martini, P., Nelson, C.H., Ho, L.C., 2003, *ApJ*, 594, L95
- [Barvainis et al. 1997] Barvainis, R., Maloney, P., Antonucci, R., Alloin, D., 1997, *ApJ*, 484, 695
- [Bastian 2002] Bastian, T.S., 2002, *Astronomische Nachrichten*, 323, 271
- [Bayet et al. 2004] Bayet, E., Gerin, M., Phillips, T.G., & Contursi, A., 2004, *A&A*, 427, 45
- [Bernes 1979] Bernes, C., 1979, *A&A*, 73, 67 Scoville, N.Z., 1999, *AJ*, 117, 2632
- [Bertoldi et al. 2003a] Bertoldi, F., Cox, P., Neri, R., Carilli, C.L., Walter, F., Omont, A., Beelen, A., Henkel, C., Fan, X., Strauss, M., Menten, K., 2003a, *A&A*, 409, L47
- [Bertoldi et al. 2003b] Bertoldi, F., Carilli, C.L., Cox, P., Fan, X., Strauss, M.A., Beelen, A., Omont, A., Zylka, R., 2003b, *A&A*, 406, L55
- [Beuzit et al. 2006] Beuzit, J.-L., Mouillet, D., Oppenheimer, B., Monnier, J. 2006, 'Direct Imaging of Extra-Solar Planets', in *Protostars and Planets V*
- [Blain et al. 1999] Blain, A.W., Kneib, J.-P., Ivison, R.J., Smail, I., 1999, *ApJ*, 512, L87
- [Blain et al. 2002] Blain, A.W., Smail, I., Ivison, R.J., Kneib, J.-P., Frayer, D.T., 2002, *PhR*, 369, 111
- [Blain et al. 2004] Blain, A.W., Chapman, S.C., Smail, I., Ivison, R., 2004, *ApJ*, 611, 725

- [Blitz et al. 2006] Blitz, L., Fukui, Y., Kawamura, A., Leroy, A., Mizuno, N., Rosolowsky, E., 2006, "Giant Molecular Clouds in Local Group Galaxies", in *Protostars and Planets V* [astro-ph/0602600]
- [Bondi 1952] Bondi, H., 1952, MNRAS, 112, 195
- [Bondi & Hoyle 1944] Bondi, H., Hoyle, F., 1944, MNRAS, 104, 273
- [Borys et al. 2005] Borys, C., Smail, I., Chapman, S.C., Blain, A.W., Alexander, D.M., Ivison, R.J., 2005, ApJ, 635, 853
- [Boss 2004] Boss, A.P., 2004, ApJ, 610, 456
- [Boss 2001] Boss, A.P., 2001, ApJ, 563, 367
- [Boss 1998] Boss, A.P., 1998, ApJ, 503, 923
- [Boss 1997] Boss, A.P., 1997, *Science*, 276, 1836
- [Boss & Myhill 1992] Boss, A.P., Myhill, E.A., 1992, ApJS, 83, 311
- [Boss & Yorke 1990] Boss, A.P., Yorke, H.W., 1990, ApJ, 353, 236
- [Bradford et al. 2003] Bradford, C.M., Nikola, T., Stacey, G., Bolatto, A.D., Jackson, J.M., Savage, M.L., Davidson, J.A., Higdon, S.J., 2003, ApJ, 586, 891
- [Bradford et al. 2005] Bradford, C.M., Stacey, G.J., Nikola, T., Bolatto, A.D., Jackson, J.M., Savage, M.L., Davidson, J.A., 2005, ApJ, 623, 866
- [Bromm & Larson 2004] Bromm, V., Larson, R.B., 2004, ARA&A, 42, 79
- [Bryant & Scoville 1999] Bryant, P., Scoville, N., 1999, AJ, 117, 2632

- [Carilli et al. 2002] Carilli, C.L., Cox, P., Bertoldi, F., Menten, K.M., Omont, A., Djorgovski, S.G., Petric, A., Beelen, A., Isaak, K.G., McMahon, R.G., 2002, ApJ, 575, 145
- [Carilli et al. 2004] Carilli, C.L., Solomon, P., Vanden Bout, P., Walter, F., Beelen, A., Cox, P., Bertoldi, F., Menten, K.M., Isaak, K.G., Chandler, C.J., Omont, A., 2004, ApJ, (astro-ph/0409054)
- [Carilli et al. 2005] Carilli, C., Solomon, P., Vanden Bout, P., Walter, F., Beelen, A., Cox, P., Bertoldi, F., Menten, K.M., Isaak, K.G., Chandler, C.J., Omont, A., 2005, ApJ, 618, 586
- [Carilli & Wang 2006] Carilli, C.L., Wang, R., 2006, ApJ, 131, 2763
- [Carilli et al. 2007] Carilli, C.L., Neri, R., Wang, R., Cox, P., Bertoldi, F., Walter, F., Fan, X., Menten, K., Wagg, J., Maiolino, R., Omont, A., Strauss, M.A., Riechers, D., Lo, K.Y., Bolatto, A., Scoville, N., 2007, ApJ, 666L, 9
- [Chakrabarti et al. 2007a] Chakrabarti, S., Cox, T.J., Hernquist, L., Hopkins, P.F., Robertson, B., Di Matteo, T., 2007a, ApJ, 658, 840
- [Chakrabarti et al. 2007b] Chakrabarti, S., Fenner, Y., Hernquist, L., Cox, T.J., Hopkins, P.F., 2007b, ApJ, submitted [astro-ph/0610860]
- [Chapman et al. 2004] Chapman, S.C., Smail, I., Windhorst, R., Muxlow, T., Ivison, R.J., 2004, ApJ, 611, 732
- [Charbonneau et al. 2006] Charbonneau, D., Brown, T., Burrows, A., Laughlin, G., 2006, 'When Extrasolar Planets Transit Their Parent Stars', in *Protostars and Planets V*
- [Chini et al. 1996] Chini, R., Krugel, E., Lemke, R., 1996, A&A, 118, 47

- [Choi et al. 1995] Choi, M.H., Evans, N.J., Gregersen, E.M., Wang, Y.S., 1995, *ApJ* 448, 742
- [Close et al. 1995] Close, L.M., Hall, P.B., Liu, C.T., Hege, E.K., 1995, *ApJ*, 452L, 9
- [Combes 1999] Combes, F., Maoli, R., Omont, A., 1999, *A&A*, 345, 369
- [Cox et al. 2004] Cox, T.J., Jonsson, P., Primack, J.R., Somerville, R.S., 2004, *ApJ*, 607, L87
- [Cox et al. 2006a] Cox, T.J., Dutta, S.N., Di Matteo, T., Hernquist, L., Hopkins, P.F., Robertson, B., Springel, V., 2006a, *ApJ*, 650, 791
- [Cox et al. 2006b] Cox, T.J., Di Matteo, T., Hernquist, L., Hopkins, P.F., Robertson, B., Springel, V., 2006b, *ApJ*, 643, 692
- [Cox et al. 2006c] Cox, T. J., Jonsson, P., Primack, J. R., & Somerville, R. S. 2006, *MNRAS*, 373, 1013
- [Cox et al. 2007] Cox, T.J., Chakrabarti, S., Di Matteo, T., Hernquist, L., Hopkins, P.F., Krause, E., Li, Y., Robertson, B., Springel, V., 2007, *ApJ*, submitted
- [Croton et al. 2006] Croton, D. J., et al. 2006, *MNRAS*, 365, 11
- [Croom et al. 2005] Croom, S.M., Boyle, B.J., Shanks, T., Smith, R.J., Miller, L., Outram, P.J., Loaring, N.S., Hoyle, F., da Angela, J., 2005, *MNRAS*, 356, 415
- [Currie 2004] Currie, T., 2005, *ApJ*, 629, 549
- [Davé et al. 1999] Davé, R., Hernquist, L., Katz, N.,
- [de Grijp et al. 1985] de Grijp, M.H.K., Miley, G.K., Lub, J., de Jong, T., 1985, *Nature*, 314, 240

- [Dietrich et al. 2003a] Dietrich, M., Hamann, F., Appenzeller, I., Vestergaard, M., 2003a, *ApJ*, 596, 817
- [Dietrich et al. 2003b] Dietrich, M., Hamann, F., Shields, J.C., Constantin, A., Heidt, J., Jager, K., Vestergaard, M., Wagner, S.J., 2003b, *ApJ*, 589, 722
- [Di Matteo et al. 2005] Di Matteo, T., Springel, V., Hernquist, L., 2005, *Nature*, 433, 604
- [Di Matteo et al. 2007] Di Matteo, T., Colberg, J., Springel, V., Hernquist, L., Sijacki, D., 2007, *ApJ*, submitted [astro-ph/0705.2269]
- [Donley et al. 2005] Donley, J.L., Rieke, G.H., Rigby, J.R., Pérez-González, P.G., 2005, *ApJ*, 634, 169
- [Downes & Solomon 1998] Downes, D., Solomon, P.M., 1998, *ApJ*, 507, 614
- [Dutrey et al. 1997] Dutrey A., Guilloteau, S. Guelin, M., 1997, *A&A*, 317, L55
- [Elmegreen & Falgarone 1996] Elmegreen, B., Falgarone, E., 1996, *ApJ*, 471, 816
- [Evans et al. 1998] Evans, A.S., Kim, D.C., Mazzarella, J.M., Scoville, N.Z., Sanders, D.B., 1999, *ApJ*, 521, 107
- [Evans 1999] Evans, N.J., 1999, *ARA&A*, 37, 311
- [Fabian 1999] Fabian, A.C., 1999, *MNRAS*, 308, L39
- [Fan et al. 2002] Fan, X., Narayanan, V.K., Strauss, M.A., White, R.L., Becker, R.H., Pentericci, L., & Rix, H., 2002, *AJ*, 123, 1247
- [Fan et al. 2003] Fan, X., et al., 2003, *AJ*, 125, 1649
- [Fan et al. 2004] Fan, X., et al., 2004, *AJ*, 128, 515

- [Farrah et al. 2003] Farrah, D., Afonso, J., Efstathiou, A., Rowan-Robinson, M., Fox, M., Clements, D., 2003, MNRAS, 343, 585
- [Faucher-Giguere et al. 2007] Faucher-Giguere, C., Lidz, A., Zaldarriaga, M., & Hernquist, L., 2007, ApJ, in press [astro-ph/0701042]
- [Ferrarese & Merritt 2000] Ferrarese, L., Merritt, D., 2000, ApJ, 539, L9
- [Finlator et al. 2006] Finlator, K., Davé, R., Papovich, C., Hernquist, L., 2006, ApJ, 639, 672
- [Finlator & Davé 2007] Finlator, K., & Davé, R. 2007, ArXiv e-prints, 704, arXiv:0704.3100
- [Freudling et al. 2003] Freudling, W., Corbin, M.R., & Korista, K.T., 2003, ApJ, 587, L67
- [Fuller & Myers 1992] Fuller, G.A., Myers, P.C., 1992, ApJ, 384, 523
- [Ganguly et al. 2006] Ganguly, R., Sembach, K.R., Tripp, T.M., Savage, B.D., Wakker, B.P., 2006, ApJ, 645, 868
- [Gao & Solomon 1999] Gao, Y., Solomon, P.M., 1999, ApJ, 512, L99
- [Gao & Solomon 2004a] Gao, Y., Solomon, P.M., 2004a, ApJS, 152, 63
- [Gao & Solomon 2004b] Gao, Y., Solomon, P.M., 2004b, 606, 271
- [Gao et al. 2005] Gao L., White S. D. M., Jenkins A., Frenk C. S., Springel V., 2005, MNRAS, 363, 379
- [Gao et al. 2007] Gao, Y., Carilli, C. L., Solomon, P. M., & Vanden Bout, P. A. 2007, ApJL, 660, L93

- [Gebhardt et al. 2000] Gebhardt, K., Bender, R., Bower, G., Dressler, A., Faber, S.M., Filippenko, A.V., Green, R., Grillmair, C., Ho, L.C., Kormendy, J., Lauer, T.R., Magorrian, J., Pinkney, J., Richstone, D., Tremaine, S., 2000, 539, L13
- [Goldreich & Kwan 1974] Goldreich, P., & Kwan, J. 1974, ApJ, 189, 441
- [Goldreich et al. 2004a] Goldreich, P., Lithwick, Y., Sari, R., 2004, ARA&A, 42,549
- [Goldreich et al. 2004b] Goldreich, P. Lithwick, Y., Sari, R., 2004, ApJ, 614,
- [Graciá-Carpio et al. 2006] Graciá-Carpio, J., García-Burillo, S., Planesas, P., & Colina, L. 2006, ApJL, 640, L135
- [Greve et al. 2005] Greve, T., Bertoldi, F., Smail, I., Neri, R., Chapman, S.C., Blain, A.W., Ivison, R.J., Genzel, R., Omont, A., Cox, P., Tacconi, L., Kneib, J.-P., 2005, MNRAS, 359, 1165
- [Greve et al. 2006] Greve, T., Sommer-Larsen, J., 2006, ApJ, in press [astro-ph/0608683]
- [Greve et al. 2006] Greve, T. R., Papadopoulos, P. P., Gao, Y., & Radford, S. J. E. 2006, ArXiv Astrophysics e-prints, arXiv:astro-ph/061037
- [Haiman & Loeb 2001)] Haiman, Z., Loeb, A., 2001, ApJ, 662, 459
- [Hainline et al. 2004] Hainline, L.J., Scoville, N.Z., Yun, M.S., Hawkins, D.W., Frayer, D.T., Isaak, K.G., 2004, ApJ, 609, 61
- [Hainline et al. 2006] Hainline, L. J., Blain, A. W., Greve, T. R., Chapman, S. C., Smail, I., & Ivison, R. J. 2006, ApJ, 650, 614
- [Hamann et al. 1997] Hamann, F., Barlow, T.A., Junkkarinen, V., 1997, ApJ, 478,

- [Hattori et al. 2004] Hattori, T., Yoshida, M., Ohtani, H., Sugai, H., Ishigaki, T., Sasaki, Houck, J., Hayashi, T., Ozaki, S., Ishii, M., Kawai, A., 2004, *AJ*, 127,736
- [Heckman et al. 2000] Heckman, T.M., Lehnert, M.D., Strickland, D.K., & Armus, L., 2000, *ApJS*, 129, 493
- [Hernquist 1989] Hernquist, L., 1989, *Nature*, 340, 687
- [Hernquist 1990] Hernquist, L., 1990, *ApJ*, 356, 359
- [Hernquist & Quinn 1987] Hernquist, L., Quinn, P.J., 1987, *ApJ*, 312, 1
- [Hernquist & Spergel 1992] Hernquist, L., Spergel, D.N., 1992, *ApJ*, 399, L117
- [Hogerheijde & van der Tak 2000] Hogerheijde, M.R., van der Tak, F.F.S., 2000, *A&A*, 362,697
- [Hogerheijde et al. 2002] Hogerheijde, M.R., Jayawardhana, R., Johnstone, D., Blake, G., Kessler, J., 2002, *ApJ*, 124,3387
- [Hollenbach & Tielens 1999] Hollenbach, D. J., & Tielens, A. G. G. M. 1999, *Reviews of Modern Physics*, 71, 173
- [Hollenbach et al. 1979] Hollenbach, D.J., Werner, M.W., & Salpeter, E.E., 1971, *ApJ*, 163, 165
- [Hopkins et al. 2005a] Hopkins, P.F., Hernquist, L., Martini, P., Cox, T.J., Robertson, B., Di Matteo, T., Springel, V., 2005a, *ApJ*, 625, L71
- [Hopkins et al. 2005b] Hopkins, P.F., Hernquist, L., Cox, T.J., Di Matteo, T., Martini, P., Robertson, B., Springel, V., 2005b, *ApJ*, 630, 705
- [Hopkins et al. 2005c] Hopkins, P.F., Hernquist, L., Cox, T.J., Di Matteo, T., Robertson, B., Springel, V., 2005c, *ApJ*, 630, 716

- [Hopkins et al. 2005d] Hopkins, P.F., Hernquist, L., Cox, T.J., Di Matteo, T., Robertson, B., Springel, V., 2005d, ApJ, 632, 81
- [Hopkins et al. 2006a] Hopkins, P.F., Hernquist, L., Cox, T.J., Di Matteo, T., Robertson, B., Springel, V., 2006a, ApJS, 163, 1
- [Hopkins et al. 2006b] Hopkins, P.F., Hernquist, L., Cox, T.J., Robertson, B., Springel, V., 2006b, ApJS, 163, 50
- [Hopkins et al. 2006c] Hopkins, P.F., Hernquist, L., Cox, T.J., Robertson, B., Di Matteo, T., Springel, V., 2006c, ApJ, 639, 700
- [Hopkins et al. 2006d] Hopkins, P.F., Somerville, R., Hernquist, L., Cox, T.J., Robertson, B., Li, Y., 2006d, ApJ, 652, 864
- [Hopkins et al. 2007a] Hopkins, P.F., Hernquist, L., Cox, T.J., Robertson, B., Krause, E., 2007a, ApJ, in press [astro-ph/0707.4005]
- [Hopkins et al. 2007b] Hopkins, P.F., Hernquist, L., Cox, T.J., Robertson, B., Krause, E., 2007b, ApJ, in press [astro-ph/0701351]
- [Hopkins et al. 2007c] Hopkins, P.F., Hernquist, L., Cox, T.J., Keres, D., 2007c, ApJ, submitted [astro-ph/0706.1243]
- [Hopkins et al. 2007d] Hopkins, P.F., Cox, T.J., Keres, D., Hernquist, L., 2007d, ApJ, submitted [astro-ph/0706.1246]
- [Hopkins et al. 2007e] Hopkins, P.F., et al., 2007e, ApJ, in preparation
- [Hopkins et al. 2007f] Hopkins, P.F., et al., 2007f, ApJ, in preparation
- [Hopkins et al. 2007g] Hopkins, P.F., et al., 2007g, ApJ, in preparation

- [Hopkins et al. 2007h] Hopkins, P.F., Richards, G.T., Hernquist, L., 2007h, *ApJ*, 654, 731
- [Hopkins et al. 2007i] Hopkins, P.F., Lidz, A., Hernquist, L., Coil, A.L., Myers, A.D., Cox, T.J., Spergel, D.N., 2007, *ApJ*, in press [astro-ph/0611792]
- [Hopkins & Hernquist 2006] Hopkins, P.F., Hernquist, L., 2006, *ApJS*, 166, 1
- [Hoyle & Lyttleton 1939] Hoyle, F., Lyttleton, R.A., 1939, in *Proceedings of the Cambridge Philosophical Society*, 405
- [Ikoma et al. 2000] Ikoma, M., Nakazawa, K., Emori, H., 2000, *ApJ*, 537, 1013
- [Imanishi 2000] Imanishi, M., 2000, *MNRAS*, 319, 331
- [Imanishi et al. 2001] Imanishi M., Dudley, C.C., Maloney, P.R., 2001, *ApJ*, 558L, 93.
- [Imanishi et al. 2003] Imanishi, M., Terashima, Y., Anabuki, N., Nakagawa, T., 2003, *ApJ*, 596L, 167
- [Iono et al. 2004] Iono, D., Ho, P.T.P., Yun, M., Matsushita, S., Peck, A., Sakamoto, K., 2004, *ApJ*, 616, L63
- [Iono et al. 2005] Iono, D., Yun, M.S., Ho, P.T.P., 2005, *ApJS*, 158, 1
- [Iono et al. 2007] Iono, D., Wilson, C.D., Takakuwa, S., Yun, M.S., Petitpas, G.R., Peck, A.B., Ho, P.T.P., Matsushita, S., Pihlstrom, Y., Wang, Z., 2007, *ApJ*, 659, 2831
- [Jiang et al. 2006] Jiang, L., Fan, X., Hines, D.C., Shi, Y., Vestergaard, M., Bertoldi, F., Brandt, W.N., Carilli, C., Cox, P., Le Floch, E., Pentericci, L., Richards, G.T.,

- Rieke, G.H., Schneider, D., Strauss, M.A., Walter, F., Brinkmann, J., 2006, *AJ*, 132, 2127
- [Jonsson 2006] Jonsson, P. 2006, *MNRAS*, 372, 2
- [Juvela 1997] Juvela, M., 1997, *A&A*, 332, 943
- [Katz et al. 1996] Katz, N., Weinberg, D.H., Hernquist, L., 1996, *ApJS*, 105, 19
- [Kauffmann & Haehnelt 2000] Kauffmann, G., Haehnelt, M.G., 2000, *MNRAS*, 311, 576
- [Kennicutt 1998a] Kennicutt, R., 1998a, *ApJ*, 498, 541
- [Kennicutt 1998b] Kennicutt, R., 1998b, *ARA&A*, 36, 189
- [Keres et al. 2003] Keres, D., Yun, M., Young, J., 2003, *ApJ*, 582, 659
- [Kessler 2004] Kessler, J., 2004, PhD Thesis, Caltech
- [Kim & Croft 2007] Kim, Y.-R. & Croft, R., 2007, *MNRAS*, in press [*astro-ph/0701012*]
- [Kim & Sanders 1998] Kim, D.-C., & Sanders, D.B., 1998, *ApJS*, 119, 41
- [Kim et al. 2002] Kim, D.-C., Veilleux, S., Sanders, D.B., 2002, *ApJS*, 143, 277
- [Komossa et al. 2003] Komossa, S., Burwitz, V., Hasinger, G., Predehl, P., Kaastra, J.S., Ikebe, Y., 2003, *ApJ*, 582, L15
- [Kormendy & Richstone 1995] Kormendy, J., Richstone, D., 1995, *ARA&A*, 33, 581
- [Kormendy et al. 2007] Kormendy, J., Fisher, D.B., Cornell, M.E., Bender, R., 2007, *ApJ*, submitted

- [Krumholz & McKee 2005] Krumholz, M. R., McKee, C. F., & Klein, R. I. 2005, *ApJL*, 618, L33
- [Krumholz & McKee 2005] Krumholz, M. R., & McKee, C. F. 2005, *ApJ*, 630, 250
- [Krumholz & Thompson 2007] Krumholz, M. R., & Thompson, T. A. 2007, *ArXiv e-prints*, 704, arXiv:0704.0792
- [Krugel et al. 1990] Krugel, E., Steppe, H., Chini, R., 1990, *A&A*, 229,17
- [Kulesa 2002] Kulesa, C.A., 2002, PhD Thesis, *Molecular Hydrogen and its Ions in Dark Interstellar Clouds and Star Forming Regions*, University of Arizona
- [Kulesa et al. 2005] Kulesa, C.A., Hungerford, A.L., Walker, C.K., Zhang, X., Lane, A.P., 2005, *ApJ*, 625, 194
- [Lawrence et al. 1991] Lawrence, A., Rowan-Robinson, M., Leech, K., Jones, D.H.P., Wall, J.V., 1991, *MNRAS*, 240, 329
- [Lee et al. 1996] Lee H-H., Bettens R.P.A., Herbst, E., 1996, *A&AS*, 119, 111L
- [Leech et al. 1994] Leech, K.J., Rowan-Robinson, M., Lawrence, A., Hughes, J.D., 1994, *MNRAS*, 267, 253
- [Li et al. 2007a] Li, Y., Hernquist, L., Robertson, B., Cox, T.J., Hopkins P., Springel, V., Gao, L., Di Matteo, T., Zentner, A., Jenkins, A., Yoshida, N., 2007a, *ApJ*, in press [astro-ph/0608190]
- [Li et al. 2007b] Li, Y., Hernquist, L., Finkbeiner, D., Springel, V., Jiang, L., Fan, X., 2007b, *ApJ*[arXiv:0706.3706]
- [Lidz et al. 2006] Lidz, A., Hopkins, P.F., Cox, T.J., Hernquist, L., Robertson, B., 2006, *ApJ*, 641, L41

- [Lidz et al. 2007] Lidz, A., McQuinn, M., Zaldarriaga, M., Hernquist, L., Dutta, S., 2007, *ApJ*, submitted [astro-ph/0703667]
- [Lintott & Viti 2006] Lintott, C., & Viti, S. 2006, *ApJL*, 646, L37
- [Madore 1977] Madore, B. F. 1977, *MNRAS*, 178, 1
- [Magorrian et al. 1998] Magorrian, J., Tremaine, S., Richstone, D., Bender, R., Bower, G., Dressler, A., Faber, S.M., Gebhardt, K., Green, R., Grillmair, C., Kormendy, J., Lauer, T., 1998, *AJ*, 115, 2285
- [Maiolino et al. 2005] Maiolino, R., Cox, P., Caselli, P., Beelen, A., Bertoldi, F., Carilli, C., Kaufman, M.J., Menten, K.M., Nagao, T., Omont, A., Weiß, A., Walmsley, C.M., Walter, F., 2005, *AA*, 440, L51
- [Maiolino et al. 2007] Maiolino, R., Neri, R., Beelen, A., Bertoldi, F., Carilli, C.L., Caselli, P., Cox, P., Menten, K.M., Nagao, T., Omont, A., Walmsley, C.M., Walter, F., Weiß, A., 2007, *A&A*, 472, 33
- [Marconi & Hunt 2003] Marconi, A. & Hunt, L.K., 2003, *ApJ*, 589, L21
- [Martin 2005] Martin, C.L., 2005, *ApJ*, 621, 227
- [Mauersberger et al. 1999] Mauersberger, B., Henkel, C., Walsh, W., Schulz, A., 1999, *A&A*, 341, 256
- [Mayor et al. 2005] Mayor, L., Wadsley, J., Quinn, T., Stadel, J., 2005, *MNRAS*, 363, 641
- [McKee & Ostriker 1977] McKee, C. F., & Ostriker, J. P. 1977, *ApJ*, 218, 148
- [Mejia 2004] Mejia, A., 2004, PhD Thesis, Indiana University

- [Mihos & Hernquist 1994a] Mihos, J.C., Hernquist, L.E., 1994a, ApJ, 437, L47
- [Mihos & Hernquist 1994b] Mihos, J.C., Hernquist, L.E., 1994b, ApJ, 431, L9
- [Mihos & Hernquist 1994c] Mihos, J.C. & Hernquist, L., 1994, ApJ, 425, L13
- [Mihos & Hernquist 1996] Mihos, J.C., Hernquist, L.E., 1996, ApJ, 464, 641
- [Mirabel et al. 1990] Mirabel, I.F., Booth, R.S., Garay, G., Johansson, L.E.B., Sanders, D.B., 1990, A&A236,327
- [Misawa et al. 2005] Misawa, T., Eracleous, M., Charlton, J., Tajitsu, A., 2005, ApJ, 629, 115
- [Misawa et al. 2007a] Misawa, T., Charlton, J.C., Eracleous, M., Ganguly, R., Tytler, D., Kirkman, D., Suzuki, N., Lubin, D., 2007a, ApJ, in press [astro-ph/0702101]
- [Misawa et al. 2007b] Misawa, T., Eracleous, M., Charlton, J.C., Kashikawa, N., 2007b, ApJ, 660, 152
- [Moro-Martin et al. 2005] Morganti, T., Tadhunter, C.N., Oosterloo, T.A., 2005, A&A, 444, L9
- [Moro-Martin et al. 2005] Moro-Martin, A., Wolf, S., Malhotra, R., 2005, ApJ, 621, 1079
- [Myers et al. 2006] Myers, A. D., Brunner, R. J., Nichol, R. C., Richards, G. T., Schneider, D. P., & Bahcall, N. A. 2006, arXiv:astro-ph/0612190
- [Narayanan et al. 2004] Narayanan, D., Hamann, F., Barlow, T., Burbidge, E.M., Cohen, R.D., Junkkarinen, V., Lyons, R., 2004, ApJ, 601, 715

- [Narayanan et al. 2005] Narayanan, D., Groppi, C., Kulesa, C., Walker, C.K., 2005, 630, 269
- [Narayanan et al. 2006a] Narayanan, D., Cox, T.J., Robertson, B., Davé, R., Di Matteo, T., Hernquist, L., Hopkins, P., Kulesa, C., Walker, C.K., 2006a, ApJ, in press [astro-ph/0604074]
- [Narayanan et al. 2006b] Narayanan, D, Kulesa, C, Boss, A., Walker, C.K., 2006b, ApJ, 657, 1426
- [Narayanan et al. 2007a] Narayanan, D., Li, Y., Cox, T.J., Hernquist, L., Hopkins, P., Chakrabarti, S., Davé, R., Di Matteo, T., Gao, L., Kulesa, C., Robertson, B., Walker, C.K., 2007, ApJ, in press [arXiv:0707.3141]
- [Narayanan et al. 2007b] Narayanan, D., Cox, T.J., Kelly, B., Davé, R., Hernquist, L., Di Matteo, T., Hopkins, P.F., Kulesa, C., Robertson, B., Walker, C.K., 2007, ApJ, in press [arXiv:]
- [Nascimento Guimaraes et al. 2007] Nascimento Guimaraes, R. et al. 2007, MNRAS, in press [astro-ph/0702369]
- [Oppenheimer & Davé 2006] Oppenheimer, B.D., Davé, R., 2006, MNRAS, 373, 1265
- [Papadopoulos 2007] Papadopoulos, P.P., 2007, ApJ, 656, 792
- [Papadopoulos et al. 2007] Papadopoulos, P. P., Isaak, K. G., & van der Werf, P. P. 2007, ArXiv e-prints, 706, arXiv:0706.0811
- [Park & Hong 1998] Park, Y.-S., Hong, S.S., 1998, ApJ, 494, 605
- [Patel et. al. 2005] Patel, N., Curiel, S., Sridharan, T.K., Zhang, Q., Hunter, T., Ho, P., Torrelles, J., Moran, J., Gomez, J., Anglada, G., 2005, *Nature*, 437

- [Pelupessy et al. 2006] Pelupessy, F.I., Papadopoulos, P.P., van der Werf, P., 2006, *ApJ*, 645, 1024
- [Pettini et al. 2002] Pettini, M., Rix, S.A., Steidel, C.C., Hunt, M.P., Shapley, A., Adelberger, K.L., 2002, *Ap&SS*, 281, 461
- [Pollack et al. 1996] Pollack, J.B., Hubickyj, O., Bodenheimer, P., Lissauer, J.J., Podolak, M., Greenzweig, Y., 1996, *Icarus*, 124, 62
- [Polletta et al. 2006] Polletta, M., et al., 2006, *ApJ*, 2006, in press [*astro-ph/0602228*]
- [Porciani & Norberg 2006] Porciani, C., & Norberg, P. 2006, *MNRAS*, 371, 1824
- [Press & Schechter 1974] Press, W.H., Schechter, P., 1974, *ApJ*, 187, 425
- [Quinn 1984] Quinn, P.J., 1984, *ApJ*, 279, 596
- [Qi et al. 2003] Qi, C., Kessler, J.E., Koerner, D.W., Sargent, A.I., Blake, G.A., 2003, *ApJ*, 597, 986
- [Qi et al. 2004] Qi, C., Ho, P., Wilner, D., Takakuwa, S., Hirano, N., Ohashi, N., Bourke, T., Zhang, Q., Blake, G., Hogerheijde, M., Saito, M., Choi, M., Yang, J., 2004, *ApJ*, 616, L11
- [Qi et al. 2005] Qi, C., Wilner, D., Calvet, N., Bourke, T., Blake, G., Hogerheijde, M., Ho, P., Bergin, E., 2006, *ApJ* 636, 157
- [Rafikov 2003] Rafikov, R.R., 2003, *AJ*, 128, 1348
- [Richards et al. 2006] Richards, G.T., et al., 2006, *AJ*, 131, 2766
- [Riechers et al. 2006a] Riechers, D.A., Walter, F., Carilli, C., Weiß, A., Bertoldi, F., Menten, K., Knudsen, K., Cox, P., 2006a, *ApJ*, in press [*astro-ph/0605437*]

- [Riechers et al. 2006b] Riechers, D.A., Walter, F., Carilli, C., Knudsen, K., Lo, K.Y., Benford, D., Staguhn, J., Hunter, T., Bertoldi, F., Henkel, C., Menten, K., Weiß, A., Yun, M., Scoville, N.Z., 2006b, *ApJ*, in press [astro-ph/0606422]
- [Rigopoulou et al. 1996] Rigopoulou, D., Lawrence, A., White, G. J., Rowan-Robinson, M., Church, S.E., 1996, *A&A*, 305, 747
- [Robertson et al. 2006a] Robertson, B., Hernquist, L., Cox, T.J., Di Matteo, T., Hopkins, P.F., Martini, P., Springel, V., 2006a, *ApJ*, 641, 90
- [Robertson et al. 2006b] Robertson, B., Bullock, J., Cox, T.J., Di Matteo, T., Hernquist, L., Springel, V., Yoshida, N., 2006b, *ApJ*, 645, 986
- [Robertson et al. 2006c] Robertson, B., Cox, T.J., Hernquist, L., Franx, Marijn, Hopkins, P.F., Martini, P., Springel, V., 2006c, *ApJ*, 641, 21
- [Robertson et al. 2007] Robertson, B., Li, Y., Cox, T.J., Hernquist, L., Hopkins, P.F., 2007, *ApJ*, in press [astro-ph/0703456]
- [Rosolowsky 2005] Rosolowsky, E., 2005, *PASP*, 117, 1403
- [Rosolowsky 2007] Rosolowsky, E., 2007, *ApJ*, 654, 240
- [Rothberg & Joseph 2004] Rothberg, B., Joseph, R.D., 2004, *AJ*, 128, 2098
- [Rothberg & Joseph 2006] Rothberg, B., Joseph, R.D., 2006, *AJ*, 131, 185
- [Rupke et al. 2005a] Rupke, D., Veilleux, S., Sanders, D.B., 2005a, *ApJS*, 160, 87
- [Rupke et al. 2005b] Rupke, D., Veilleux, S., Sanders, D.B., 2005b, *ApJS*, 160, 115
- [Rupke et al. 2005c] Rupke, D., Veilleux, S., Sanders, D.B., 2005c, *ApJ*, 632, 751
- [Rupke & Veilleux 2005] Rupke, D., Veilleux, S., 2005, *ApJ*, 631, L37

- [Sakamoto et al. 1999] Sakamoto, K., Scoville, N.Z., Yun, M., Crosas, M., Genzel, R., & Tacconi, L.J., 1999, ApJ, 514, 68
- [Sakamoto et al. 2004] Sakamoto, K., Matsushita, S., Peck, A.B., Wiedner, M.C., Iono, D., 2004, ApJ, 616, L59
- [Sakamoto et al. 2006] Sakamoto, K., Ho, P.T.P., Peck, A., 2006, ApJ, 644, 862
- [Sanders et al. 1988a] Sanders, D.B., Soifer, B.T., Elias, J.H., Neugebauer, G., Matthews, K., 1988a, ApJ, 328, L35
- [Sanders et al. 1988b] Sanders, D.B., Soifer, B.T., Elias, J.H., Madore, B.F., Matthews, K., Neugebauer, G., Scoville, N.Z., 1988b, ApJ, 325, 74
- [Sanders et al. 1991] Sanders, D.B., Scoville, N.Z., Soifer, B.T., 1991, ApJ, 370, 158
- [Sanders et al. 1993] Sanders, D.B., in *Back to the Galaxy*, ed. F. Verter (Dordrecht: Kluwer), 1993, 311
- [Sanders & Mirabel 1996] Sanders, D.B., Mirabel, I.F., 1996, ARA&A, 34, 749
- [Sanders et al. 2003] Sanders, D.B., Mazzarella, J.M., Kim, D-C., Surace, J.A., Soifer, B.T., 2003, AJ, 126:1607
- [Saumon] Guillot 2004Saumon, D., Guillot, T., 2004, ApJ, 609, 1170
- [Schmidt 1959] Schmidt, M., 1959, ApJ, 129, 243
- [Schoier 2000] Schoier, F.L., 2000, Ph.D. Thesis, University of Stockholm
- [Schoier et al. 2005] Schoier, F.L., van der Tak, F.F.S., van Dishoeck, E.F., Black, J.H., 2005, A&A, 432, 369
- [Scoville 2003] Scoville, N., Young, J.S., 1983, ApJ, 265, 148 x

- [Scoville & Sanders 1987] Scoville, N.Z., Sanders, D., 1987, in *Interstellar Processes*, ed. H. Thronson & D. Hollenbach (Dordrecht: Reidel),21
- [Scoville et al. 1986] Scoville, N.Z., Sanders, D.B., Sargent, A.I., Soifer, B.T., Scott, S.L., Lo, K.Y., 1986, ApJ, 311, L47
- [Scoville et al. 1989] Scoville, N.Z., Sanders, D.B., Sargent, A.I., Soifer, B.T., Tinney, C.G., 1989, ApJ, 345,25
- [Scoville et al. 1995] Scoville, N.Z., Yun, M.S., Brown, R.L., Vanden Bout, P.A., 1995, ApJ, 449,L109
- [Scoville et al. 1997] Scoville, N.Z., Yun, M.S., Bryant, P.M., 1997, ApJ, 484, 702
- [Scoville et al. 2000] Scoville, N.Z., Evans, A.S., Thompson, R., Rieke, M., Hines, D.C., Low, F.J., Dinshaw, N., Surace, J.A., Armus, L., 2000, AJ, 119, 991
- [Scoville 2003] Scoville, N.Z., 2003, JKAS, 36:167
- [Seljak & Zaldarriaga 1996] Seljak, U., & Zaldarriaga, M., 1996, ApJ, 469, 437
- [Semenov et al. 2004] Semenov, D., Wiebe, D., Henning, Th., 2004, A&A, 417,93
- [Semenov et al. 2005] Semenov,D., Pavlyuchenkov, Ya., Schreyer, K., Henning, Th., Dullemond, C., Bacmann, A., 2005, ApJ, 621,853
- [Shapley et al. 2003] Shapley, A.E., Steidel, C.C., Pettini, M., Adelberger, K.L., 2003,ApJ, 588, 65
- [Shen et al. 2007] Shen, Y., Strauss, M., Oguri, M., Hennawi, J., Fan, X., Richards, G., Hall, P., Gunn, J., Schneider, D., Szalay, A., Thakar, A., Vanden Berk, D., Anderson, S., Bahcall, N., Connolly, A., Knapp, G., 2007, AJ, in press [astro-ph/0702214]

- [Sheth & Tormen 2002] Sheth, R.K., Tormen, G., 2002, MNRAS, 329, 61
- [Shields et al. 2006] Shields, G.,A., Menezes, K.L., Massart, C.A., Vanden Bout, P., 2006, ApJ, 641, 683
- [Shirley et al. 2003] Shirley, Y. L., Evans, N. J., II, Young, K. E., Knez, C., & Jaffe, D. T. 2003, ApJS, 149, 375
- [Sijacki et al. 2007] Sijacki, D, Springel, V., Di Matteo, T., Hernquist, L., 2007, MNRAS, submitted [astro-ph/0705.2238]
- [Silk & Rees 1998] Silk, J., Rees, M.J., 1998, A&A, 331, L1x
- [Silk & Spaans 1997] Silk, J., Spaans, M., 1997, ApJ, 488, L79
- [Smail 2006] Smail, I., 2006, in *Infrared Diagnostics of Galaxy Evolution*, ed. R.-R. Chary
- [Soifer et al. 1987] Soifer, B.T., Sanders, D.B., Madore, B.F., Neugebauer, G., Danielson, G.E., Elias, J.H., Lonsdale, C.J., Rice, W.L., 1987, ApJ, 320, 238
- [Solomon et al. 1987] Solomon, P.M., Rivolo, A.R., Barrett, J., Yahil, A., 1987, ApJ, 319, 730
- [Solomon & Barrett 1991] Solomon, P. M., & Barrett, J. W. 1991, Dynamics of Galaxies and Their Molecular Cloud Distributions, 146, 235
- [Solomon et al. 1992] Solomon, P.M., Downes, D., Radford, S.J.E., 1992, ApJ, 387, L55
- [Solomon et al. 1997] Solomon, P.M., Downes, D., Radford, S.J.E., Barrett, J.W., 1997, ApJ, 478, 144

- [Solomon & Vanden Bout 2005] Solomon, P.M., Vanden Bout, P., 2005, *ARA&A*, 43, 677
- [Soifer et al. 1987] Soifer, B.T., Sanders, D.B., Madore, B.F., Neugebauer, G., Danielson, G.E., Elias, J.H., Lonsdale, C.J., Rice, W.L., 1987, *ApJ*, 320, 238
- [Soifer et al. 1989] Soifer, B.T., Boehmer, L., Neugebauer, G., Sanders, D.B., 1989, *AJ*, 98, 3
- [Springel 2000] Springel, V. 2000, *MNRAS*, 312, 859
- [Springel 2005] Springel, V., 2005, *MNRAS*, 364, 1105
- [Springel & Hernquist 2002] Springel, V., Hernquist, L., 2002, *MNRAS*, 333, 649
- [Springel & Hernquist 2003] Springel, V., Hernquist, L., 2003, *MNRAS*, 339, 312
- [Springel & Hernquist 2005] Springel, V., Hernquist, L., 2005, *ApJ*, 622, L9
- [Springel et al. 2005a] Springel, V., Di Matteo, T., Hernquist, L., 2005a, *MNRAS*, 361, 776
- [Springel et al. 2005b] Springel, V., Di Matteo, T., Hernquist, L., 2005b, *ApJ*, 620L, 79
- [Springel & Hernquist 2005c] Springel, V., Hernquist, L., 2005, *ApJ*, 622, L98
- [Springel et al. 2005] Springel, V., White, S.D.M., Jenkins, A., Frenk, C., Yoshida, N., Gao, L., Navarro, J., Thacker, R., Croton, D., Helly, J., Peacock, J., Cole, S., Thomas, P., Couchman, H., Evrard, A., Pearce, F., 2005, *Nature*, 435, 639
- [Surace et al. 1998] Surace, J., Sanders, D.B., Vacca, W., Veilleux, S., Mazzarella, J., 1998, *ApJ*, 492, 116

- [Tacconi et al. 1999] Tacconi, L. J., Genzel, R., Tecza, M., Gallimore, J. F., Downes, D., & Scoville, N. Z. 1999, *Ap&SS*, 266, 157
- [Tacconi et al. 2006] Tacconi, L.J., Neri, R., Chapman, S.C., Genzel, R., Smail, I., Ivison, R.J., Bertoldi, F., Blain, A., Cox, P., Greve, T., Omont, A., 2006, *ApJ*, 640, 228
- [Tan 2000] Tan, J. C. 2000, *ApJ*, 536, 173
- [Taniguchi & Shioya 1998] Taniguchi, Y., Shioya, Y., 1998, *ApJL*, 501,L167
- [Tinney et al. 1990] Tinney C.G., Scoville, N.Z., Sanders, D.B., Soifer, B.T.,1990, *ApJ*, 362,473
- [Tran et al. 2001] Tran, Q.D., Lutz, D., Genzel, R., Rigopoulou, D., Spoon, H.W.W., Sturm, E., Gerin, M., Hines, D.C., Moorwood, A.F.M., Sanders, D.B., Scoville, N., Taniguchi, Y., Ward, M., 2001, *ApJ*, 552, 527
- [Tremonti et al. 2004] Tremonti, C. A., et al. 2004, *ApJ*, 613, 898
- [Tremonti et al. 2007] Tremonti, C.,A., Moustakas, J., Diamond-Stanic, A.M., 2007, *ApJ*, in press [arXiv0706.0527]
- [Trump et al. 2006] Trump, J.R., Hall, P.B., Reichard, T.A., Richards, G.T., Schneider, D.P., Vanden Berk, D.E., Knapp, G.R., Anderson, S.F., Fan, X., Brinkman, J., Kleinman, S.J., Nitta, A., 2006, *ApJS*, 165, 1
- [Udry et al. 2006] Udry, S., Fischer, D., Queloz, D., 2006, 'A Decade of Radial-Velocity Exoplanet Discoveries', in *Protostars and Planets V*
- [van Zadelhoff et al. 2002] van Zadelhoff, G-J., Dullemond, C., van der Tak, F.F.S., Yates, J.A., Doty, S.D., Ossenkopf, V., Hogerheijde, M.R., Juvela, M., Wiesemeyer, H., Schoier, F.L, 2002, *A&A*, 395, 373

- [Varniere et al. 2006] Varniere, P., Bjorkman, J.E., Frank, A., Quillen, A., Carciofi, A.C., Whitney, B., Wood, K., 2006, astro-ph/0508630
- [Veilleux et al. 2002] Veilleux, S., Kim, D.-C., Sanders, D.B., 2002, ApJS, 143, 315
- [Veilleux et al. 2005] Veilleux, S., Cecil, G., Bland-Hawthorn, J., 2005, ARA&A, 43, 769
- [Volonteri & Rees 2005] Volonteri, M., Rees, M.J., 2005, ApJ, 633, 624
- [Wada & Tomisaka 2005] Wada, K., Tomisaka, K., 2005, ApJ, 619, 93
- [Wagg et al. 2005] Wagg, J., Wilner, D. J., Neri, R., Downes, D., & Wiklind, T. 2005, ApJL, 634, L13
- [Wagg et al.2007] Wagg, J., Hughes, D. H., Aretxaga, I., Chapin, E. L., Dunlop, J. S., Gaztañaga, E., & Devlin, M. 2007, MNRAS, 375, 745
- [Walker et al. 1990] Walker, C.K., Adams, F.C., Lada, C.J., 1990, ApJ, 349, 515
- [Walker et al. 1994] Walker, C.K., Narayanan, G., Boss, A.P., 1994, ApJ, 431,767
- [Walker et al. 1994] Walker, C.K., Maloney, P.R.,Serabyn, E., 1994, ApJ, 437, L127
- [Walter et al. 2002] Walter, F., Weiß, A., Scoville, N., 2002, ApJ, L21-L25
- [Walter et al. 2003] Walter, F., Bertoldi, F., Carilli, C., Cox, P., Lo, K.Y., Neri, R., Fan, X., Omont, A., Strauss, M., Menten, K., 2003, *Nature*, 424, 406
- [Walter et al. 2004] Walter, F., Carilli, C., Bertoldi, F., Menten, K., Cox, P., Lo, K.Y., Fan, X., Strauss, M., 2004, ApJ, 615,L17
- [Ward-Thompson et al. 1994] Ward-Thompson, D., Scott, P.F., Hills, R.E., Andre, P., 1994, MNRAS, 268, 276

- [Wang et al. 2001] Wang, Z., Scoville, N.Z., Sanders, D.B., 1991, ApJ, 368,112
- [Wang et al. 2004] Wang, J., Zhang, Q., Wang, Z., Ho, P.T.P., Fazio, G., Wu, Y., 2004, ApJ, 616L, 67
- [Wang et al. 2007] Wang, R., Carilli, C., Beelen, A., Bertoldi, F., Fan, X., Walter, F., Menten, K., Omont, A., Cox, P., Strauss, M., Jiang, L., 2007, AJ, [astro-ph 0704.2053]
- [Weil & Hernquist 1992] Weil, M., Hernquist, L., 1992, Nature, 358, 734
- [Weil & Hernquist 1993] Weil, M., Hernquist, L., 1993, ApJ, 405, 142
- [Weiß et al. 2005a] Weiß, A., Downes, D., Walter, F., Henkel, C., 2005a, A&A, 440,L45
- [Weiß et al. 2005b] Weiß, A., Walter, F., Scoville, N.Z., 2005b, A&A, 438, 533
- [Weiß et al. 2007] Weiß, A., Downes, D., Neri, R., Walter, F., Henkel, C., Wilner, D.J., Wagg, J., Wiklind, T., 2007, A&A, in press [arXiv:astro-ph/0702669]
- [Willott et al. 2003] Willott, C.J., McLure, R.J., Jarvis, M.J., 2003, ApJ, 587, L15
- [Wolf & D'Angelo 2005] Wolf, S., D'Angelo, G., 2005, ApJ, 619, 1114
- [Wise et al. 2004] Wise, J.H., Eracleous, M., Charlton, J., Ganguly, R., 2004, ApJ, 613, 129
- [Wu et al. 2005] Wu, J., Evans, N.J., II, Gao, Y., Solomon, P.M., Shirley, Y.L., Vanden Bout, P.A., 2005, ApJ, 635, L173
- [Wu 2007] Wu, X-B., 2007, ApJ, 657, 177

- [Yamada et al. 2007] Yamada, M., Wada, K., & Tomisaka, K. 2007, ArXiv e-prints, 708, arXiv:0708.1045
- [Yao et al. 2003] Yao, L., Seaquist, E.R., Kuno, N., Dunne, L., 2003, ApJ, 588, 771
- [Yoshida et al. 2006] Yoshida, N., Omukai, K., Hernquist, L., Abel, T., 2006, ApJ, in press [astro-ph/0606106]
- [Young & Scoville 1982] Young, J., Scoville, N., 1982, ApJ, 258,467
- [Young et al. 1995] Young, J. et al. 1995, ApJS, 98,219
- [Yun & Scoville 1998] Yun, M., Scoville, N.Z., 1998, ApJ, 507,774